Title 40 CFR Part 191
Subparts B and C
Compliance Recertification Application 2026
for the
Waste Isolation Pilot Plant

Appendix SOTERM-2026
Actinide Chemistry Source Term

United States Department of Energy
Waste Isolation Pilot Plant

Carlsbad Field Office
Carlsbad, New Mexico

Compliance Recertification Application 2026
Appendix SOTERM-2026
Actinide Chemistry Source Term

Table of Contents

SOTERM-1.0 Introduction 1
SOTERM-2.0 Ambient Geochemical Conditions, Repository Conditions, Emplacement Chemistry, and Processes that Affect the WIPP Actinide Source Term 3
SOTERM-3.0 Post-emplacement Inventory, Chemical, and Radiolytic Processes 8
SOTERM-3.1 Effects of the Updated Inventory and Change to the Minimum Brine Volume for a DBR on the Actinide Source Term 8
SOTERM-3.2 WIPP Brine Chemistry 9
SOTERM-3.3 Complexation of Actinides by Organic Complexing Agents 10
SOTERM-3.3.1 Projected Concentration of Organic Complexing Agents under WIPP-relevant Conditions 10
SOTERM-3.3.2 Stability Constants for Organic Complexation with Actinides 11
SOTERM-3.3.3 New Literature on Organic Complexation Studies Since CRA-2019 11
SOTERM-3.3.4 WIPP-specific Data on Organic Complexation Effects Since CRA-2019 12
SOTERM-3.4 Radiolysis Effects on the Disposal System 13
SOTERM-3.4.1 Radiation Chemistry of Brine Systems 13
SOTERM-3.4.2 Potential Radiolytic Effects on Actinide Speciation and Solubility 13
SOTERM-3.4.3 WIPP-specific Data Since the CRA-2019 14
SOTERM-3.5 Actinide Colloids 18
SOTERM-3.5.1 Actinide Colloids in WIPP-related and WIPP-specific Conditions Since the CRA-2019 19
SOTERM-4.0 Microbial Effects in the WIPP 23
SOTERM-4.1 Microbial Viability and Constraints on Activity 23
SOTERM-4.1.1 Studies on Microbial Viability and Activity Since the CRA-2019 23
SOTERM-4.1.2 Metabolic and Energetic Constraints in the Near-field 26
SOTERM-4.2 Implications for Gas Generation from the Biodegradation of CPR and the Actinide Source Term 27
SOTERM-4.3 Microbial-Actinide Interactions 29
SOTERM-4.3.1 Actinide Toxicity Towards Microorganisms in the Disposal System 29
SOTERM-4.3.2 Bioreduction of Multivalent Actinides 29
SOTERM-4.3.3 Biological Influence on Actinide Solubility via Association, Induced Precipitation, or Mineralization 30
SOTERM-4.3.4 New Information on Microbial Colloids Since CRA-2019 30
SOTERM-5.0 WIPP-Relevant Actinide Chemistry 34
SOTERM-5.1 Actinide Inventory in the WIPP 34
SOTERM-5.2 Thorium Chemistry: Background and Behavior under Repository Conditions 38
SOTERM-5.2.1 Literature Review Since the CRA-2019 39
SOTERM-5.2.2 WIPP-specific Results Since the CRA-2019 40

SOTERM-5.3 Uranium Chemistry: Background and Behavior under Repository Conditions 40
SOTERM-5.3.1 Literature Review Since the CRA-2019 44
SOTERM-5.3.2 WIPP-specific Results Since the CRA-2019 46
SOTERM-5.4 Neptunium Chemistry: Background and Behavior under Repository Conditions 52
SOTERM-5.4.1 Literature Results Since the CRA-2019 54
SOTERM-5.4.2 WIPP-specific Results Since the CRA-2019 55
SOTERM-5.5 Plutonium Chemistry: Background and Behavior under Repository Conditions 66
SOTERM-5.5.1 Thermodynamic Stability of Higher-valent Plutonium: PuO_{2+x} 69
SOTERM-5.5.2 Literature Results Since the CRA-2019 69
SOTERM-5.5.3 WIPP-specific Results Since the CRA-2019 74
SOTERM-5.6 Americium and Curium Chemistry: Background and Behavior under Repository Conditions 81
SOTERM-5.6.1 Literature Results Since the CRA-2019 82
SOTERM-5.6.2 WIPP-specific Results Since the CRA-2019 PA 85
SOTERM-6.0 the WIPP Actinide Source Term 91
SOTERM-6.1 The WIPP Conceptual Models and the Actinide Source Term 91
SOTERM-6.2 Changes Implemented for the CRA-2026 92
SOTERM-6.3 Oxidation State Distributions 93
SOTERM-6.4 Actinide Speciation Reactions Used in CRA-2026 94
SOTERM-6.4.1 The Trivalent Actinides: Ac(III), Pu(III), Am(III), Cm(III) 94
SOTERM-6.4.2 The Tetravalent Actinides: Th(IV), U(IV), Pu(IV), Np(IV) 96
SOTERM-6.4.3 The Pentavalent Actinides: Np(V) 97
SOTERM-6.4.4 The Hexavalent Actinides: U(VI) 99
SOTERM-6.5 Calculating the Actinide Source Term 99
SOTERM-6.5.1 Actinide Solubilities 99
SOTERM-6.5.2 The Dissolved Actinide Source Term 100
SOTERM-6.5.3 The Colloidal Actinide Source Term 101
SOTERM-6.5.4 The Actinide Source Term 101
SOTERM-7.0 References 106

List of Figures

Figure SOTERM-1. A) Structure of Fully Protonated EDTA Ligand and EDTA-Metal Chelate. B) Structure of Fully Protonated DOTA Ligand and DOTA-Metal Chelate (Favela Morales and Lucchini 2024). 14

Figure SOTERM-2. HPLC Chromatograms of A) 3.5 mM EDTA Standard and B) Irradiated 2.5 mM EDTA Solution (from Favela Morales and Lucchini 2024). 15

Figure SOTERM-3. EDTA Calibration Curve (Black Dots) with Plotted Irradiated Data Points (Red Dots, A and B). A) 5.0 mM Diluted to 2.5 mM and B) 50.0 mM Diluted to 5.0 mM. Data Were Regressed through the Origin (from Favela Morales and Lucchini 2024). 16

Figure SOTERM-4. HPLC Chromatograms of A) 3.0 mM Citrate Standard, Showing Peaks at 1.20 min and 2.15 min Belonging to Sodium Citrate (mass-to-charge ratio (m/z): 294.9407) and Citric Acid (m/z: 193.0355), Respectively, and B) Irradiated 1.79 mM Solution, Showing the Two Starting Material Peaks Along with Two New, Large Peaks at 1.73 min and 1.98 min. Note that Higher Peak Area Corresponds to Decreased Degradation (from Favela Morales and Lucchini 2024). 17

Figure SOTERM-5. Citrate Calibration Curve (Black Dots) with A) 1.79 mM Irradiated Data Point, B) 17.9 mM Diluted to 1.79 mM Irradiated Data Point, and C) 50.0 mM Diluted to 2.50 mM Irradiated Data Point. The Data Were Regressed Through the Origin (from Favela Morales and Lucchini 2024)..... 18

Figure SOTERM-6. 3D Image Showing Data for Various Briny Matrices. Green Dots are Data Projected Into the *x,y* and *y,z* Planes. Dashed Lines Mark the Upper and Lower Limits of the Chaotrope/Kosmotrope Ratio (i.e., “Habitability Index”) and the Water Activity Limit. Between the Two Dashed Lines on the log(C/K) Axis, Growth is Minimal and/or Questionable. Cyan = WIPP-relevant Brines (Simulated Brines, Seeps, Fluid Inclusions); Light Blue = Brines from Boulby Salt Mine in UK; Royal Blue = German Brines (Q, Asse Salt Mine); Red = Experimental Broths; Gray = Cement-reacted Brines (Kienzler et al. 2000); Black = Cement/MgO-reacted WIPP Brines. See Swanson (2022) Appendix C for All Data and Associated References. 25

Figure SOTERM-7. Percent of Biologically Influenced Neodymium in Experiments with WIPP Halite Isolates Over the Course of the First Week, in Simple NaCl Solutions. Results from Experiments with *Bacillus* Spores are Also Included for Comparison (from Swanson 2024a). 32

Figure SOTERM-8. Comparison of the Percent of Biologically Influenced Nd by All Tested Organisms in Simple NaCl (circles), GWB (squares), and ERDA-6 (triangles) (from Swanson 2024a). *Halobacterium* sp. Results (from Swanson et al. 2019) are Provided for Comparison. 33

Figure SOTERM-9. Graphical Representation of the Sum of CH and RH Actinide Activities over Time (in Total Ci), from Tables 5-3 and 5-4 of the IS PAIR 2024 (after Van Soest 2025). Actinides are Discussed in Sections 5.2–5.6. 37

Figure SOTERM-10. Uranium Concentration in ERDA-6 (Filled Symbols) and GWB (Open Symbols) Versus pC_{H+} in N_2 Controlled Atmosphere, in the Presence or Absence of Carbonate (2×10^{-4} M and 2×10^{-3} M). The Carbonate Systems' Data Correspond to 17 Samplings Performed Over 994 Days. (See Lucchini et al. 2010a for the Determination of Uncertainties) (from Lucchini et al. 2013a). 43

Figure SOTERM-11. Effect of Borate Concentration (mM) on [U] Solubility as a Function of Time in pC_{H+} 9 Brine. B Denotes Borate. 0-10-50-100 Denotes the Borate Concentrations in Solution. Error bars represent the standard deviation from the mean of 4-6 replicate measurements (Kutahyali Aslani 2024)..... 47

Figure SOTERM-12. Effect of Presence of Organics on [U] Solubility as a Function of Time in pC_{H+} 9 Brine. ORG: Organics, AC: Acetate, OX: Oxalate, CIT: Citrate (from Kutahyali Aslani 2024)..... 48

Figure SOTERM-13. Effect of Presence of Citrate Alone and All Organics on [U] Solubility as a Function of Time (a) and pC_{H+} (b) in WIPP-specific Brines (from Kutahyali Aslani 2025). 49

Figure SOTERM-14. Effect of Presence of Citrate Alone and All Organics on [U] Solubility as a Function of Time (a) and pC_{H+} (b) in 5 M NaCl (from Kutahyali Aslani 2025). 51

Figure SOTERM-15. Solubility of $NpO_2(OH)_{(am, fresh)}$ in the Absence and Presence of Organic Ligands (Citrate: 2.30×10^{-3} M, Acetate: 2.83×10^{-2} M, Oxalate: 1.13×10^{-2} M, EDTA: 7.92×10^{-5} M), and Carbonate (16×10^{-3} M) in Synthetic WIPP Brine and 5 M NaCl Solutions as a Function of Time (a) and pC_{H+} (b). The Maximum Uncertainty is ± 15 % (from Kaplan 2025a). 57

Figure SOTERM-16. Solubility of $NpO_2(OH)(am)$ in the Presence of $[B]_{tot}$ ($0 \le [B]_{tot} \le 160$ mM) in 5 M NaCl Solutions as a Function of pC_{H+} Determined Herein (as Colored Triangles), as well as Previous Experimental Solubility Data in the Presence and Absence of Borate (Petrov et al. 2017; Hinz et al. 2020) (Half-Shaded Diamonds) (a). Solubility of $NpO_2(OH)_{(am)}$ in Synthetic WIPP Brine in the Presence and Absence of 160 mM Borate as a Function of pC_{H+} is Also Illustrated (b). Maximum Uncertainty is ± 15 % (from Kaplan 2025a). 58

Figure SOTERM-17. Solubility of $NpO_2(OH)(am)$ in the Presence of 1 mM $\le [CO_3^{2-}]_{tot} \le$ 100 mM in 5 M NaCl as a Function of pC_{H+}. Maximum Error is ± 15 % (from Kaplan 2025a). 60

Figure SOTERM-18. Np L_{III}-edge XANES Spectra of Solid and Aqueous Np(IV) and Np(V) References and Experimental Samples with Corresponding Linear Combination Fits (from Kaplan 2025a [present work]). 61

Figure SOTERM-19. EXAFS Data Summary. Panel a: Np L_{III}-edge EXAFS Spectra with Corresponding EXAFS FT: exp. (Experimental) Data and Best Fit of Investigated Sample Np(V) in Synthetic WIPP Brine at pC_{H+} 9 with 16 mM Carbonate and Considering Np-C Shell. Panel b: Same Sample but Not Considering Np-C Shell During EXAFS Calculation. Panel c: Np L_{III}-edge EXAFS Spectra with Corresponding EXAFS FT: exp. Data and Best Fit

of Investigated Sample Np(IV)O_2(cr). Data Magnitude (mag) (Black), Model Magnitude (Blue), Data "Real Part" (Red) and Model "Real Part" (Green). The "Real Part" of the FT Provides Information on the Distances to Neighboring Atoms (i.e., Bond Lengths) and Their Scattering Properties; This Shows the Contribution of Different Atomic Shells to the Overall EXAFS Signal. Also Shown are Single Scattering Paths (from Kaplan 2025a) R, Interatomic Distance; Δ, Deviation of R from the Reference. 63

Figure SOTERM-20. Experimental Solubility Data for Pu Reported in the Literature. The Solubility Models are Calculated Using Selected Pu Solid-Phase Analogs Used in the WIPP Model to Represent Bounding Solubility Behavior Under WIPP Conditions. Solid Lines Show the Calculated Solubility of PuO_2(am,hyd)(black) and Pu(OH)$_3$(am)(grey) at *I* = 0. The Dotted Line Represents the Solubility of PuO_2(am,hyd) at *I* = 5.0 M NaCl in Equilibrium with $[Pu]_{tot}$ = Pu(III)(aq) + Pu(IV)(aq) at pe + pH = 2. The Dashed Gray Line Shows the Solubility of Pu(OH)$_3$(am) at *I* = 5.0 M NaCl in Equilibrium with $[Pu]_{tot}$ = Pu(III)(aq) (from Appendix SOTERM-2019). Differences Between the Curves Reflect Not Only Ionic Strength Effects but also Differences in Redox Conditions and Aqueous Speciation 68

Figure SOTERM-21. Preparation of Samples for XAS Analysis of Pu Oxidation State (from Kaplan 2025b). 75

Figure SOTERM-22. Background-subtracted and Normalized Pu L_{III}-Edge XANES Spectra, Obtained by Measuring the Solid Phase in the Solubility Experiments in the Presence of Fe^0 and Organics, are Shown Together with the Corresponding LCF. Experimental Data are Compared with the Corresponding Linear Combination Fits of Pu(III), Pu(IV). Contributions of the Individual Components are Included (from Kaplan 2025b). 76

Figure SOTERM-23. Background-subtracted and Normalized Pu L_{III}-Edge XANES Spectra, Obtained by Measuring the Solid Phase in the Solubility Experiments in the Presence of Magnetite and Organics, are Shown Together with the Corresponding LCF. Experimental Data are Compared with the Corresponding Linear Combination Fits of Pu(III), Pu(IV). Contributions of the Individual Components are Included (from Kaplan 2025b). 77

Figure SOTERM-24. The Oxidation State Distribution of Pu in % (± 10%) in Both Precipitate Solid Phases and on the Surface of Iron Corrosion Products in the Presence and Absence of Organics (Modified from Kaplan 2025b). 78

Figure SOTERM-25. Pu Solubility as a Function of pC_{H+} a) in Different WIPP Brines in the Presence and Absence of Organics and Iron Corrosion Products (Fe^0 and Magnetite; Maximum Error of ± 15 %) and b) Reported in the Literature for Pu in Alkaline Systems (from Kaplan 2025b). 80

Figure SOTERM-26. XRD Patterns of Crystalline (Blue) and Amorphous (Black) Nd(OH)$_3$ 85

Figure SOTERM-27. [Nd] as a Function of pC_{H+} in 0.1 M NaCl (A) and 5 M NaCl (B). 01M and 5M Denote 0.1 M and 5 M NaCl, O Denotes Organics (EDTA and Citrate), am and Cr Denote Amorphous and Crystalline, Respectively (After ~250 Days of Equilibration) (from Kutahyali Aslani 2022) 87

Figure SOTERM-28. [Nd] as a Function of pC_{H+}-specific WIPP Brines. X denotes pC_{H+} 7, 9 and 11, O Denotes Organics (EDTA and Citrate) and am Denotes Amorphous (After ~250 Days of Equilibration) (from Kutahyali Aslani 2022). 88

Figure SOTERM-29. [Nd] as a Function of Time in 0.1 M NaCl. 01M Denotes 0.1 M NaCl, O Denotes Organics (EDTA and Citrate), am and Cr Denote Amorphous and Crystalline, Respectively (from Kutahyali Aslani 2022). 89

Figure SOTERM-30. [Nd] as a Function of Time in 5 M NaCl. 5M Denotes 5 M NaCl, O Denotes Organics (EDTA and Citrate), am and Cr Denotes Amorphous and Crystalline, Respectively (from Kutahyali Aslani 2022). 89

Figure SOTERM-31. [Nd] Concentration as a Function of Time in pC_{H+}-specific Brines. X Denotes 7, 9 and 11, O Denotes Organics (EDTA and Citrate) (from Kutahyali Aslani 2022). 90

List of Tables

Table SOTERM-1. WIPP Geochemical and Physical Conditions, Repository-Relevant Processes and Parameters, and Model Assumptions Relevant to the Actinide Source Term. 3

Table SOTERM-2. Simulated WIPP Brine Compositions as a Function of pC_{H+} (Lucchini et al. 2013c, Table 11). 10

Table SOTERM-3. Concentration Range of Acetate, Oxalate, Citrate, and EDTA in the Disposal System, (Domski 2025a). Based on the Minimum Brine Volume (1X = 6,314 m^3) and 5X the Minimum Brine Volume for DBR.* 11

Table SOTERM-4. Colloid Enhancement Parameters Used in CRA-2026 and CRA-2019 (Appendix SOTERM-2019)..... 21

Table SOTERM-5. CRA-2026 WIPP Radionuclide Inventory Decay-corrected to 2083 35

Table SOTERM-6. Selected Equilibrium Constants for Solubility and Hydrolysis Reactions of Uranium Considered for Thermodynamic Calculations (from NEA-TDB 2020). 41

Table SOTERM-7. Thermodynamic Data Relevant to Np Solubility and Reaction Chemistries (from NEA-TDB 2020)..... 53

Table SOTERM-8. Energy Positions of the Np L_{III}-edge XANES First Inflection Point and White Line Maximum for Aqueous and Solid Np(V) References, Seven Samples from the Present Work, and Two Reference Spectra (Np(IV) and Np(V)). Values in eV (Calibration Error ±0.4 eV). (from Kaplan 2025a). 61

Table SOTERM-9. Best-Fit of Np L_{III}–Edge EXAFS Model Parameters ($\boldsymbol{S02}$(k) = 0.9 Fixed) (from Kaplan 2025a) 65

Table SOTERM-10. Oxidation State Distribution of the Actinides in the WIPP Used in the CRA-2026 PA. 94

Table SOTERM-11. Solubility Constants and Formation Reactions of Am Species in the WIPP Model. 94

Table SOTERM-12. Predominant Species for the An(III) Actinides (Domski 2025a) 96

Table SOTERM-13. Solubility Constants and Formation Reactions of Th Species in the WIPP Model. 96

Table SOTERM-14. Predominant Species for the An(IV) Actinides (Domski 2025a) 97

Table SOTERM-15. Solubility Constants and Formation Reactions of Np Species in the WIPP Model. 98

Table SOTERM-16. Predominant Speciation for the An(V) Actinides in the WIPP (Domski 2025a). 99

Table SOTERM-17. Actinide Baseline Solubilities Calculated for the CRA-2019 PA (Domski and Sisk-Scott 2019), the RPPCR PA (Domski 2023b), and the CRA-2026 PA (Domski 2025a; King 2025). 100

Table SOTERM-18. Actinide Solubility and Colloidal Contributions for the CRA-2026 (U.S. DOE 2026, Appendix PA-4.4) 102

Table SOTERM-19. Concentrations (M) of Dissolved, Colloidal, and Total Mobile Actinides Obtained Using Median Parameter Values for the CRA-2019 PA and CRA-2026 PA (King 2019; 2025). 104

Acronyms and Abbreviations

%	percent
α	alpha particle
Å	Angstrom
Ac	acetate
Ae^{2+}	alkaline earth metal cation
a_w	water activity
(am)	amorphous phase
aq	aqueous
atm	atmosphere
β	(apparent) stability constant
°C	degrees Celsius
C	concentration
CAPHUM	maximum (cap) actinide concentration associated with mobile humic colloids
CAPMIC	maximum actinide concentration associated with microbes
CCA	Compliance Certification Application
CE-ICP-MS	capillary electrophoresis-inductively coupled plasma-mass spectrometry
CFR	Code of Federal Regulations
Ci	curie
Cit	citrate
CN	coordination number in EXAFS calculations
coll	colloid
CONCINT	actinide concentration associated with mobile actinide intrinsic colloids
CONCMIN	actinide concentration associated with mobile mineral fragment colloids
CPR	cellulosic, plastic, and rubber materials
(cr)	crystalline phase
CRA	Compliance Recertification Application
DBR	direct brine release
DFT	density functional theory
DNA	deoxyribonucleic acid
DOE	U.S. Department of Energy

DOTA	2,2′,2″,2‴-(1,4,7,10-Tetraazacyclododecane-1,4,7,10-tetrayl)tetraacetic acid
DRZ	disturbed rock zone
E_0'	standard potential
E_h	oxidation/reduction (redox) potential
EDTA	ethylenediaminetetraacetic acid
EPA	U.S. Environmental Protection Agency
EQ3/6	software program for geochemical modeling of aqueous systems
ERDA	Energy Research and Development Administration
eV	electron volt
EXAFS	extended X-ray absorption fine structure
°F	degrees Fahrenheit
FT	Fourier transform
γ	gamma
g	gram
(g)	gaseous (phase label, e.g., H_2(g))
G	molecular yield in molecules/100 eV of absorbed ionizing radiation
GEOCHEM	Appendix GEOCHEM, Implementation of Chemistry Conceptual Models
GWB	generic weep brine
HPLC-(MS)	high-performance liquid chromatography-(mass spectrometry)
I	ionic strength
ISA	isosaccharinic acid
K	degree Kelvin or stability constant
K_d	distribution coefficient
kg	kilogram
kGy	kilogray
K_{sp}	solubility product
L	liter, or ligand
LANL	Los Alamos National Laboratory
LCF(A)	linear combination fitting (analysis)
log	logarithm
$\log_{10}$	logarithm base 10

µm	micron, micrometer
m	meter, molal (mol·kg^{-1})
M	molarity; moles of solute per liter
M	metal
m^3	cubic meter
MeV	mega-electron volt
min	minute
mM	millimole per liter
mol	mole
mol·dm^{-3}	moles per cubic decimeter
MPa	megapascal
mV	millivolt
m/z	mass-to-change ratio
n	neutron, or number
N	degree of polymerization number; normality
nA	nanoamperes
NEA	Nuclear Energy Agency
NEA-TDB	Nuclear Energy Agency Thermochemical Database
nm	nanometer
nZVI	(nanoscale) zero-valent iron
O_{ax}	axial oxygen
O_{eq}	equatorial oxygen
PA	Performance Assessment
PAIR	Performance Assessment Inventory Report
pC_{H+}	negative logarithm of H^+ concentration in moles per liter
p_{CO2}	partial pressure of carbon dioxide
pe	negative logarithm of the electron activity (-log[e$^-$])
pH	negative logarithm of H^+ activity
pH_C	negative logarithm of H^+ concentration in moles per liter
pHm	negative logarithm of H^+ concentration in molal

PHUMCIM	proportionality constant for the actinide concentration associated with mobile humic colloids, in Castile brine
PHUMSIM	proportionality constant for the actinide concentration associated with mobile humic colloids, in Salado brine
pm	picometer
ppm	parts per million
PROPMIC	proportionality constant describing the bioassociation of actinides with mobile microorganisms
s	second
(s)_	solid
SEM-EDS	scanning electron microscopy-energy dispersive X-ray spectroscopy
SIT	Specific Ion Interaction Theory
SOTERM	Appendix SOTERM, Actinide Chemistry Source Term
T	temperature
t	time
$t_{½}$	half-life
TIC	total inorganic carbon
TODGA	N,N,N´,N´-tetraoctyldiglycolamide
TRLFS	time-resolved laser fluorescence spectroscopy
TRU	transuranic
UV-Vis-NIR	ultraviolet-visible-near infrared spectroscopy
V	volt
Vis-NIR	visible-near infrared spectroscopy
WL	white line
WIPP	Waste Isolation Pilot Plant
XAFS	X-ray absorption fine structure
XANES	X-ray absorption near edge structure
XAS	X-ray absorption spectroscopy
XPS	X-ray photoelectron spectroscopy
XRD	X-ray diffraction
yr	year

Elements and Chemical Compounds

Am	Americium
Am(III)	Americium in the +3 oxidation state
Am(IV)	Americium in the +4 oxidation state
Am(V)	Americium in the +5 oxidation state
Am(VI)	Americium in the +6 oxidation state
Am^{3+}	Americium cation, aqueous form of americium in the +3 oxidation state
$Am_2(C_2O_4)_3 \cdot 10H_2O$	Americium (III) oxalate decahydrate
$AmOHCO_3$	Americium (III) hydroxycarbonate
AmO_2^+	Americyl (V) ion, aqueous form of americium in the +5 oxidation state
AmO_2^{2+}	Americyl (VI) ion, aqueous form of americium in the +6 oxidation state
$AmOH^{2+}$	Americium (III) hydroxide cation – (1:1) complex
$Am(OH)_2^+$	Americium (III) hydroxide cation – (1:2) complex
$Am(OH)_3$	Americium hydroxide
$AmPO_4$	Americium (III) phosphate
$Am(SO_4)_n^{(3-2n)}$	Americium (III) sulfate complex with n = 1 or 2
An	General actinide
An(III)	General actinide in the +3 oxidation state
An(IV)	General actinide in the +4 oxidation state
An(V)	General actinide in the +5 oxidation state
An(VI)	General actinide in the +6 oxidation state
$An(V)O_2^+$ or AnO_2^+	Aqueous form of the actinide in the +5 oxidation state
$An(VI)O_2^{2+}$ or AnO_2^{2+}	Aqueous form of the actinide in the +6 oxidation state
$An(OH)_3$	Hydroxide of the actinide (III)
B	Boron
$B_4O_7^{2-}$	Tetraborate anion
$Br_2^{\bullet-}$	Bromine radical anion
Br^-	Bromide anion
C	Carbon

CH_4	Methane
$CH_3CO_2^-$	Acetate anion
$C_2O_4^{2-}$	Oxalate anion
$C_6H_5O_7^{3-}$	citrate
$C_6H_{12}O_6$	isosaccharinic acid, glucose
$C_{10}H_{16}N_2O_8$	ethylenediaminetetraacetic acid
Ca	Calcium
Ca(II)	Calcium in the +2 oxidation state
Ca^{2+}	Calcium cation
$CaCl_2$	Calcium chloride
$CaCO_3$	Calcium carbonate
$Ca[M(OH)_3]^{2+}$	Calcium metal (III) hydroxide cation – (1:1:3) complex
$Ca_2[M(OH)_4]^{3+}$	Calcium metal (III) hydroxide cation – (2:1:4) complex
$Ca_3[M(OH)_6]^{3+}$	Calcium metal (III) hydroxide cation – (3:1:6) complex
$Ca(OH)_2$	Calcium hydroxide
$Ca_xNpO_2(OH)_2 \cdot yH_2O$	Calcium neptunyl hydroxide hydrate
$Ca_3[NpO_2(OH)_5]_2$	Tricalcium bis(pentahydroxidoneptunate (V)
$CaNpO_2(OH)_xCl_y \cdot 2H_2O$	Calcium neptunyl hydroxychloride dihydrate
$Ca_4[Th(OH)_8]^{4+}$	Tetracalcium thorium (IV) hydroxide cation complex
$Ca_4Th(H_2ISA)_2$	Tetracalcium thorium di-isosaccharinic acid
$Ca_2UO_2(CO_3)_3 \cdot 10H_2O$	Dicalcium uranyl (VI) tricarbonate decahydrate, liebigite
$Ca_4[U(OH)_8]^{4+}$	Tetracalcium uranium (IV) hydroxide cation complex
Cf	Californium
Cl	Chlorine
$Cl\bullet$	Chlorine radical
Cl^-	Chloride ion
Cl_2	Molecular chlorine
Cl_2^-	Dichloride anion
Cl_3^-	Trichloride anion
$ClBr\bullet^-$	Chloro bromide radical
$ClBr^-$	Chloro bromide anion

ClO^-	Hypochlorite anion
ClO_2	Chlorine dioxide
ClO_2^-	Chlorine dioxide anion
ClO_3^-	Chlorate anion
ClO_4^-	Perchlorate anion
Cm	Curium
Cm(III)	Curium in the +3 oxidation state
$Cm(EDTA)^-$	Curium(III)-EDTA complex
$Cm(OH)_n(EDTA)^{1-n}$	Curium(III) hydroxy-EDTA complex
$Cm_2(C_2O_4)_3 \cdot 10H_2O$	Curium (III) oxalate decahydrate
CO_2	Carbon dioxide
CO_3^{2-}	Carbonate anion
Cs	Cesium
Eu	Europium
$Eu_2(CO_3)_3$	Europium carbonate
$Eu_2(C_2O_4)_3 \cdot 10H_2O$	Europium oxalate decahydrate, europium sesquioxalate decahydrate
Eu_2O_3	Europium oxide
$Eu(OH)_3$	Europium hydroxide
F^-	Fluoride anion
Fe	Iron
Fe^{2+}	Aqueous form of iron in the +2 oxidation state, ferrous cation
Fe^{3+}	Aqueous form of iron in the +3 oxidation state, ferric cation
Fe^0	Zero-valent iron, metallic iron
$Fe_2Cl(OH)_3$	Hibbingite, iron(II) hydroxy chloride
Fe(II)	Iron in the +2 oxidation state
Fe(III)	Iron in the +3 oxidation state
$Fe_2O_3 \cdot xH_2O$	Ferrihydrite, hydrated iron(III) oxide
$Fe(OH)_3$	Ferric hydroxide, iron(III) hydroxide
$Fe(OH)_2$	Ferrous hydroxide, iron(II) hydroxide
Fe(O)OH	Goethite, iron (III) oxide hydroxide

H	Hydrogen (atomic)
H•	Hydrogen radical
H^+	Hydrogen cation
^3H	Tritium
H_2	Hydrogen (molecular)
$H_2C_2O_4$	Oxalic acid
HCO_3^-	Bicarbonate anion, hydrogen carbonate anion
He^{2+}	Helium cation
H_2	Hydrogen
HF	Hydrofluoric acid
HNO_3	Nitric acid
H_2O	Water
$(H_3O)(UO_2)(PO_4)\cdot 3H_2O$	Chernikovite
H_2O_2	Hydrogen peroxide
HOCl	Hypochlorous acid
H_2S	Hydrogen sulfide
H_2SO_4	Sulfuric acid
K	Potassium
K^+	Potassium cation
KCl	Potassium chloride
$KNpO_2CO_3\cdot 2H_2O$	Potassium neptunyl (V) carbonate dihydrate
$K_3Na(UO_2)(CO_3)_3$	Tripotassium sodium triscarbonato dioxouranate (VI)
$K_3NpO_2(CO_3)_2\cdot 0.5H_2O$	Tripotassium neptunyl (V) dicarbonate hemihydrate
KOH	Potassium hydroxide
K_2SO_4	Potassium sulfate
$K_2U_2O_7$	Potassium diuranate
$K_2U_2O_7\cdot H_2O$	Potassium diuranate hydrate
La	Lanthanum
La_2O_3	Lanthanum oxide
$La(OH)_3$	Lanthanum hydroxide
Li	Lithium

Li^+	Lithium ion
Ln(III)	General lanthanide in the +3 oxidation state
$Ln_2(CO_3)_3 \cdot xH_2O$	Lanthanide carbonate hydrate
Mg	Magnesium
Mg^{2+}	Magnesium cation
$MgCl_2$	Magnesium chloride
$Mg_3Cl(OH)_5 \cdot 4H_2O$	Magnesium pentahydroxychloride tetrahydrate
$MgCO_3$	Magnesite, magnesium carbonate
$Mg_5(CO_3)_4(OH)_2 \cdot 4H_2O$	Hydromagnesite
MgO	Periclase, magnesium oxide
$Mg(OH)_2$	Brucite, magnesium hydroxide
$Mg_2(OH)_3Cl \cdot 4H_2O$	Magnesium chloride hydroxide hydrate, magnesium oxychloride
Mn	Manganese
N_2	Nitrogen (molecular)
Na	Sodium
Na^+	Sodium cation
$NaAm(CO_3)_2$	Sodium americium (III) carbonate
$Na_2CaUO_2(CO_3)_3 \cdot 6H_2O$	Disodium calcium uranyl tricarbonate hexahydrate, andersonite
NaCl	Sodium chloride, halite
$NaClO_4$	Sodium perchlorate
Na_2CO_3	Sodium carbonate
$NaHCO_3$	Sodium bicarbonate
$NaNO_3$	Sodium nitrate
$NaNpO_2$-borate	Sodium neptunyl (V) borate
$Na_3NpO_2(CO_3)_2$	Trisodium neptunyl (V) dicarbonate
$NaNpO_2CO_3 \cdot 3.5H_2O$	Sodium neptunyl (V) carbonate 3.5 hydrate
NaOH	Sodium hydroxide
Na_2SO_4	Sodium sulfate
$Na_2S_2O_4$	Sodium hydrosulfite
$Na_2U_2O_7 \cdot xH_2O$	Sodium diuranate hydrate
Nd	Neodymium

Nd^{3+}	Neodymium cation, aqueous form of Nd in the +3 oxidation state
Nd(III)	Neodymium in the +3 oxidation state
$NdCl_3$	Neodymium (III) chloride
$NdCl^{2+}$	Chloroneodymium (III) ion
$NdCl_3 \cdot 6H_2O$	Neodymium chloride hexahydrate
$NdCl_2^+$	Dichloroneodymium (III) ion
$Nd_2(C_2O_4)_3 \cdot 10H_2O$	Neodymium (III) oxalate decahydrate
$Nd(OH)_3$	Neodymium (III) hydroxide
$NdOH^{2+}$	Hydroxoneodymium (III) dication
$Nd(OH)_2^+$	Dihydroxoneodymium (III) cation
$Nd(OH)_2Cl$	Neodymium (III) hydroxychloride
$Nd(OH)_3 \cdot NdCl_3$	Neodymium (III) hydroxide chloride double salt
NO_3^-	Nitrate anion
Np	Neptunium
Np(IV)	Neptunium in the +4 oxidation state
Np(V)	Neptunium in the +5 oxidation state
Np(VI)	Neptunium in the +6 oxidation state
Np^{4+}	Neptunium cation, aqueous form of neptunium in the +4 oxidation state
$Np(CO_3)_4^{4-}$	Neptunium (IV) tetracarbonate ion
$Np(CO_3)_5^{6-}$	Neptunium (IV) pentacarbonate ion
NpO_2	Neptunium (IV) oxide
Np_2O_5	Neptunium (V) oxide
NpO_2^+ or $Np(V)O_2^+$	Neptunyl cation, aqueous form of neptunium in the +5 oxidation state
NpO_2^{2+} or $Np(VI)O_2^{2+}$	Neptunyl cation, aqueous form of neptunium in the +6 oxidation state
NpO_2Ac	Neptunyl (V) acetate
$NpO_2(Ac)_2^-$	Neptunyl (V) acetate
$NpO_2(CO_3)_2^{3-}$	Neptunyl (V) carbonate ion – (1:2) complex
$NpO_2(CO_3)_3^{5-}$	Neptunyl (V) carbonate ion – (1:3) complex
$Np(OH)_3^+$	Neptunium (IV) trihydroxide ion

$Np(OH)_3^{3+}$	Trihydroxo neptunium (VI) ion
$Np(OH)_4$	Neptunium (IV) tetrahydroxide
NpO_2OH	Neptunium (V) oxyhydroxide
$NpO_2(OH)_2^-$	Neptunium(V) dihydroxide anion
NpO_2Ox^-	Neptunyl (V) oxalate
O	Oxygen
O_2	Oxygen (molecular)
OBr^-	Hypobromite anion
OCl^-	Hypochlorite anion
OH^-	Hydroxide anion
OH•	Hydroxyl radical
Ox^{2-}, Ox^-	oxalate anion
Pb	Lead
$PbCO_3$	Lead (II) carbonate
$2PbCO_3.Pb(OH)_2$	Hydrocerussite
PbO	Lead (II) oxide
PO_4^{3-}	Phosphate anion
$Pr_2(C_2O_4)_3 \cdot 10H_2O$	Praseodymium (III) Oxalate decahydrate
Pu	Plutonium
Pu(III)	Plutonium in the +3 oxidation state
Pu(IV)	Plutonium in the +4 oxidation state
Pu(V)	Plutonium in the +5 oxidation state
Pu(VI)	Plutonium in the +6 oxidation state
Pu(VII)	Plutonium in the +7 oxidation state
Pu^{3+}	Plutonium cation, aqueous form of plutonium in the +3 oxidation state
$Pu(CO_3)_4^{4-}$	Plutonium (IV) tetracarbonate
$Pu(CO_3)_6^{5-}$	Plutonium (VII) hexacarbonate
$Pu_2(C_2O_4)_3 \cdot 10H_2O$	Plutonium (III) oxalate
$[Pu(NO_3)_6]^{2-}$	Plutonium (IV) hexanitrate dianion
PuO_2	Plutonium (IV) dioxide

$PuO_2 \cdot xH_2O$	Plutonium (IV) dioxide hydrate
PuO_{2+x}	Oxidized plutonium (IV) dioxide
PuO_2^+ or $Pu(V)O_2^+$	Plutonyl cation, aqueous form of plutonium in the +5 oxidation state
PuO_2^{2+} or $Pu(VI)O_2^{2+}$	Plutonyl cation, aqueous form of plutonium in the +6 oxidation state
$Pu(OH)_3$	Plutonium (III) hydroxide
$Pu(OH)_4$	Plutonium (IV) hydroxide
$Pu(OH)_2(CO_3)_2^{2-}$	Dihydroxo dicarbonatoplutonium (IV)
S^0	Elemental sulfur
S_x^{2-}	Polysulfide anion
$Si(OH)_4$	Silicon hydroxide
Sm	Samarium
$Sm_2(CO_3)_3$	Samarium carbonate
Sn(II)	Tin in the +2 oxidation state
$S_2O_3^{2-}$	Thiosulfate anion
SO_4^{2-}	Sulfate anion
SO_3^{2-}	Sulfite anion
Sr	Strontium
Th	Thorium
Th(IV)	Thorium in the +4 oxidation state
Th^{4+}	Thorium cation, aqueous form of thorium in the +4 oxidation state
$ThAcetate^{3+}$	Thorium acetate cation
$Th(Acetate)_2^{2+}$	Thorium acetate dication
$ThCitrate^+$	Thorium citrate cation
$Th(CO_3)_5^{6-}$	Thorium (IV) pentacarbonate anion
ThEDTA	Thorium EDTA complex
$ThLactate^{3+}$	Thorium lactate trication
$Th(Lactate)_2^{2+}$	Thorium lactate dication
ThO_2	Thorium dioxide
$ThO_2 \cdot 2H_2O$	Thorium dioxide dihydrate

$Th_6(OH)_{15}^{9+}$	Thorium (IV) hydroxide cluster
$Th(OH)_4$	Thorium hydroxide
$Th(OH)(CO_3)_4^{5-}$	Thorium (IV) hydroxide carbonate ion – (1:1:4) complex
$Th(OH)_3CO_3^-$	Thorium (IV) hydroxide carbonate ion – (1:3:1) complex
$Th(OH)EDTA^-$	Thorium (IV) hydroxy EDTA complex
$Th(OH)_2EDTA^{2-}$	Thorium (IV) hydroxy EDTA complex
$ThOxalate^{2+}$	Thorium oxalate dication
$Th(SO_4)_3^{2-}$	Thorium (IV) sulfate ion – (1:3) complex
$Th(SO_4)_2$	Thorium (IV) sulfate
$Th(SO_4)_2 \cdot 8H_2O$	Thorium sulfate octahydrate
$Th(SO_4)_2 \cdot 9H_2O$	Thorium sulfate nonahydrate
$Th(SO_4)_2 \cdot K_2SO_4 \cdot 4H_2O$	Thorium potassium sulfate tetrahydrate double salt
$Th(SO_4)_2 \cdot 2K_2SO_4 \cdot 2H_2O$	Thorium potassium sulfate dihydrate double salt
$Th(SO_4)_2 \cdot 3.5K_2SO_4$	Thorium potassium sulfate 3.5 hydrate double salt
$Th(SO_4)_2 \cdot Na_2SO_4 \cdot 6H_2O$	Thorium sodium sulfate hexahydrate double salt
Tm	Thulium
Tm_2O_3	Thulium (III) oxide
U	Uranium
U(III)	Uranium in the +3 oxidation state
U(IV)	Uranium in the +4 oxidation state
U(V)	Uranium in the +5 oxidation state
U(VI)	Uranium in the +6 oxidation state
U^{3+}	Uranium cation, aqueous form of uranium in the +3 oxidation state
U^{4+}	Uranium cation, aqueous form of uranium in the +4 oxidation state
$U(CO_3)_5^{6-}$	Uranium (IV) pentacarbonate anion
UO_2	Uraninite, uranium (IV) dioxide
UO_2^+	Uranyl (V) ion
UO_2^{2+} or $U(VI)O_2^{2+}$	Uranyl cation, aqueous form of uranium in the +6 oxidation state
UO_2CO_3	Rutherfordine, uranium (VI) carbonate
$UO_2(CO_3)_2^{2-}$	Uranyl (VI) dicarbonate ion – (1:2) complex

$UO_2(CO_3)_3^{4-}$	Uranyl (VI) tricarbonate ion – (1:3) complex or triscarbonato complex
$UO_2(CO_3)_3^{5-}$	Uranyl (V) tricarbonate ion - (1:3) complex or triscarbonato complex
$(UO_2)_3(CO_3)_6^{6-}$	Uranyl (VI) hexacarbonate ion – (3:6) complex
$(UO_2)_2(CO_3)(OH)_3^-$	Uranyl (VI) hydroxycarbonate ion – (2:1:3) complex
$(UO_2)_{11}(CO_3)_6(OH)_{12}^{2-}$	Uranyl (VI) hydroxycarbonate ion – (11:6:12) complex
$U(OH)_4$	Uranium (IV) hydroxide
$U(OH)_4(ISA)_2^{2-}$	Uranium (IV) hydroxide ISA complex
$UO_2(OH)^+$	Uranyl (VI) hydroxide ion, 1:1 complex
$UO_2(OH)_2$	Uranyl dihydroxide, dihydroxo-uranyl complex
$UO_2(OH)_3^-$	Uranyl (VI) hydroxide ion – (1:3) complex
$UO_2(OH)_4^{2-}$	Uranyl (VI) hydroxide ion – (1:4) complex
$(UO_2)_2OH^{3+}$	Uranyl (VI) hydroxide ion, 2:1 complex
$(UO_2)_2(OH)_2^{2+}$	Uranyl (VI) hydroxide ion, 2:2 complex
$(UO_2)_3(OH)_4^{2+}$	Uranyl (VI) hydroxide ion, 3:4 complex
$(UO_2)_3(OH)_5^+$	Uranyl (VI) hydroxide ion, 3:5 complex
$(UO_2)_3(OH)_7^-$	Uranyl (VI) hydroxide ion, 3:7 complex
$(UO_2)_4(OH)_7^+$	Uranyl (VI) hydroxide ion, 4:7 complex
$UO_2(OH)_3(ISA)_2^{3-}$	Uranyl (VI) hydroxide ISA complex
U_4O_9	Tetrauranium nonoxide, mixed-valence uranium oxide
$UO_2.xH_2O$	Hydrous uranium (IV) dioxide
$UO_3 \cdot xH_2O$	Metaschoepite, uranium (VI) trixodide hydrate
$UO_3 \cdot 2H_2O$	Schoepite, uranium (VI) trixodide dihydrate
Zr	Zirconium

SOTERM-1.0 INTRODUCTION

Appendix SOTERM-2026 (Actinide Chemistry Source Term) summarizes the U.S. Department of Energy's (DOE's) understanding of actinide chemistry and behavior in the Waste Isolation Pilot Plant (WIPP), with reference to the conceptual models for chemical conditions, dissolved actinides, colloid formation, and gas generation. The information in this Appendix supports the 2026 Compliance Recertification Application (CRA-2026) Performance Assessment (PA) (Appendix PA-2026). The actinide source term is a critical conceptual and process model for the WIPP and contributes to assessing compliance with 40 Code of Federal Regulations (CFR) Part 191 (U.S. EPA 1993).

For WIPP PA, the transuranic (TRU) radionuclides of primary consequence are the alpha (α)-emitting isotopes of plutonium (Pu), americium (Am), neptunium (Np), curium (Cm), and californium (Cf). These TRU actinides contribute to the waste unit factor (curies of TRU isotopes in the repository) used to calculate the normalized release from the disposal system in U.S. Environmental Protection Agency (EPA) units, as required by 40 CFR Part 191 (U.S. EPA 1993). In Appendix SOTERM-2026, the chemical behavior of thorium (Th) and uranium (U) is also discussed, since these actinides contribute to the radionuclide inventory and waste unit factor, and their chemistry is analogous to some TRU components. Based on concentration, solubility, activity, and the potential for colloid transport, the most important radioelements that contribute to the actinide source term and consequently impact the long-term performance of the WIPP are Pu and Am (Appendix PA-4.3).

The actinide source term is calculated to determine if potential cumulative releases at the land withdrawal boundary over the 10,000-year regulatory period are within specified limits. Three release pathways are considered in PA: 1) a direct brine release (DBR); 2) release through the Salado Formation and Culebra Dolomite Member; and 3) release from cuttings, cavings, and spallings (Appendix PA-2.1 and 7.2). The source term is calculated from the dissolved and colloidal species, and therefore, is only considered in the first two pathways.

Actinide chemistry and behavior in the disposal system are affected by site geochemical and physical conditions and site biology, the chemistry and biology of the emplaced waste, and interactions between the site and waste. These effects on the mobile source term will be reviewed in this appendix, as follows:

- A list of near-field geochemical and physical conditions that can affect actinide chemistry and behavior (Appendix SOTERM-2.0).
- An overview of brine chemistry; the conditions imposed by engineered barriers and emplaced waste; and the post-emplacement factors that can also affect actinide chemistry and behavior. These include changes resulting from the updated WIPP inventory (Van Soest 2025) and changes in the minimum volume required for a DBR (Brunell 2025), the presence of organic complexants (Van Soest 2025), and radiolysis (Appendix SOTERM-3.0).

- A description of microbial processes and their effects on actinides in the source term (Appendix SOTERM-4.0).
- An updated actinide chemistry overview; a summary of new literature; and a summary of WIPP results for the key actinides since the CRA-2019 (Appendix SOTERM-5.0).
- A summary of how the current conceptual models and their assumptions inform the source term and the approach to calculating the source term (Appendix SOTERM-6.0).

Each of these sections identifies any important new information since the CRA-2019 (U.S. DOE 2019).

SOTERM-2.0 AMBIENT GEOCHEMICAL CONDITIONS, REPOSITORY CONDITIONS, EMPLACEMENT CHEMISTRY, AND PROCESSES THAT AFFECT THE WIPP ACTINIDE SOURCE TERM

The actinide source term is affected by near-field geochemical conditions, repository conditions, emplacement chemistry, engineered processes, and other chemical, physical, and biological processes expected to occur in the repository. Geochemical conditions, the expected repository conditions, and PA assumptions have been discussed in detail previously in the Compliance Certification Application (CCA; U.S. DOE 1996) and subsequent recertification applications (CRA-2004 [U.S. DOE 2004], Chapters 2 and 6; CRA-2019 [U.S. DOE 2019] Appendix SOTERM-2.0) and are summarized in Table SOTERM-1, along with cross-references to CRA-2026 Appendix GEOCHEM and other appendices.

Table SOTERM-1. WIPP Geochemical and Physical Conditions, Repository-Relevant Processes and Parameters, and Model Assumptions Relevant to the Actinide Source Term.

Repository Condition, Parameter, or Process	Integration into CRA-2026 PA	Appendix Referenced-2026 (unless otherwise specified)	Changes since CRA-2019
Ambient Geochemistry	Predominantly halite of the Salado Formation, with clay/anhydrite interbeds and inclusions; accessory evaporite minerals include anhydrite, gypsum, polyhalite, magnesite, and clays.	CRA-2019, Appendix GEOCHEM-1.2.1 and -1.2.2	None
Temperature	Ambient temperature is 27 degrees Celsius (°C), ~81 degrees Fahrenheit (F°). A transient increase of up to 11 °C (~ 52 F°) is possible as a result of various exothermic reactions of waste materials.	Appendix GEOCHEM-2.1.2; CRA-2019, Appendix GEOCHEM-1.2.5.2; Appendix SCR-6.3.4.1.4.7 and 6.5.1.2.4	None

Repository Condition, Parameter, or Process	Integration into CRA-2026 PA	Appendix Referenced-2026 (unless otherwise specified)	Changes since CRA-2019
Humidity	~73 percent (%) relative humidity at the repository temperature.	CRA-2019, Appendix GEOCHEM-1.2.5.3	None
Water Content	Host rock is groundwater-saturated with inclusions in the salt that range from 0.057% to 3% by mass. Repository is initially unsaturated until intrusion occurs. An intrusion is not expected to occur until after active institutional control ceases (100 years after closure).	CRA-2019, Appendix GEOCHEM-1.2.5.3 and 1.2.2	None
Pressure	A maximum pressure in the repository of about 15 megapascals (MPa) (148 atmospheres [atm]), equivalent to the lithostatic stress at the repository level; a hydrostatic pressure of about 8 MPa (79 atm) at the bottom of an intrusion borehole at repository depth.	CRA-2019, Appendix GEOCHEM-1.2.5.1	None
Gas Phase	Initially oxic at repository closure but rapidly transitions to an anoxic atmosphere dominated by hydrogen (H_2) with smaller amounts of methane (CH_4) and nitrogen (N_2). Trace amounts of carbon dioxide (CO_2), hydrogen sulfide (H_2S), and other microbially generated gases may be present.	Appendix GEOCHEM-2.0	None
Disturbed Rock Zone (DRZ)	Upper bound of 12 meters (m) above the repository and 2 m below the repository horizon.	CRA-2019, Appendix PA-4.2.1; Brunell (2025)	None

Repository Condition, Parameter, or Process	Integration into CRA-2026 PA	Appendix Referenced-2026 (unless otherwise specified)	Changes since CRA-2019
Minimum Brine Volume for DBR	The calculated minimum volume of brine from any source needed for DBR release is 6,314 cubic meters (m^3). This volume is based on the 12-panel representation of an "interim state repository."	Appendix GEOCHEM-1.1.1; Appendix PA-1.0 and 1.3.1.6	From 17,400 m^3 to 6,314 m^3 (Brunell 2025)
WIPP Brine	High ionic strength Salado and Castile Formation brines that vary with pH and reaction with magnesium oxide (MgO) but are bracketed by generic weep brine (GWB) and Energy Research and Development Administration (ERDA)-6 brine formulations used in the WIPP project.	Appendix GEOCHEM-3.1.1 and 3.2.1	None
pH	The expected pH is ~9 (ionic strength-corrected to pC_{H+} of 9.5) and controlled by MgO.	Appendix GEOCHEM-3.3	None
MgO	Engineered barrier for the WIPP that will sequester CO_2 and control pH by precipitating brucite $Mg(OH)_2$, hydromagnesite $Mg_5(CO_3)_4(OH)_2{\cdot}4H_2O$, and magnesite $MgCO_3$.	Appendix GEOCHEM-3.0 and 3.1.4	See Appendix MgO-2026
Corrosion	Container steel and metals in WIPP waste will react to remove oxygen and produce H_2. These produce Fe(II) phases, which can give rise to mixed Fe(II)/Fe(III) phases.	Appendix GEOCHEM-2.1.3, CRA-2019, Appendix GEOCHEM-2.2.1 and 3.2.8	Iron reactants; see Appendix GEOCHEM-2026

Repository Condition, Parameter, or Process	Integration into CRA-2026 PA	Appendix Referenced-2026 (unless otherwise specified)	Changes since CRA-2019
Iron (Fe) and Lead (Pb) Chemistry	Iron and lead can affect the source term through sorption processes and competition for ligands, but this chemistry is selectively implemented in PA. Iron corrosion products can affect the redox potential in the repository.	Appendix GEOCHEM-6.1; CRA-2019, Appendix GEOCHEM-4.1.6 and 4.1.7	Iron and lead reactants; see Appendix GEOCHEM-2026
Organic Complexing Agents	The four organic complexing agents tracked in the inventory and addressed by PA are acetate, oxalate, citrate, and ethylenediaminetetraacetic acid (EDTA). These are assumed not to degrade under the expected WIPP conditions; their concentrations are defined by their inventory (except for oxalate, which is solubility-limited); these agents form complexes with actinides, increasing the source term.	Appendix GEOCHEM-3.1.5 and 4.1.6	None, except as affected by the new minimum volume required for DBR
Cellulosic, Plastic, and Rubber materials (CPR)	These materials are introduced to WIPP as waste, packaging material, and emplacement material. Their biodegradation leads to the formation of CO_2 that dissolves in brine to form carbonate species that affect pH and complex actinides.	Appendix GEOCHEM-2.1.5, 2.2.2, and 2.4.2	See updated inventory data in SOTERM-3.1
Microbial Processes	Gas generation, primarily CO_2 and H_2S, resulting from the biodegradation of CPR materials; creation of reducing conditions; and colloid contributions. Microbial processes are assumed to occur in all PA realizations.	Microbial gas generation Appendix GEOCHEM-2.2.2 and 2.3.2; microbial colloids 5.3.4	See new data in SOTERM-4.0

Repository Condition, Parameter, or Process	Integration into CRA-2026 PA	Appendix Referenced-2026 (unless otherwise specified)	Changes since CRA-2019
Radiolysis	Localized oxidizing effects possible near high specific-activity actinides, but overall radiolytic processes are controlled by the bulk in-room chemistry. Radiolytic gas generation is more significant due to increased plutonium inventory and changes in the screening argument for CRA-2019 (gas generation from brine radiolysis screened in; from CPR screened out; Day 2019).	Appendix GEOCHEM-2.1.9; Appendix SCR-6.5.1.7 (FEP W52) and 6.5.1.8 (FEP W53)	See new scope in SOTERM-3.4

SOTERM-3.0 POST-EMPLACEMENT INVENTORY, CHEMICAL, AND RADIOLYTIC PROCESSES

Several important processes occur in the WIPP after repository closure. In a salt repository, post-emplacement chemical conditions are defined by the reactions of high-ionic-strength brines with emplaced waste and materials, as well as possible microbial interactions. Although altered somewhat by the host geology, repository chemical conditions (e.g., pH, redox potential [E_h], solubility, and colloidal tendencies) will be defined considerably by what is emplaced (i.e., both TRU waste and packaging). Therefore, it is important to define the post-emplacement chemical conditions, beginning with an inventory update. The Interim State Performance Assessment Inventory Report 2024 (IS PAIR 2024) (Van Soest 2025) is being used for the CRA-2026. These inventory data are compared to the CRA-2019 inventory and briefly discussed for their relevance to the actinide source term. Given that repository chemical conditions are controlled largely by the composition of the emplaced materials, the next section presents the CRA-2026 inventory on which these evaluations are based.

SOTERM-3.1 Effects of the Updated Inventory and Change to the Minimum Brine Volume for a DBR on the Actinide Source Term

The non-radioactive waste, packaging, and cement materials identified in the CRA-2026 PA are summarized in Tables 5-5 through 5-9 of the IS PAIR 2024 (Van Soest 2025). Changes in the CRA-2026 inventory from the CRA-2019 inventory include:

- decreases in lead (1.38×10^7 kilograms [kg] to 2.43×10^6 kg, ~82%), aluminum-based metals/alloys (5.57×10^5 kg to 3.87×10^5 kg, ~31%), and other inorganic materials (1.05×10^7 kg to 6.25×10^6 kg, ~40%)
- increases of ~ 30% in iron-based metals/alloys (1.54×10^7 kg to 1.99×10^7 kg) and ~44% in other metal/alloys (9.84×10^5 kg to 1.42×10^6 kg)
- a ~22% increase in CPR (1.78×10^7 kg to 2.27×10^7 kg), mostly due to a ~39% increase in cellulosics (5.97×10^6 kg to 9.71×10^6 kg)
- an ~8% increase in organic ligands, mostly due to a 39% increase in citrate/citric acid (7.71×10^3 kg to 1.08×10^4 kg) with a smaller (~6%) increase in acetate/acetic acid (2.96×10^4 kg to 3.14×10^4 kg), and little change in oxalate/oxalic acid and EDTA

Changes in the inventory, along with the new brine volume, result in changed concentrations of these components. Collectively, these changes affect the mobile actinide source term in the following ways:

- Changes in lead concentration could affect calculations of actinide solubility, since it is included as a reactant in these calculations. Lead reactions with organic ligands are not included in the solubility calculations, and there is no assumed competition with actinides for the ligands.

- Although the iron inventory and concentration in brine have increased, it has always dominated the disposal system. The abundance of Fe^0 will contribute to aqueous Fe^{2+} species, thus promoting reducing and anoxic conditions which can affect actinide oxidation state and solubility. Increased iron could also affect actinide solubilities, as it is included as a reactant in these calculations.
- The increase in CPR provides more substrate for biodegradation. This results in an increase in the MgO inventory to maintain buffering capacity and limit CO_2 partial pressure (p_{CO2}). However, production of other gases (e.g., N_2, H_2S) can affect pressures and brine movement.
- Although the total mass of organic complexing agents did not change significantly, the increased concentrations due to the updated minimum volume required for a DBR will increase dissolved actinide concentrations. This is true for all ligands regardless of the change in inventory but is more pronounced for citrate, which is a strong complexant, especially for An(III).

SOTERM-3.2 WIPP Brine Chemistry

Brine compositions were determined based on analyses of weep fluids from within the WIPP and from Castile brine flows (DOE 1996; Snider 2003; Popielak et al. 1983; CRA-2026 Appendix GEOCHEM-3.0). The end-member brines, GWB (high magnesium, representing seep brine) and ERDA-6 (higher pH, low Mg, representing the underlying Castile Formation brine), bracket the range of brine composition expected. These brines are stable against precipitation over multiple years (see Table SOTERM-2). The modeling approach and associated mineral and chemical equilibrium reactions are described in Appendix GEOCHEM-3.2.1 and -4.1.2.

Generic Weep brine, ERDA-6, and/or pC_{H+}-specific brines have been used in most recent WIPP-relevant laboratory studies (Beam 2023; Borkowski et al. 2009; Kaplan 2025b; Kutahyali Aslani 2022, 2024; Lucchini et al. 2010a, 2013a, 2013c; Reed et al. 2006; Reed et al. 2010). Brines are typically diluted by 5 or 10% to avoid salt precipitation when sampling long-term experiments and to minimize mineral colloid and pseudo-colloid formation. It should be noted that the use of diluted brines that are not equilibrated with MgO, organics, iron, lead, halite, or anhydrite could have an impact on solubility data. GWB and ERDA-6 are site-specific and have been instrumental in identifying impacts of the lesser components—e.g., bromide (Br^-), sulfate (SO_4^{2-}), and tetraborate ($B_4O_7^{2-}$)—that would have been overlooked in simplified brine studies.

Table SOTERM-2. Simulated WIPP Brine Compositions as a Function of pC_{H+} (Lucchini et al. 2013c, Table 11).

pC_{H+} or Brine	[1]Element/Species - Measured Concentrations (Molar [M])								
	Na^+	K^+	Mg^{2+}	Ca^{2+}	Li^+	$B_4O_7^{2-}$	Cl^-	SO_4^{2-}	Br^-
GWB	3.53	4.67×10^{-1}	1.02	1.38×10^{-2}	4.48×10^{-3}	3.95×10^{-2}	5.60	1.77×10^{-1}	2.66×10^{-2}
9	3.50	4.58×10^{-1}	1.03	1.35×10^{-2}	3.75×10^{-3}	3.89×10^{-2}	5.43	1.76×10^{-1}	2.35×10^{-2}
9.5	3.72	4.59×10^{-1}	8.50×10^{-1}	1.31×10^{-2}	3.70×10^{-3}	1.64×10^{-2}	5.55	1.76×10^{-1}	2.42×10^{-2}
10	4.59	4.50×10^{-1}	1.17×10^{-1}	1.34×10^{-2}	3.57×10^{-3}	2.77×10^{-3}	5.35	1.69×10^{-1}	2.34×10^{-2}
10.5	4.91	4.54×10^{-1}	2.86×10^{-2}	1.24×10^{-2}	3.54×10^{-3}	1.66×10^{-2}	5.39	1.69×10^{-1}	2.32×10^{-2}
ERDA-6	4.87	9.70×10^{-2}	1.90×10^{-2}	1.20×10^{-2}	N/A	1.58×10^{-2}	4.80	1.17×10^{-1}	1.10×10^{-2}
11	4.96	4.49×10^{-1}	1.11×10^{-2}	1.09×10^{-2}	3.54×10^{-3}	3.05×10^{-2}	5.31	1.68×10^{-1}	2.30×10^{-2}
12	5.02	4.54×10^{-1}	1.05×10^{-2}	6.97×10^{-3}	3.46×10^{-3}	3.29×10^{-2}	5.31	1.69×10^{-1}	2.32×10^{-2}
13	5.11	4.52×10^{-1}	9.74×10^{-3}	2.14×10^{-3}	3.55×10^{-3}	2.99×10^{-2}	5.32	1.67×10^{-1}	2.35×10^{-2}

[1]Concentrations are derived from pH titration experiments with 100% saturated GWB and ERDA-6 brines. Uncertainties in the analytical data are ± 10%.

These simulated brine compositions, however, cannot be used to collect thermodynamic data due to their inherent complexity. Therefore, simpler binary brines are used for this purpose; e.g., sodium chloride (NaCl), magnesium chloride ($MgCl_2$), and calcium chloride ($CaCl_2$). The ranges in pH, E_h, total inorganic carbon (TIC), and ionic strength (I) are summarized in Appendix GEOCHEM-3.3 and help define the range in parameters for experimental studies.

SOTERM-3.3 Complexation of Actinides by Organic Complexing Agents

The complexation of actinides with organic ligands in the TRU-waste inventory can significantly increase their solubility. At the buffered pH of WIPP, only EDTA and citrate form complexes strong enough to enhance actinide concentrations in solution. This complexation mostly affects the An(III) oxidation state, but it can also have significant effects on the An(IV) state.

SOTERM-3.3.1 Projected Concentration of Organic Complexing Agents under WIPP-relevant Conditions

The concentrations of the four organic complexing agents used for the CRA-2026 are shown in Table SOTERM-3. Dissolved concentrations are calculated at 5 brine volumes (1X – 5X the minimum volume required for a DBR) to help establish uncertainties. In PA, these are assumed to persist for the regulatory period of 10,000 years and can significantly affect the calculated actinide solubilities. Because of the decreased minimum volume for a DBR for the Interim State PA, the concentrations of organic complexing agents in solution have increased, thereby affecting the actinide source term.

Table SOTERM-3. Concentration Range of Acetate, Oxalate, Citrate, and EDTA in the Disposal System, (Domski 2025a). Based on the Minimum Brine Volume (1X = 6,314 m^3) and 5X the Minimum Brine Volume for DBR.*

Organic Complexant	Concentration in 1X Brine Volume (M)	Concentration in 5X Brine Volume (M)	CRA-2019 Concentration in 1X Brine Volume (M)*
Acetic acid	8.29×10^{-2}	1.66×10^{-2}	2.83×10^{-2}
Oxalic acid	3.08×10^{-2}	6.17×10^{-3}	1.13×10^{-2}
Citric acid	8.88×10^{-3}	1.78×10^{-3}	2.30×10^{-3}
EDTA	2.13×10^{-4}	4.25×10^{-5}	7.92×10^{-5}

*17,400 m^3

Note: no credit is given in PA to either biodegradation or radiolytic degradation of ligands.

SOTERM-3.3.2 Stability Constants for Organic Complexation with Actinides

The stability constants for organic ligand-actinide complexation were presented in CRA 2019 Appendix SOTERM-3.3.2 and in previous CRAs, and nothing has changed. These data demonstrate trends in actinide complexation:

- For acetate, oxalate, and citrate, the strength of the complex formed is in the same order: An(IV) > An(VI) > An(III) > An(V).
- For EDTA, complex strength is An(IV) > An(III) > An(VI) > An(V).

For the most part, the III and IV actinides are strongly affected by organic complexation. Based on their formation constants, only citrate and EDTA are expected to form strong enough complexes to influence the aqueous speciation of actinides and potentially increase dissolved actinide concentrations under the expected conditions in the WIPP. This was confirmed in previous studies with the An(III) analog, neodymium (Nd) (Borkowski et al. 2009; CRA-2019 Appendix SOTERM-3.3.3) and in more recent studies with both Nd and U(VI) (Kutahyali Aslani 2022, 2024, 2025). However, at the expected repository pH and ligand inventory, the aqueous speciation of An(IV) is expected to be dominated by hydrolysis and carbonate complexation, rather than by organic complexation (Borkowski et al. 2012; Domski 2025a).

SOTERM-3.3.3 New Literature on Organic Complexation Studies Since CRA-2019

Since the CRA-2019, An-organic complexation has remained an active field of research. A summary of the most relevant publications on this topic is provided in this section.

The existence of four Ca–An(III)–EDTA complexes was proposed in a recent study on the impact of calcium on the solubility, redox, and speciation of the An(III)–EDTA (An= Pu or Cm) system under reducing and anoxic conditions in 3.5 M $CaCl_2$ solutions and in WIPP brines (DiBlasi et al.

2022). Calcium was found to stabilize An(III)-EDTA complexes at concentrations as low as 1 millimole per liter (mM). In another study, DiBlasi et al. (2021a) demonstrated that EDTA reduces Pu(VI) to Pu(V), oxidizes Pu(III) to Pu(IV), and ultimately stabilizes Pu(IV) under anoxic conditions and at different pH values. Those studies were conducted at lower ionic strengths.

Using capillary electrophoresis-inductively coupled plasma-mass spectrometry (CE-ICP-MS), the stability constants of acetate complexes of Am(III), Th(IV), Np(V), and U(VI) were determined in low ionic strength solutions (Willberger et al. 2019). Their results agreed with others in the literature, except for Np-acetate, which formed only the 1:1 complex. Maiwald et al. (2018) investigated Np complexation as a function of acetate concentration and temperature in NaCl solutions varying from 0.5 – 4 m ($mol \cdot kg^{-1}$). Three species were identified (NpO_2^+, NpO_2Ac, and $NpO_2(Ac)_2^-$), but only the higher complex increased with increasing temperature. At 20 °C and ~ 0.08 m acetate concentrations, the predicted fraction of NpO_2Ac (~60%) is in agreement with solubility calculations in GWB and ERDA-6 (Domski 2025a).

Xiong and Wang (2021a) investigated the stability constants for aqueous and solid uranyl oxalate complexes in high ionic strength environments, and they developed a thermodynamic model for the UO_2^{2+} - Na^+ - H^+ - Cl^- - ClO_4^- - $C_2O_4^{2-}$ - NO_3^- - H_2O system in ionic strength up to ~11 m. Maiwald et al. (2020) determined the speciation, thermodynamics, and structure of Np(V) complexes with oxalate (Ox^{2-}) by a variety of spectroscopic techniques.

Citrate and gluconate were found to significantly enhance the solubility of Th(IV) and U(VI) in the research work performed by Adam et al. (2021) in NaCl, $MgCl_2$, and $CaCl_2$ systems at high pH. Citrate also increased Nd solubility, but its impact weakened in the $MgCl_2$ systems due to competition with magnesium. However, in another study, no effect of gluconate on the solubility and speciation of Cm(III) and Nd(III) was observed in NaCl and concentrated (> 0.25 M) $CaCl_2$ at high pH (Rojo et al. 2021). In diluted $CaCl_2$ solutions with less calcium competition, there was no effect of gluconate. Comins et al. (2024a) observed enhanced rates of Pu reduction in the presence of citrate at alkaline pH in addition to radiolytic-induced degradation of citrate and concomitant Pu reduction.

SOTERM-3.3.4 WIPP-specific Data on Organic Complexation Effects Since CRA-2019

The solubilities of U(VI), Nd(III), Pu(III), and Np(V) were investigated in WIPP brines in the presence of WIPP-relevant organics (EDTA, citrate, acetate, oxalate) using an undersaturation approach (Kutahyali Aslani 2022, 2024, 2025; Kaplan 2025a). Additional experiments also included iron (Beam 2023; Kaplan 2025b). The main results of these experimental studies are summarized below. More details on these experiments are provided in the dedicated subsections on WIPP-specific results since the CRA-2019 in section SOTERM-5.0.

In the presence of all four organics (EDTA = 7.9×10^{-5} M, citrate = 2.3×10^{-3} M, acetate = 2.83×10^{-2} M, oxalate = 1.13×10^{-2} M), the solubility of U(VI) in pC_{H+} 9 brine reached ~4×10^{-6} M, as compared to the control without organics (~5×10^{-7} M; Kutahyali Aslani 2024). This was

primarily due to citrate. Similarly, the presence of these same organics increased the solubility of Pu(III) and Nd(III) in pC_{H+}-specific brines and 5 M NaCl, respectively (Beam 2023; Kutahyali Aslani 2022). In contrast, the influence of organics on Np(V) solubility decreased over time, and after ~900 days, no measurable effect was observed at either pC_{H+} 9 or pC_{H+} 11 (Kaplan 2022). Uranium(VI) reduction in the presence of citrate in WIPP brines was also observed by Kutahyali Aslani et al. (2024).

Overall, these recent WIPP-specific experimental data reflect the increased solubility trends observed in other studies on organic complexation of An (see sections SOTERM-3.3.2 and SOTERM-3.3.3).

SOTERM-3.4 Radiolysis Effects on the Disposal System

Radiolysis effects on the disposal system are caused by the interaction of ionizing radiation (α) with the brines present in the repository. Although radiolysis can lead to localized conditions that could oxidize multivalent actinides, the brine chemistry, metal corrosion, and microbiological activity together will overwhelm these effects and lead to overall reducing conditions (CRA-2019 Appendix SOTERM-3.4.1). However, the relative importance of radiolytic gas generation has increased due to EPA's concern over higher TRU content in the WIPP, resulting in changes to the screening argument (Day 2019). In addition, there is new interest in the fate of organic complexants due to radiolysis.

SOTERM-3.4.1 Radiation Chemistry of Brine Systems

Brine radiolysis is included in the conceptual model for gas generation but not for its effects on actinide speciation, because of the assumptions that a well-mixed repository does not permit chemical microenvironments and actinide redox reactions are not at equilibrium. Brine radiation chemistry and the generation of oxidants and reductants via brine radiolysis have been discussed in detail previously (CRA-2019 Appendix SOTERM-3.4).

SOTERM-3.4.2 Potential Radiolytic Effects on Actinide Speciation and Solubility

Of new interest are the effects of radiolysis on the emplaced organic complexants. These compounds are assumed to persist for the 10,000-year regulatory period. Breakdown of these compounds could affect actinide solubility and also result in oxidation state changes, both of which can affect the source term.

While the gamma (γ) radiolysis of organic ligands has been researched extensively, there are only a handful of studies involving the alpha radiolysis of organics (Tseng et al. 1980; Fiegel et al. 2019; Malmbeck and Banik 2020). The Tseng group performed alpha irradiation of a cobalt-EDTA complex in 0.8 N H_2SO_4 via an *in situ* $^{6}Li(n, \alpha)^{3}H$ reaction. They observed decreased G(Co(III)-EDTA) as the dose rate increased and reported that temperature effects were negligible (25-60°; 77-140°F). Malmbeck and Banik used ^{244}Cm as their He^{2+} source to irradiate TODGA (N,N,N´,N´-tetraoctyldiglycolamide) in 0.5 M HNO_3. TODGA was almost completely degraded after irradiation at a rate of 2.8 kilogray (kGy)/hour for 3 months. While the

degradation by-products were not completely characterized, it was hypothesized that the mechanism for α-radiolysis was analogous to that of γ-radiolysis. Radiolysis experiments performed by Fiegel et al. (2019) used a helium ion (He^{2+}) beam to irradiate a closely related EDTA analog, DOTA (2,2′,2″,2‴-(1,4,7,10-Tetraazacyclododecane-1,4,7,10-tetrayl)tetraacetic acid)) in water (Figure SOTERM-1). The DOTA experiments are more relevant to the WIPP because they were performed in neutral aqueous conditions as opposed to acidic conditions. A total dose of 110 kGy degraded nearly 30% of the DOTA in solution. Additionally, Fiegel et al. provided full characterization of several degradation products. While all three alpha radiolysis studies discussed above are important, none of them addresses how high ionic strength systems and high pH will affect the alpha radiolysis of organics. This is the focus of new studies described in the next section.

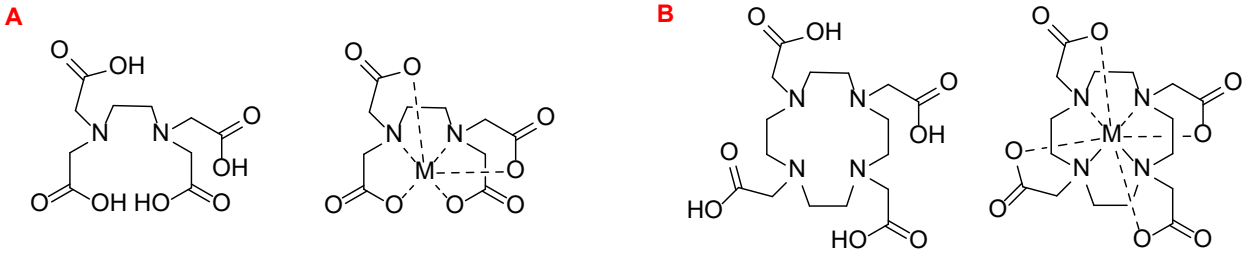


Figure SOTERM-1. A) Structure of Fully Protonated EDTA Ligand and EDTA-Metal Chelate. B) Structure of Fully Protonated DOTA Ligand and DOTA-Metal Chelate (Favela Morales and Lucchini 2024).

SOTERM-3.4.3 WIPP-specific Data Since the CRA-2019

New experiments are underway to investigate the effects of alpha radiolysis on the degradation of EDTA and citrate in brines to address the issue of ligand permanence (Favela Morales and Lucchini 2024). EDTA and citrate solutions were irradiated by using a He^{2+} beam as the source of α-particles. The He^{2+} flux was estimated to be around 30 nanoamperes (nA) over 30 minutes, which corresponds to a total dose of ~200 kGy (2×10^{14} alpha particles). While this absorbed dose (provided by 5.1 mega-electronvolt [MeV] alpha particles) greatly exceeds that expected to exist at any given moment in the WIPP, it was chosen to bound the long-term effects that alpha-emitting radionuclides would have on organics over thousands of years. Radiolytic breakdown products were analyzed by high-performance liquid chromatography-mass spectrometry (HPLC-MS). Preliminary data from scoping experiments show radiolytically-induced loss of both parent compounds as a function of the ligand concentration being irradiated. This supports the assumption that ligand permanence results in an overprediction of actinide solubilities.

The HPLC chromatograms in Figure SOTERM-2 compare a non-irradiated EDTA standard (Figure SOTERM-2A) and an irradiated EDTA solution (Figure SOTERM-2B). The EDTA standard shows a single peak, while the irradiated sample has a broader main peak and the appearance of shoulders, indicating the formation of by-products with similar structures to EDTA. These

products have not yet been identified. Due to structural similarity between DOTA and EDTA, it is possible that analogous degradation products will be observed, as in Fiegel et al. (2019).

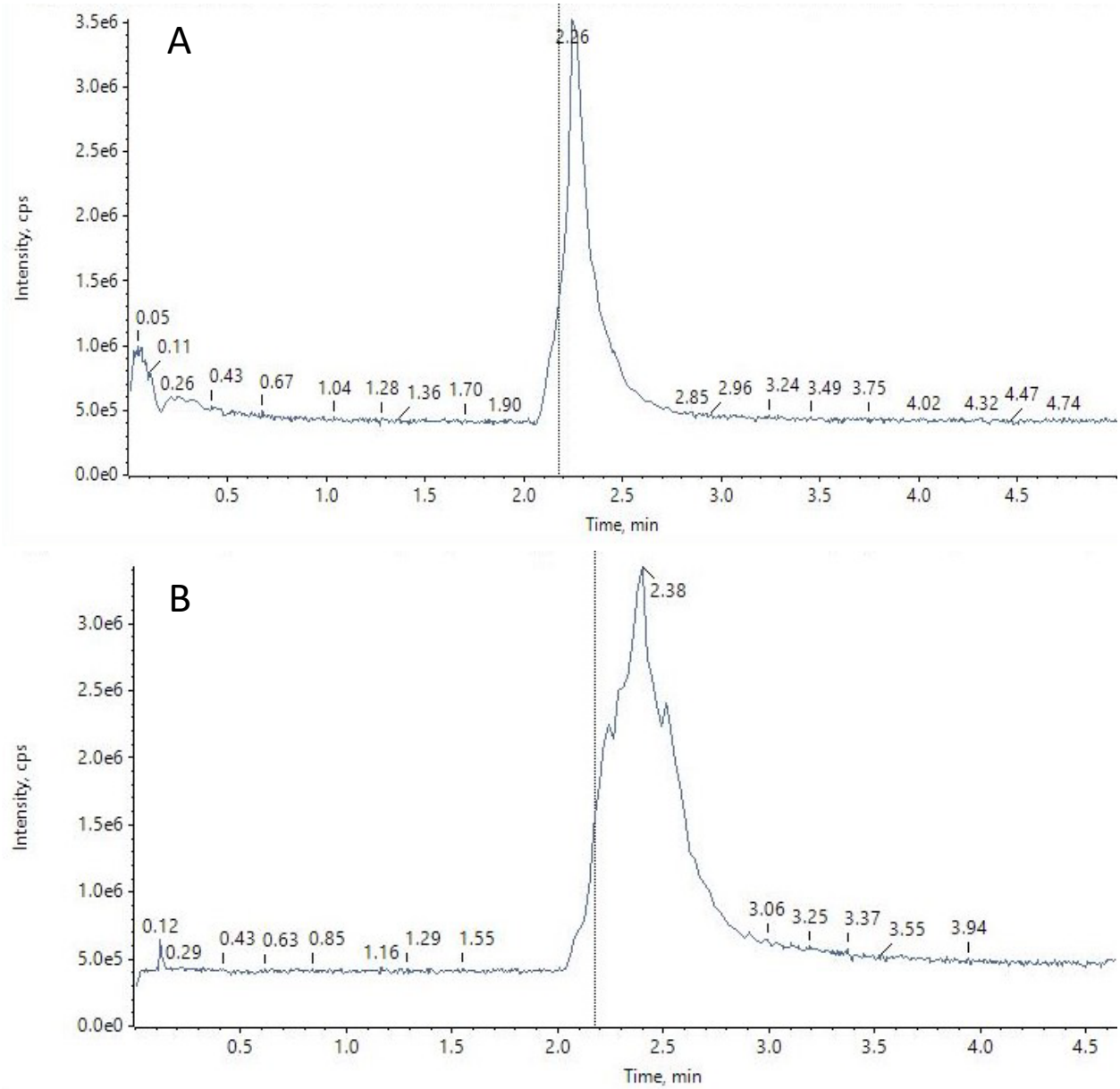


Figure SOTERM-2. HPLC Chromatograms of A) 3.5 mM EDTA Standard and B) Irradiated 2.5 mM EDTA Solution (from Favela Morales and Lucchini 2024).

A series of EDTA concentrations (ranging from 0.5 mM to 500 mM) were irradiated to determine the extent of ligand degradation as a function of ligand concentration. Samples had to be diluted prior to measurement to accommodate the instrumentation. Similar to the results from DOTA radiolysis (Fiegel et al. 2019), a higher degree of degradation was observed as

concentrations increased (Figure SOTERM-3). A concentration of 5.0 mM (sample A) led to 32% degradation, and the 50.0 mM (sample B) was degraded by nearly 70%.

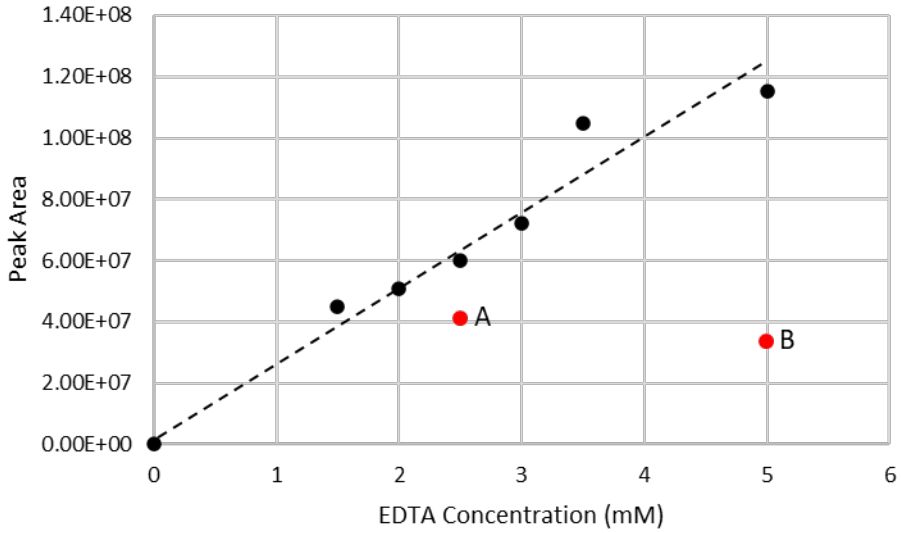


Figure SOTERM-3. EDTA Calibration Curve (Black Dots) with Plotted Irradiated Data Points (Red Dots, A and B). A) 5.0 mM Diluted to 2.5 mM and B) 50.0 mM Diluted to 5.0 mM. Data Were Regressed through the Origin (from Favela Morales and Lucchini 2024).

Citrate showed the same trend as EDTA, with more degradation at higher citrate concentrations (Figure SOTERM-4). The difference in polarity between citrate and EDTA, due to the lack of the amine functional groups, allows the degradation by-products to be more easily separated by HPLC-MS.

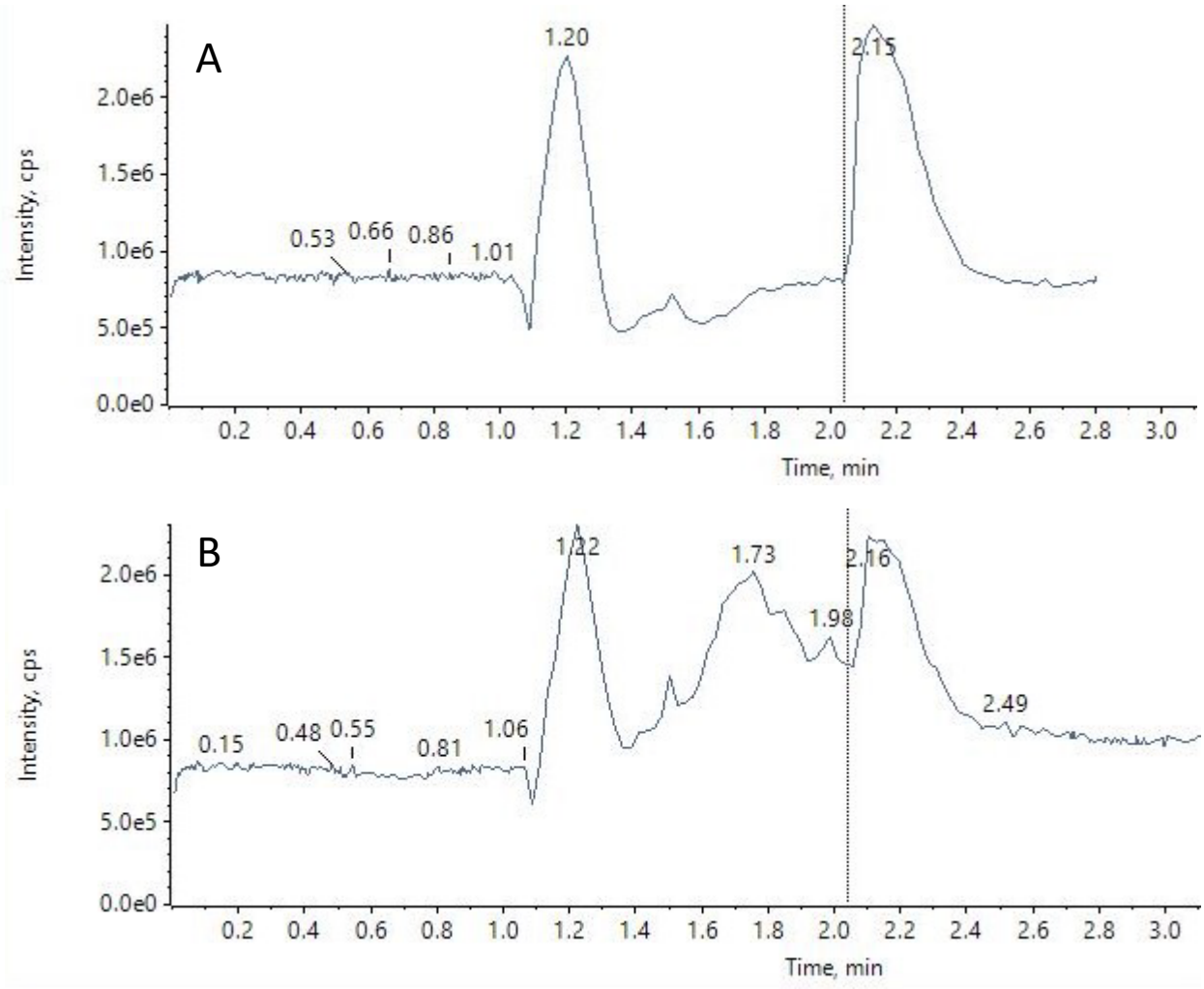


Figure SOTERM-4. HPLC Chromatograms of A) 3.0 mM Citrate Standard, Showing Peaks at 1.20 min and 2.15 min Belonging to Sodium Citrate (mass-to-charge ratio (m/z): 294.9407) and Citric Acid (m/z: 193.0355), Respectively, and B) Irradiated 1.79 mM Solution, Showing the Two Starting Material Peaks Along with Two New, Large Peaks at 1.73 min and 1.98 min. Note that Higher Peak Area Corresponds to Decreased Degradation (from Favela Morales and Lucchini 2024).

Similar to EDTA, various concentrations of citrate (1.79 mM to 50 mM) were irradiated and analyzed by HPLC-MS. Following the trend established by the EDTA experiments, higher concentrations led to increasing levels of ligand degradation (Figure SOTERM-5). Sample A exhibits 34% ligand degradation. Increasing the concentration ten-fold (Sample B) resulted in a slight increase in degradation to 43%. A substantial increase in concentration to 50 mM citrate (Sample C) afforded a significant rise in degradation to 58%.

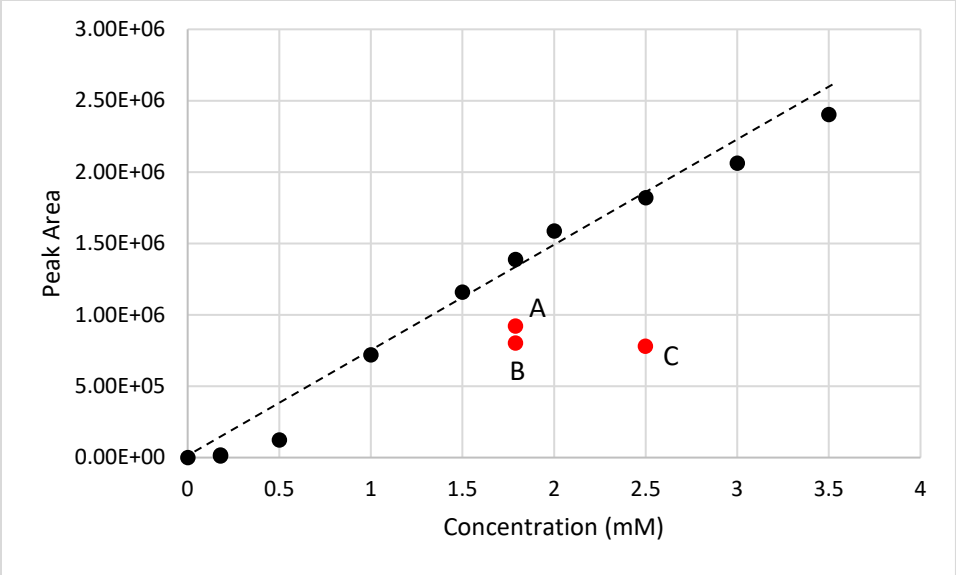


Figure SOTERM-5. Citrate Calibration Curve (Black Dots) with A) 1.79 mM Irradiated Data Point, B) 17.9 mM Diluted to 1.79 mM Irradiated Data Point, and C) 50.0 mM Diluted to 2.50 mM Irradiated Data Point. The Data Were Regressed Through the Origin (from Favela Morales and Lucchini 2024).

SOTERM-3.5 Actinide Colloids

There has been no change to the colloid model since its conception for the CCA and initial certification by the EPA. The actinide source term is defined in the WIPP PA as the sum of contributions from dissolved actinide species and four types of colloidal species.

The current WIPP colloidal model addresses four potential colloidal contributions to the mobile actinide source term (U.S. DOE 1996, Appendix SOTERM):

1. Mineral fragment colloids: mineral fragments, such as iron corrosion products or other waste constituents, may act as substrates for actinide sorption or they may consist of precipitated or coprecipitated actinide solids.
2. Actinide intrinsic colloids: formed by intrinsic chemistry, such as hydrolysis reactions, may generate macromolecules that, in some cases, may mature into a mineral-fragment-type colloid. These are nanometers (nm) in size.
3. Humic colloids: these are discussed in CRA-2026 Appendix GEOCHEM-5.0 and Mariner 2025.
4. Microbial colloids: microorganisms may act as substrates for extracellular actinide sorption, or they may accumulate actinides intracellularly.

Colloids can affect the mobile actinide source term by increasing actinide concentrations in suspension and solution. They can also be transported differently than dissolved species in the Salado and Culebra. Colloidal and dissolved species are modeled the same in the Salado.

Intrinsic, mineral fragment, and microbial colloids are not modeled in the Culebra. This section provides a brief update of WIPP-relevant colloid studies since 2019. Earlier studies are discussed elsewhere (Reed et al. 2013).

SOTERM-3.5.1 Actinide Colloids in WIPP-related and WIPP-specific Conditions Since the CRA-2019

There have been a considerable number of publications on actinide colloid chemistry but few that specifically address ionic strength effects on colloid formation, stability, and mobility. Many of the studies on actinide mineral fragment colloids pertain to the effects of engineered barriers and backfilling agents, such as bentonite and cement.

Zhou et al. (2019a) studied the formation of Pu(IV) colloids in groundwater with an ionic strength of 1 M. Pseudo-colloids formed immediately but sorbed onto container walls. The remaining suspended colloids progressed from Fe/Manganese (Mn) oxides to carbonate species over time and precipitated from solution.

The potential for An(III/IV)-silicate colloids to form at the WIPP was discounted in studies using Nd and U(IV) in 5 M NaCl (Beam 2022). Hydrolysis was a stronger force than silicate complexation for both Nd and U(IV) at WIPP-relevant pH values. No Nd-silicate colloids were detected with sequential filtration. U(IV)-silicate colloids were detected but only at pH > 10.

Cevirim-Papaioannou et al. (2018a) found that hydrolysis of U(IV) in high salt solutions resulted in a solubility-controlling phase (nanocrystalline $UO_2 \cdot H_2O$) that was at “equilibrium” with the colloidal fraction. Initial increases in U(IV) solubility were attributed to the colloidal fraction, but solubility decreased over time, suggesting that these species became unstable. This effect was less pronounced at 5 M NaCl than at 2 M NaCl. Later studies, at 1 m NaCl, determined that U(IV) solid phases formed initially via hydrolysis followed by polymer then colloid formation, and ultimately precipitation (Grambow et al. 2023).

These studies support the assumption that colloid concentrations lead to an overestimation of the source term. Other colloid literature and/or experimental updates are addressed in the individual actinide sections and in the microbiology section (Appendix SOTERM-5.0 and -4.0, respectively).

The WIPP colloid enhancement parameters used in the CRA-2026 and CRA-2019 (U.S. DOE 2019) are given in Table SOTERM-4. The mineral colloid parameters have remained at the same fixed value since the CCA, which is double the solubility limit derived from early experimental data (U.S. DOE 1996, Appendix-SOTERM-6.3). The intrinsic colloid parameters were updated for the CRA-2026, as described in Kaplan et al. (2025). Both mineral and intrinsic colloid parameters are implemented on an elemental basis for the CRA-2026. Microbial parameters for An(III) were updated for the CRA-2026, based on new experimental data (Swanson 2024a; Kaplan et al. 2025), and were implemented on an element-oxidation state basis. Other microbial parameters were updated based on a recalculation of earlier data and to conform with the biomass-based

approach (Kaplan et al. 2025). Humic colloid proportionality constants for An(III) and An(IV) were updated to be consistent with the baseline solubility calculations for the CRA-2026 (Mariner 2025). The colloidal actinide source term is discussed in Section 6.5.

Table SOTERM-4. Colloid Enhancement Parameters Used in CRA-2026 and CRA-2019 (Appendix SOTERM-2019)

CRA-2026							
Actinide and Oxidation State	Mineral CONCMIN[1] (M)	Intrinsic CONCINT[2] (M)	Microbial		Humic[5]		
			PROPMIC[3]	CAPMIC[4] (M)	Proportionality Constant		CAPHUM[8] (M)
					PHUMSIM[6]	PHUMCIM[7]	
Th(IV)	2.60×10^{-8}	4.80×10^{-7}	3.10×10^{0}	6.95×10^{-4}	2.0×10^{-2}	1.0×10^{-2}	1.1×10^{-5}
U(IV)	2.60×10^{-8}	1.40×10^{-6}	2.10×10^{-3}	9.65×10^{-6}	2.0×10^{-2}	1.0×10^{-2}	1.1×10^{-5}
U(VI)					1.2×10^{-1}	5.1×10^{-1}	
Np(IV)	2.60×10^{-8}	4.30×10^{-8}	1.20×10^{1}	1.52×10^{-7}	2.0×10^{-2}	1.0×10^{-2}	1.1×10^{-5}
Np(V)					9.1×10^{-4}	7.4×10^{-3}	
Pu(III)	2.60×10^{-8}	4.30×10^{-8}	2.92×10^{0}	4.97×10^{-7}	3.0×10^{-1}	3.0×10^{-1}	1.1×10^{-5}
Pu(IV)			3.00×10^{-1}	4.07×10^{-9}	2.0×10^{-2}	1.0×10^{-2}	
Am(III)	2.60×10^{-8}	6.70×10^{-7}	2.92×10^{0}	4.97×10^{-7}	3.0×10^{-1}	3.0×10^{-1}	1.1×10^{-5}
CRA-2019							
Actinide and Oxidation State	Mineral CONCMIN[1] (M)	Intrinsic CONCINT[2] (M)	Microbial		Humic[5]		
			PROPMIC[3]	CAPMIC[4] (M)	PHUMSIM[6]	PHUMCIM[7]	CAPHUM[8] (M)
Th(IV)	2.60×10^{-8}	4.30×10^{-8}	2.10×10^{-1}	3.80×10^{-8}	1.00×10^{-2}	1.00×10^{-2}	1.10×10^{-5}
U(IV)	2.60×10^{-8}	4.30×10^{-8}	2.10×10^{-1}	3.80×10^{-8}	1.00×10^{-2}	1.00×10^{-2}	1.10×10^{-5}
U(VI)	2.60×10^{-8}	1.40×10^{-6}	2.10×10^{-1}	3.80×10^{-8}	1.20×10^{-1}	5.10×10^{-1}	1.10×10^{-5}
Np(IV)	2.60×10^{-8}	4.30×10^{-8}	2.10×10^{-1}	3.80×10^{-8}	1.00×10^{-2}	1.00×10^{-2}	1.10×10^{-5}
Np(V)	2.60×10^{-8}	4.30×10^{-8}	2.10×10^{-1}	3.80×10^{-8}	9.10×10^{-4}	7.40×10^{-3}	1.10×10^{-5}
Pu(III)	2.60×10^{-8}	9.50×10^{-9}	2.10×10^{-1}	3.80×10^{-8}	2.00×10^{-1}	2.00×10^{-1}	1.10×10^{-5}
Pu(IV)	2.60×10^{-8}	4.30×10^{-8}	2.10×10^{-1}	3.80×10^{-8}	1.00×10^{-2}	1.00×10^{-2}	1.10×10^{-5}
Am(III)	2.60×10^{-8}	9.50×10^{-9}	3.00×10^{-2}	2.30×10^{-9}	2.00×10^{-1}	2.00×10^{-1}	1.10×10^{-5}

[1] In units of moles of mineral-bound actinide per liter.

[2] In units of moles colloidal actinide per mole total dissolved actinide; results from Borkowski et al. (2010, 2012) and Altmaier et al. (2004) used for CRA-2026. These are implemented as element-specific parameters in PA. When values differ, the higher value is chosen.

[3] In units of moles of microbe-bound actinide/moles dissolved actinide.

[4] Maximum concentration of actinide associated with mobile microbes in units of moles of microbe-bound actinide per liter.

[5]All values from Mariner 2025.
[6]Proportionality constant for humic colloids in Salado brine; units of moles colloidal actinide per mole dissolved actinide.
[7]Proportionality constant for humic colloids in Castile brine; units of moles colloidal actinide per mole dissolved actinide.
[8]Maximum concentration of actinide associated with humic colloids.

SOTERM-4.0 MICROBIAL EFFECTS IN THE WIPP

Microbial activities that can potentially affect the fate and transport of actinides from deep geological waste repositories have been reviewed elsewhere (Lloyd and Macaskie 2002; Pedersen 2005; Wang and Francis 2005; Ruiz-Fresneda et al. 2023). The relevance and relative importance of these effects for salt-based repositories have also been noted (CRA-2019 Appendix SOTERM-4.0; Swanson et al. 2021a; Gregory et al. 2024). The WIPP PA considers gas generation and biocolloid formation to have the largest potential impact on the actinide source term. This consideration is based on assumptions about microbial ecology and activity in the WIPP that are still uncertain. This section will review how WIPP conditions affect microbial viability, activity, and metabolism and will discuss the implications for the conceptual models for microbial gas generation and biocolloid transport, as they affect the actinide source term.

SOTERM-4.1 Microbial Viability and Constraints on Activity

Effects on repository performance caused by gas generation depend upon microbial activity. However, microbial activity under WIPP conditions remains highly uncertain due to the multiple, severe constraints imposed by both the geochemical conditions of subterranean salt and the repository environment itself (Swanson et al. 2021a; Appendix SOTERM-2019). These constraints include high ionic strength, low water activity (a_w), high chaotropicity, anoxia, radioactivity, alkaline pH, and a lack of ideal substrates.

To survive in hypersaline environments, microorganisms must osmoregulate by either accumulating ions (“salting in”) or small organic compatible solutes (“salting out”). The energetic cost of osmoregulation not only determines which types of metabolism are thermodynamically feasible but can also determine which organisms remain viable.

The high ionic strength of WIPP brines (~5.32-8.08) and the presence of chaotropic solutes, such as magnesium or calcium, result in low water activity. High concentrations of chaotropes can inhibit microbial activity, by denaturing cellular macromolecules, such as proteins and nucleic acids (Hallsworth et al. 2007).

SOTERM-4.1.1 Studies on Microbial Viability and Activity Since the CRA-2019

A recent study of the extreme haloarchaeon and WIPP isolate, *Halobacterium* sp., found that chaotropicity (due to elevated magnesium chloride concentrations) had a greater effect on growth than water activity (Swanson 2022). However, a combination of interrelated factors (pH, a_w, and the relative contributions of chaotropes and kosmotropes), rather than one single parameter, provided the best predictor of growth. A “habitability index” was proposed to help define the chemical boundary conditions that delimit microbial viability and activity in extreme environments, such as the WIPP (Swanson 2022). This index is calculated as the ratio of the concentrations of chaotropic to kosmotropic solutes (C/K) in brine and can be extended to include emplaced MgO, nitrates, phosphates, and cement. When considered along with water activity and pH, these three parameters appear to collectively define a three-dimensional

habitable space in which microbial viability is possible, whether or not it is probable (Figure SOTERM-6). The space falls within a log(C/K) range of -0.03-1.09, a pH range of 5.0-9.5, and a_w between 0.698-0.918. In Figure SOTERM-6, this appears as the cluster of data points in the upper left portion of the *x,y* plane and the middle left portion of the *y,z* plane. It should be noted that this space was defined based on experimental data from the WIPP extreme halophile (*Halobacterium* sp.). The window for non-halophiles shifts toward a water activity value between 0.9-1.0 and a log(C/K) value of 0. Others have suggested using the Mg^{2+}/Na^{+} ratio as a proxy for "chaotropicity" (e.g., Klempay et al. 2021), but counterions in WIPP brines (e.g., Cl^{-} versus SO_4^{2-}) significantly affect a_w calculations and can also affect microbial growth.

Both GWB and ERDA-6 brines (including brines reacted with MgO and some cement-reacted formulations) fall within this habitable space. While high chloride concentrations are predominantly responsible for lowering water activity, and magnesium chloride promotes chaotropic effects, these effects are somewhat mitigated by high sodium, potassium, and sulfate kosmotrope concentrations in both brines. Boron also factors in as a strong chaotrope. Calcium concentrations in both GWB and ERDA-6 are low enough to not have a large chaotropic effect, but when brines are reacted with cement, the concentrations can become chaotropic. Overall, this suggests that WIPP brines are habitable and that indigenous extreme halophiles will be able to grow. This has been confirmed in 95% dilutions of each brine, amended with organics and supplements (Swanson et al. 2013a; Swanson and Reed 2018). However, this growth occurred under aerobic conditions only. Although no anaerobic, extreme halophiles have been cultivated from the WIPP near-field to date, the haloarchaea will remain viable, but inactive. The measured pH of WIPP brine seeps and fluid inclusions is between 5 and 6, but can be as low as 4.5, falling outside of this 3D space (Deal et al. 1995; Roedder 1984). This suggests that such inclusions and seeps would not be sources of microorganisms.

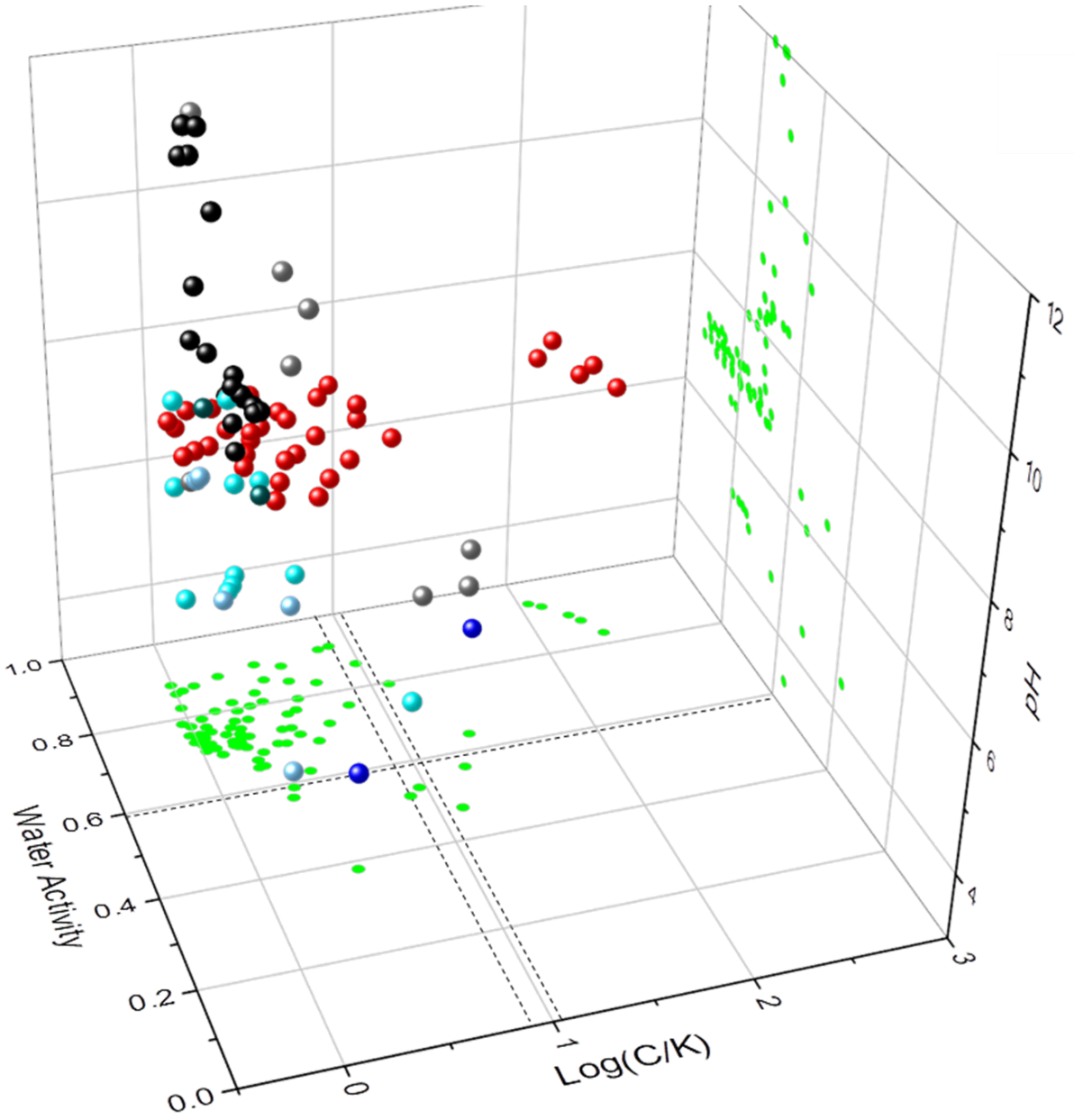


Figure SOTERM-6. 3D Image Showing Data for Various Briny Matrices. Green Dots are Data Projected Into the *x,y* and *y,z* Planes. Dashed Lines Mark the Upper and Lower Limits of the Chaotrope/Kosmotrope Ratio (i.e., "Habitability Index") and the Water Activity Limit. Between the Two Dashed Lines on the log(C/K) Axis, Growth is Minimal and/or Questionable. Cyan = WIPP-relevant Brines (Simulated Brines, Seeps, Fluid Inclusions); Light Blue = Brines from Boulby Salt Mine in UK; Royal Blue = German Brines (Q, Asse Salt Mine); Red = Experimental Broths; Gray = Cement-reacted Brines (Kienzler et al. 2000); Black = Cement/MgO-reacted WIPP Brines. See Swanson (2022) Appendix C for All Data and Associated References.

These habitability criteria reflect findings from studies on the effects of chaotropic salts on protein denaturation temperatures (or agar gelation temperatures, as a proxy for protein), in addition to the effects of pH extremes in hypersaline settings (Cray et al. 2013; Carré et al. 2023; Belilla et al. 2019). Different haloarchaea may exhibit different tolerances to chaotropes, suggesting that more work is required in this area of study (Carré et al. 2023).

Another recent study extrapolated the a_w limit for anabolic microbial activity based on single-cell substrate uptake experiments in various hypersaline brines (Paris et al. 2023). While the predicted value, 0.540, is far lower than any empirically shown limits, the percentage of cells assimilating substrates at their lowest tested a_w (0.717) was < 1% (compare to GWB a_w ~0.722-0.732). Even if organisms are able to assimilate carbon to remain viable at such low a_w, this does not necessarily mean that they are active or can catabolize substrates like CPR to produce gas.

SOTERM-4.1.2 Metabolic and Energetic Constraints in the Near-field

The two modes of metabolism considered in PA are denitrification and sulfate reduction, which are responsible for 4% and 96% of gas generated, respectively. This assumption does not reflect what is known about microbial communities in hypersaline environments but results in conservative gas generation calculations.

The energy required to maintain osmotic balance in a hypersaline environment limits many modes of metabolism (Oren 2011). Thus, the majority of microorganisms found in such settings are obligately aerobic, heterotrophic haloarchaea, since they use the less costly salting-in strategy of osmoregulation and because aerobic respiration affords them the highest energy yield. Anaerobic respiration is not a fundamental mode of metabolism for haloarchaea, although some are capable of denitrification.

Halophilic bacteria also exist, but their use of the more costly salting-out strategy results in an inability to survive in the highest salt concentrations. A small group of anaerobic or fermentative, extremely halophilic bacteria also exist that use the salting-in strategy. These are the only bacteria likely to survive at WIPP, but they are not considered in the conceptual model for microbial gas generation, since they reduce neither nitrate nor sulfate. It should be noted that fermentation products were detected by Gillow and Francis (2006) in their gas generation experiments.

Denitrification

Denitrification can be performed by both haloarchaea and bacteria. A recent analysis of 122 haloarchaeal genomes found that 12% of the sequenced genomes contained genes encoding complete denitrification (from nitrate to N_2; Families *Haloarculaceae*, *Haloferacaceae*, and *Natrialbaceae*; Miralles-Robledillo et al. 2021). Fifty-eight percent contained genes encoding only partial denitrification, while 30% possessed no denitrification genes. Gene presence only indicates potential function. Even so, the genetic potential for denitrification among

haloarchaea is more widespread than previously thought. However, the fact that most of the surveyed genomes revealed partial or no ability to denitrify, suggests that the production of N_2 gas from complete denitrification could still be low. No haloarchaeal families capable of complete denitrification have been detected in the WIPP near-field (Swanson et al. 2013b). A genome analysis of the WIPP isolate, *Halobacterium* sp., revealed genes for denitrification, but this organism could not denitrify when tested (Swanson 2017). However, the organisms present in G-seep brine were never fully characterized, and it is possible that members of these families were present in the brine and could have accounted for the denitrification observed by Francis and Gillow (1994). Deoxyribonucleic acid (DNA) from both *Haloferax* and *Haloarcula* spp. has been detected in salt mines in Ireland and Pakistan, while *Haloarcula* sequences were detected in a salt mine in the UK (Megaw et al. 2019; Payler et al. 2019; Cycil et al. 2020; Thompson et al. 2021).

Sulfidogenesis via Sulfate Reduction

Rates of dissimilatory sulfate reduction decrease with increasing salinity (Brandt et al. 2001; Kjeldsen et al. 2007; Kulp et al. 2007; Porter et al. 2007; Kjeldsen et al. 2010; Schwab et al. 2023). Nevertheless, sulfate reduction has been shown to occur at concentrations as high as 3.4 M NaCl (Schwab et al. 2023), although no haloarchaea are known to reduce sulfate. Schwab et al. also reported a decrease in sulfate concentrations after ~4 years in 4.4 M NaCl incubations, but unfortunately no data were shown for their 4-year sampling. Most of the DNA-sequencing evidence pointed toward other sulfidogenic organisms, rather than sulfate-reducing prokaryotes. Notably, all documented hypersaline incubations that have enriched sulfate-reducing bacteria have been inoculated with sediments and/or their porewaters, overlying brine, or produced waters. There have been no sulfate-reducing organisms isolated from the WIPP near-field.

SOTERM-4.2 Implications for Gas Generation from the Biodegradation of CPR and the Actinide Source Term

There has been no change in the CPR biodegradation model since the CRA-2009, and the gas generation rates derived by Gillow and Francis (2006) and used in PA have not changed (Francis and Gillow 1994; Francis et al. 1997; CRA-2019 Appendix GEOCHEM-2.1.5, CRA-2019 Appendix PA-4.2). The PA assumes that CPR materials will be consumed through denitrification (4%) and sulfate reduction (96%) (Wang and Brush 1996; Nemer and Stein 2005; CRA-2019 Appendix SOTERM-4.1). However, studies on the organisms present at WIPP, combined with studies on microbial activity and modes of metabolism under WIPP-like conditions suggest that these assumptions lead to an overestimation of the rates and extent of microbial gas generation. The effects of CO_2 generation on actinide solubility are already negated by the MgO backfill, and lower gas pressures will reduce radionuclide transport through the Salado in a disturbed scenario (Appendix PA-2.3).

Cellulose Degradation by Halophiles, Including New Studies Since the CRA-2019

A survey of over 5,000 bacterial genomes found that cellulose degradation potential is not a universal capability, although it is widely distributed: 24% of the genomes surveyed possessed degradation capability, 56% reflected opportunistic degraders, and 20% possessed no relevant enzymes (Berlemont and Martiny 2013). A more recent, comprehensive survey of genes from 200,000 environmental microbiomes found that cellulose degradation potential was lower in saline environments than non-saline and that saline waters contained the lowest abundance of cellulase-encoding genes (Li et al. 2023). The distinction was not made between bacteria and archaea.

An analysis of the relative abundances of cellulase and glycoside-hydrolase genes (encoding cellulose-degrading enzymes) in 155 haloarchaeal genomes revealed potential cellulose degradation capability in 13 of these organisms (Elcheninov et al. 2023). This is a lower percentage than found in the earlier study mentioned above (Berlemont and Martiny 2013). Despite the evidence for genetic potential, cellulase production, and growth on soluble celluloses of WIPP-relevant haloarchaea (e.g., carboxymethylcellulose; Karray et al. 2018; Siham et al. 2020; Kasirajan and Maupin-Furlow 2020), only three studies have enriched cellulotrophic haloarchaea (from brine lake sediments) that were able to degrade various forms of insoluble cellulose, such as those found in WIPP waste (e.g., Whatman filter papers; Sorokin et al. 2015, 2018, 2019). Microcolony formation on crystalline fibers was a prerequisite for degradation. In an earlier study, a mixed culture enriched from G-seep brine (presumably archaea) reportedly adhered to and altered Kimwipe fibers, as observed microscopically (Vreeland et al. 1998). It is noteworthy that all these studies were carried out under aerobic conditions, since anaerobic processes account for only 5–10% of cellulose degradation (Pathak and Navneet 2017).

"Natural Analogue" for CPR Degradation

An archaeological site in Hallstatt, Austria, provides an excellent analog for long-term cellulose degradation in the WIPP environment. A wooden staircase, aged 1108 BC, was uncovered and retrieved from a Bronze and Iron Age salt mine. Although numerous halophilic organisms were detected and cultivated from the wood, the staircase did not begin to deteriorate until it was removed from its salt encasing, i.e., placed in oxic conditions (Piñar et al. 2016). Other excavated materials, including grass ropes and textiles, were also found to be well preserved (Grabner et al. 2021). The lack of significant degradation over a time frame equivalent to ~30% of WIPP's 10,000-year lifetime is evidence of either very little, or extremely slow, cellulose degradation in anoxic salt.

SOTERM-4.3 Microbial-Actinide Interactions

SOTERM-4.3.1 Actinide Toxicity Towards Microorganisms in the Disposal System

Actinide toxicity is one of many factors that will constrain microbial activity in WIPP (Section 4.1). This has been addressed previously (CRA-2019 Appendix SOTERM-4.3), and there are no new WIPP studies on this topic. However, new data are available relevant to organisms introduced in the soil fraction of the waste.

Ongoing monitoring of microbial communities at the Chernobyl and Fukushima sites has confirmed previous findings at contaminated sites in the U.S., namely: 1) community structural diversity generally decreases with increasing contamination, with a selection for specific groups of organisms; 2) 74% of the variance in population structure is explained by absorbed radiation doses, but is also dependent on environmental conditions and the presence and amount of organic matter; 3) Pu accounts for the majority of the total absorbed dose and hence toxicity; 4) there is a synergistic effect of associated contaminating metals; and 5) WIPP inventories of radionuclides per gram of introduced soil are orders of magnitude greater than the concentrations measured in Chernobyl soils, suggesting that the diversity of organisms present in soil waste within the drums is limited to organisms most tolerant of radioactivity and capable of utilizing whatever organic carbon was available in the drum (Barnhart et al. 1980; Fredrickson et al. 2004; Chapon et al. 2012; Theodorakopoulos et al. 2017; Hoyos-Hernandez et al. 2019; Lopez-Fernandez et al. 2021; Rogiers et al. 2021; Swanson et al. 2015). However, once drums are breached, the additional stressors of high ionic strength and chaotropicity will further affect the introduced community, especially as it is not halophilic. In summary, these introduced organisms are unlikely to be active but could act as colloids once released.

SOTERM-4.3.2 Bioreduction of Multivalent Actinides

The microbially-induced reduction of higher-valent actinides would represent a beneficial process for the WIPP, since lower-valent species tend to be less soluble. However, there are few data concerning metal reduction in hypersaline environments, and this mode of metabolism has never been observed in haloarchaea (Sorokin and Muyzer 2010; Oren 2011; Emmerich et al. 2012). While incubations of Culebra groundwaters have resulted in iron reduction, these were at lower ionic strengths than the WIPP near-field (maximum 3.5 M NaCl) and contained organisms other than haloarchaea (Swanson et al. 2013b).

There have been no new publications on the bioreduction of Np or Pu in over a decade, and there are no new WIPP-relevant data for any TRU elements. Uranium bioreduction at low salt concentrations in the WIPP far-field is discussed elsewhere (Swanson 2024b).

SOTERM-4.3.3 Biological Influence on Actinide Solubility via Association, Induced Precipitation, or Mineralization

Biological influence on the dissolved concentrations of actinides in WIPP brine has been discussed in detail previously (CRA-2019 Appendix SOTERM-4.3). Data from bioassociation studies have been used to determine the PROPMIC parameter for the PA colloid model since its inception (for more detail, see SOTERM-3.5). Both PROPMIC and CAPMIC parameters were updated for the CRA-2019 (Reed et al. 2019) and again for the CRA-2026 (Kaplan et al. 2025; Tables SOTERM-5 and -6).

The changes in parameter values for 2019 raised concerns that were further addressed at technical exchanges and in issued reports (U.S. EPA 2022; Swanson 2024a). As a result of these discussions, changes were again made to parameter values for all but An(III). These are presented in detail in Kaplan et al. (2025). The treatment of biocolloid data is discussed in CRA-2026 Appendix PA-4.4, King (2025), and SOTERM-3.5.

Unlike gas generation, bioassociation does not require that microorganisms be active or even alive. Here, the term is used to encompass surface sorption, surface mineralization, or internal uptake. The model assumes that all microorganisms can take up actinides, either externally or internally, and although mobility is assumed, it is not specifically linked to live organisms. Actinide association with mobile microorganisms contributes to releases from the repository.

A series of experiments was conducted to determine whether the WIPP isolate, *Halobacterium* sp., could transport the An(III) analog, neodymium, in the WIPP environment (Swanson et al. 2019). Most of this work was conducted in simplified 3.42 M NaCl brine, in order to establish behavior under controlled conditions. These were then extended to GWB and ERDA-6 brines at 90% strength. Results of these experiments showed that biological influence on neodymium solubility is a function of biomass concentration, test matrix, and the presence of EDTA, but not a function of neodymium concentration over an extended time frame.

The concentration of neodymium in solution was significantly affected by the test matrix, with very little loss from either GWB or pC_{H+} 9.5-specific brine and significant loss from ERDA-6. The results from these studies were used to calculate the new PROPMIC parameter values for the +3 case for the CRA-2019 (Reed et al. 2019; SOTERM-2019).

SOTERM-4.3.4 New Information on Microbial Colloids Since CRA-2019

Two recent studies have investigated the interaction of uranium with halophilic microorganisms. *Halobacterium* sp. GP5 1-1, isolated from halite from the Gorleben salt dome, was tested for association with uranium (Hilpmann et al. 2022). Uranium was immobilized in phosphate biominerals at low concentrations and by carboxylate groups in biofilm-like structures at higher concentrations. When compared to previous studies on a different *Halobacterium* species (DSM 15987; Bader et al. 2018), the organisms show similar interactions

with, but different tolerances to, uranium, suggesting that *Halobacterium* species in the disposal system will produce similar precipitated minerals, leading to immobilization.

Halophilic fungi isolated from mangrove sediment removed a significant amount of uranium from solution (Azam et al. 2024). Two of the tested isolates fall within the same genera as fungi detected in WIPP-bound waste (*Aspergillus* and *Penicillium*; Swanson et al. 2015). A third (*Engyodontium alba*) was isolated from WIPP halite (Swanson et al. 2013b). Although it is not expected that fungi will survive in WIPP brines under anoxic conditions, their capacity to take up uranium within a waste drum could contribute to immobilization once inundation occurs.

Additional neodymium studies have been carried out since the CRA-2019. The first of these studies investigated spores of a *Bacillus* sp. isolated from WIPP-bound waste (Swanson et al. 2021b). The spores were exposed to Nd in simplified solutions containing 0.15 M, 2 M, and 4 M NaCl. In these experiments, the spores released the ligand, dipicolinate, which led to resolubilization of Nd over time, although no bioassociation occurred.

A final series of neodymium experiments was carried out with the remaining WIPP halite isolates, including two haloarchaea (as yet unidentified) and four bacteria (*Chromohalobacter* sp., *Salinicoccus* sp., *Nesterenkonia* sp., and spores of *Thalassobacillus* sp.). These experiments found that, over time (up to one month), all Nd was removed from solution regardless of organism or salt concentration (Figure SOTERM-7; Swanson et al. 2023; Swanson 2024a).

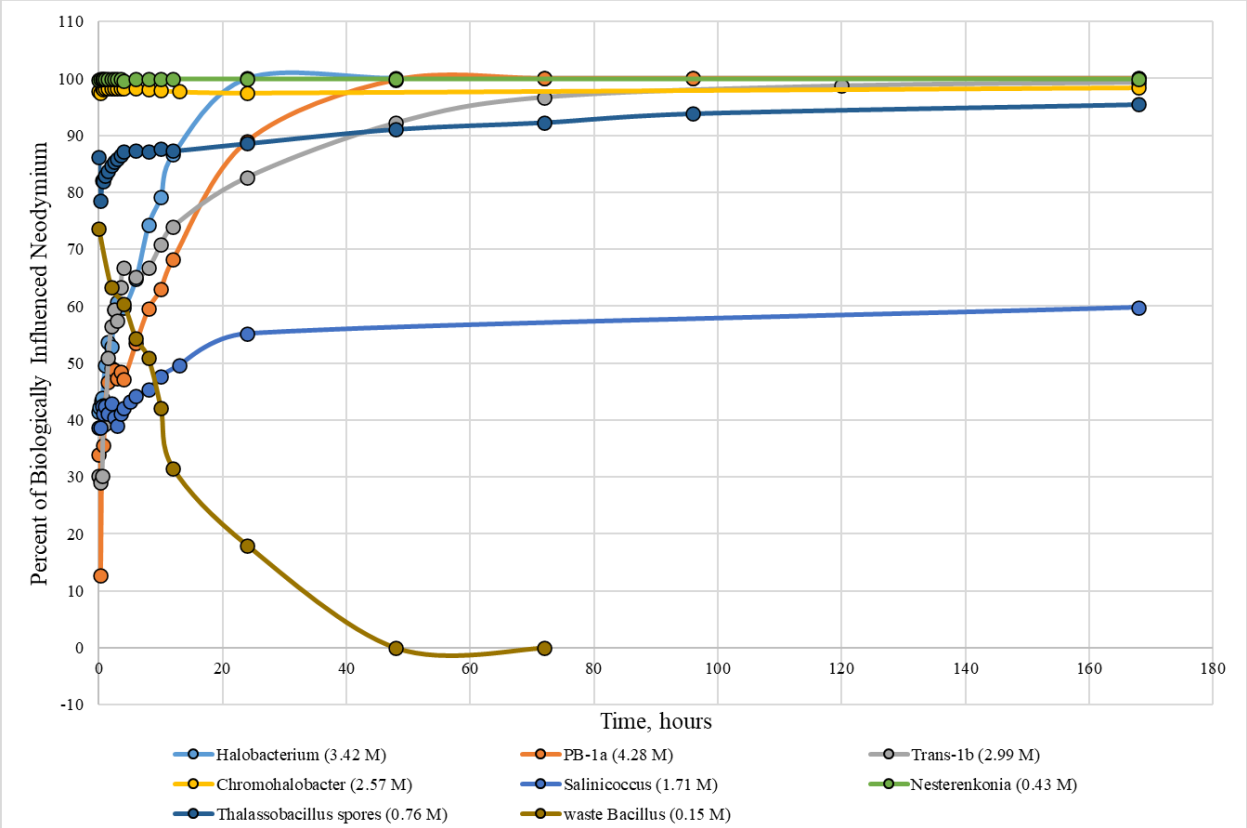


Figure SOTERM-7. Percent of Biologically Influenced Neodymium in Experiments with WIPP Halite Isolates Over the Course of the First Week, in Simple NaCl Solutions. Results from Experiments with *Bacillus* Spores are Also Included for Comparison (from Swanson 2024a).

Possible explanations for Nd removal include its association with microbial cells, cellular debris, or extracellular substances that settled out of suspension, as well as the biologically induced formation of Nd-containing precipitates or minerals.

When experiments were extended to GWB, Nd remained in solution (Figure SOTERM-8). Magnesium competition with Nd for cell surface sites was determined to be the reason for this, as evidenced by reduced bioassociation at concentrations above 0.6 M magnesium chloride (Swanson et al. 2023). When experiments were extended to ERDA-6, Nd was removed over time, as in simple NaCl solutions. This behavior is likely due to similar matrix composition with the predominance of NaCl in ERDA-6 (Figure SOTERM-8). These results suggest that in reacted WIPP brine with magnesium chloride concentrations up to 1 M, An(III) association with microbial colloids will be minimized. Results from this work led to the selection of An(III) biocolloid parameters for the CRA-2026 (Swanson 2024a; Kaplan et al. 2025).

Results from these experiments were used to determine the updated An(III) PROPMIC and CAPMIC parameters. PROPMIC (moles microbe-bound Nd/moles dissolved Nd) and CAPMIC (maximum moles microbe-bound Nd/L) values were calculated from the association data for

each tested organism in each brine at the final time point of the experiments (~ 1 month). The upper quartile value was selected as the parameter, bounding the majority of the data.

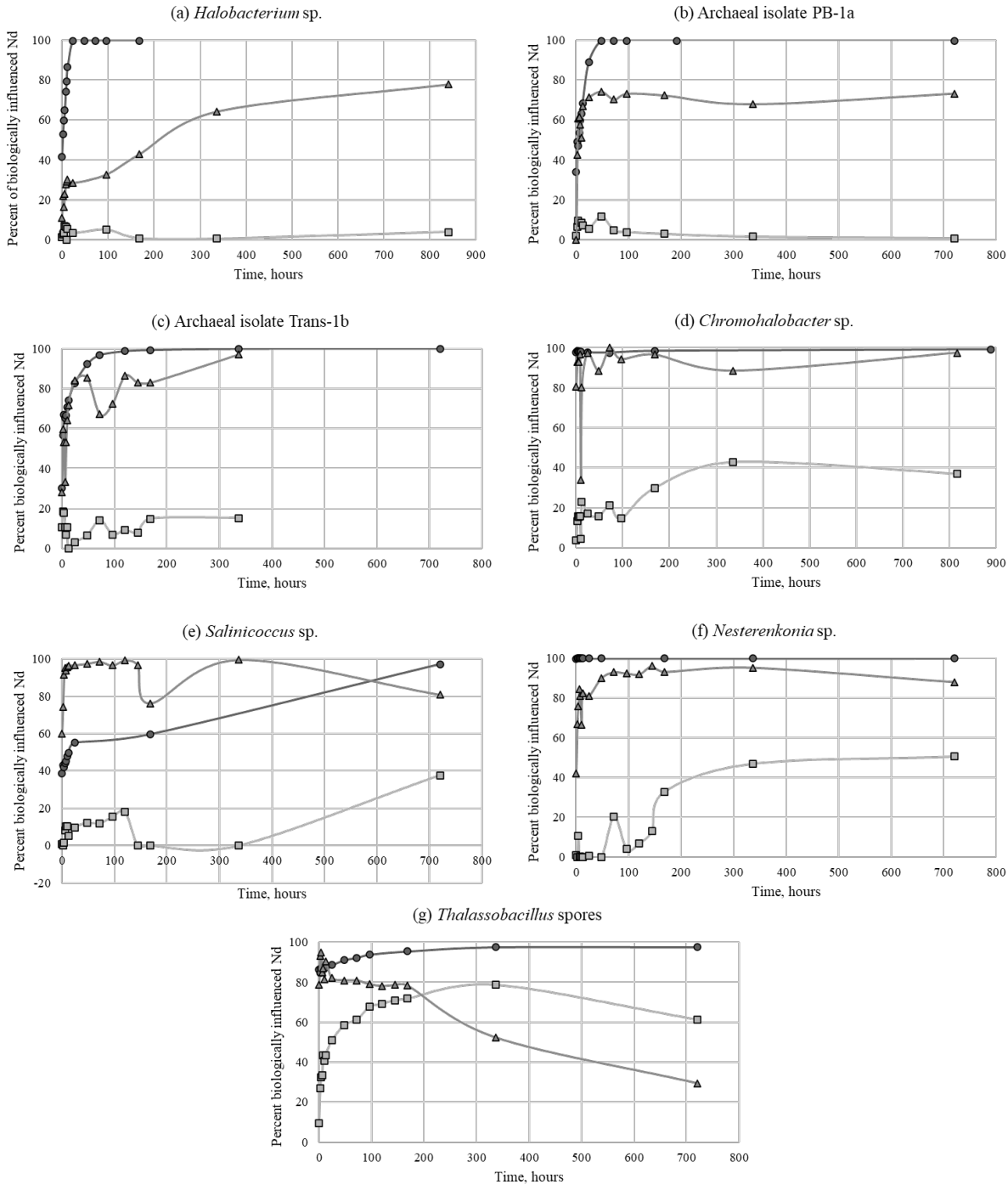


Figure SOTERM-8. Comparison of the Percent of Biologically Influenced Nd by All Tested Organisms in Simple NaCl (circles), GWB (squares), and ERDA-6 (triangles) (from Swanson 2024a). *Halobacterium* sp. Results (from Swanson et al. 2019) are Provided for Comparison.

In experiments conducted for the CRA-2019, 10^{-4} M EDTA was also added to the batch sorption tests using *Halobacterium* sp. as a test organism. In this case, there was no measurable biological influence on neodymium in solution in any of the tested brines (Swanson et al. 2019). As with the spore experiments, this suggests that the presence of ligands in the matrix could mitigate any biological effect on (im)mobilization.

SOTERM-5.0 WIPP-RELEVANT ACTINIDE CHEMISTRY

The actinide source term is affected by actinide concentrations, speciation, solubility, and colloid formation. Dissolved concentrations depend on the inventory and brine volume, but solubility behavior is governed by the chemical conditions in the repository (e.g., MgO-buffered pH, iron) that affect speciation and redox chemistry. Colloid formation depends on the presence of mineral, microbe, or humic substrates, while certain actinide oxidation states tend to form intrinsic colloids (e.g., IV).

Lower-valent actinides (III and IV oxidation states) are generally less soluble than higher-valent states (V and/or VI). For each oxidation state, solubility is affected by complexation with the inorganic and organic ligands that are part of the emplaced TRU waste or that are produced by post-emplacement processes. The reducing conditions established by the microbial consumption of oxygen and iron corrosion and maintained by anoxic iron corrosion lead to the lower-valent oxidation states.

In the CRA-2026 PA (CRA-2026 Appendix PA-4.3 and 4.4), the contributions of Pu, Am, U, Th, Cm, and Np are calculated, although only Pu and Am contribute significantly to TRU release from the WIPP, as they make up over 99% of the waste unit factor. An(III) and An(IV) are the more important oxidation states for WIPP, but An(III) is the most important based on the conceptual model assumption that Am always exists in the III state and the fact that the III oxidation state is generally more soluble than IV (depending on available ligands, especially EDTA (see SOTERM-6.4). In this CRA, a new parameter is introduced for Pu oxidation state distribution: Pu exists in the III state in ~25% of the vectors.

In this section, a summary of relevant actinide chemistry and a literature update are provided for the key actinides that comprise the WIPP mobile actinide source term: Th, U, Np, Pu, Am, and Cm.

SOTERM-5.1 Actinide Inventory in the WIPP

Table SOTERM-5 provides the activities and masses, at repository closure, of the main isotopes that contribute to radionuclide releases (Appendix PA-4.3; based on the IS PAIR, Van Soest 2025). The table also provides a comparison between the dissolved concentration calculated for each element and its solubility in brine (Domski 2025a). With the exception of Cm, the concentrations of all radionuclides exceed their solubility limits at closure.

Table SOTERM-5. CRA-2026 WIPP Radionuclide Inventory Decay-corrected to 2083

Selected Radionuclides	Activity curie (Ci)	Mass (kg)	Element-specific Inventory – Activity in Ci (Amount in kg)	Inventory-defined Dissolved Concentration[1] (M)	Predicted Solubility in 1X Brine Volume[2] (GWB ERDA-6) (M)
Actinides					
^{229}Th	6.31×10^{0}	2.99×10^{-2}	1.05×10^{2} (1.01×10^{3})	6.91×10^{-4}	5.34×10^{-8} 5.63×10^{-8}
^{230}Th	4.40×10^{-1}	2.13×10^{-2}			
^{232}Th	1.10×10^{-1}	1.01×10^{3}			
^{234}Th	9.77×10^{1}	4.22×10^{-6}			
^{233}U	3.29×10^{2}	3.43×10^{1}	1.09×10^{3} (2.91×10^{5})	1.94×10^{-1}	As U(VI) 3.00×10^{-6} 3.00×10^{-6} As U(IV), see Th(IV)
^{234}U	6.55×10^{2}	1.05×10^{2}			
^{235}U	2.79×10^{0}	1.28×10^{3}			
^{236}U	3.10×10^{0}	4.80×10^{1}			
^{238}U	9.77×10^{1}	2.90×10^{5}			
^{237}Np	7.22×10^{1}	1.02×10^{2}	1.71×10^{2} (1.02×10^{2})	6.84×10^{-5}	9.75×10^{-7} 4.01×10^{-6}
^{239}Np	9.93×10^{1}	4.28×10^{-7}			
^{238}Pu	1.37×10^{6}	8.02×10^{1}	6.30×10^{6} (6.08×10^{4})	4.03×10^{-2}	As Pu(III), see Am(III) As Pu(IV), see Th(IV)
^{239}Pu	3.51×10^{6}	5.66×10^{4}			
^{240}Pu	9.29×10^{5}	4.09×10^{3}			
^{241}Pu	4.89×10^{5}	4.71×10^{0}			
^{242}Pu	2.49×10^{2}	6.32×10^{1}			
^{244}Pu	5.84×10^{-2}	3.24×10^{0}			
^{241}Am	1.55×10^{6}	4.53×10^{2}	1.55×10^{6} (4.54×10^{2})	2.98×10^{-4}	1.45×10^{-5} 1.44×10^{-5}
^{243}Am	9.93×10^{1}	4.97×10^{-1}			
^{244}Cm	3.31×10^{3}	4.09×10^{-2}	3.54×10^{3} (7.79×10^{-1})	5.02×10^{-7}	See Am(III)
^{246}Cm	2.25×10^{2}	7.38×10^{-1}			
^{249}Cf	1.70×10^{1}	4.15×10^{-3}	1.70×10^{1} (4.15×10^{-3})	2.64×10^{-9}	Not calculated
Fission Products[3]					
^{137}Cs	3.18×10^{4}	3.66×10^{-1}	3.18×10^{4} (3.66×10^{-1})	4.23×10^{-7}	Not calculated

Selected Radionuclides	Activity curie (Ci)	Mass (kg)	Element-specific Inventory – Activity in Ci (Amount in kg)	Inventory-defined Dissolved Concentration[1] (M)	Predicted Solubility in 1X Brine Volume[2] (GWB ERDA-6) (M)
Actinides					
^{90}Sr	1.95×10^{4}	1.41×10^{-1}	1.95×10^{4} (1.41×10^{-1})	2.49×10^{-7}	Not calculated

[1]Moles in the inventory divided by the minimum brine volume for a DBR (6,314 m^3).

[2]From Domski 2025a.

[3]Fission products are not TRU but are required by 40 CFR 191 in PA calculations of release limits.

Based on the inventory, Pu and Am contribute to over 99% of the waste unit factor and to releases from the WIPP in a disturbed scenario. Pu isotopes, estimated at ~6.08×10^4 kg at the time of closure, represent approximately 80% of the Ci content in TRU waste at emplacement. This increases over time to ~93% at 1,000 years and over 99% at 10,000 years after closure due to radioactive decay and the relatively long half-life of ^{239}Pu (24,110 yr). There are five isotopes of Pu that make a significant contribution to the Pu inventory, but ^{239}Pu, ^{238}Pu, and ^{241}Pu are the major contributors to the Ci content.

Americium is present in relatively small quantities in TRU waste, with an estimated inventory of approximately 450 kg at emplacement (Van Soest 2025). Despite its limited mass, Am plays a significant role in potential actinide release from the WIPP, from the high specific activity of ^{241}Am (3.443 Ci/g). Its relative contribution decreases significantly after 7,000 years due to its half-life, 432 years.

Uranium is not classified as a TRU element, but it is the predominant actinide by mass in the WIPP. Thorium is also not a TRU component, although an estimated 1.01×10^3 kg of Th will be in the WIPP at closure. Over the regulatory period, U inventory increases slightly, and Th inventory is stable, but these remain a relatively small fraction of the mobile actinide source term based on Ci content.

Curium is also present in very small quantities in the WIPP (~ 40.9 g) (Van Soest 2025). Due to the high activity of isotope ^{244}Cm ($t_{½}$ = 18.11 years), Cm may be important during the early stages of repository evolution. However, because the half-life of ^{244}Cm is less than 20 years, it is not included in the waste unit factor. Other Cm isotopes with longer half-lives (such as ^{246}Cm) are also present and are included in the WIPP PA.

The WIPP repository is expected to contain ~102 kg of Np as of closure in 2083 according to the IS PAIR 2024 (Van Soest 2025). Neptunium is primarily present as the ^{237}Np isotope (half-life [$t_{½}$] = 2.144×10^6 yr) and its inventory is expected to increase with time, from the decay of ^{241}Am and possibly ^{238}U (n, 2n) reactions, to 462 kg at 1,000 years after closure (Van Soest 2025,

Tables 5-3 and 5-4). At these masses, ^{237}Np is expected to be the 44th most common actinide isotope within the WIPP at closure and to reach the level of 5th most abundant actinide isotope by 12083 based on current inventory information. Other isotopes of neptunium will be present at only relatively trace levels. For example, only ~0.43 mg of ^{239}Np is expected at closure and will not be associated with analogous increases in mass.

Although some cesium (Cs) and strontium (Sr) are initially present in the WIPP, these fission products can only contribute significantly to releases during the first century of repository history and are not significant beyond the period of institutional control (i.e., 100 years after repository closure; 40 CFR 194.41).

In Figure SOTERM-9, the activities of the actinides discussed in sections SOTERM-5.2 to SOTERM-5.6 are shown for the years 2083 through 12083 as the sum of CH and RH activities (from Tables 5-3 and 5-4 in Van Soest 2025).

The following sections discuss the chemistry of Th, U, Np, Pu, Am, and Cm, including chemical characteristics, dominant oxidation states, complexation behavior, and solubility controls that govern each radionuclide in the disposal system. This provides a basis for linking inventory changes and chemistry to potential mobility and influence on repository performance.

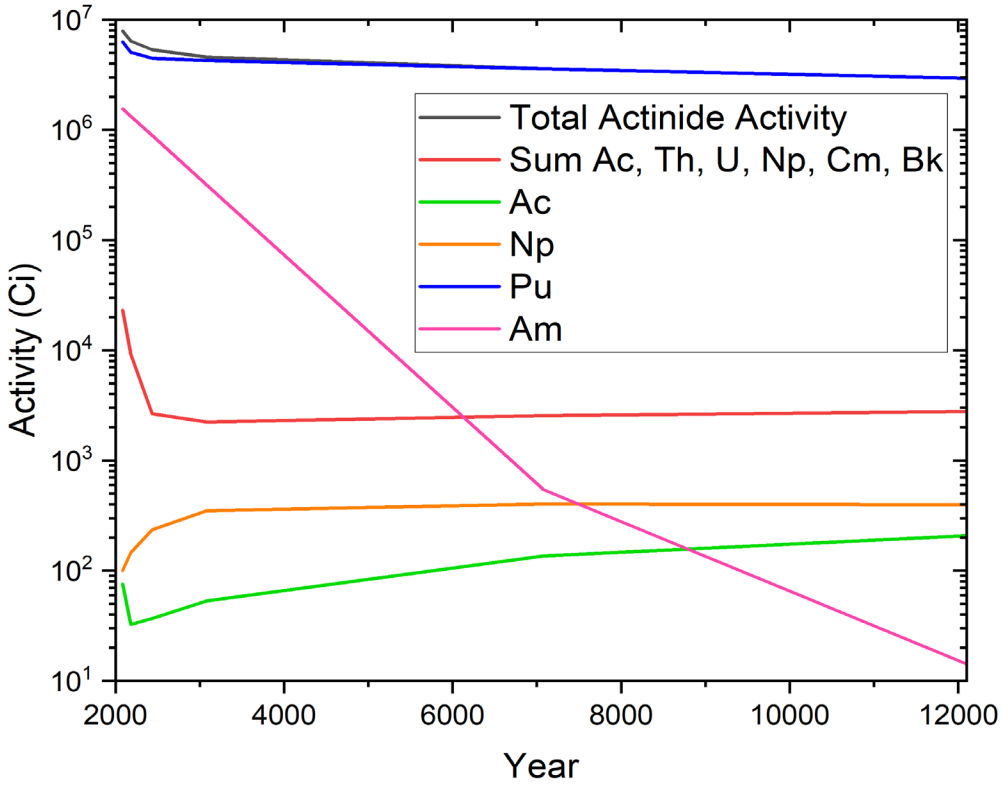


Figure SOTERM-9. Graphical Representation of the Sum of CH and RH Actinide Activities over Time (in Total Ci), from Tables 5-3 and 5-4 of the IS PAIR 2024 (after Van Soest 2025). Actinides are Discussed in Sections 5.2–5.6.

SOTERM-5.2 Thorium Chemistry: Background and Behavior under Repository Conditions

Thorium does not significantly contribute to the overall release of activity from the WIPP. Its relevance to the disposal system is due to its one stable oxidation state, Th(IV), which makes it useful as a redox-invariant analog for the IV actinides—Pu(IV), Np(IV), and U(IV). However, the use of thorium as an analog is contestable due to its large ionic radius in comparison to the periodic trend of actinide contraction and variance in ionic radii of the heavier actinides (U, Np, Pu, Am), which will have an effect on precipitation, complexation, and solubility in the repository. This limited chemical analogy results in an overprediction of Pu(IV) solubility. Zimmerman et al. (2014) also demonstrated significant differences between Th(IV) and Pu(IV) complexation with humic acid, with Pu(IV) exhibiting approximately 3 orders of magnitude stronger binding under identical experimental conditions. These results again highlight important limitations to the use of Th(IV) as a direct chemical analog for Pu(IV). Recent evaluations have identified Np(IV), and to a lesser extent U(IV), as better analogs, due to more similar chemical behavior and solubility characteristics (Altmaier et al. 2017b). Nevertheless, thorium is the only redox invariant An(IV). As such, the thermodynamic data for Th(IV) form the basis for An(IV) solubility calculations (Appendix SOTERM-6.5.1). Further discussion on the use of An(IV) analogs can be found in the respective sections for relevant actinides (Sections 5.4 and 5.5).

Several factors have a noticeable impact on the measured solubility of thorium including chemical form, crystallinity, the presence of complexants, and pH. Many thorium solubility studies are based on the chemical forms thorium dioxide [ThO_2] and thorium hydroxide [$Th(OH)_4$], and the solubilities of these two phases are significantly different. A multiparametric study on the dissolution of ThO_2(cr) was performed by Simonnet et al. (2016), identifying ThO_2(cr) as a poorly soluble material. None of the complexing agents tested, other than hydrofluoric acid (HF) in concentrated HNO_3, would provide total dissolution. Vandenborre et al. (2010) investigated bulk versus grain boundary solubilities of crystalline ThO_2. The differences were addressed as hydrated grain-boundary oxide materials resulting in the formation of $Th(OH)_4$ that enhanced solubility along the grain boundaries leaving behind bulk crystalline ThO_2. Nishikawa et al. (2018) investigated Th(IV) solubility at different aging and measurement temperatures. $Th(OH)_4$(am) solubility agreed with the experimental thermodynamic data reported in the literature. Felipe-Sotelo et al. (2015 and 2017) studied ThO_2(am) solubility in 95%-saturated $Ca(OH)_2$ at pH 12.3. Oversaturation and undersaturation experimental results are consistent with the known solubility of ThO_2(am) in equilibrium with $Th(OH)_4$(aq).

Chemical components in the disposal system available to complex with thorium include oxyanions (carbonate and sulfate), organic ligands (EDTA, citrate, acetate, and oxalate) and divalent metal salts (Ca^{2+} and Mg^{2+}). The resulting chemical forms change with increasing alkalinity and thorium hydrolysis. Hydrolysis is a critically important factor in defining the overall solubility of actinides in the IV oxidation state. At the buffered repository pH (9-10),

incomplete hydrolysis of thorium and other actinides, combined with multiple available complexing agents, complicate identification of predominant actinide species.

Carbonate complexation can significantly impact the solubility of Th(IV). However, added MgO and mildly alkaline conditions promoting hydrolysis will limit the formation of the thorium penta-carbonate species (Östhols et al. 1994; Altmaier et al. 2005).

Divalent cationic salts (Ca^{2+} and Mg^{2+}) affect the solubility of An(IV). The formation of $Ca_4[Th(OH)_8]^{4+}$ ion pairs in alkaline $CaCl_2$ solution causes a substantial increase in An(IV) solubility at pH > 11. The increased solubility is observed at $CaCl_2$ concentrations above 0.5 M (Brendebach et al. 2007; Altmaier et al. 2008). Kim et al. (2010) did not observe solubility enhancement below a calcium concentration of 1.25 mM. Calcium concentrations in the repository brine are predicted to be < 15 mM at pH of 9-10, although anhydrite provides an additional source of calcium that could result in an overestimation of dissolved Th(IV) (CRA-2026 Appendix GEOCHEM-4.4.2.2).

Due to their complex solution chemistry and strong tendency to hydrolyze, An(IV) form colloidal species. An(IV) will show different chemical properties in ionic, polymeric, and colloid forms, which in turn impact its respective migration patterns. In neutral-to-alkaline solutions, colloids can form as thorium oxyhydroxide independent of ionic strength (Altmaier et al. 2004).

Borkowski et al. (2012) data showed colloids can form but at a fraction much lower than the ~99% reported by Altmaier et al. (2004). Differences in brine composition and the presence of MgO colloids in the Altmaier study explain the discrepancies. The Borkowski studies observed an equilibration of the intrinsic colloidal fraction and the dissolved thorium species that shift overall solubility to lower values consistent with WIPP modeling predictions. The long-term shift can explain both the solubility values obtained in the German and WIPP data as metastable concentrations of thorium and the apparent discrepancy between model-predictions and experimental results. These solubility data support the conceptual model assumptions on An(IV) solubility

SOTERM-5.2.1 Literature Review Since the CRA-2019

New literature data regarding thorium chemistry have varying relevance to the WIPP.

Nisbet et al. (2019) investigated sulfate effects on the solubility of ThO_2 in 1 m NaCl solutions at hydrothermal temperatures. While higher temperatures are not WIPP-relevant, sulfate is present in the waste and in anhydrite interbeds of the Salado and assumed to be available for interaction with actinides, as well as reduction by microorganisms, potentially forming actinide, lead, or iron sulfide precipitates in the process.

Dumpala et al. (2021) performed a study to account for intrinsic colloid formation on thorium solubility. The colloid accountability and precipitate characterization explained the discrepancies in estimated solubility limits. Saturated thorium solutions equilibrated for ~3

years under various pH (5–11) and ionic strengths (0-3 M $NaClO_4$) were analyzed. pH decreased after the equilibration period, attributed to the release of H^+ ion when thorium forms polynuclear chains by double oxo-bridging resulting in colloid formation. $Th_6(OH)_{15}^{9+}$ was the predominant colloid in the pH range 4–10, while above 10, $Th(OH)_4$ was the end product. There was no colloid formation observed at pH 11 at all tested ionic strengths, due to the high probability of $Th(OH)_4$ precipitation rather than colloid aggregation. Quantification determined colloids as small as 13 nm and concentrations as low as 10^{10} particles/milliliter. For a constant ionic strength, the concentration of colloid particles decreased with increasing initial pH due to hydrolysis forming precipitates at higher pH. There is a cumulative influence of both the ionic strength and pH on colloid formation at higher pH. The amount of thorium, which excludes the colloid contribution, present as soluble polymeric species in the supernatant contributes to the solubility of thorium. Both the total thorium, thorium as Th^{4+}, and the contribution of colloids follows a descending order with an increase in initial pH of the sample. This can be attributed to hydrolysis as the initial pH of the sample increases. The samples kept at 0.1 M ionic strength showed no thorium as Th^{4+} or colloidal and the very low amount of thorium detected was predominantly in the polymeric form. The thorium content present in samples at an initial pH of 11 and 13 at ionic strength (I) = 1.0 and 3.0 M $NaClO_4$ was below detection limits, indicating a complete precipitation of the thorium.

The above studies provide insights into the role of intrinsic colloid particles on solubility (solubility product, log K_{sp}) estimation. The precipitate formed was also characterized by X-ray diffraction (XRD), and thermogravimetric analysis-density scanning calorimetry, which showed that the precipitate formed is neither completely $Th(OH)_4$ nor $ThO_2{\cdot}2H_2O$, but intermediate between the two forms. The thorium content contributing to non-colloidal form (ionic or polymeric species) was used to estimate the true solubility and solubility products of amorphous thorium hydroxide. Including Th colloids in the solubility calculations resulted in estimated solubilities that were 2–4 orders of magnitude higher than those in which only ionic and polymeric species were considered. This highlights the impact that colloids can have on the apparent solubility of amorphous thorium hydroxide. While the studies were performed in perchlorate, the alkaline and high ionic strength conditions are pertinent to WIPP-relevant colloid formation. It can be argued that use of perchloric acid as a minimally interactive “spectator” electrolyte better serves to establish colloidal formation behavior and can be used as a baseline for future colloid studies.

SOTERM-5.2.2 WIPP-specific Results Since the CRA-2019

There are no new WIPP-specific results on the chemistry and speciation of Th since the CRA-2019.

SOTERM-5.3 Uranium Chemistry: Background and Behavior under Repository Conditions

In typical oxidizing conditions, uranium predominantly exists as U(VI) in the form of UO_2^{2+}, which is stable even under mildly reducing conditions. U(VI) solubility in the repository is

expected to result from the combined effects of two processes: hydrolysis leading to oxyhydroxide phase formation, and carbonate complexation leading to U-carbonate phase formation. Both processes involve complex systems with numerous proposed speciation schemes. In carbonate-free or low-carbonate solutions, U(VI) speciation is primarily governed by hydrolysis.

However, under the strongly reducing and anoxic conditions expected in the repository, U(VI) may be reduced to U(IV) via interactions with reduced iron phases (Appendix SOTERM-2019). In PA, U speciates as U(IV) in the reduced PA vectors and as U(VI) in the oxidized vectors (Appendix SOTERM-6.4). Relevant thermodynamic data are listed in Table SOTERM-6.

Table SOTERM-6. Selected Equilibrium Constants for Solubility and Hydrolysis Reactions of Uranium Considered for Thermodynamic Calculations (from NEA-TDB 2020).

Reaction	$Log_{10}K°$	Equation
Solubility and Hydrolysis		
$UO_2(am, hyd) + 2H_2O (l) \leftrightarrow U^{4+} + 4OH^-$	– (54.500 ± 1.00)	SOTERM.1
$UO_3 \cdot 2H_2O(cr) + 2H^+ \leftrightarrow UO_2^{2+} + 3H_2O$	(5.350 ± 0.130)	SOTERM.2
$0.5\ Na_2U_2O_7 \cdot H_2O(cr) + 3H^+ \leftrightarrow Na^+ + UO_2^{2+} + 2H_2O(l)$	(12.200 ± 0.200)	SOTERM.3
$U^{4+} + H_2O(l) \leftrightarrow UOH^{3+} + H^+$	– (0.540 ± 0.060)	SOTERM.4
$U^{4+} + 2H_2O(l) \leftrightarrow U(OH)_2^{2+} + 2H^+$	– (1.900 ± 0.200)	SOTERM.5
$U^{4+} + 3H_2O(l) \leftrightarrow U(OH)_3^+ + 3H^+$	– (5.200 ± 0.400)	SOTERM.6
$U^{4+} + 4H_2O(l) \leftrightarrow U(OH)_4(aq) + 4H^+$	– (10.000 ± 1.400)	SOTERM.7
$UO_2^{2+} + H_2O(l) \leftrightarrow UO_2OH^+ + H^+$	– (5.250 ± 0.240)	SOTERM.8
$UO_2^{2+} + 2H_2O(l) \leftrightarrow UO_2(OH)_2(aq) + 2H^+$	– (12.150 ± 0.070)	SOTERM.9
$UO_2^{2+} + 3H_2O(l) \leftrightarrow UO_2(OH)_3^- + 3H^+$	– (20.250 ± 0.420)	SOTERM.10
$UO_2^{2+} + 4H_2O(l) \leftrightarrow UO_2(OH)_4^{2-} + 4H^+$	– (32.400 ± 0.680)	SOTERM.11
$2UO_2^{2+} + H_2O(l) \leftrightarrow (UO_2)_2OH^{3+} + H^+$	– (2.700 ± 1.000)	SOTERM.12
$2UO_2^{2+} + 2H_2O(l) \leftrightarrow (UO_2)_2(OH)_2^{2+} + 2H^+$	– (5.620 ± 0.080)	SOTERM.13
$3UO_2^{2+} + 4H_2O(l) \leftrightarrow (UO_2)_3(OH)_4^{2+} + 4H^+$	– (11.900 ± 0.300)	SOTERM.14
$3UO_2^{2+} + 5H_2O(l) \leftrightarrow (UO_2)_3(OH)_5^+ + 5H^+$	– (15.550 ± 0.120)	SOTERM.15
$3UO_2^{2+} + 7H_2O(l) \leftrightarrow (UO_2)_3(OH)_7^- + 7H^+$	– (32.200 ± 0.800)	SOTERM.16
$4UO_2^{2+} + 7H_2O(l) \leftrightarrow (UO_2)_4(OH)_7^+ + 7H^+$	– (21.900 ± 1.000)	SOTERM.17
Carbonate Reactions		
$UO_2^{2+} + CO_3^{2-} \leftrightarrow UO_2CO_3\ (aq)$	(9.940 ± 0.030)	SOTERM.18
$UO_2^{2+} + 2CO_3^{2-} \leftrightarrow UO_2(CO_3)_2^{2-}$	(16.610 ± 0.090)	SOTERM.19
$UO_2^{2+} + 3CO_3^{2-} \leftrightarrow UO_2(CO_3)_3^{4-}$	(21.840 ± 0.040)	SOTERM.20
$UO_2^+ + 3CO_3^{2-} \leftrightarrow UO_2(CO_3)_3^{5-}$	(6.950 ± 0.360)	SOTERM.21
$U^{4+} + 5CO_3^{2-} \leftrightarrow U(CO_3)_5^{6-}$	(34.000 ± 0.900)	SOTERM.22
$3UO_2^{2+} + 6CO_3^{2-} \leftrightarrow (UO_2)_3(CO_3)_6^{6-}$	(54.000 ± 1.000)	SOTERM.23

Reaction	$Log_{10}K°$	Equation
$2UO_2^{2+} + CO_2(g) + 4H_2O \leftrightarrow (UO_2)_2CO_3(OH)_3^- + 5H^+$	– (19.010 ± 0.500)	SOTERM.24

*Numbers are displayed as calculated from thermodynamic database.

The solubility data from the studies of Yamazaki et al. (1992), Diaz-Arocas and Grambow (1998), Altmaier et al. (2017a), Yalçıntaş et al. (2019), and Lucchini et al. (2013b), in high ionic strength solutions—including 5 M NaCl and $MgCl_2$, synthetic brines, and WIPP brines—ranged from 10^{-5} to 10^{-8} M U(VI), depending on the experimental conditions. Altmaier et al. (2017a), Cevirim-Papaioannou et al. (2018a), Cevirim-Papaioannou et al. (2018a, b), and Yalçıntaş et al. (2019) published a series of experimental solubility data for U(VI) in NaCl, KCl, and $MgCl_2$ solutions. These studies also included chemical, thermodynamic, and activity (Specific Ion Theory [SIT]/Pitzer [1973]) models based on extensive solid and aqueous phase characterization as well as an extensive evaluation of other existing data and models in the literature. The solid phase controlling the solubility from near-neutral to hyperalkaline pH was determined to be $UO_3 \cdot 2H_2O$(cr), $Na_2U_2O_7 \cdot H_2O$(cr), or $K_2U_2O_7 \cdot H_2O$(cr) depending on the salt type and concentration.

Carbonate plays a critical role in controlling the solubility and speciation of U(VI), particularly under near-neutral pH conditions, where carbonate or bicarbonate is available (Clark et al. 1995; NEA-TDB 2020). The three monomeric complexes, $UO_2(CO_3)$, $UO_2(CO_3)_2^{2-}$, and $UO_2(CO_3)_3^{4-}$, are present under these conditions. Additionally, evidence from electrochemical, solubility, and spectroscopy data supports the presence of $(UO_2)_3(CO_3)_6^{6-}$, $(UO_2)_2(CO_3)(OH)_3^-$, and $(UO_2)_{11}(CO_3)_6(OH)_{12}^{2-}$ polynuclear species, particularly under high metal ion concentrations or high ionic strength (Clark et al. 1995). At uranyl concentrations above 10^{-3} M, the trimeric cluster $(UO_2)_3(CO_3)_6^{6-}$ can be present in significant concentrations (Clark et al. 1995).

Several experimental studies have examined the influence of carbonate on U(VI) solubility in highly saline environments (Yamazaki et al. 1992; Reed and Wygmans 1997; Lin et al. 1998; Fanghänel and Neck 2002). Lin et al. (1998) investigated U(VI) solubility under saline conditions up to 5 M NaCl and found that $UO_2(CO_3)_3^{4-}$ became the dominant aqueous species at carbonate concentrations above 10^{-7} M. The solubility-controlling solid phase varied with CO_2 partial pressure: UO_2CO_3(s), under high CO_2 partial pressures, and sodium diuranate under low CO_2 partial pressures. Yamazaki et al. (1992), studying synthetic brine under atmospheric conditions, reported uranium concentrations in the millimolar range at $pC_{H+} = 8.4$, identifying the solid phase as poorly crystalline metaschoepite ($UO_3 \cdot xH_2O$). Thermodynamic modeling indicated that solubility decreases above this pC_{H+} were due to a shift from carbonate to hydroxide complexes, such as $UO_2(OH)_n^{2-n}$, driven by $CaCO_3$ precipitation and the transformation of schoepite into potassium diuranate. Reed and Wygmans (1997) investigated the behavior of U(VI), Np(VI), and Pu(VI) in two different brines (ERDA-6 at pH 8 and 10, and in G-Seep at pH 5 and 7) both with and without added carbonate (10^{-4} M), under a hydrogen atmosphere at 25 ± 5 °C. Their results showed that in ERDA-6 brine at pH 10, U(VI) concentrations remained stable around 1×10^{-4} M over time in the presence of carbonate. In G-seep brine, a two-order of magnitude decrease was observed in experiments conducted at

pH 7. These concentrations appeared to approach steady state values at ~2 × 10^{-6} M. These findings were later expanded upon by Lucchini et al. (2010a, 2010b, 2013a, 2013b), who conducted comprehensive solubility studies of U(VI) in GWB and ERDA-6 brine, under varied conditions. These results are summarized in Figure SOTERM-10. In the absence of carbonate, U(VI) solubility was ~ 10^{-6} M in GWB brine at $pC_{H+} \geq 7$ and between 10^{-8}–10^{-7} M in ERDA-6 at $pC_{H+} \geq 8$. These results put an upper solubility limit of about 10^{-6} M for uranyl in carbonate-free WIPP brines. At the expected pC_{H+} in the WIPP (~9.5), the measured uranium solubility was between 10^{-7} M and 10^{-6} M. However, in the presence of carbonate, the highest uranium solubility obtained experimentally was ~10^{-4} M. This was in experiments with a carbonate concentration 10 times higher than that predicted for WIPP (CRA-2026 Appendix GEOCHEM-3.3). It is important to note that the solubility without carbonate was 10 to 100 times lower than values reported in some earlier studies (Yamazaki et al. 1992; Diaz-Arocas and Grambow 1998), which might reflect less stringent control over CO_2 levels.

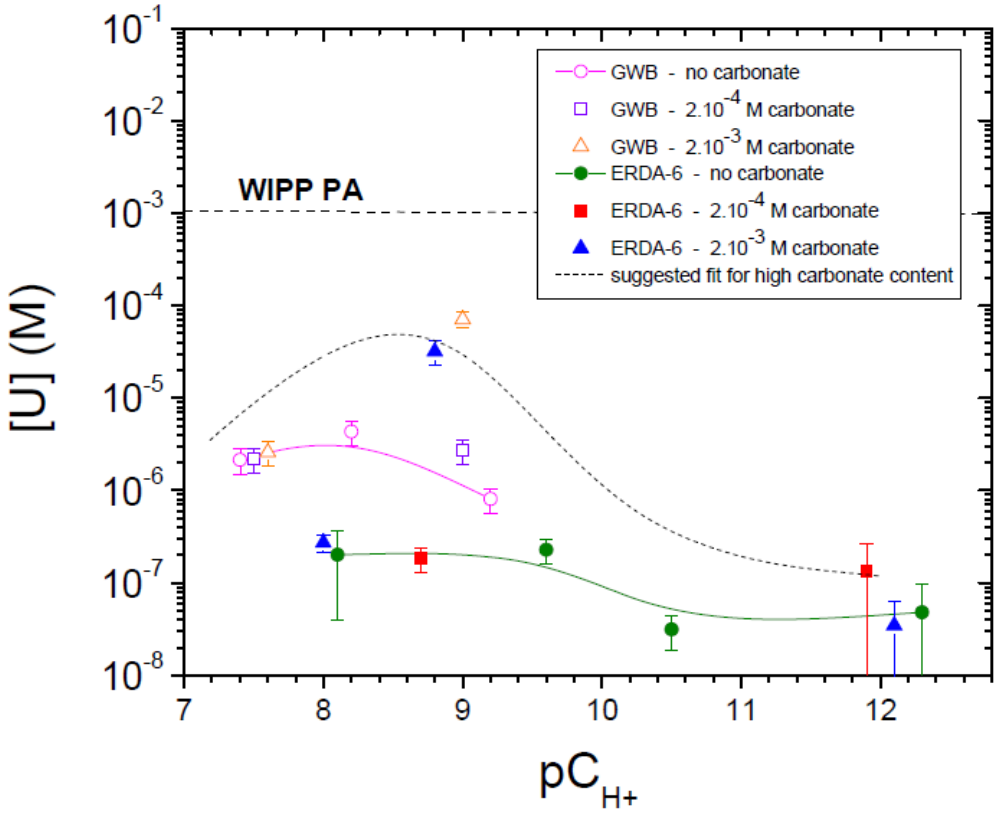


Figure SOTERM-10. Uranium Concentration in ERDA-6 (Filled Symbols) and GWB (Open Symbols) Versus pC_{H+} in N_2 Controlled Atmosphere, in the Presence or Absence of Carbonate (2×10^{-4} M and 2×10^{-3} M). The Carbonate Systems' Data Correspond to 17 Samplings Performed Over 994 Days. (See Lucchini et al. 2010a for the Determination of Uncertainties) (from Lucchini et al. 2013a).

SOTERM-5.3.1 Literature Review Since the CRA-2019

Recently, several studies have been dedicated to U reduction and uptake processes with nanoscale zero-valent iron (nZVI) for environmental remediation purposes. Various modification methods were applied, i.e., $Mg(OH)_2$-coated nZVI (Chen et al. 2021), biochar-supported ZVI (Zhang et al. 2019), nZVI for continuous reactors (Hua et al. 2021), nZVI encapsulated in graphene oxide (Tang et al. 2021), and carboxymethyl cellulose -ZVI nanoparticles for reductive immobilization of uranium (Zhao et al. 2020). In these studies, the removal mechanism under oxic conditions was determined to be adsorption of UO_2^{2+}, while under anoxic conditions, U removal from solution resulted from reduction, reductive immobilization/sorption, and co-precipitation processes. Pan et al. (2020) investigated the reduction of uranium using magnetite nanoparticles at neutral pH values observing U(VI) to be reduced gradually to a U(V)/U(IV) mixture, which remained for an extended period before complete reduction to U(IV).

Bender and Becker (2020) investigated the redox behavior and kinetics of complex formation between actinyl tricarbonate complexes of uranyl, neptunyl, and plutonyl with Fe^{2+} and H_2S to see if carbonate had a protective effect against reduction. The results suggest that the tricarbonate complex serves as an effective shield against actinide reduction in the tested reactions and will maintain actinyl solubility at elevated pH conditions. These findings are based on quantum-chemical modeling under idealized conditions, not under WIPP conditions.

The solubility and thermodynamic stability of a synthetic liebigite, $Ca_2UO_2(CO_3)_3 \cdot 10H_2O(cr)$, was investigated by Lee et al. (2019) in NaCl and $NaClO_4$ solutions within a wide range of ionic strength (0.03 m ≤ I_m ≤ 5.61 m), pH (7 ≤ pH_m ≤9, with $pH_m = -\log [H^+]$), and temperature (22 °C ≤ temperature (T) ≤ 80 °C; 72 ≤ T ≤ 176 °F) conditions. At room temperature, liebigite remained stable and controlled the solubility of U(VI) in the investigated NaCl and $NaClO_4$ systems with I_m ≤ 0.51 m. For the same temperature but high ionic strength (5.61m NaCl), liebigite transformed into andersonite ($Na_2CaUO_2(CO_3)_3 \cdot 6H_2O(cr)$), resulting in a decrease in solubility of approximately two orders of magnitude at $pH_m \approx 8$.

Deng et al. (2023) re-evaluated the equilibrium relationships between uranium (U^{6+}/U^{4+}) and iron (Fe^{3+}/Fe^{2+}) in hydrothermal fluids, using recent thermodynamic data and modeling of fluid inclusions from volcanic- and unconformity-related uranium deposits. Their geochemical modeling demonstrates that high concentrations of both U (>10 to >100 parts per million [ppm]) and Fe (>1,000 ppm) can be dissolved in acidic (pH < ~3.3), chloride-rich fluids (55–250 grams per liter Cl^-) at 150–250 °C, across a wide range of redox conditions. Four dominant speciation regimes were identified based on pH and redox conditions: U^{6+}–Fe^{3+}, U^{4+}–Fe^{2+}, U^{6+}–Fe^{2+}, and U^{4+}–Fe^{3+}, depending on oxygen fugacity. Importantly, the modeling showed that U^{6+} and Fe^{2+} can coexist and be stably transported, indicating that uraninite can precipitate without an external reducing agent. This finding expands the range of geochemical conditions under which uranium mineralization can occur, highlighting the critical influence of both pH and redox state. The authors concluded that local reduction occurs at mineral surfaces where clay

minerals and hematite act as catalytic sites promoting uranium reduction and precipitation through sorption–reduction mechanisms.

Ferguson et al. (2022) investigated citrate-promoted dissolution of a uranyl phosphate mineral, chernikovite [$(H_3O)(UO_2)(PO_4)\ 3H_2O$], by determining the extent of uranium release from chernikovite over a wide range of citrate concentrations. Experiments indicate that increasing citrate concentrations from 0.1 mM to 50 mM increases the concentration of dissolved uranium. Willberger et al. (2019) determined stability constants for acetate complexes with the actinides Am(III), Th(IV), Np(V), and U(VI) at an ionic strength of I = 0.3 M using CE-ICP-MS. Three U(VI) acetate complexes with $\log(\beta_1^\circ) = 3.01 \pm 0.12$, $\log(\beta_2^\circ) = 5.27 \pm 0.07$, and $\log(\beta_3^\circ) = 6.82 \pm 0.09$ were determined. The effects of EDTA complexation on the kinetics and thermodynamics of redox reactions of uranium at the pyrite-solution interface was investigated by Wang et al. (2022). Kim et al. (2021) used in situ electrochemical atomic force microscopy for imaging reduction products of uranyl as mediated by magnetite and ilmenite in the absence or presence of the organic ligands, EDTA, and oxalate. Kobayashi et al. (2019) investigated the effect of α-isosaccharinic acid (α-ISA) on the solubility and redox of tetravalent and hexavalent uranium [U(IV), U(VI)] in the pH_c range of 6–13 and at total ISA concentrations between 10^{-4}–10^{-1} M. The dependence of U(IV) solubility on the pH_c and $[ISA]_{tot}$ suggested the existence of $U(OH)_4(ISA)_2^{2-}$ as the dominant species in the pH_c range of 6–12. For the U(VI)-ISA system, $UO_2(OH)_3(ISA)_2^{3-}$ was suggested as a dominant species at pH_c 7–13. Xiong and Wang (2021a) investigated the stability constants for aqueous and solid uranyl oxalate complexes in high ionic strength environments, and developed a thermodynamic model for the UO_2^{2+}–Na^+–H^+–Cl^-–ClO_4^-–$C_2O_4^{2-}$–NO_3^-–H_2O system to ionic strength up to ~11 m. The computer code EQ3/6 Version 8.0a was employed as a modeling platform.

Yan et al. (2024) developed updated chemical, thermodynamic, and Pitzer activity models for the U^{4+}–Na^+–Mg^{2+}–Ca^{2+}–H^+–Cl^-–OH^-–H_2O system. The study is based on a comprehensive solubility dataset covering dilute to concentrated NaCl, $MgCl_2$, and $CaCl_2$ solutions, disregarding chloride complexation. Using the NEA-TDB reference values as a foundation, the models incorporate two hydrous U(IV) oxide phases, $UO_2{\cdot}2H_2O$(am) and $UO_2{\cdot}H_2O$(ncr), as well as the ternary complex $Ca_4[U(OH)_8]^{4+}$, identified by analogy to Th(IV), Np(IV), and Pu(IV). These refinements reflect the solubility changes due to particle ageing (Ostwald ripening) and improve geochemical modeling accuracy for uranium behavior, especially in concentrated brine conditions relevant to nuclear waste disposal.

Plyasunov (2023) presented the SIT parameters for the interactions of the uranyl ion (UO_2^{2+}) with chloride (Cl^-) and nitrate (NO_3^-) in aqueous solution at 25 °C (77 °F) and derived interaction coefficients: $\varepsilon(UO_2^{2+}, Cl^-) = 0.32$; $\varepsilon(UO_2Cl^+, Cl^-) = 0.32$; $\varepsilon(UO_2^{2+}, NO_3^-) = 0.28$ kg mol^{-1}, $\varepsilon(UO_2NO_3^+, NO_3^-) = 0.34 \pm 0.02$ kg mol^{-1}. They noted that the evaluated SIT interaction coefficients depend relatively strongly on the values of β_1^0 used in the calculation procedure. If the recommendations are changed, then the SIT interaction coefficients should be recalculated.

Grambow et al. (2023) investigated the formation of solid phase UO_{2+y} from 1 M NaCl solutions containing U(VI) and U(IV) and the solubility of the resulting precipitates under well-controlled reducing conditions as a function of pH, particle size, and supersaturation. Solid/liquid interaction experiments were performed under reducing hydrogen saturated conditions, approaching solubility equilibria either from supersaturated or undersaturated conditions. Their results show that the formation of tetramers and colloids is a critical initial step, and precipitation is nucleation-controlled rather than growth-controlled with critical nuclei dimensions of one unit cell of UO_2. No amorphous phases were observed; all precipitates were crystalline. The reduction of U(VI) leads to uraninite solid phases with oxidation states between UO_2 and U_4O_9. Solubilities at pH > 4 were higher than those predicted in H_2-saturated systems. Discrepancies were attributed to oxidation to U_4O_9, particle size effects, and presence of trace oxygen. Precipitation rates were controlled by nucleation kinetics and homogeneous nucleation led to colloid formation at pH > 1.7, while pseudocolloids were observed at lower pH. However, under natural conditions, homogeneous nucleation is not expected, because U(IV) concentration is not higher than 10^{-5} m.

McLean et al. (2025) investigated the inhibition of uranium dissolution in mixed uranium thorium dioxide under geological disposal conditions. Mixed oxide fuel pellets containing uranium and thorium dioxide were fabricated and their dissolution studied under conditions relevant to geological disposal composed of a clay host rock, anoxic synthetic Callovian Oxfordian groundwaters, containing hydrogen carbonate ions, and hydrogen peroxide. Dissolution was found to be independent of hydrogen peroxide concentration and controlled by the formation of conduction holes. Hole conduction appears more limiting in the case of mixed uranium-thorium oxide pellets. The doping of UO_2 with 25% ThO_2 reduced uranium release by a factor of five compared to undoped UO_2.

The paper written by Reiller (2024) provides a comprehensive review of existing thermodynamic data and estimates the predominance of triscarbonatoactinyl(VI) complexes with alkaline earth metals (Ae^{2+}) in carbonate-rich environments. Utilizing data from the NEA–TDB, the study predicts the predominance domains of the $Ae_nUO_2(CO_3)_3^{(4-2n)-}$ complexes in terms of pH, activities of HCO_3^-, Ca^{2+}, and Mg^{2+}, redox potentials (pe, E_h, or dissolved O_2), salinity, and temperature. Linear free energy relationships, based on widely accepted thermochemical data, have been used to estimate the potential predominance of $Ae_nAnO_2(CO_3)_3^{(4-2n)-}$ for Pu and Np.

SOTERM-5.3.2 WIPP-specific Results Since the CRA-2019

Since the CRA-2019, two key studies have been conducted to investigate the solubility behavior of U(VI) under conditions relevant to the WIPP. The first study (Kutahyali Aslani 2024) focused on the influence of borate and organic ligands on U(VI) solubility in WIPP brine at pC_{H+} 9, while the second study (Kutahyali Aslani 2025) specifically examined the complexation of U(VI) with citrate under similar conditions. These investigations provided essential data on U(VI) solubility and offered insights into the roles of borate and organics. The two studies aimed to address conditions specific to the WIPP repository by examining uranium solubility in brine solutions

containing varying concentrations of individual borate and organic components, as well as a mixture of all organic constituents.

In the 2024 study, U(VI) solubility was investigated in anoxic 90% WIPP brine at pC_{H+} 9 using an undersaturation approach over a 609-day period with freshly precipitated uranyl hydroxide ($UO_2(OH)_2$) as the solid phase. Experiments were conducted in the absence and presence of borate (0–140 mM) and in the presence of WIPP-relevant concentrations of organic ligands: EDTA, citrate, acetate, and oxalate (note that the ligand concentrations used in these experiments were based on the 2018 PAIR and the 17,400 m^3 brine volume; Van Soest 2018, Clayton 2008).

The solubility behavior of U(VI) in the presence of borate is illustrated in Figure SOTERM-11 demonstrating uranium solubility increases with increasing borate concentration. Experiments conducted with 100 mM borate in WIPP brine showed slightly higher solubility compared to those with lower borate concentrations. This aligns with earlier findings by Lucchini et al. (2013a). In that study, enhanced U(VI) solubility was observed in ERDA-6 brine at initial pC_{H+} values of 8.1, 9.6, and 10.5 when saturated with sodium tetraborate (~5×10^{-2} M).

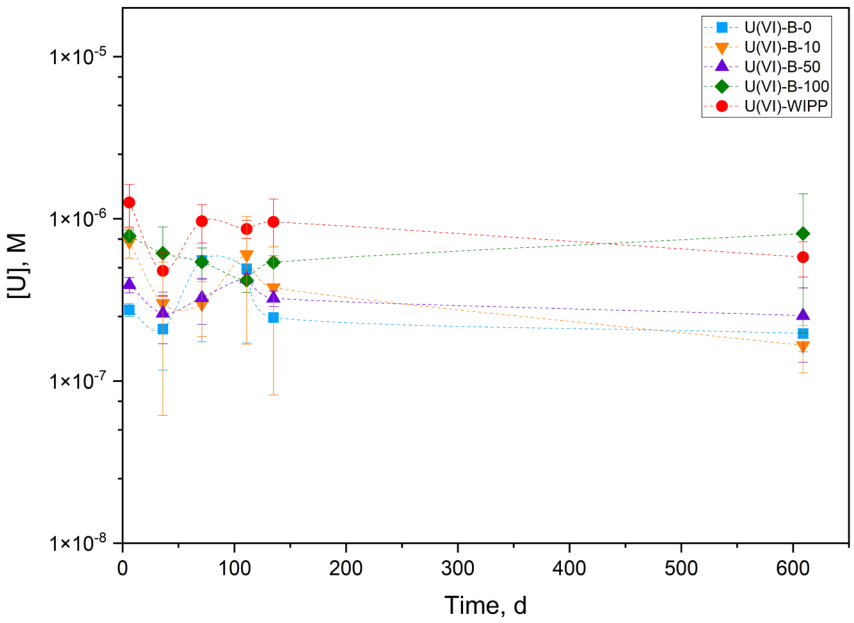


Figure SOTERM-11. Effect of Borate Concentration (mM) on [U] Solubility as a Function of Time in pC_{H+} 9 Brine. B Denotes Borate. 0-10-50-100 Denotes the Borate Concentrations in Solution. Error bars represent the standard deviation from the mean of 4-6 replicate measurements (Kutahyali Aslani 2024).

Figure SOTERM-12 shows U(VI) concentrations as a function of time in the presence of acetate, oxalate, citrate, EDTA, and a combined mixture of all four. The results show that the solubility

of uranium was higher when all WIPP-relevant organics were present and that this increased solubility was predominantly due to citrate complexation.

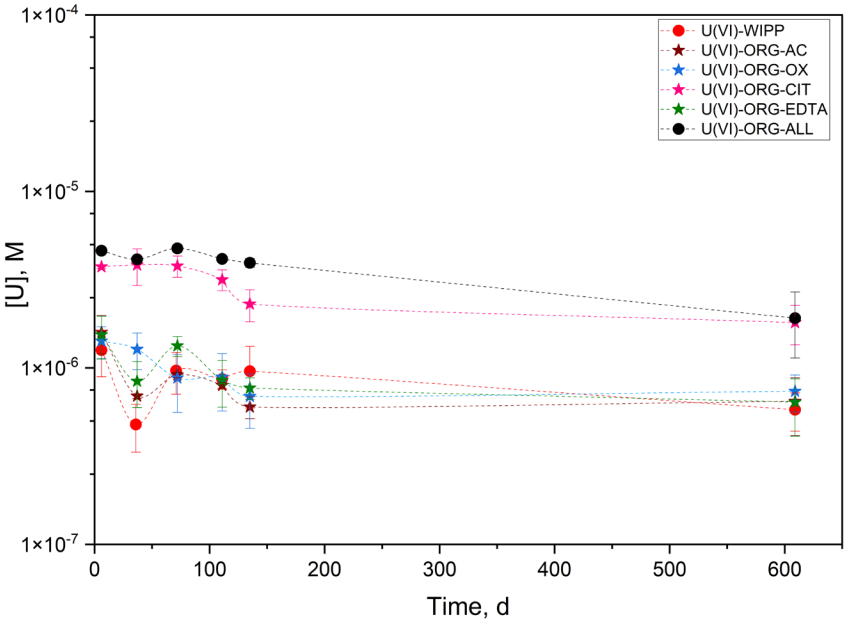


Figure SOTERM-12. Effect of Presence of Organics on [U] Solubility as a Function of Time in pC_{H+} 9 Brine. ORG: Organics, AC: Acetate, OX: Oxalate, CIT: Citrate (from Kutahyali Aslani 2024).

Based on these findings, the second study (Kutahyali Aslani 2025) focused specifically on the influence of citrate and varying pC_{H+} levels on U(VI) solubility under WIPP-relevant conditions. Using an undersaturation approach, experiments were conducted under anoxic conditions at room temperature in three synthetic WIPP brines (GWB at pC_{H+} 7, transitional brines at pC_{H+} 9 and 11) as well as in 5 M NaCl at pC_{H+} 7, 9, and 11 using $UO_2(OH)_2$ as the solid phase.

Figure SOTERM-13 shows the solubility of uranium in the presence and absence of citrate in undersaturation experiments in WIPP brines. Figure SOTERM-13 (a) shows the highest uranium solubility was observed at pC_{H+} 7 in the presence of citrate alone and all organic compounds. Although this pC_{H+} value does not fully represent the conditions at the WIPP, the effect of organics is clearly evident, as their presence increased the solubility of uranium nearly two orders of magnitude as compared with the control. At pC_{H+} 9, a similar pattern was observed with organics, particularly citrate, enhancing U(VI) solubility by approximately one order of magnitude. In contrast, at pC_{H+} 11, although citrate and organics still led to the highest solubility values, the difference relative to the control was less pronounced. Figure SOTERM-13 (b) shows the results after approximately 125 days, confirming that across all tested pC_{H+} values, the presence of organics enhances uranium solubility. Citrate is identified as the dominant complexing agent contributing to this effect.

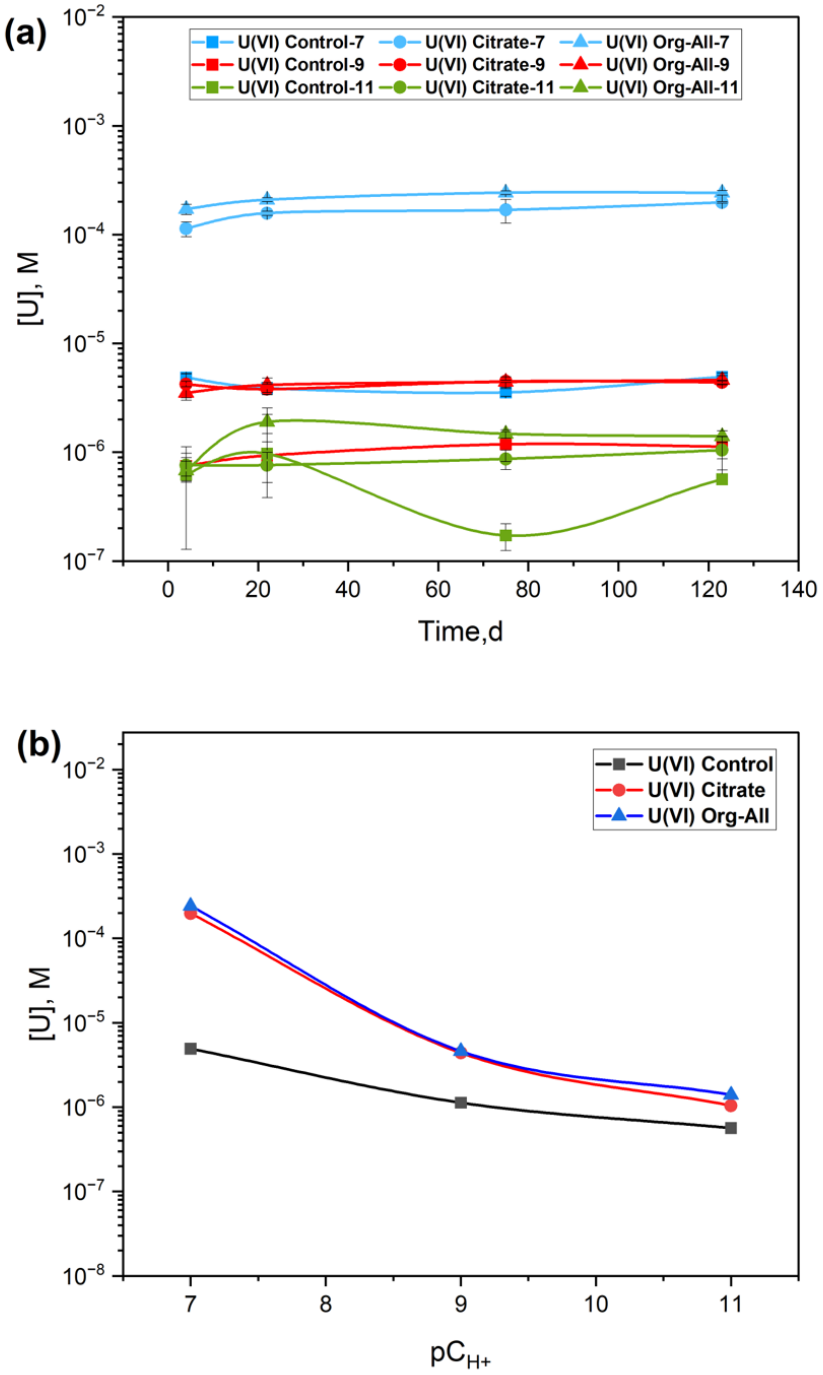


Figure SOTERM-13. Effect of Presence of Citrate Alone and All Organics on [U] Solubility as a Function of Time (a) and pC_{H+} (b) in WIPP-specific Brines (from Kutahyali Aslani 2025).

Figure SOTERM-14 (a) illustrates uranium solubility over time in 5 M NaCl at undersaturation conditions, comparing the presence and absence of citrate and mixed organic ligands. The solubilities are enhanced by the presence of organics at pC_{H+} 7 and 9. However, at pC_{H+} 11, organic effects on solubility diminished over time, and by the end of the experiment, no significant difference was observed between organic and control conditions. Figure SOTERM-14 (b) shows the solubility results after approximately 125 days, confirming that organics enhance uranium solubility at pC_{H+} 7 and 9, but have minimal impact on solubility at pC_{H+} 11.

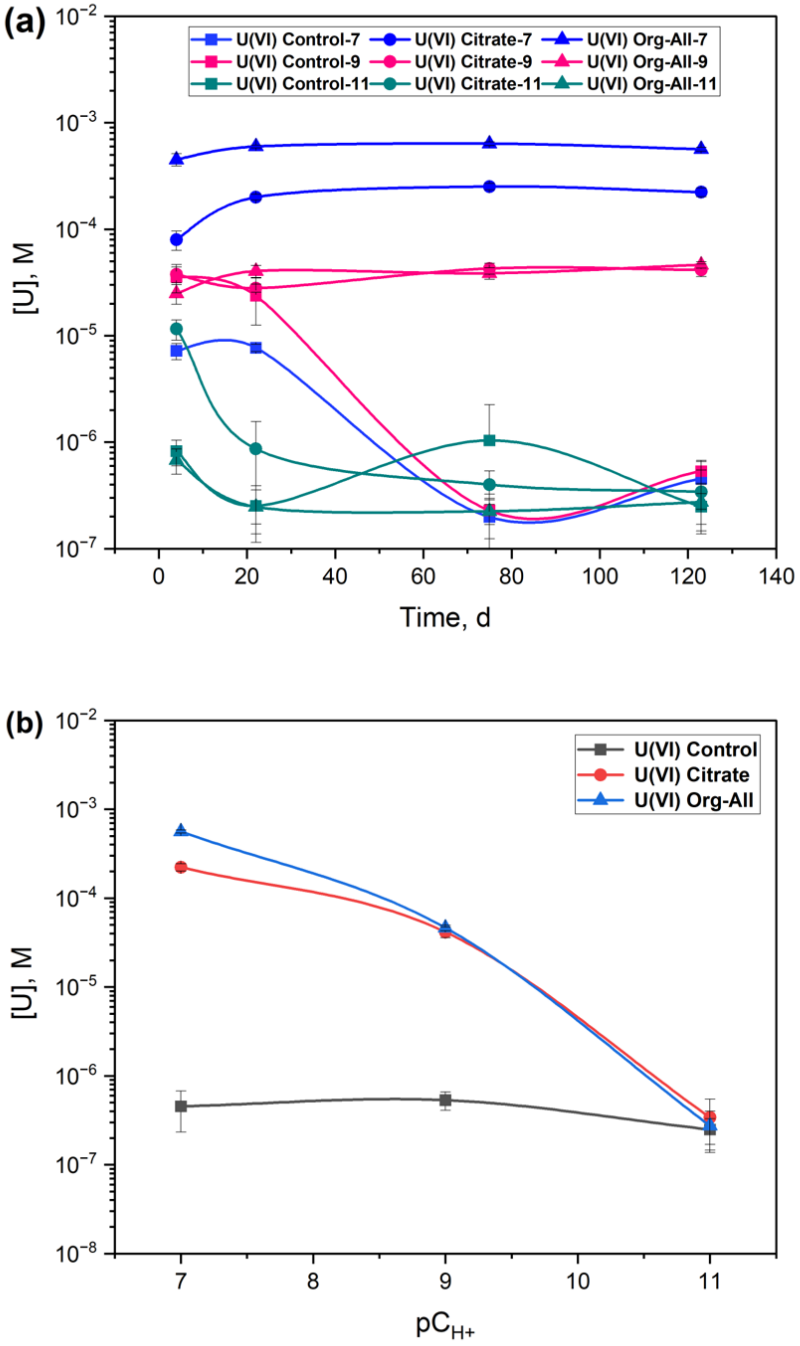


Figure SOTERM-14. Effect of Presence of Citrate Alone and All Organics on [U] Solubility as a Function of Time (a) and pC$_{H+}$ (b) in 5 M NaCl (from Kutahyali Aslani 2025).

U(VI) solubility is approximately one order of magnitude higher in 5 M NaCl than in pC$_{H+}$ 9 brine. This difference is attributed to the simpler composition of NaCl, which lacks the multivalent

cations (e.g., Ca^{2+}, Mg^{2+}) and anions (e.g., SO_4^{2-}) present in WIPP brine that can form insoluble uranium complexes or promote precipitation, thereby reducing dissolved U(VI) concentrations (Hummel et al. 2005; Appendix SOTERM-2019). Additionally, differences in pH buffering capacity and redox conditions between the two systems may influence uranium speciation, with WIPP brines exhibiting slightly lower E_h values in the presence of organics—potentially indicating mildly reducing conditions. Experimental data show that organic complexants, particularly citrate, significantly increase U(VI) solubility, reaching concentrations as high as ~3×10^{-6} M. These findings demonstrate that, under pC_{H+} 9 conditions representative of the WIPP repository, measured uranium solubility—whether in the presence or absence of organics—remains substantially lower than the 1 mM solubility value previously specified by EPA for use in performance assessments. These findings were used to recommend a new An(VI) solubility (SOLMOD6) of 3×10^{-6} M (Kaplan et al. 2025).

SOTERM-5.4 Neptunium Chemistry: Background and Behavior under Repository Conditions

Although the neptunium inventory at the WIPP increases over time through the decay of ^{241}Am, it is not expected to be a primary contributor to potential release. In PA, Np is assumed to be present in the IV and V oxidation states. Np speciates as Np(IV) in 50% of the PA vectors and as Np(V) in the other 50% of the PA vectors.

While neptunium can exist in several oxidation states (III–VII) in aqueous systems, Np(IV) and Np(V) are the most environmentally relevant (Lemire et al. 2001). Np(V), present as the neptunyl ion (NpO_2^+), is generally the more soluble and mobile species (Silva and Nitsche 1995), whereas Np(IV) forms strongly hydrolyzed, low-solubility species under reducing conditions (Rai and Ryan 1985; Eriksen et al. 1993). The difference between Np(IV) and Np(V) solubility depends on brine composition and the availability of complexing ligands (Neck and Kim 2001; Kaszuba and Runde 1999).

The redox behavior and aqueous speciation of Np are controlled primarily by pH, Eh, and complexation with inorganic ligands. Carbonate is the dominant complexing ligand for Np(V) and Np(VI), whereas hydrolysis becomes increasingly important at elevated pH (Lieser and Mühlenweg 1988; Clark et al. 1995). In carbonate-rich systems, neptunyl carbonate solids such as $MNpO_2CO_3 \cdot xH_2O$ and $M_3NpO_2(CO_3)_2$ (M = Na^+, K^+) may limit Np solubility (Neck et al. 1995; Novak et al. 1996; Al Mahamid et al. 1998). Np(IV) preferentially forms hydrolyzed species with substantially lower solubility (Kaszuba and Runde 1999; Kim 2006; Lierse et al. 1985).

Yang et al. (2017) observed Np(V) reduction to a disordered Np(IV)-bearing phase on metallic iron and magnetite under anoxic conditions. Although these experiments were conducted at low ionic strength, they provide mechanistic support for the possible stabilization of Np(IV) in the presence of iron corrosion products. Np(IV) is gaining relevance as an An(IV) analog, and long-term redox control techniques have been developed (Altmaier et al. 2017b), with potential WIPP applications. WIPP-specific studies support existing PA vector assignments between

Np(IV) and Np(V). For instance, Np(VI) was reduced to Np(V) in ERDA-6 brine at pH 10 and fully reduced in G-Seep brine at pH 7 without iron or microbes (Reed and Wygmans 1997).

Novak et al. (1996) investigated Np(V) and Np(VI) solubility under WIPP-relevant conditions to assess the applicability of models like the Fanghänel et al. (1995) Np(V)-Na^+-H^+-Cl^--ClO_4^--HCO_3^--CO_3^{2-}-CO_2(aq)-OH^--H_2O model. Np(V) solubility was measured in synthetic Na-K-Mg-Cl brines (I: 0.84, 2.97, 7.78 M) with CO_2(g), using an oversaturation approach. Dissolved Np(V) decreased several orders of magnitude within 100 days. Solid phases were identified as $KNpO_2CO_3 \cdot xH_2O$(s) by XRD.

Organic ligands influence actinide speciation by forming oxidation-state-specific complexes that enhance solubility and stabilize the redox state (Runde 2000). In the presence of oxalate, citrate, and EDTA, Np(VI) is rapidly reduced to Np(V), followed by slower formation of Np(IV). Neck et al. (1995) confirmed the stability of Np(V) carbonate complexes in 5 M NaCl. However, under WIPP-relevant reducing, anoxic conditions with Fe(II), Np(IV) is expected to dominate (Rai and Ryan 1985; Rai et al. 1982; Kim et al. 1985; Pryke and Rees 1986). Relevant thermodynamic data are listed in Table SOTERM-7.

Table SOTERM-7. Thermodynamic Data Relevant to Np Solubility and Reaction Chemistries (from NEA-TDB 2020).

Reaction	$Log_{10}K°$	Equation
Solubility and Hydrolysis of Np (IV)		
NpO_2 (am,hyd) ↔ $Np^{4+} + 4OH^-$	-56.7 ± 0.5	SOTERM.25
$Np^{4+} + H_2O(l) \leftrightarrow Np(OH)^{3+} + H^+$	0.55 ± 0.2	SOTERM.26
$Np^{4+} + 2H_2O(l) \leftrightarrow Np(OH)_2^{2+} + 2H^+$	0.35 ± 0.3	SOTERM.27
$Np^{4+} + 4H_2O(l) \leftrightarrow Np(OH)_4(aq) + 4H^+$	-8.3 ± 1.1	SOTERM.28
Solubility and Hydrolysis of Np(V)		
NpO_2OH (am,aged) + $H^+ \leftrightarrow NpO_2^+ + H_2O(l)$	4.7 ± 0.5	SOTERM.29
NpO_2OH (am,fresh) + $H^+ \leftrightarrow NpO_2^+ + H_2O(l)$	5.3 ± 0.2	SOTERM.30
$NpO_2^+ + H_2O(l) \leftrightarrow NpO_2OH$ (aq) + H^+	-11.3 ± 0.7	SOTERM.31
$NpO_2^+ + 2H_2O(l) \leftrightarrow NpO_2(OH)_2^- + 2H^+$	-23.6 ± 0.5	SOTERM.32
Carbonate Reactions		
NpO_2 (am,hyd) + $4CO_3^{2-} + 2H_2O \leftrightarrow Np(CO_3)_4^{4-} + 4OH^-$	-17.79 ± 0.22	SOTERM.33
$Np(CO_3)_4^{4-} + CO_3^{2-} \leftrightarrow Np(CO_3)_5^{6-}$	-1.07 ± 0.30	SOTERM.34
$NpO_2^+ + CO_3^{2-} \leftrightarrow NpO_2CO_3^-$	4.96 ± 0.06	SOTERM.35
$NpO_2CO_3^- + CO_3^{2-} \leftrightarrow NpO_2(CO_3)_2^{3-}$	1.57 ± 0.08	SOTERM.36
$NpO_2(CO_3)_2^{3-} + CO_3^{2-} \leftrightarrow NpO_2(CO_3)_3^{5-}$	-1.03 ± 0.11	SOTERM.37

$Log_{10}K°$ = the standard equilibrium constant of the reaction, logarithmic

SOTERM-5.4.1 Literature Results Since the CRA-2019

Maiwald et al. (2020) investigated Np(V)-oxalate (Ox^{2-}) speciation, thermodynamics, and structure using visible-near infrared spectroscopy (Vis-NIR), extended X-ray absorption fine structure (EXAFS) spectroscopy, and quantum chemical calculations. Vis-NIR spectra were collected as a function of [Ox^{2-}], ionic strength (0.5–4.0 m), and temperature (20–85 °C). Increasing [Ox^{2-}] caused a bathochromic shift and new absorption bands at 988 nm and 995 nm, with isosbestic points at 984.2 ± 0.2 and 990.9 ± 0.2 nm. Higher temperatures led to decreased molar fractions of 1:1 and 1:2 complexes due to their endothermic destabilization. Peak deconvolution showed distinct spectra for NpO_2^+ and $NpO_2(Ox)_n^{1-2n}$ (n = 1, 2) at both temperatures. EXAFS and quantum calculations confirmed that both $NpO_2(Ox)^-$ and $NpO_2(Ox)_2^{3-}$ form 5-membered ring chelate structures.

The WIPP inventory includes plastics, typically man-made from petroleum (e.g., polyethylene, polyvinyl chloride). Ioannis et al. (2022) studied Np(V) interactions with two microplastics—polyethylene terephthalate and polyamide nylon 6—across pH 2, 4, 7, and 9, and under seawater conditions with different ionic strength (0.1, 0.5, and 1 M NaCl). K_d (L/kg) values were evaluated. No major differences were observed between the plastics. In seawater, sorption coefficients dropped significantly due to high ionic strength and competing cations like Ca^{2+} and Fe^{2+}.

Vitova et al. (2020) combined multiple spectroscopic methods (EXAFS, X-ray absorption near edge structure [XANES]/High Resolution-XANES, XRD, scanning electron microscopy-energy dispersive X-ray spectroscopy [SEM-EDS], Raman) with thermodynamic modeling (Finite Difference Method Near-Edge Structure code) to investigate U(VI) and Np(V) reactivity in K/Na carbonate-rich solutions. Their results strongly suggested the formation of discrete neptunium- and uranium-carbonate solids, including $KNp(V)O_2CO_3$, $K_3Np(V)O_2(CO_3)_2$, and $K_3Na(UO_2)(CO_3)_3$. Importantly, no clear evidence was found for the co-incorporation of U or Np into the same crystalline or amorphous phases. Instead, Np and U precipitated as separate carbonate phases. Thermodynamic modeling identified $K_3Na(UO_2)(CO_3)_3$ and $K_3[NpO_2(CO_3)_2]\cdot nH_2O$(cr) as thermodynamically favored species, but the authors noted that equilibrium may not have been reached during the short time scale of these experiments and that the modeling results should not be overinterpreted due to existing thermodynamic data uncertainties. At pH 10.5 and oxic conditions, Np concentrations decreased by two orders of magnitude, and Np(V)-rich phases predominated, highlighting the structural stability of Np(V) carbonates in K-bearing solutions.

Hinz et al. (2020) studied Np(V)–borate interactions ($[B]_{tot}$ 0.004–0.16 M, where $[B]_{tot}$ is the concentration of all boron species present) via solubility experiments in 0.1–5.0 M NaCl and 0.25–4.5 M $MgCl_2$ at pH_m 7.2–10.0, using X-ray photoelectron spectroscopy (XPS), XRD, SEM-EDS, ultraviolet-visible-near infrared spectroscopy [UV-Vis-NIR]) spectroscopy, and synchrotron-based XANES/EXAFS. UV-Vis-NIR spectroscopy indicated weak Np(V)–borate complexation at mildly alkaline pH. While minimal effects on solubility were seen at near-neutral pH, solubility dropped 3–4 orders of magnitude in NaCl and dilute $MgCl_2$ at $[B]_{tot}$ = 0.16 M and $pH_m \leq 9$. Spectroscopy confirmed Np(V)–borate complexation at $[B]_{tot} \geq 0.04$ M. Solid characterization

identified Na– and Mg–Np(V)–borate phases. In 4.5 M $MgCl_2$, Mg–Np(V)–borate(cr) had low solubility, but transformation of NpO_2OH(am) was not observed (within the time frame of this study) in such concentrated brines.

In a study by Townsend et al. (2022), the interactions of Np(V) with iron-bearing minerals—specifically ferrihydrite, goethite, and mackinawite—were investigated using X-ray absorption spectroscopy (XAS). The results showed that Np(V)O_2^+ adsorbs to Fe(III) oxyhydroxide surfaces, likely forming inner-sphere complexes. However, EXAFS analysis could only reliably resolve the axial and equatorial oxygen shells (O_{ax} and O_{eq}), with no clear indication of Fe or carbonate coordination. In the goethite system, carbonate was present (10 mM $NaHCO_3$, pH 7) to reflect environmentally relevant aqueous conditions, yet no distinct carbonate coordination to Np could be resolved. In more reducing conditions, particularly in Fe(II)-containing mackinawite systems, Np(V) was reduced to Np(IV) and precipitated as nanocrystalline Np(IV)O_2. These findings highlight that Np speciation is highly dependent on the redox environment and mineralogy.

Kuzenkova et al. (2023) investigated the formation and structural characteristics of Np(V) carbonates in the presence of alkali (Na^+, K^+) and alkaline earth (Ca^{2+}) cations. Using chemical precipitation and ion exchange methods, they synthesized and characterized three distinct Np(V) carbonate phases: triclinic $NaNpO_2CO_3{\cdot}3H_2O$, hexagonal $KNpO_2CO_3$, and $Ca_{0.5}NpO_2CO_3$. XRD and EXAFS analyses revealed consistent structural models and highlighted the role of carbonate oxygen coordination. $NaNpO_2CO_3{\cdot}3H_2O$ contains interlayer solvated Na^+ ions, while $KNpO_2CO_3$ exhibits higher thermodynamic stability at neutral pH. The Ca-containing phase, $Ca_{0.5}NpO_2CO_3$, demonstrated even greater stability and was easily formed in mixed-cation systems.

SOTERM-5.4.2 WIPP-specific Results Since the CRA-2019

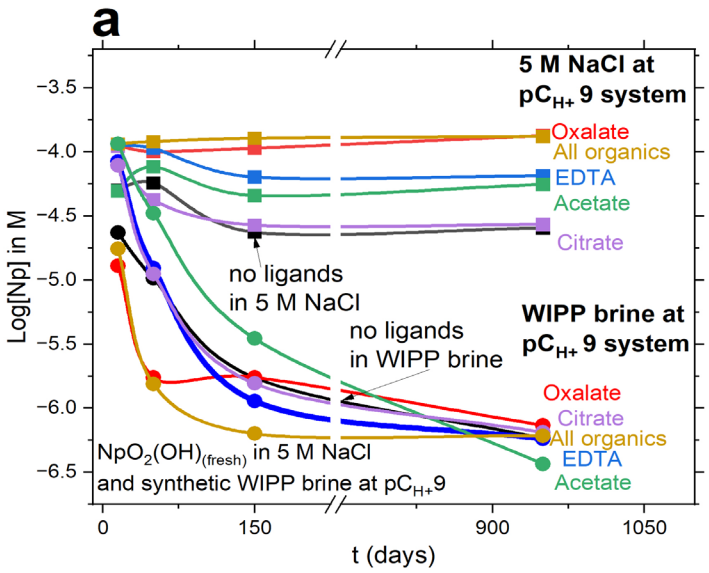
The aqueous chemistry of Np(V) in 5 M NaCl and synthetic WIPP brines as a function of pC_{H+} in the presence and absence of borate, WIPP-relevant ligands (EDTA, oxalate, citrate, acetate), and carbonate at T = 23 ± 2 °C (73.4 ± 3.6 °F) was studied by long-term batch solubility experiments (approximately 950 days) from an undersaturation approach (Kaplan 2025a). The data obtained in this study quantitatively evaluated the effects of WIPP-relevant concentrations of organics, borate, and carbonate on the solubility of Np(V). All experimental details and supporting information used to generate these results are reported in Kaplan (2025a).

Organic effect on solubility of Np(V) in 5 M NaCl and in WIPP brine

Figure SOTERM-15 summarizes the results reported by Kaplan (2025a) for Np solubility in the presence and absence of citrate, acetate, oxalate, and EDTA from undersaturated conditions in synthetic WIPP brine and 5 M NaCl as a function of time (up to 950 days) and pC_{H^+} (7, 9, 11). Np solubility was ~2 orders of magnitude higher in 5 M NaCl than in WIPP brine. Differences among organics were more pronounced in 5 M NaCl at pC_{H^+} 9 after 950 days, with oxalate yielding the highest solubility. In citrate samples, E_h values were significantly lower, suggesting more

reducing conditions and partial reduction of Np(V) to less soluble Np(IV). This aligns with reports showing citrate-mediated reduction of Np(V) and U(VI) to tetravalent forms (Bonin et al. 2008; Francis and Dodge 2008). Np(V) solubility in WIPP brine varied over time. Initially, organics caused notable differences, but their effect decreased, and after ~1 year, solubilities converged. By day 950, all samples except acetate reached similar levels. Early on, oxalate yielded the lowest solubility but later showed different behavior due to initial oversaturation at pH 9, followed by gradual redissolution and complex formation.

In contrast to experiments in WIPP brine, Kaplan (2025a) observed that organics increased Np solubility by up to two orders of magnitude in NaCl. This is likely due to stable Mg^{2+}/Ca^{2+}–ligand complexes that compete with Np for binding (Serne et al. 2002; Hummel et al. 2005; CRA-2019). These cations may also stabilize ternary/quaternary Np–ligand complexes (e.g., Ca/Mg–An–L or Ca/Mg–An–OH–L) (Felipe-Sotelo et al. 2015; DiBlasi et al. 2021b). Domski and Sisk-Scott (2019) modeled Np(V) speciation in GWB with organic ligands and 16 mM carbonate using the geochemical equilibrium modeling code EQ3/6, assuming $KNpO_2CO_3(s)$ as the solubility-controlling phase. Predicted dominant species at $pC_{H^+} \cong 9.5$ were NpO_2Ac, NpO_2^+, $NpO_2CO_3^-$, and NpO_2Ox^-, with NpO_2Ox^- being the most significant. Kaplan (2025a) results confirm that organic matter has a time-dependent decreasing effect on Np solubility. The model predicted a soluble Np concentration of 4.02×10^{-7} M, closely matching the experimental value of 3.84×10^{-7} M. Figure SOTERM-15b shows that organic ligands have minimal impact on Np solubility in synthetic WIPP brine across pC_{H^+} 7–9, with slight increases only at pC_{H^+} 11 due to ternary Np–carbonate–ligand complexes.



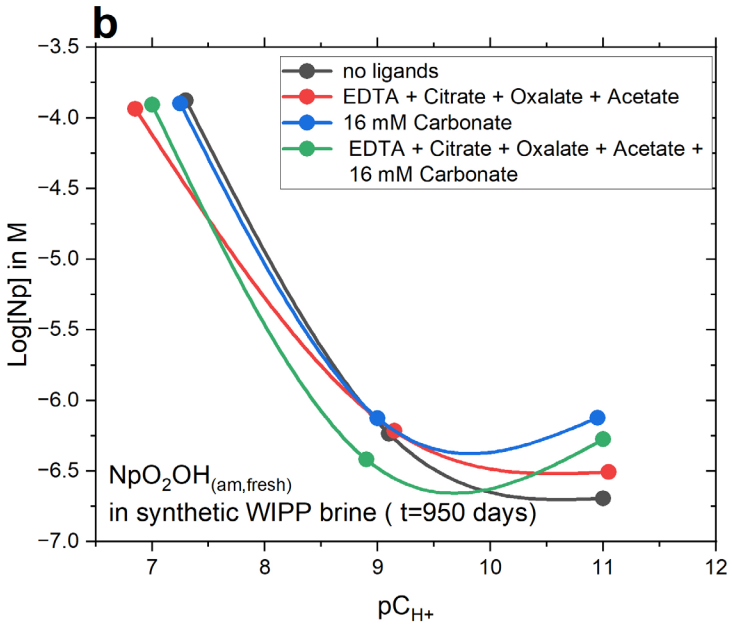


Figure SOTERM-15. Solubility of $NpO_2(OH)_{(am, fresh)}$ in the Absence and Presence of Organic Ligands (Citrate: 2.30 ×10^{-3} M, Acetate: 2.83 ×10^{-2} M, Oxalate: 1.13 × 10^{-2} M, EDTA: 7.92 × 10^{-5} M), and Carbonate (16 ×10^{-3} M) in Synthetic WIPP Brine and 5 M NaCl Solutions as a Function of Time (a) and pC_{H+} (b). The Maximum Uncertainty is ± 15 % (from Kaplan 2025a).

Borate effect on Np(V) solubility in 5 M NaCl and WIPP brine

The effect of boron species ($0 \le [B]_{tot} \le 160$ mM) on Np solubility in 5 M NaCl and synthetic WIPP brines at pC_{H+} 7, 9, and 11 is summarized in Figures SOTERM-16a and 16b (Kaplan 2025a), and includes previous solubility data for $NpO_2(OH)(am)$ (Petrov et al. 2017), $NpO_2(OH)(am, fresh)$, and $NaNpO_2$-borate(cr) (Hinz et al. 2020). The observed Np solubility under alkaline conditions in the absence of borate is in reasonable agreement with the previously reported solubility of $NpO_2OH(am)$ in a 5 M NaCl solution (Petrov et al. 2017). The presence of borate had virtually no effect on Np solubility in 5 M NaCl solution or WIPP brine at pC_{H+} 7 and 11. The effect of borate became apparent at pC_{H+} 9, where the concentration of aqueous Np significantly decreased with increasing borate concentration in 5 M NaCl solution. In the presence of $[B]_{tot}$ 160 mM, the solubility limit of Np(V) in 5 M NaCl was more than 3 orders of magnitude lower than that observed in the absence of borate at pC_{H+} 9. These results support the formation of Np-borate solid phases controlling solubility at pC_{H+} 9 in 5 M NaCl. Hinz et al. (2020) performed multi-method solid phase characterization using XRD, XPS, SEM–EDS, transmission electron microscopy, and XAS to confirm the formation of hitherto unknown Na–Np(V)–borate(cr) solid phases in NaCl (Hinz et al. 2020). The presence of borate in synthetic WIPP brine at pC_{H+} 9 had a less pronounced effect on Np solubility compared to the NaCl system, with a decrease of less than 0.5 log units observed.

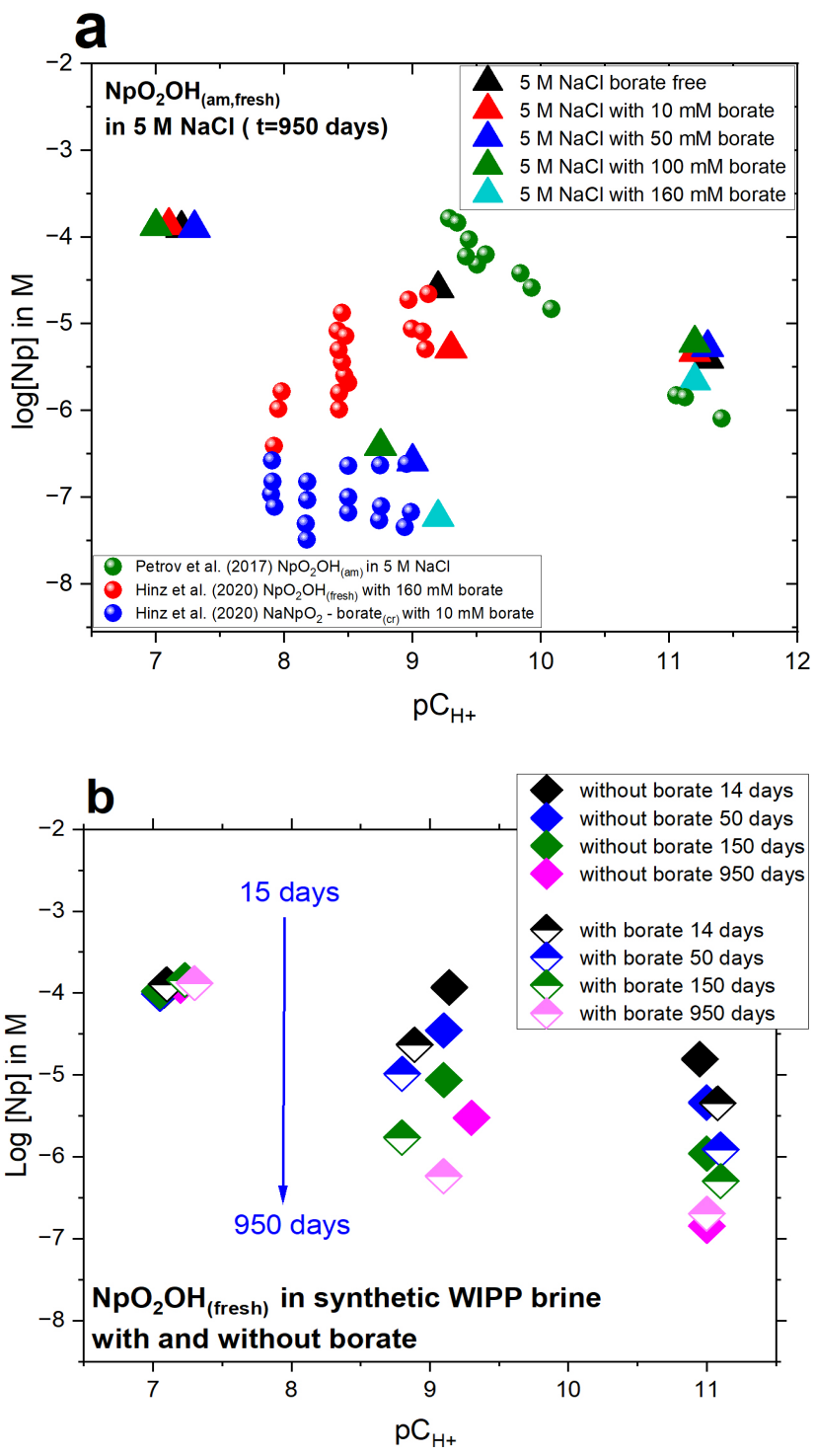


Figure SOTERM-16. Solubility of $NpO_2(OH)(am)$ in the Presence of $[B]_{tot}$ ($0 \leq [B]_{tot} \leq 160$ mM) in 5 M NaCl Solutions as a Function of pC_{H+} Determined Herein (as Colored Triangles), as well as Previous Experimental Solubility Data in the Presence and Absence of Borate (Petrov et al. 2017; Hinz et al. 2020) (Half-Shaded Diamonds) (a). Solubility of $NpO_2(OH)_{(am)}$ in Synthetic WIPP

Brine in the Presence and Absence of 160 mM Borate as a Function of pC_{H+} is Also Illustrated (b). Maximum Uncertainty is ± 15 % (from Kaplan 2025a).

Carbonate effect on Np(V) solubility in 5 M NaCl

The solubility of $NpO_2(OH)(am)$ was investigated as a function of pC_{H^+} and carbonate concentration (1–100 mM in 5 M NaCl; 16 mM in synthetic WIPP brine) at pC_{H^+} 7, 9, and 11 using an undersaturation experimental approach (Figure SOTERM-17; Kaplan 2025a). Since NaCl solutions have low pC_{H^+} buffering capacity, the addition of carbonate caused slight shifts in pC_{H^+}. Samples were equilibrated over 950 days. In 5 M NaCl, $NpO_2(OH)(am)$ solubility showed no significant change at pC_{H^+} 7. At pC_{H^+} 9, a slight decrease in Np concentration was observed with increasing carbonate. This trend is consistent with findings by Nitsche et al. (1992), who reported a small drop in Np solubility in Yucca Mountain groundwater where $[CO_3^{2-}]$ = 11.44 mM at pC_{H^+} 6.7 compared to 2.81 mM at pC_{H^+} 7.0. At pC_{H^+} 11 with 100 mM carbonate, solubility increased significantly, reflecting dominant carbonate complexation under alkaline conditions. Since carbonate concentrations in WIPP brines are only predicted to reach ~ 16 mM, this represents an extreme upper bound (Appendix-GEOCHEM-3.0). Runde (2000) investigated Np(V) solid-liquid equilibria in 5 M NaCl with varying carbonate concentrations. He demonstrated that at low carbonate levels, the solubility-controlling phase was $NaNpO_2CO_3{\cdot}3.5H_2O(s)$, a kinetically favored but thermodynamically unstable ternary Np(V) carbonate. Over time, this phase converts into the thermodynamically stable $Na_3NpO_2(CO_3)_2{\cdot}nH_2O(s)$. This phase transition explains the observed decrease in Np solubility at lower carbonate concentrations. Thus, solubility behavior in the Np-carbonate system reflects the dynamic between kinetic precipitation of $NaNpO_2CO_3{\cdot}3.5H_2O(s)$ and its transformation to the more stable $Na_3NpO_2(CO_3)_2{\cdot}nH_2O(s)$, especially under long-term equilibration over months to years (Neck et al. 1995; Runde 2000).

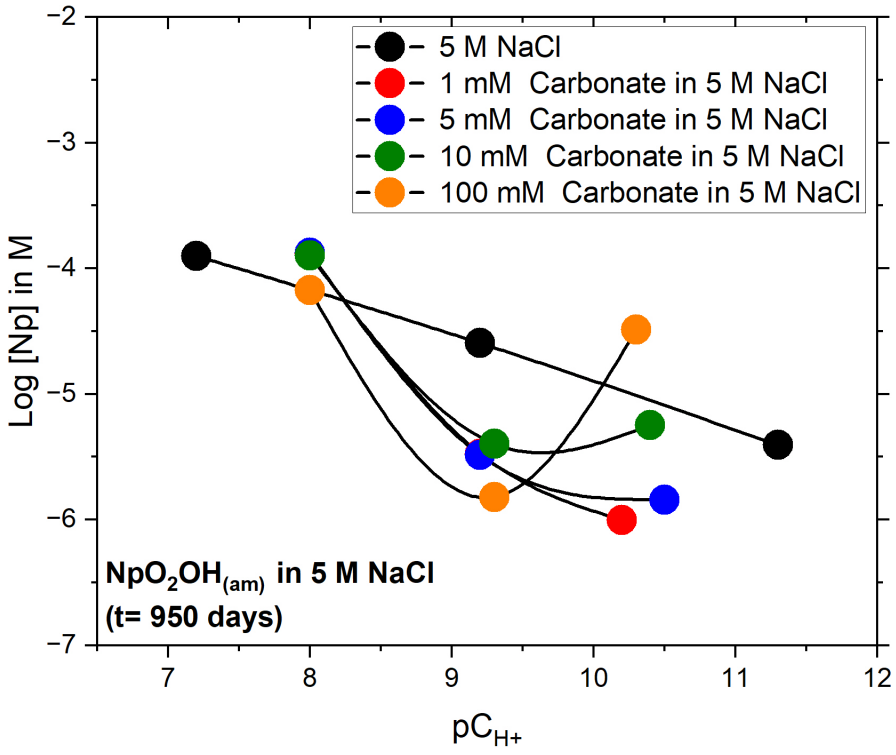


Figure SOTERM-17. Solubility of $NpO_2(OH)(am)$ in the Presence of 1 mM ≤ $[CO_3^{2-}]_{tot}$ ≤ 100 mM in 5 M NaCl as a Function of pC_{H+}. Maximum Error is ± 15 % (from Kaplan 2025a).

Determination of solid phase speciation

Np L_{III}-edge XAS spectra were collected over 6 months from ongoing solubility experiments (Kaplan 2025a). Figure SOTERM-18 presents solid-state reference spectra of $Np(IV)O_2(s)$ and $Np(V)O_2(OH)(s)$, along with aqueous-phase spectra of Np(IV)(aq) and Np(V)(aq). Differentiation between Np(IV) and Np(V) in L_{III}-edge XANES is attributed to the axial "yl" oxygen atoms, with the Np=O bond appearing as a "yl" shoulder in the spectrum (see Figure SOTERM-18). Figure SOTERM-18 and Table SOTERM-8 show that the oxidation state transition from Np(IV) to Np(V) results in a ~1 electron volt (eV) shift in the white line (WL). The WL shape and position indicate an oxidation state consistent with solid Np(V) reference samples shown in Figure SOTERM-18 and Table SOTERM-8. To quantify the Np oxidation state, linear combination fitting analysis (LCF[A]) was conducted on the XANES region (17,585–17,700 eV), using solid Np(IV) and Np(V) references. LCF(A) results reveal that all samples consist of 95–99% Np(V), with ± 8% uncertainty. The LCF(A) fits and experimental data are displayed in Figure SOTERM-18.

Table SOTERM-8. Energy Positions of the Np L_{III}-edge XANES First Inflection Point and White Line Maximum for Aqueous and Solid Np(V) References, Seven Samples from the Present Work, and Two Reference Spectra (Np(IV) and Np(V)). Values in eV (Calibration Error ±0.4 eV). (from Kaplan 2025a).

Sample matrix	White line maximum (eV)
$Np(IV)_{(aq)}$ reference [Reich et al. 2000]	17618.0
$Np(V)_{(aq)}$ reference [Reich et al. 2000]	17617.0
$Np(IV)O_{2(s)}$ reference to LCF(A)	17618.2
$Np(V)O_2(OH)_{(s)}$ reference to LCF(A) and starting material	17617.2
Np(V) WIPP in 5 M NaCl at pC_{H+} 9	17617.2
Np(V) synthetic WIPP brine at pC_{H+} 9	17616.3
Np(V) 5 M NaCl at pC_{H+} 9 – 100 mM carbonate	17616.5
Np(V) in synthetic WIPP brine at pC_{H+} 9 – 16 mM carbonate	17616.6

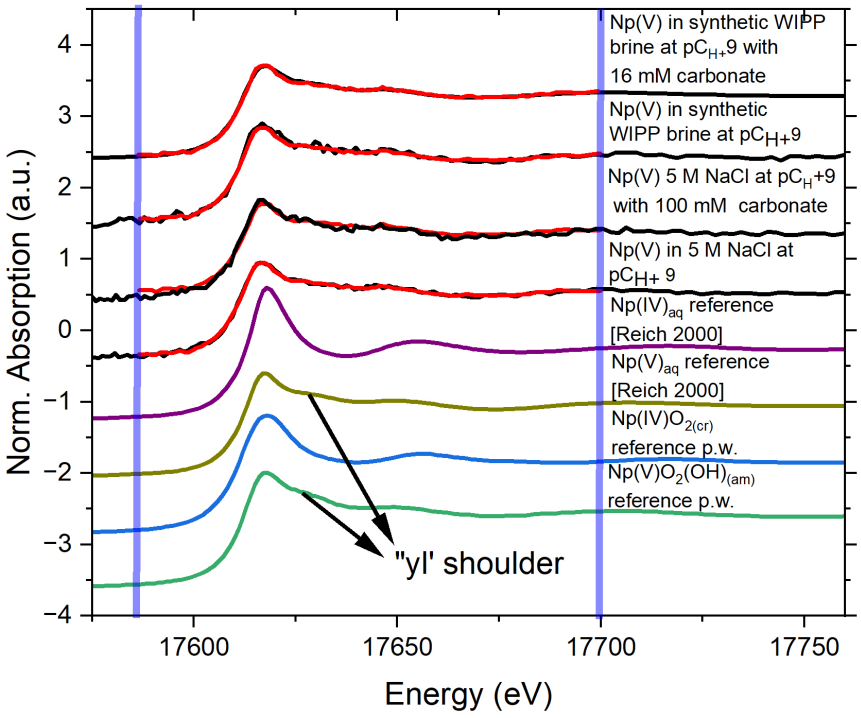


Figure SOTERM-18. Np L_{III}-edge XANES Spectra of Solid and Aqueous Np(IV) and Np(V) References and Experimental Samples with Corresponding Linear Combination Fits (from Kaplan 2025a [present work]).

To investigate the local atomic environment of Np**,** Np L_{III}-edge EXAFS spectra were analyzed for solids equilibrated at $pC_{H^+} \approx 9$ with 16 mM carbonate in synthetic WIPP brine (Kaplan 2025a). The $Np(IV)O_2$(cr) sample was also studied to distinguish between $Np{=}O_{ax}$ and $Np{-}O_{eq}$ interactions, which separate Np(V) from Np(IV). The relevant EXAFS structural parameters are

summarized in Table SOTERM-9. As shown in Figure SOTERM-19, samples exhibit distinct EXAFS patterns due to differences in ligand types and coordination environments. Curve fitting was challenging because of low signal-to-noise ratios at low Np concentrations and the overlap of neighboring shells. For Np(IV)O_2(cr), the Fourier Transform (FT) shows a prominent peak arising from approximately 8 O atoms at 2.33 angstrom (Å). Although tetravalent actinides typically coordinate with 8 O atoms, reported values vary across studies (Conradson et al. 1998; Choppin 1983). A Np–Np scattering contribution at ~3.7 Å, indicative of An(IV)O_2 precipitation, was also detected (Balboni et al. 2020; Conradson et al. 1998; Allen et al. 1997). For Np(V) equilibrated in WIPP brine, the first shell at 1.86–1.89 Å corresponds to Np=O_{ax} bonds, consistent with previously reported values for Np(V)O_2(OH)(am) in 5 M NaCl (Petrov et al. 2017) and 4.5 M $CaCl_2$ (Fellhauer et al. 2016). The second shell at 2.49–2.59 Å likely reflects equatorial O atoms from water molecules or carbonate groups. The narrow range of Np=O bond lengths indicates that the neptunyl units are stable, with no significant structural degradation.

Linear combination fitting analysis of XANES spectra and EXAFS fitting for Np–O_{eq} distances at 2.54 Å confirmed the presence of well-ordered Np(V) species (Kaplan 2025a). Additionally, a Np–C interaction at 3.03 Å was observed. Secondary modeling showed that excluding the Np–C interaction worsened the fit, whereas including it resulted in a better fit (Figure SOTERM-19). This strongly supports the coordination of carbonate groups to Np(V). Slightly shorter Np–O_{eq} distances reported previously (Petrov et al. 2017; Fellhauer et al. 2016) suggest that carbonate ions may influence Np(V) stability. A potassium contribution at ~4.1 Å was also detected. No significant formation of polynuclear Np species or intense Np–Np scattering was observed, indicating minimal precipitation under the studied conditions. Studies have shown that K-containing Np(V) phases can precipitate under alkaline conditions, even when Na^+ concentrations are much higher (Fanghänel et al. 1995; Novak et al. 1997). As K–Np(V) phases have lower solubility compared to Na–Np(V) analogs, it is likely that a K-containing phase formed during the experiments, impacting Np(V) mobility and stability. In conclusion, EXAFS and XANES data highlight the significant role of carbonate and potassium in controlling the structure and solubility of Np(V). These findings confirm the selection of the solid phase used in calculations of Np(V) solubility and provide important insights for predicting the long-term geochemical behavior of Np at the WIPP (Kaplan 2025a).

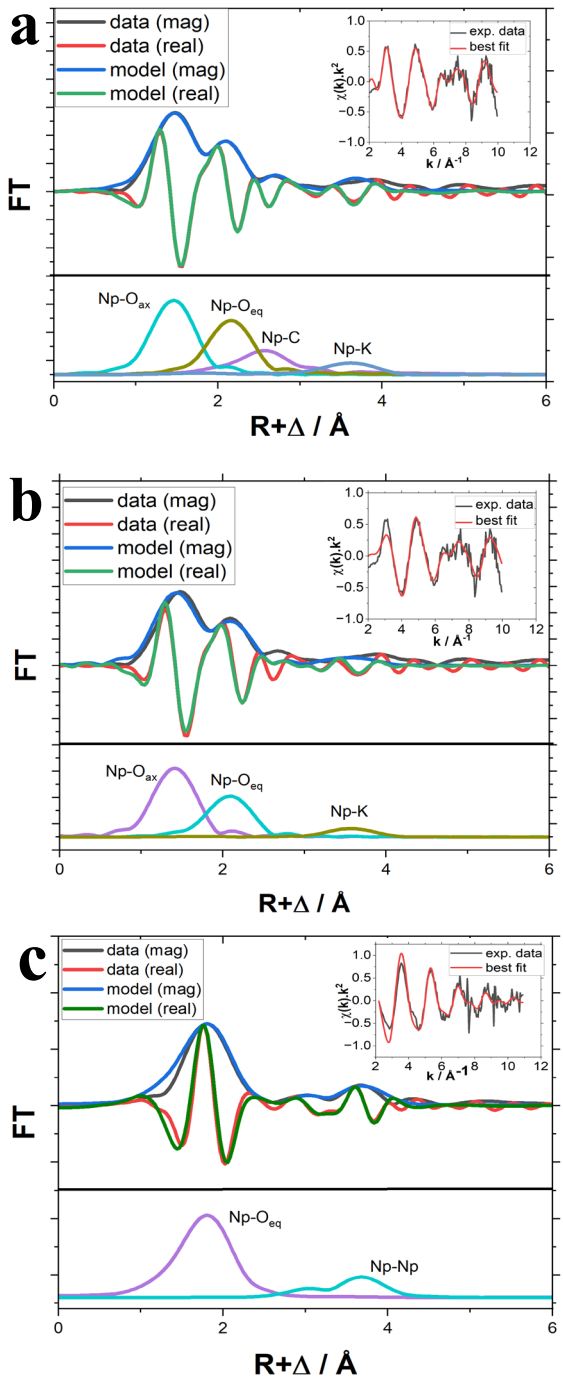


Figure SOTERM-19. EXAFS Data Summary. Panel a: Np L_{III}-edge EXAFS Spectra with Corresponding EXAFS FT: exp. (Experimental) Data and Best Fit of Investigated Sample Np(V) in Synthetic WIPP Brine at pC_{H+} 9 with 16 mM Carbonate and Considering Np-C Shell. Panel b: Same Sample but Not Considering Np-C Shell During EXAFS Calculation. Panel c: Np L_{III}-edge EXAFS Spectra with Corresponding EXAFS FT: exp. Data and Best Fit of

Investigated Sample Np(IV)O_2(cr). Data Magnitude (mag) (Black), Model Magnitude (Blue), Data "Real Part" (Red) and Model "Real Part" (Green). The "Real Part" of the FT Provides Information on the Distances to Neighboring Atoms (i.e., Bond Lengths) and Their Scattering Properties; This Shows the Contribution of Different Atomic Shells to the Overall EXAFS Signal. Also Shown are Single Scattering Paths (from Kaplan 2025a) R, Interatomic Distance; Δ, Deviation of R from the Reference.

Table SOTERM-9. Best-Fit of Np L_{III}–Edge EXAFS Model Parameters (S_0^2(k) = 0.9 Fixed) (from Kaplan 2025a)

	Np=O_{ax}			Np-O_{eq}			Np-C			Np-K			Np-Np			**ΔE_0**	**Red. error**
	N	R(Å)	σ^2(Å^2)	N	R(Å)	σ^2(Å^2)	N	R(Å)	σ^2(Å^2)	N	R(Å)	σ^2(Å^2)	N	R(Å)	σ^2(Å^2)		
Np(IV)O_2(cr)	-	-	-	8.10*	2.33	0.014	-	-	-	-	-	-	5.55	3.79	0.013	10.6	0.07
$NpO_2(OH)(am)$ + 160 mM [CO_3^{2-}] in WIPP brine at pC_{H+} 9 modeling with carbon	1.27	1.89	0.001	2.58	2.59	0.003	3.59	3.03	0.008	3.03	4.14	0.013	-	-	-	14.7	0.01
$NpO_2(OH)(am)$ + 160 mM [CO_3^{2-}] in WIPP brine at pC_{H+} 9 modeling without carbon	1.17	1.86	0.003	3.46	2.49	0.003*	-	-	-	1.11	4.11	0.004	-	-	-	11.4	0.05
Np(IV)(aq) (Reich et al. 2000)	-	-	-	11	2.39	0.012	-	-	-	-	-	-	-	-	-	-	-
Np(IV)(aq) (Reich et al. 2000)	1.9	1.82	0.023	3.6	2.48	0.061	-	-	-	-	-	-	-	-	-	-	-
(Vitova et al. 2020)	U=O_{ax}			U-$_{Oeq}$			U-C			U-K			U-Np				
	N	R(Å)	σ^2(Å^2)	N	R(Å)	σ^2(Å^2)	N	R(Å)	σ^2(Å^2)	N	R(Å)	σ^2(Å^2)	N	R(Å)	σ^2(Å^2)		
	2.4	1.78	0.001	5.9	2.44	0.004	3.5	2.91	0.004	5	4.02	0.008	-	-	-	3.2	0.7
(Kuzenova et al. 2023)	Np=Oax			N-Oeq			Np-C			N-K			Np-O				
	N	R(Å)	σ^2(Å^2)	N	R(Å)	σ^2(Å^2)	N	R(Å)	σ^2(Å^2)	N	R(Å)	σ^2(Å^2)	N	R(Å)	σ^2(Å^2)		
	2*	1.83	0.003	6*	2.56	0.006	3*	2.96	0.005	6	4.2	0.008	6*	4.28	0.0004	-	0

*Parameter fixed at constant value during fit. N, coordination number; R, interatomic distance; ΔR, deviation of R from reference; σ^2, Debye-Waller Factor; ΔE_0, energy shift; S_0^2, amplitude reduction factor.

SOTERM-5.5 Plutonium Chemistry: Background and Behavior under Repository Conditions

Plutonium is a key TRU component that contributes significantly to the mobile actinide source term in all release mechanisms considered by PA. Under the conditions expected in the WIPP, Pu(IV) was predicted to be the predominant oxidation state (Ding et al. 2006).

In the WIPP PA, all the Pu is assumed to be reduced and present in the III or IV oxidation state. One quarter of the PA vectors model Pu as being in the (III) state, and three quarters of the vectors model Pu as being in the (IV) state (Kaplan et al. 2025). The two higher-valent Pu oxidation states, Pu(V) and Pu(VI), are not considered in PA because they have been shown to not persist under the expected reducing and anoxic conditions in the WIPP. It is important to note that Pu(III/IV) continues to predominate over Pu(V/VI), and no new project-specific data contradict this result. Recent data, as referenced in SOTERM-5.5.4, reaffirm this result. These altogether continue to support the WIPP actinide oxidation-state distribution model and its PA implementation in the CRA-2026.

Typically, Pu can exist in oxidation states III, IV, V, VI, and VII (Clark et al. 2006), with each state exhibiting unique solubilities, redox behavior, and sorption characteristics. Of the available states, only Pu(VI), Pu(V), Pu(IV), and Pu(III) are expected to be important under environmentally relevant oxidizing and reducing conditions, respectively. Pu(VII) is very unstable and exists only in extremely basic solutions (for example, 7 M NaOH) that are not expected in the WIPP.

Pu(VI) and Pu(V) can persist in the WIPP in the absence of reductants, but they are readily reduced in the presence of Fe(II/0) species, reduced by many organic chelators (Reed et al. 1998), and possibly reduced in anaerobic, biologically active systems (Reed et al. 2007; Icopini et al. 2007). The reduction of Pu(VI/V), under WIPP-relevant conditions, was shown by Clark and Tait (1996) and Reed and Wygmans (1997). In consequence, only Pu(III) and Pu(IV) oxidation state species are expected to be present under WIPP-relevant conditions.

Higher-valent Pu, specifically Pu(V) and Pu(VI), can be present in near-surface oxidizing groundwaters (Orlandini et al. 1986). The association of Pu(V) with organic colloidal material was proposed as the mechanism by which subsurface migration occurred. Pu(VI), in near-neutral systems, is strongly and irreversibly hydrolyzed (Okajima and Reed 1993). It is also readily reduced by organics and reduced metal species, even when oxygen is present to form Pu(V), and is not generally stable under most groundwater-relevant conditions.

There is a large body of work examining Pu redox and solubility behavior in acidic and neutral solutions under relatively low ionic strength conditions (<1 M). However, limited data are available under alkaline to hyperalkaline conditions and under high ionic strengths. As part of the WIPP project, Felmy et al. (1989) investigated the solubility of $Pu(OH)_3$(am) in deionized water containing Fe^0 powder and in two synthetic brines: the Permian Basin Brine-1 (I ~ 6 M mainly NaCl brine) and Permian Basin Brine-3 (I ~ 10 M Na-Mg-Cl brine). The measured

solubility of $Pu(OH)_3$ was several orders of magnitude higher in brines than in deionized water at the same hydrogen ion concentration. The authors did not consider Pu(III) hydrolysis species in their model calculations, and sufficient solid phase characterization was not performed (Felmy et al. 1989).

The pe + pH conditions can be varied and set by different reducing agents such as Fe(II), Fe^0, hydroquinone, tin, and $Na_2S_2O_4$ (Fujiwara et al. 2002; Rai et al. 2002; Altmaier et al. 2009). Cho et al. (2016) updated the thermodynamic data for the solubility of $Pu(OH)_3$(am) by combining spectroscopy with solubility experiments under well-controlled reducing conditions and reported a lower solubility product ($\log^* K^o_{s,0}$ = 14.58) than the currently accepted value ($\log^* K^o_{s,0}$ = 15.8) in the NEA-TDB (2020). It should be noted that the Cho experiments were conducted at low ionic strength, which may limit their direct applicability to WIPP. A study by Tasi et al. (2018) also investigated the solid phase controlling Pu solubility at pH_m = 9 and 12, at low ionic strength, and in the presence of Sn(II) (pe + pH = 2) by EXAFS measurements after 146 days of contact time. The authors reported the presence of Pu(III)(s) together with Pu(IV)(s) in both cases, although the aqueous Pu concentration remained in the 10^{-11} M range, which implied that the concentration was being defined by the solubility limit of PuO_2(am,hyd) in equilibrium with $Pu(OH)_4$(aq). These results validate the conceptual model assumption that the least soluble solid phase controls overall solubility. The experimental data from these studies in comparison with current solubility model calculations are shown in Figure SOTERM-20. All these studies and current thermodynamic data confirm the complexity of the Pu(III)/Pu(IV) redox chemistry at neutral to alkaline pH and thus, pH, reducing conditions, and ionic strength are most critical in geologic repository applications.

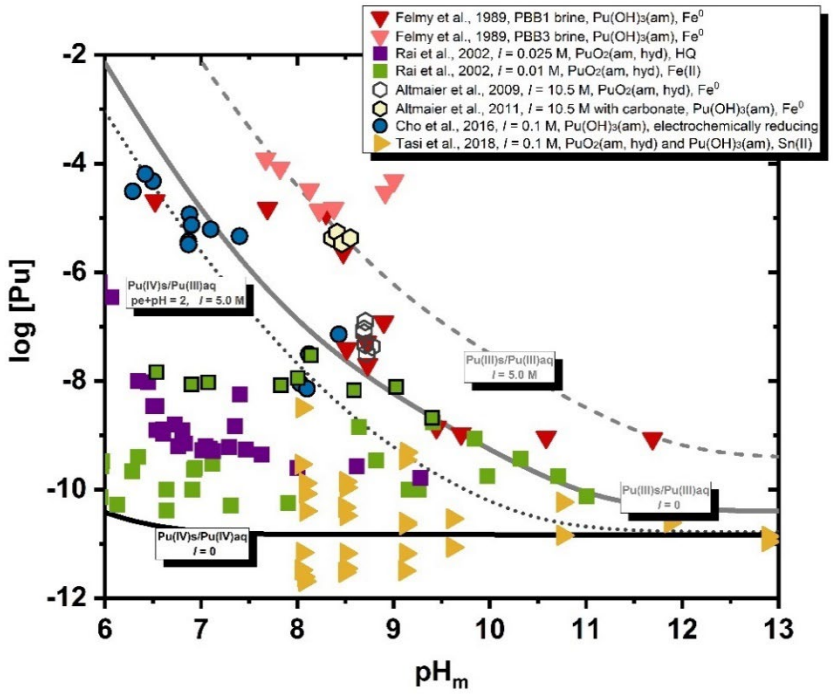


Figure SOTERM-20. Experimental Solubility Data for Pu Reported in the Literature. The Solubility Models are Calculated Using Selected Pu Solid-Phase Analogs Used in the WIPP Model to Represent Bounding Solubility Behavior Under WIPP Conditions. Solid Lines Show the Calculated Solubility of PuO_2(am,hyd)(black) and $Pu(OH)_3$(am)(grey) at *I* = 0. The Dotted Line Represents the Solubility of PuO_2(am,hyd) at *I* = 5.0 M NaCl in Equilibrium with $[Pu]_{tot}$ = Pu(III)(aq) + Pu(IV)(aq) at pe + pH = 2. The Dashed Gray Line Shows the Solubility of $Pu(OH)_3$(am) at *I* = 5.0 M NaCl in Equilibrium with $[Pu]_{tot}$ = Pu(III)(aq) (from Appendix SOTERM-2019). Differences Between the Curves Reflect Not Only Ionic Strength Effects but also Differences in Redox Conditions and Aqueous Speciation.

Although the effect of organic complexation on Pu oxidation state has been investigated since the late 1950s (Thakur et al. 2015; Al Mahamid et al. 1996; DiBlasi et al. 2021a, b; DiBlasi et al. 2022; Comins et al. 2024a), difficulties arise in directly adapting and comparing these results to the WIPP system. A prime difficulty is the presence of divalent cations in the WIPP system. It is known that WIPP-relevant organics are prone to complex with divalent cations such as Ca^{2+}, Mg^{2+}, or Fe^{2+} (Serne et al. 2002; Delegard and Barney 1983). In this case, the probability of Pu-organic ternary/quaternary complexes with Ca^{2+}/Mg^{2+}/Fe^{2+} forming under repository conditions (high ionic strength, high alkalinity, and hydroxide formation) is very high. This causes some difficulties in the correct interpretation of the experimental data. Another difficulty is how to address the effects of chemical, microbial, and radiolytic degradation, not previously considered in experiments examining or interpreting Pu-organic interactions (Toste

1992; Toste and Lechner-Fish 1993; Francis et al. 2006). It is clear that Pu(V) and Pu(VI) are reduced by EDTA, as is the case with other organic complexants such as citrate. This observation was confirmed in WIPP-specific experiments (Reed and Wygmans 1997). However, there are mixed results in the literature on the reduction of Pu(IV) and/or the oxidation of Pu(III), and this process is clearly pH dependent and impacted by ionic strength.

In geochemical systems, redox control is often interpreted in terms of the iron, and in a broader sense, reduced metal, mineralogy, and associated aqueous chemistry (Sanchez et al. 1985; White et al. 1985). In the WIPP case, iron will undergo anoxic corrosion, producing Fe^{2+}. Both metallic iron-Fe^0 and Fe^{2+} have been shown to quantitatively reduce Pu(VI) in WIPP brines to either Pu(IV) or Pu(III) (Reed et al. 2010; Clark and Tait 1996). Neretnieks (1982) has shown that when dissolved actinides in moving groundwater came in contact with Fe(II), the actinides were reduced to a much-less-soluble oxidation state and precipitated.

SOTERM-5.5.1 Thermodynamic Stability of Higher-valent Plutonium: PuO_{2+x}

It has long been held that Pu oxide, as PuO_2, is the thermodynamically favored form of Pu oxide. This oxide is likely the predominant form of Pu in TRU waste and is believed to be the most important phase under WIPP-relevant conditions.

The behavior of higher-valent Pu oxides in repository settings has been widely discussed in the literature. If a prolonged unsaturated phase were to occur at the WIPP, the formation of some PuO_{2+x} species may be possible. However, these species would be rapidly eliminated in an aqueous environment, and the higher-valent Pu would be reduced to Pu(III/IV) in the presence of iron corrosion products (Altmaier et al. 2009; Dumas et al. 2019; Tasi et al. 2018; Kirsch et al. 2011). Although a fraction of higher-valent Pu may transiently exist, the overall dissolved Pu concentration at thermodynamic equilibrium is controlled by the least soluble, stable solid phase.

SOTERM-5.5.2 Literature Results Since the CRA-2019

The long-term stability and relative importance of Pu(IV) and Pu(III) under environmental conditions that are WIPP-relevant continues to be an active area of research within the actinide community.

Dumas et al. (2019) examined the potential for magnetite (as a by-product of anoxic corrosion on stainless steel drums) to engage in redox reactivity with plutonium, including the sorption of plutonium onto magnetite surfaces or incorporation into the magnetite crystal lattice as it forms. Experiments consistently showed Pu(III) concentration in solution dropping below the detection limit (< 10^{-9} M), reflecting either Pu(III) precipitation via hydrolysis or, as confirmed by EXAFS spectroscopy, sorption, and co-precipitation with the magnetite. The lesser extent of plutonium incorporation into the magnetite structure relative to surface sorption is attributed to the structural incompatibility of the large Pu(III) ion with the octahedral sites in magnetite, which are normally occupied by smaller Fe(II) ions. This mismatch resulted in significant complexity in the phases that formed and subsequently recrystallized, as revealed by EXAFS

measurements. From a WIPP perspective, magnetite retains an inherent thermodynamic stability under a wide range of conditions that overlap what is expected in the WIPP, in part when radiolysis in brines is factored in. It should be noted that these experiments were conducted at high pH (~ 12.5) and in low ionic strength solutions.

A similar theme was evaluated in Balboni et al. (2020), who studied sorption interactions of Pu(IV) with the Fe(III) mineral ferrihydrite ($Fe(OH)_3 \cdot xH_2O$; x is variable) and its subsequent alteration product goethite (Fe(O)OH), as measured by various spectroscopic techniques. These results confirmed those of Smith et al. (2019) below, indicating that Pu(IV) binds directly to ferrihydrite. While these studies were performed under alkaline conditions (pH 8 for ferrihydrite, 10-11 for goethite), their applicability is dependent on the degree to which these Fe(III) minerals will exist in the WIPP environment following steel corrosion, and the extent to which Pu(IV) will exist in soluble form.

In a related study, Smith et al. (2019) studied the sorption of plutonium onto growing ferrihydrite nanocrystals, which were precipitated via hydrolysis through the addition of sodium hydroxide (NaOH) to an acidic solution containing Pu(IV) and Fe(III). While sodium hydroxide addition continued until the solution pH reached 9, most of the precipitation occurred between pH 2-3. As determined by EXAFS, the majority of the plutonium was incorporated as Pu(IV) ions onto the ferrihydrite structure with minor amounts of PuO_2 present, with very little change observed as ferrihydrite was re-crystallized into hematite, suggesting strong plutonium sorption that was maintained throughout the process. Interactions with iron surfaces remain a topic of interest in evaluating plutonium speciation and solubility, as with the study by Dumas et al. (2019).

Two papers from different research groups examined a related theme of the chemistry of Pu(IV) oxide in the form of colloids and clusters. The speciation and reaction kinetics of Pu(IV) and its colloids spiked into samples of saline groundwater was studied by Zhou et al. (2019). While regarded in this report as “highly saline,” the low ionic strength (I = 1M) falls well below what would be encountered in a WIPP brine. The vast majority of Pu(IV) was observed to readily sorb onto natural colloid suspensions and subsequently precipitated along the container walls. Having been initially spiked with Pu(IV) and in an oxic environment, over time the remaining plutonium in solution was largely Pu(IV) with minor amounts of Pu(V) and Pu(VI) detected during aging.

Schramke et al. (2020) reviewed the existing literature regarding the redox chemistry and solubility of plutonium during long-term disposal at the WIPP and supplemented this review with new modeling calculations. A summary of the conclusions of this review is provided here. The main thrust involves an assumption that the large quantities of metallic iron from TRU waste and the waste containers will undergo extensive anoxic corrosion upon brine intrusion after repository closure, which will cause strongly reducing conditions and an increase in hydrogen gas pressure. The resulting combination is predicted to favor highly reduced plutonium solids and aqueous species during the lifetime of the repository. Notably, plutonium

colloidal formation is largely omitted from the scope of this review, which under-represents an important facet of Pu(IV) speciation and solubility.

The review in Schramke et al. (2020) is supplemented by new geochemical modeling calculations, including updated Pourbaix diagrams that incorporate the effects of higher hydrogen gas pressure. The model results reinforce the authors' position that plutonium solubilities in WIPP brines should be represented by dissolution of the $Pu(OH)_3$ (am) to form Pu(III) aqueous species, which would in turn result in higher plutonium concentrations than if the dominant formation of Pu(IV) solids is assumed. These model results and the general conclusions of the review – i.e., that plutonium in the WIPP during long-term disposal should be assumed to be all Pu(III) – differs from the 50:50 position that has been assumed since the CCA. However, the new model presented in Schramke et al. (2020) is based upon the SIT database parameters and methodology that are inapplicable at higher ionic strength. Additionally, it is worth noting that the effects of radiolysis, which would generally favor Pu(IV) speciation, are largely ignored in these thermodynamic calculations. Assuming extensive corrosion of the steel TRU waste drums and related iron materials, Schramke et al. (2020) postulated that the resulting significant buildup of molecular hydrogen (H_2) could, through its inherent reactivity (primarily as a reducing agent), alter the speciation of plutonium such that the more soluble Pu(III) becomes the dominant form over the course of long-time disposal. However, radiolysis tends to produce oxidizing transients (e.g., OBr^-, OCl^-, H_2O_2) that may stabilize Pu(IV) or even transient Pu(V/VI) species. Although the formation of these oxidants is expected, their persistence and long-term influence under repository conditions remain uncertain. These effects are not included in Schramke et al. (2020). In the context of these considerations, the EPA has sought documentation that considers the impact of the reactivity of hydrogen with plutonium over a 10,000-year time frame.

The reactivity of radiolytically produced hydrogen with various forms of plutonium has been explored in detail over many years. Notably, this reaction does not represent hydrogen acting as a reducing agent. In contrast, the dominant form of plutonium expected to be disposed at the WIPP, solid PuO_2 (especially if the inventory of surplus plutonium is included), has been characterized as being both chemically inert and unreactive in the presence of hydrogen (Haschke et al. 2000). For example, where plutonium metal is coated with an oxide surface, reactions of hydrogen only commence once the oxide layer has been penetrated (i.e., where the underlying metal has been exposed). Despite longstanding interest in hydrogen reactivity with the actinides, there remains a paucity of data on hydrogen interactions in the aqueous phase, particularly with PuO_2. In contrast, a substantial body of work exists on the reactivity of hydrogen and its isotopes with metallic Pu and U.

Micheau et al. (2020) evaluated the impact of the synthesis procedure upon the size, morphology, and local structure of plutonium colloids. The colloids were structurally characterized in detail by synchrotron small angle X-ray scattering and XAS, which showed that colloids prepared from the hydrolysis route were both smaller (~ 2 nm) and more spherical. The non-invasive spectroscopic techniques employed in this study also offer a potentially useful tool for *in situ* colloid characterization. However, these results should be considered in the context

of the WIPP; colloids were synthesized by hydrolysis from weakly acidic solutions with nitrate as the sole other constituent.

DiBlasi et al. (2021a) evaluated the impact of EDTA on plutonium oxidation state as a function of pH, which established that EDTA promoted the reduction of Pu(VI) to Pu(V) and the oxidation of Pu(III) to Pu(IV) under anoxic conditions with varying solution pH. All scenarios eventually showed EDTA stabilizing Pu(IV) over time, regardless of initial oxidation state. At higher pH, increasing competition from hydrolysis led to lower plutonium solubility.

DiBlasi et al. (2021b, 2022) extended their previous work on Pu and EDTA by considering the added impact of Ca(II) at higher ionic strengths (one at 3.5 M $CaCl_2$; another a WIPP brine). Pu(IV)-EDTA solubility was found to be lower relative to previous thermodynamic models under alkaline conditions in the absence of calcium ion and did not follow the model prediction for a decrease in solubility when calcium was present (DiBlasi et al. 2021b). In particular, samples at higher ionic strength (including WIPP simulated brines) systematically showed higher solubility.

The formation of quaternary Ca-Pu(IV)-OH-EDTA complexes was postulated to account for these observations. This is consistent with other reports of analogous ternary and quaternary combinations of high valent actinides with chelating ligands including EDTA. Modification to the modeling strategy of PuO_2 solubility was proposed to attempt to reconcile discrepancies between the experimental results from this work and others with previous thermodynamic models. The derived thermodynamic data in this paper were used to provide updated Pourbaix diagrams, which showed an increased field of stability for Pu(IV) at higher pH, with speciation and equilibria dependent on the relative abundance of the individual constituents and the physical form of PuO_2.

The third paper from this group, DiBlasi et al. (2022), focused on the impact of EDTA and calcium ion on the speciation and redox behavior of Pu(III) at higher pH and under reducing anoxic conditions. Results for samples examined in the absence of Ca(II) were consistent with existing thermodynamic models, while the addition of Ca(II) stabilized Pu(III) with respect to oxidation to Pu(IV). Mismatches between experimental observations and thermodynamic modeling were speculated to result from transitory Pu(III) solubility behavior that reflected an evolution towards a mixed Pu(III)/Pu(IV) system. As with the Pu(IV) studies in DiBlasi et al. (2021b), increased solubility was observed in the Pu(III)-EDTA systems in the presence of calcium at higher ionic strength (including WIPP-simulated brines), which were again accounted for by the formation of ternary Ca-Pu(III)-EDTA and/or quaternary Ca-Pu(III)-OH-EDTA species. Additional theoretical modeling of this system using density functional theory (DFT) supported the stability of Pu(III)-EDTA complexes that incorporate calcium.

These studies support the WIPP position that the plutonium oxidation state remains favored as Pu(IV) in the presence of organic ligands such as EDTA, especially at higher pH conditions, and that reduction to Pu(III) requires reducing agents such as Fe^0. However, while the projected inventory of EDTA in the WIPP repository is anticipated to be significant, the extent to which it will be commingled with plutonium is uncertain, although assumed to be well mixed. Additional factors to be considered in evaluating the WIPP applicability of these results include the ionic

strength and chloride ion content, the use of ^{242}Pu to artificially inhibit the effects of alpha-radiolysis, and the overall prevalence of EDTA and its access to plutonium in the WIPP inventory.

The NEA-TDB (2020) presented an update to the plutonium stability constant (log K) for the solubility of amorphous $Pu(OH)_3(am)$, adopting results reported by Cho et al. (2016). (Note this parameter has since been adjusted again by Cho et al. [2022] – see discussion above regarding this work.) In general, the revised data suggested that $Pu(OH)_3(am)$ was less soluble by approximately an order of magnitude relative to previous thermodynamic models.

Kobayashi et al. (2021) investigated the solubility of PuO_2(am, hyd) in alkaline solutions (pH 8-11), focusing on low carbonate concentration in solution with dilute to concentrated levels of nitrate ion (0.1-5.0 $mol \cdot dm^{-3}$). At low to moderate nitrate concentrations, the solubility data were found to be in good agreement with existing model calculations for such species as $Pu(CO_3)_4^{4-}$, $Pu(CO_3)_6^{5-}$, and $Pu(OH)_2(CO_3)_2^{2-}$. However, above 2 $mol \cdot dm^{-3}$ $NaNO_3$, solubility was approximately one order of magnitude higher than the values predicted for these complex species.

Pan et al. (2021) studied the kinetics and mechanism of redox transformations of plutonium(IV) in the presence of iron(II) and humic acid that had been reacted with hydrogen peroxide (H_2O_2). The results showed varying degrees of Pu(IV) oxidation that was dependent on pH. While hydrogen peroxide is a common product of radiolysis in aqueous systems, its concentration in WIPP brines is expected to be minor and therefore not a significant factor affecting the redox chemistry of plutonium (see Appendix SOTERM-3.4). Further, the reactivity of hydrogen peroxide with Fe(II) is primarily an acidic/neutral phenomenon that is not relevant to alkaline solutions, such as WIPP brines. Similarly, while humic acid is a major constituent of naturally occurring organic matter in soils, and the relatively acidic conditions (pH 3.5 and 6) in the experiments from this study are consistent with associated groundwater systems, this scenario is not representative of the WIPP. Finally, ^{238}Pu was selected in these experiments, a strong alpha emitter, as compared to ^{242}Pu, that would artificially enhance radiolysis (affecting hydrogen peroxide in particular) well beyond the radiolytic field expected at the WIPP.

Cho et al. (2022) obtained thermodynamic parameters associated with the hydrolysis of trivalent Pu and the solubility of $Pu(OH)_3$ (am) under reducing conditions in 0.1 M $NaClO_4$. Spectrophotometric data were used to determine the first formation constant $*\beta'_1$ for the hydrolysis reaction:

$$Pu^{3+} + H_2O\ (l) \leftrightarrows Pu(OH)^{2+} + H^+ \qquad \text{(SOTERM.38)}$$

And the equilibrium constant $*K'_{s,0}$ for the solubility of the obtained solid:

$$Pu(OH)_3\ (am) + 3H^+ \leftrightarrows Pu^{3+} + 3H_2O\ (l) \qquad \text{(SOTERM.39)}$$

With measurements obtained at three different temperatures (10, 17, 40 °C; 50, 62.6, 104 °F), this study may be the first to report experimental enthalpy and entropy changes for the

hydrolysis and dissolution of a trivalent actinide. Notably, this recent set of results is consistent with those previously reported by Cho et al. (2016), further validating the latter being adopted by the updated NEA-TDB (2020). A caveat applies that these studies were undertaken under conditions of low ionic strength.

Comins et al. (2024a) performed complexation studies in Pu(VI)-citrate and Pu(III)-citrate systems (pH = 2.5-11.0, I =0.1 M NaCl under anoxic conditions). Pu(VI) species were found to be less stable in the presence of citrate (time [t] = 168 days); the rate of reduction increased with increasing pH, and the observed Pu(III) stability increased in the presence of citrate (t = 293 days). Higher concentrations of Pu(III) were favored at lower pH. The highlight of this study provided evidence of a radiolysis-driven mechanism for the citrate-mediated reduction of Pu that involves electron transfer from the oxidative breakdown of citrate.

SOTERM-5.5.3 WIPP-specific Results Since the CRA-2019

A summary of all WIPP-specific work issued since the CRA-2019 is given below.

Long-term Pu solubility experiments providing data obtained under WIPP-relevant conditions to support a realistic oxidation state ratio for Pu in the WIPP PA model have concluded (Kaplan 2025b). These experiments included tests in the presence and absence of metallic iron and magnetite, as well as in the presence and absence of four organic ligands relevant to the WIPP—oxalate, acetate, citrate, and EDTA—in an alkaline WIPP brine solution within a pC_{H+} range of 8-10. Note that the ligand concentrations used in these experiments were derived from the 2018 PAIR and the 17,400 m^3 minimum volume for a DBR.

One of the key aspects of this study is the analysis of the Pu oxidation state and speciation, both on the surface area of the corrosion products and in the precipitated solid phase. This dual sampling approach has not been previously reported in the literature. Figure SOTERM-21 illustrates the preparation of samples for the analysis of the oxidation state of Pu. Furthermore, the analysis of the Pu oxidation state on the surface of the iron mineral is more relevant to the performance of nuclear waste disposal systems than short-term batch experiments (such as plutonium-iron phase experiments like those conducted by Kirsch et al. 2011 and Dumas et al. 2019). An additional advantage of the 800-day duration is a better consideration of radiolysis effects by ^{239}Pu, which is critical for accurately assessing long-term behavior.

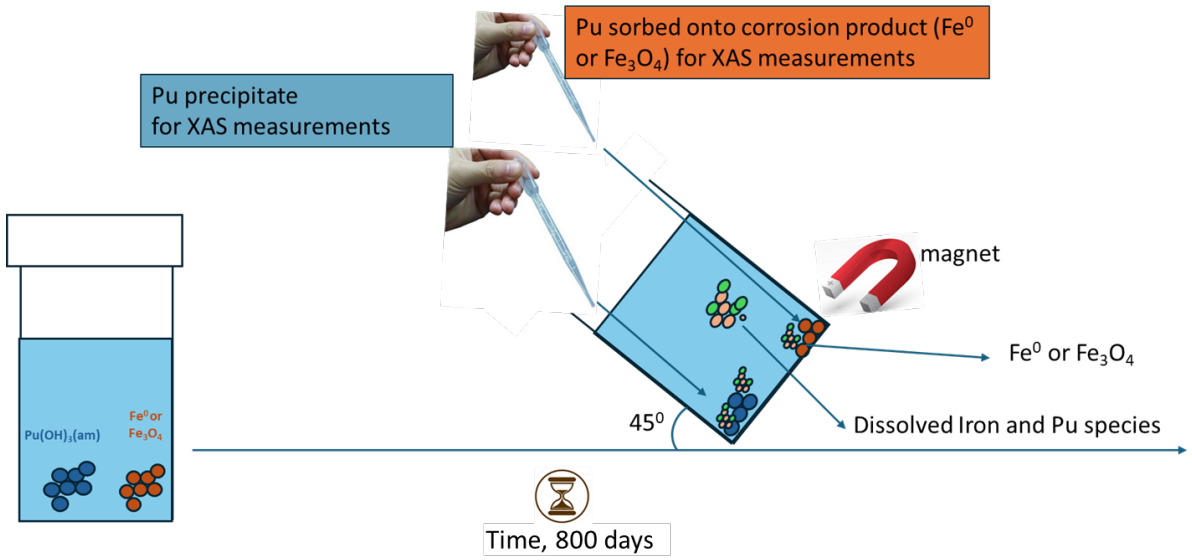


Figure SOTERM-21. Preparation of Samples for XAS Analysis of Pu Oxidation State (from Kaplan 2025b).

Samples were prepared for oxidation state analysis by XAS, as shown in Figure SOTERM-21, without disturbing their inherent conditions, and were measured under anoxic conditions using the non-destructive XAS method at the Stanford Synchrotron Radiation Lightsource. Pu oxidation state distribution, in percentage contribution, was calculated by LCF(A) by using Pu(III) and Pu(IV) reference spectra (Schmeide et al. 2006; Martin et al. 2007). No shoulder features associated with Pu=O bonding, characteristic of Pu (V/VI), were observed in the XANES spectra. Kaplan (2025b) also conducted EXAFS analyses, which confirmed the absence of the $Pu{=}O_{ax}$ bond at 1.7–1.8 Å, further supporting the exclusion of higher oxidation states in the LCF results (Reich et al. 2001). The fit range was chosen to cover both the onset energy and the entire absorption feature (18025–18150 eV). All LCF results are presented in Figures SOTERM-22 and 23, along with the component spectra and the residual of the fit.

Figure SOTERM-24 shows the oxidation state distribution calculated using LCF(A) in both the precipitated solid phase and on the surface of iron corrosion products, in the presence and absence of organics. XANES analysis showed that Pu oxidation state was different on the metal surface and in the precipitated solid. Pu(III) was the dominant oxidation state in the metallic iron (Fe^0) systems in the presence and absence of organics and in both the precipitated solid Pu phase and the Pu phase on the metallic iron surface (Figure SOTERM-24a). In contrast, Pu(IV) was the dominant oxidation state in the magnetite systems in the presence and absence of organics and in both the precipitated phase and the sorbed phase (Figure SOTERM-24b). Additionally, organics stabilized Pu(IV) in the magnetite systems.

The observed differences in Pu oxidation state were primarily associated with the different iron corrosion products. In WIPP brines containing metallic iron, the E_h values ranged from -300 to -437 mV, reflecting a strongly reducing environment that stabilized Pu(III). In contrast, the E_h values in the magnetite system ranged between +30 and +309 mV. These measured E_h values

represent mixed electrochemical potentials of the heterogeneous experimental systems rather than equilibrium redox potentials representative of the long-term repository environment. Nevertheless, the higher measured E_h values in the magnetite systems were consistent with the independently determined Pu oxidation states from XANES and with the broad stability field of magnetite predicted by thermodynamic Pourbaix calculations (Colàs et al. 2020). These results highlight the importance of iron corrosion products in controlling Pu redox chemistry and demonstrate that the selected corrosion phases in these experiments successfully bracket the range of redox conditions expected for the WIPP. In contrast, the presence or absence of organics in the system had only a minor influence on the Pu oxidation state. The Pu(III)/Pu(IV) ratios between samples with and without organics were within 10–15 %. However, some studies have demonstrated that radiation will lead to the degradation of organic compounds (Toste 1992; Fiegel et al. 2019; Favela Morales and Lucchini 2024). Therefore, the effect of organics will become even less significant over time.

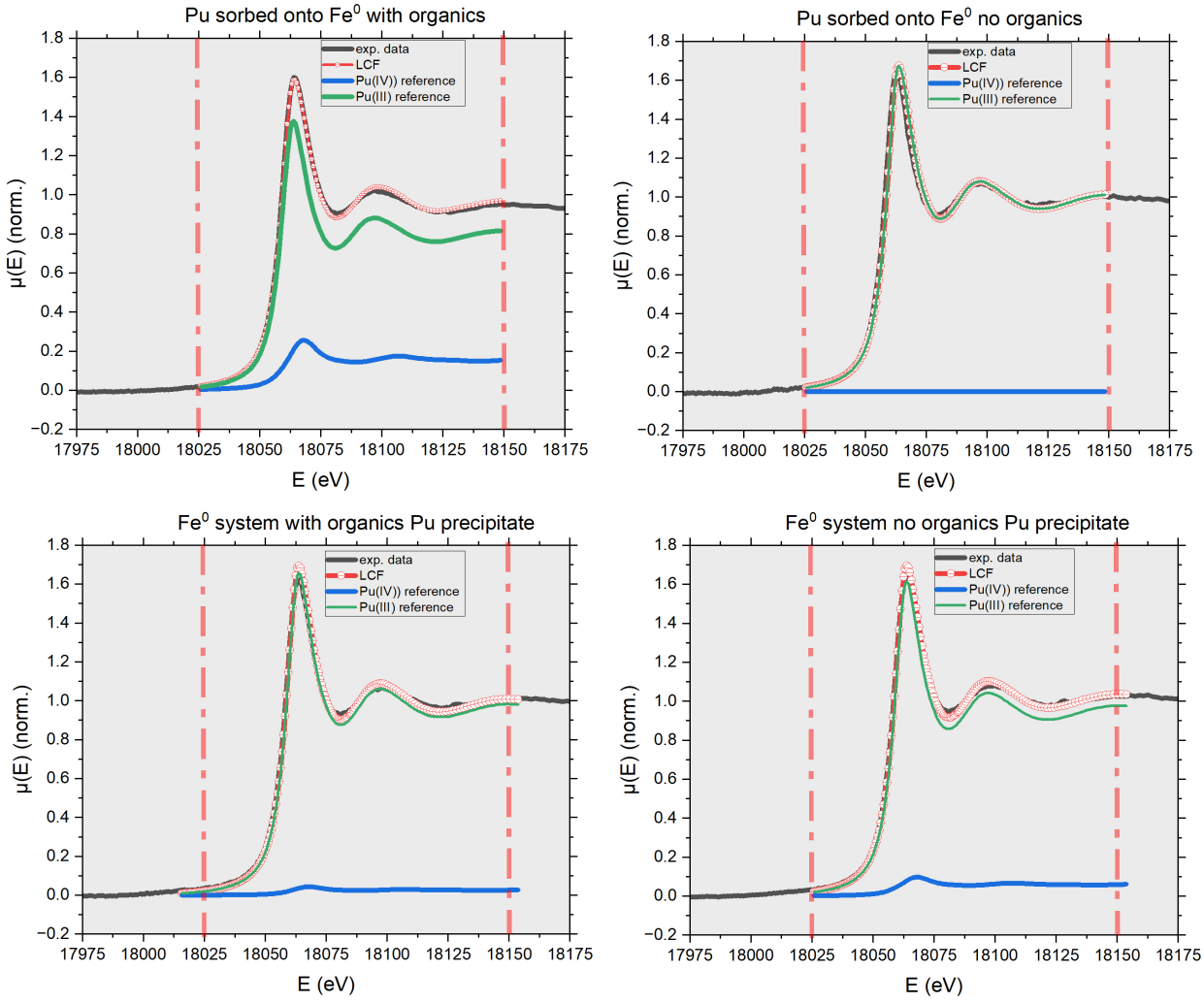


Figure SOTERM-22. Background-subtracted and Normalized Pu L_{III}-Edge XANES Spectra, Obtained by Measuring the Solid Phase in the Solubility Experiments in

the Presence of Fe^0 and Organics, are Shown Together with the Corresponding LCF. Experimental Data are Compared with the Corresponding Linear Combination Fits of Pu(III), Pu(IV). Contributions of the Individual Components are Included (from Kaplan 2025b).

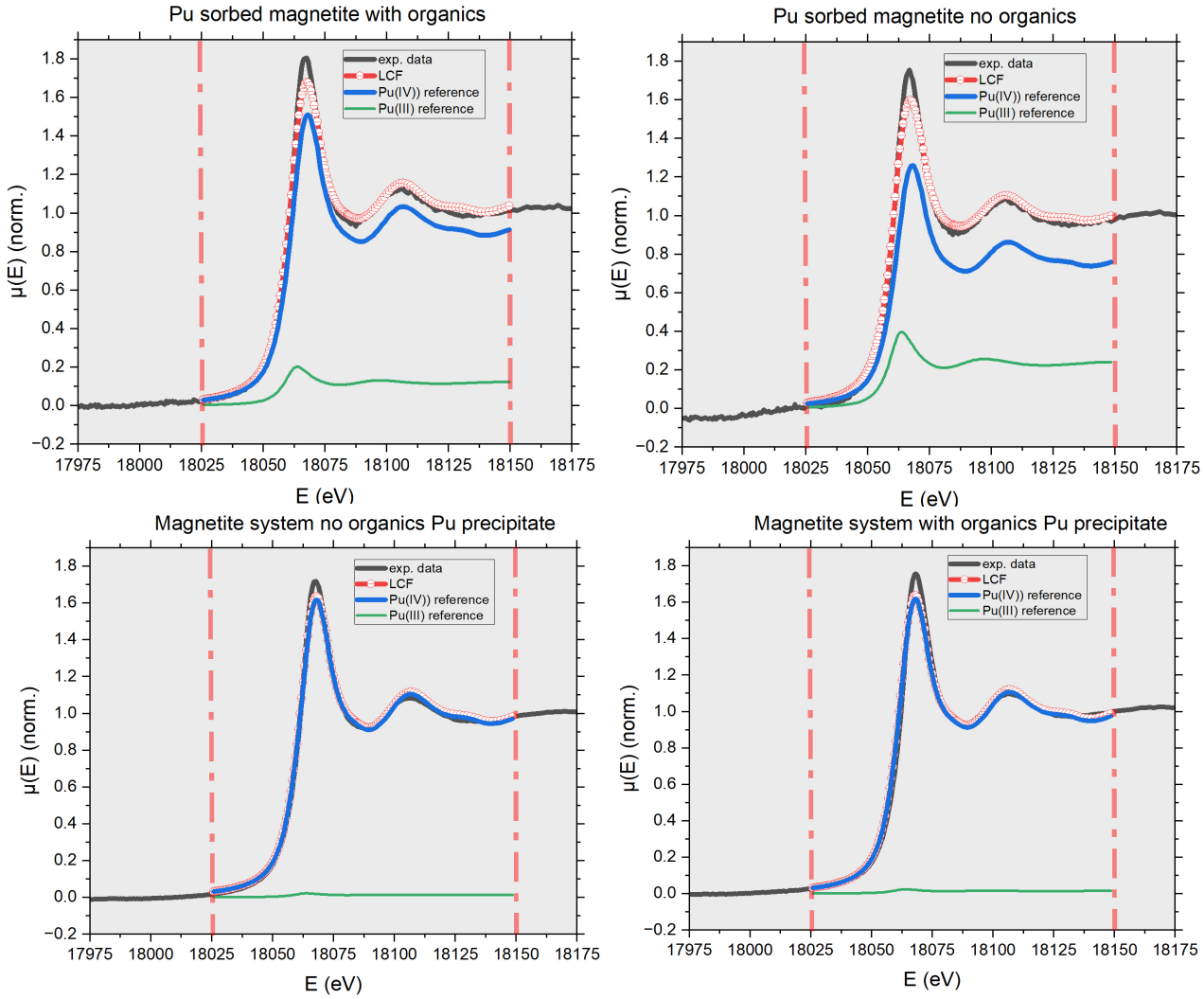


Figure SOTERM-23. Background-subtracted and Normalized Pu L_{III}-Edge XANES Spectra, Obtained by Measuring the Solid Phase in the Solubility Experiments in the Presence of Magnetite and Organics, are Shown Together with the Corresponding LCF. Experimental Data are Compared with the Corresponding Linear Combination Fits of Pu(III), Pu(IV). Contributions of the Individual Components are Included (from Kaplan 2025b).

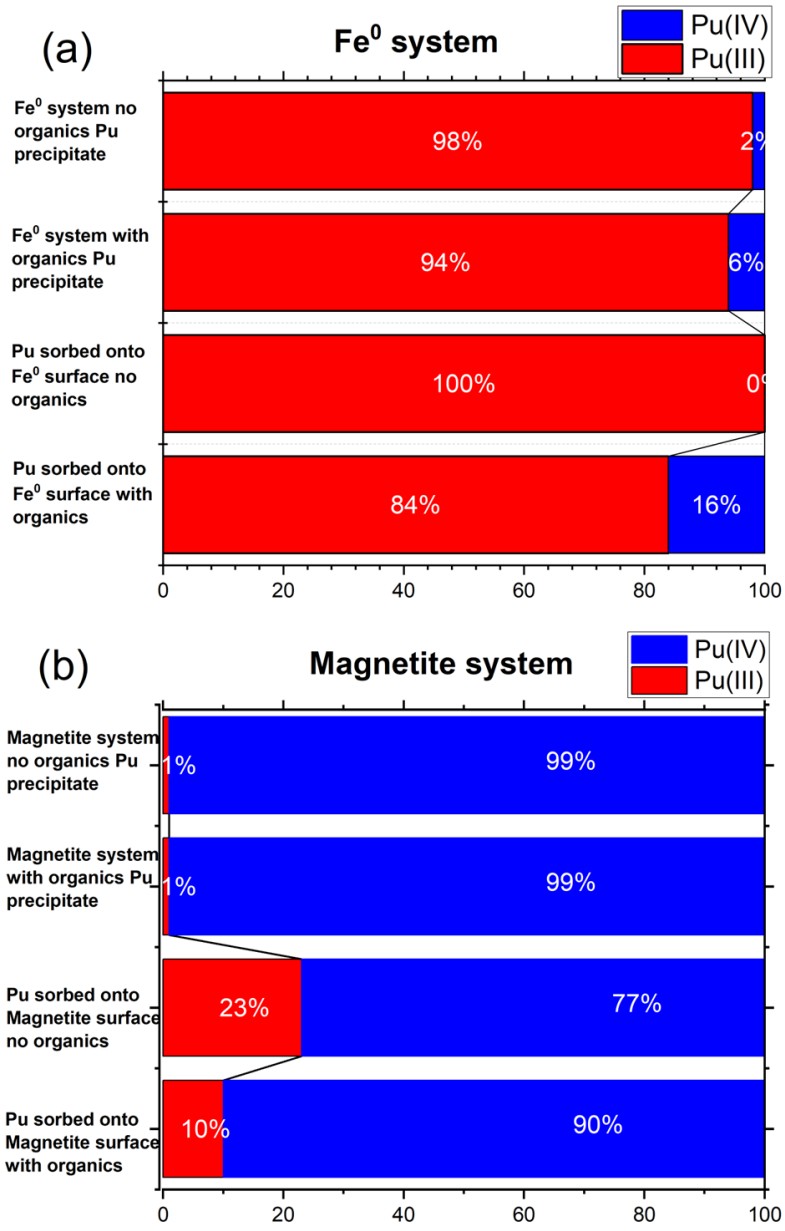


Figure SOTERM-24. The Oxidation State Distribution of Pu in % (± 10%) in Both Precipitate Solid Phases and on the Surface of Iron Corrosion Products in the Presence and Absence of Organics (Modified from Kaplan 2025b).

In addition, plutonium speciation at the molecular level was determined by EXAFS analysis. This analysis found no evidence of Pu–C interactions and that Pu was structurally associated with iron phases. These observations align with XANES results and emphasize the role of corrosion products in controlling Pu speciation. Together, these findings provide a strong basis for interpreting Pu solubility under WIPP-relevant conditions. Details on the EXAFS results can be found in Kaplan (2025b).

Solubility

The log[Pu] (M) solubility in WIPP brine, with and without organics and iron corrosion products (Fe^0, magnetite), is shown in Figure SOTERM-25a. Solubility varies by up to three orders of magnitude, with the greatest spread at $pC_{H^+} = 9$. Similar variability for Pu(III) with Fe^0 in brine was noted by Felmy et al. (1989). This is due to complex Pu-Fe chemistry near neutral pH, where multiple phases may coexist, e.g., Fe-organic, organic-brine-Pu, Pu-Fe, or Pu-colloid (DiBlasi et al. 2022; Altmaier et al. 2009; Dumas et al. 2019; Micheau et al. 2020; Cobos and Søgaard 2022).

In simple brine systems, Pu(IV) concentrations were below or near detection limits at neutral/alkaline pH (Tasi et al. 2018). Similar results were shown by Altmaier et al. (2009). In their experiments, despite identical conditions, Pu(IV) remained near detection limits, while Pu(III) showed two orders of magnitude higher solubility (Altmaier et al. 2009). We observed the same in WIPP brine: Pu(III) solubility was ~100× higher than Pu(IV), suggesting Pu(III) stability in solution. In systems with Fe^0, Pu(III) was also dominant in the liquid phase (Altmaier et al. 2009; Felmy et al. 1989).

Pu solubility in $MgCl_2$ brine increases with Mg^{2+} concentration (0.25 to 3.5 M) in the presence of Fe^0 (Altmaier et al. 2009). Since WIPP brine has higher ionic strength than most of the tested matrices in Altmaier et al. (2009), this supports the high Pu concentrations observed. In this study, no clear relationship was found between organics and Pu solubility in either the magnetite or Fe^0 system. EXAFS results indicate Pu is more likely to complex with Fe than bind with C and brine components such as Ca^{2+} or Mg^{2+}. Additionally, complexes between divalent cations (Ca^{2+}, Mg^{2+}) or Fe^{2+} and organics have been reported (Cobos and Søgaard 2022; Serne et al. 2002). Interestingly, at pC_{H+} ~9, the observed solubility of $Pu(III)(OH)_3$ in the presence of Fe^0 closely matches the reported solubility of $Pu(IV)(OH)_4$. While sorption of Pu onto Fe^0 surfaces may contribute to lower aqueous concentrations, this correspondence suggests that a Pu(IV)-bearing solid phase may control solubility under these conditions. Such behavior is consistent with thermodynamic expectations that the least soluble stable phase governs dissolved concentrations, even in systems where reducing conditions favor Pu(III) in solution.

Rai et al. (2008) studied PuO_2(am) solubility with ferrihydrite and EDTA in dilute solutions from pH 2.3 to 11.5. Measured Pu concentrations were much higher than expected from Pu(IV) and Fe(III) complexation by EDTA. Solvent extraction showed Pu(III) dominated below pH 8, and Pu(V) or Pu(VI) above pH 8. Pu(IV) reduction to Pu(III) was attributed to trace Fe(II) in ferrihydrite. Rai et al. (2008) concluded Pu(IV)-EDTA complexation was overstated and that Pu(III)-EDTA complexes likely influence Pu mobility under reducing conditions (Rai et al. 2008).

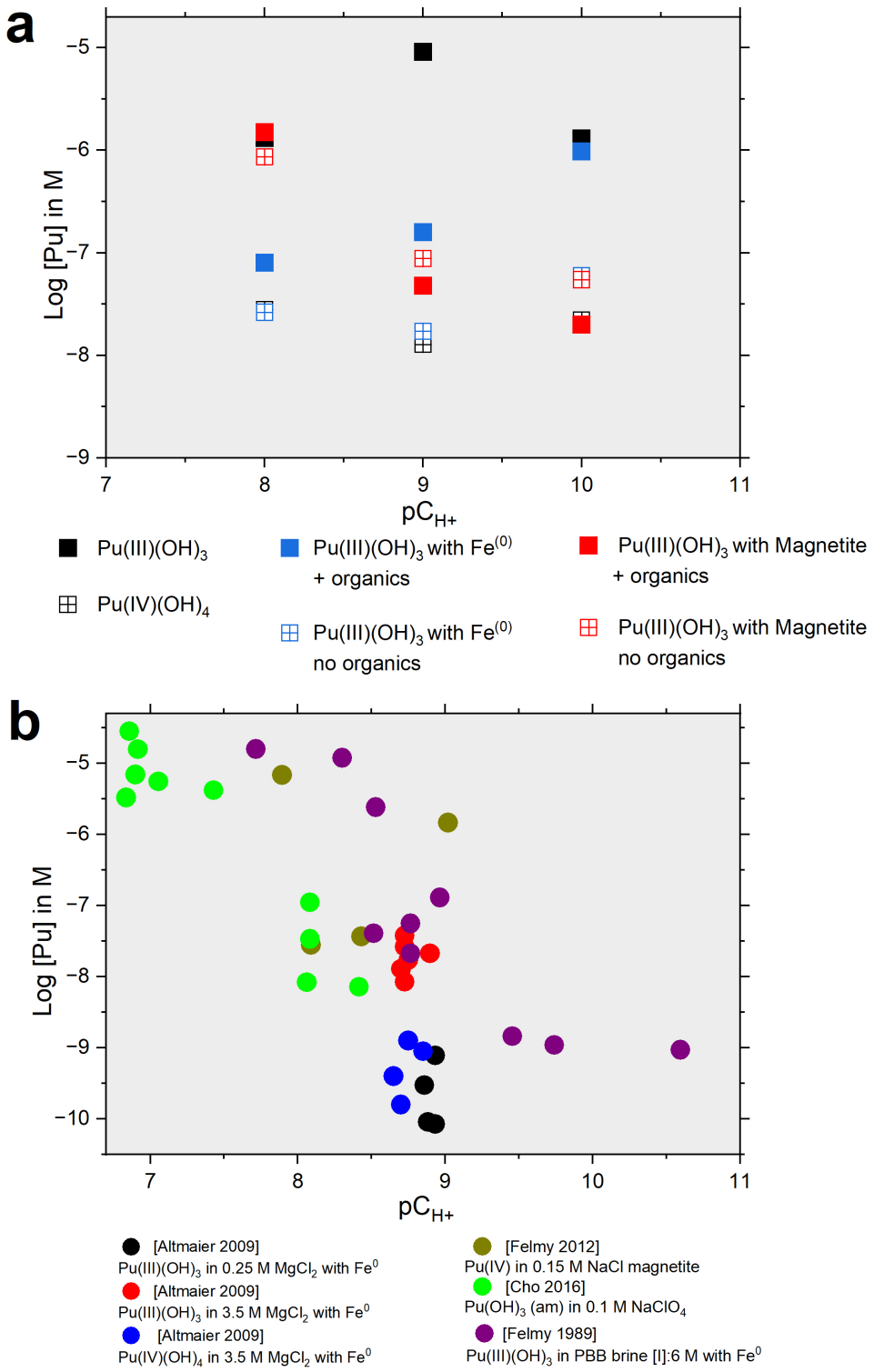


Figure SOTERM-25. Pu Solubility as a Function of pC_{H+} a) in Different WIPP Brines in the Presence and Absence of Organics and Iron Corrosion Products (Fe^0 and Magnetite; Maximum Error of ± 15 %) and b) Reported in the Literature for Pu in Alkaline Systems (from Kaplan 2025b).

SOTERM-5.6 Americium and Curium Chemistry: Background and Behavior under Repository Conditions

Americium(III) is the most stable and prevalent oxidation state (Runde and Schulz 2006), and it is notably resistant to oxidation in aqueous media (Hobart et al. 1982). The Am(III) ion exhibits an ionic radius of 97.5 picometers (pm) (coordination number [CN]=6). Given its comparable ionic radius and charge density, Am(III) can be used as an analog for Pu(III) (100 pm at CN=6) and Cm(III) (97 pm at CN=6) (Shannon 1976). In the chemical conditions conceptual model, americium is represented exclusively in the trivalent oxidation state. In solubility calculations, its aqueous speciation includes Am(III) complexes and colloidal forms.

The environmental chemistry of curium closely resembles that of americium, and thus, much of the discussion regarding Am(III) speciation, solubility, and complexation is equally applicable to Cm(III). Curium is also distinguished from the lighter actinides by the stability of its +3 oxidation state with respect to oxidation or reduction (Lumetta et al. 2006). The oxidation of Cm(III) to Cm (IV) is achieved only with the strongest oxidizing agents.

The solubility and speciation of Am(III) in groundwater under mildly alkaline conditions are primarily governed by hydrolysis and carbonate complexation. These processes significantly influence the mobility and long-term behavior of americium in subsurface environments relevant to nuclear waste repositories. A broad body of experimental work has been conducted to characterize Am(III) solubility under varying geochemical conditions, including pH, ionic strength, carbonate concentration, and the presence of competing cations such as calcium and sodium (Silva and Nitsche 1995).

Kim et al. (1984) explored the influence of carbonate on Am(III) solubility in $NaClO_4$ media in the presence (p_{CO2} =$10^{-3.5}$ atm) and absence of CO_2. Their results were interpreted as contributions from hydroxy-, carbonato-, and mixed hydroxy-carbonato complexes. Although the solid phase was not characterized, the results supported the proposed formation of a carbonate-containing solid phase, likely $AmCO_3OH(s)$. Similar solubility trends were reported by Felmy et al. (1990), who examined $AmCO_3OH(cr)$ under slightly different CO_2 conditions. Both studies observed pH-dependent solubility consistent with carbonate complexation.

Further investigation into analog systems revealed that Nd(III) exhibits similar solubility behavior under high ionic strength conditions. Borkowski et al. (2009) reported that Nd concentrations were two to three orders of magnitude higher than those of Am(III) at comparable pH values, likely due to the increased ionic strength of the 5 M NaCl solutions.

Hinz et al. (2015) studied the complexation behavior of borate with neodymium and curium in NaCl, $MgCl_2$, and $CaCl_2$ solutions. Borate was demonstrated to decrease neodymium solubility in dilute NaCl and $MgCl_2$ solutions at $pC_{H+} \leq 9$ with [B] ≥ 40 mM as well as in concentrated NaCl and $MgCl_2$ solutions with [B] ≥ 160 mM. Curium studies indicated that two different borate species are likely responsible for the solubility behaviors observed.

A series of experiments, reported for CRA-2009, were performed to determine the solubility of Nd(III) as an analog for Pu(III) and Am(III) solubility in brines (Borkowski et al. 2009). These experiments were conducted in GWB and ERDA-6 brines over a pH range of 6–12, and across various carbonate concentrations. Neodymium solubility was not greatly affected by carbonate, due to dominant borate complexation. Solubility trends, as a function of pC_{H+}, were similar in GWB and ERDA-6 brines. At $pC_{H+} > 10$, Nd solubility was primarily controlled by hydroxide concentration and decreased with increasing pC_{H+}. These results expanded upon earlier studies in simplified brines and provided a more complete representation of solubility behavior in realistic repository-relevant conditions.

SOTERM-5.6.1 Literature Results Since the CRA-2019

Xiong and Wang (2021b) and Xiong et al. (2023) conducted studies using the Pitzer model to describe activity coefficients of aqueous species under high ionic strength conditions. In their 2021 study, Xiong and Wang (2021b) determined the solubility constants for $Pr_2(C_2O_4)_3{\cdot}10H_2O$ and $Nd_2(C_2O_4)_3{\cdot}10H_2O$ through solubility experiments performed in HNO_3 and mixed HNO_3 - $H_2C_2O_4$ solutions at 23.0 ± 0.2 °C. $Pr_2(C_2O_4)_3{\cdot}10H_2O$ was selected as an analog for $Pu_2(C_2O_4)_3{\cdot}10H_2O$, while $Nd_2(C_2O_4)_3{\cdot}10H_2O$ served as an analog for $Am_2(C_2O_4)_3{\cdot}10H_2O$ and $Cm_2(C_2O_4)_3{\cdot}10H_2O$. Based on the experimental data, they developed a thermodynamic model for these oxalate complexes in mixed acid solutions at high ionic strengths, applying the Pitzer formalism to calculate activity coefficients.

In a subsequent study, Xiong et al. (2023) investigated the Nd(III)–sulfate interaction at high ionic strengths, motivated by the abundance of sulfate in WIPP brines and nuclear waste streams. They developed a thermodynamic model capable of describing the interaction of Nd(III) with sulfate at ionic strengths up to ~16.5 $mol{\cdot}kg^{-1}$ and temperatures up to 100 °C, employing the Pitzer model to account for activity coefficients of aqueous species. The Xiong et al. studies have been questioned by Oakes et al. (2021).

Oakes et al. (2021) developed a conventional and speciated Pitzer ion interaction model to predict the behavior of An(III) compounds under geologic conditions at 298 kelvin (K) and 0.1 MPa. Using neodymium (Nd^{3+}) as a chemical analog for An(III), the model accurately reproduces the properties of $NdCl_3$(aq) and its interactions with evaporite-type brine components over a broad pH range (2–13). The model includes key aqueous species—Nd^{3+}, $NdOH^{2+}$, $Nd(OH)_2^{+}$, $Nd(OH)_3^{0}$, $NdCl^{2+}$, and $NdCl_2^{+}$—and was fitted to isopiestic, electromotive force, and $NdCl_3{\cdot}6H_2O$ solubility data. Notably, the model was extended to pH values where solid $Nd(OH)_3$, $Nd(OH)_2Cl$, and a proposed double salt, $Nd(OH)_3{\cdot}NdCl_3$, become stable. The inclusion of these hydroxychloride phases ensures thermodynamic continuity between the solubility domains of $NdCl_3{\cdot}6H_2O$ and $Nd(OH)_3$ across the full pH range. Compared to previous models, this framework is both simpler and broader in its compositional coverage while offering improved predictive accuracy. It provides a thermodynamic basis for modeling Nd(III) and, by analogy, An(III) behavior in chloride-rich environments such as salt-based nuclear waste repositories. It should be noted that this model did not include carbonate. More details can be found in CRA-2026 Appendix GEOCHEM-4.3.1.1 and -4.3.1.2.

Adam et al. (2021) worked on the effect of selected organic cement additives or model compounds (adipic acid, methyl acrylate, citric acid, melamine, ethylene glycol, phthalic acid, and gluconic acid) on the solubility of Nd(III), as well as Th(IV) and U(VI). They performed screening experiments from undersaturation conditions in alkaline NaCl, $MgCl_2$, and $CaCl_2$ solutions at elevated ionic strength with $9 \leq pH_m \leq 13$ ($pH_m = -\log[H^+]$) on the molal scale. According to their results, adipic acid, methyl acrylate, melamine, ethylene glycol, and phthalic acid did not impact the solubility of Nd(III) in the investigated systems. Citrate significantly enhanced the solubility of Nd(III) in NaCl systems.

Rojo et al. (2021) studied the effect of gluconate on the solubility and aqueous speciation of An(III) and Ln(III) using a combination of Nd(III) solubility experiments, Cm(III) time-resolved laser fluorescence spectroscopy (TRLFS), and DFT calculations. The experiments were performed in NaCl (0.1–5.0 M) and $CaCl_2$ (0.1–3.5 M) solutions with $9 \leq pH_c \leq 13$ and 10^{-6} M ≤ $[\text{gluconate}]_{tot} \leq 10^{-2}$ M. According to the experimental results, the solubility of $Nd(OH)_3(s)$ remained mostly unaffected in NaCl solutions with $[\text{gluconate}]_{tot} = 10^{-3}$ M, whereas a clear increase in solubility was observed in dilute $CaCl_2$ solutions with the same $[\text{gluconate}]_{tot}$ and $pH_c \geq 11$. In concentrated $CaCl_2$ solutions, gluconate did not affect the solubility of Nd(III) due to the competition with Ca– gluconate complexes.

Trumm et al. (2022) conducted a comprehensive experimental and theoretical investigation of the complexation behavior of Cm(III) with EDTA in alkaline aqueous solutions (pH 7–12), using TRLFS, vibronic side-band spectroscopy, and quantum chemical calculations. Experimental measurements were performed with $[Cm] = 10^{-7}$ M, $[EDTA]_{tot} = 10^{-3}$ M. The TRLFS spectra and fluorescence lifetime data indicated the predominance of the $Cm(EDTA)^-$ species at pH 7, followed by the subsequent formation of hydrolysis species $Cm(OH)_n(EDTA)^{-1-n}$ with increasing pH. Quantum chemical calculations provided detailed structural and thermodynamic data on the Cm:EDTA 1:1 and 1:2 complexes, such as bond distances, stability constants, reaction enthalpy, and entropy in the pH range 7–12.

The Kim research group published two articles on the solubility behavior of americium (Am), europium (Eu), and samarium (Sm), in synthetic groundwater representative of the Korean Atomic Energy Research Institute Underground Research Tunnel environment (Kim and Cho 2022; Kim et al. 2024). Kim and Cho (2022) investigated Am(III) solubility in oversaturation conditions for a period of 70 days. Combined geochemical modeling and experimental investigations indicated that Am(III) solubility was controlled by amorphous $AmCO_3OH$ instead of crystalline phases. Within the pH range of 7.5-10.5, Am(III) concentrations converged to ~ 2×10^{-7} M over the 70-day period. No transformation from the amorphous phase to a crystalline phase was observed during the experiment. In a subsequent study, Kim et al. (2024) examined the solubility behavior of Sm and Eu in undersaturated conditions over 223 days, confirming the persistence of crystalline phases. When $Ln_2(CO_3)_3 \cdot xH_2O(cr)$ (Ln = Sm, Eu) solid compounds were equilibrated in the synthetic groundwater, the dissolved Sm and Eu concentrations were $(3.98 \pm 0.04) \times 10^{-8}$ and $(6.08 \pm 0.05) \times 10^{-8}$ M at pH 8.19 and 8.26, respectively. These values were comparable to those of $Sm_2(CO_3)_3(s)$ and $Eu_2(CO_3)_3(s)$ as evaluated by geochemical modeling. In experiments similar to their 2022 investigations, Kim et al. (2024), measured Am(III) solubility

over 231 days in oversaturation conditions. These yielded lower Am concentrations than the 70-day experiments ($5.48 \pm 1.3 \times 10^{-8}$ M at pH 8.45).

Yang et al. (2023) used the geochemical modeling codes PHREEQC-3 and PhreePlot along with thermodynamic data primarily from the NEA-TDB to calculate the solubility and speciation of americium under both near- and far-field conditions at China's proposed Deep Geologic Repository in Beishan, Gansu Province. Groundwater from the near-field is more reducing than the undisturbed far-field groundwater. The thermodynamically metastable amorphous phase $AmCO_3OH$(am, hyd) was assumed to be the solubility-limiting solid phase under both conditions. The results indicated americium solubilities of 6.3×10^{-7} mol/kg in the near field and 2.4×10^{-6} mol/kg in the far field. While these values indicated relatively low solubility, the authors emphasized that processes such as sorption and colloid formation may play a more significant role in controlling Am mobility in natural groundwater systems.

Zhou et al. (2025) worked on the solubility, speciation, and sorption of americium in Beishan groundwaters with CHEMSPEC code. The results indicated that Am solubility is 2.3×10^{-8} mol/L in the near field and 1.57×10^{-7} mol/L in the far field. The speciation of americium was found to be significantly influenced by inorganic complexing anions, with the order of impact being $HCO_3^- > F^- > SO_4^{2-} > Si(OH)_4$(aq). Sorption modeling using three different surface complexation models showed the sorption of Am onto quartz under low-concentration conditions. However, the potential for colloid-facilitated transport via quartz particles suggested a possible pathway for enhanced Am mobility in repository environments.

Comins et al. (2024b) investigated the interactions of Cm(III) with citrate in both the presence and absence of calcium, under alkaline to hyperalkaline conditions relevant to nuclear waste repositories. Using a combined approach of TRLFS and quantum chemical calculations, they characterized the chemical reactions governing the binary Cm(III)-citrate and ternary Ca–Cm(III)-citrate systems. Their findings provide an updated speciation model for the binary Cm-citrate system, demonstrating a stepwise coordination and deprotonation of citrate hydroxyl groups with increasing pH. Additionally, they presented new evidence for the formation of stable ternary Ca–Cm–citrate complexes, which are stabilized through shared carboxylate and hydroxyl functional groups between calcium and curium. The presence of these shared groups highlights the enhanced stability of the ternary complexes. Together, these results form a basis for future thermodynamic studies and modeling of An(III) speciation under repository-relevant geochemical conditions.

Research by Moniruzzaman et al. (2020 and 2021) provides insights into the solubility and solid-phase behaviors of trivalent lanthanide compounds, which are crucial for understanding the long-term stability of nuclear waste forms. In his 2020 study, Moniruzzaman and colleagues employed an undersaturation approach to investigate the solubility and solubility-limiting solid phases of La, Eu, and Thulium (Tm) in solutions with an ionic strength of 0.1 mol/L and a pH range of 6 to 12, after aging at temperatures between 25 to 90 °C (77 to 194 °F) for up to 12 weeks. The XRD patterns revealed that La_2O_3 transformed to $La(OH)_3$, Eu_2O_3 remained stable at 25 °C but converted to $Eu(OH)_3$ at 90 °C, and Tm_2O_3 did not undergo transformation at either

temperature. Thermodynamic analysis of the temperature dependence of solubility products corroborated these observations. In a subsequent 2021 study, Moniruzzaman and his team focused on the solubility of mixed lanthanide hydroxide and oxide solid solutions. The researchers found that phase transformations in binary and ternary systems led to the formation of solid solutions such as (La, Nd)$(OH)_3$, (La, Eu)$(OH)_3$, and (La, Nd, Eu)$(OH)_3$. Conversely, systems containing Tm_2O_3 retained oxide-based solid solutions, and their solubility behaviors were dominated by congruent dissolution.

SOTERM-5.6.2 WIPP-specific Results Since the CRA-2019 PA

Neodymium solubility in the presence of organic ligands and under WIPP conditions was investigated by Kutahyali Aslani (2022). The study focused on the effects of complexation with citrate and EDTA ions and their impact on neodymium solubility (note that the concentrations of organics added to these experiments were based on the 2018 PAIR and the 17,400 m^3 minimum volume for a DBR; Van Soest 2018). To assess the influence of these strong complexants, experiments were conducted using both initially amorphous and crystalline phases of $Nd(OH)_3$ in 0.1 M and 5 M NaCl, as well as in simulated WIPP brines. The systems were equilibrated over approximately 250 days at adjusted pC_{H+} values of 7, 9, and 11. Powder XRD analysis confirmed the structure of the solid phases, with the amorphous phase exhibiting microcrystalline features (Figure SOTERM-26). These results are applicable, by analogy, to the behavior of trivalent actinides expected in the WIPP repository.

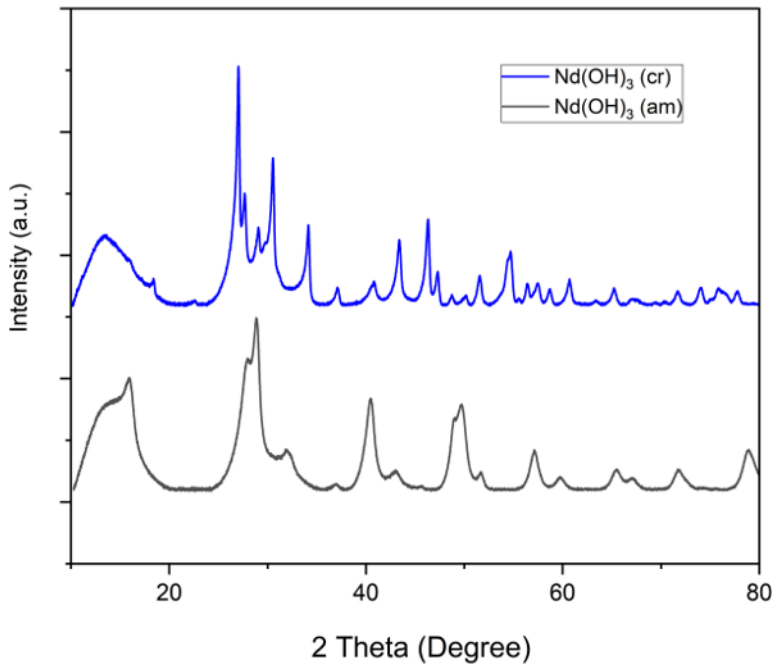


Figure SOTERM-26. XRD Patterns of Crystalline (Blue) and Amorphous (Black) $Nd(OH)_3$

The solubility of neodymium (III) with respect to amorphous and crystalline phases of $Nd(OH)_3$ in 5 M NaCl and 0.1 M NaCl solutions is presented in Figure SOTERM-27. The data clearly show that the presence of organic ligands increases Nd solubility. When organics are present, Nd solubility remains relatively constant across pC_{H+} values of 7, 9, and 11, with only a slight decrease observed in 5 M NaCl at pC_{H+} 9 and 11. This suggests that, under these conditions, solubility is largely independent of pC_{H+}. In contrast, in the absence of organics, a significant decrease in solubility is observed at higher pC_{H+} values, as compared to samples with organics. These data appear to match well with the model predicted by Oakes et al. (2021).

Additionally, in both sets of conditions, the crystalline phase exhibits slightly higher solubility than the amorphous phase in the presence of organics. The lower solubility of the amorphous phase with organics may be attributed, in part, to the presence of microcrystalline domains within the sample, as evidenced by the broader peaks in its XRD pattern. These domains reduce the overall free energy of the material and dissolve more slowly than the surrounding amorphous matrix, thereby diminishing the solubility advantage typically associated with a fully amorphous phase (Nishizawa 2008; Porter et al. 2009; Nishinaga 2016). Consequently, the measured solubility of the amorphous phase approached that of the crystalline phase. On the other hand, as shown in Figure SOTERM-27a and b, in the absence of organic ligands, Nd solubility exhibited similar behavior for both crystalline and amorphous phases in 0.1 M NaCl. However, in 5 M NaCl without organics, the amorphous phase showed higher solubility at pC_{H+} 7 and 9.

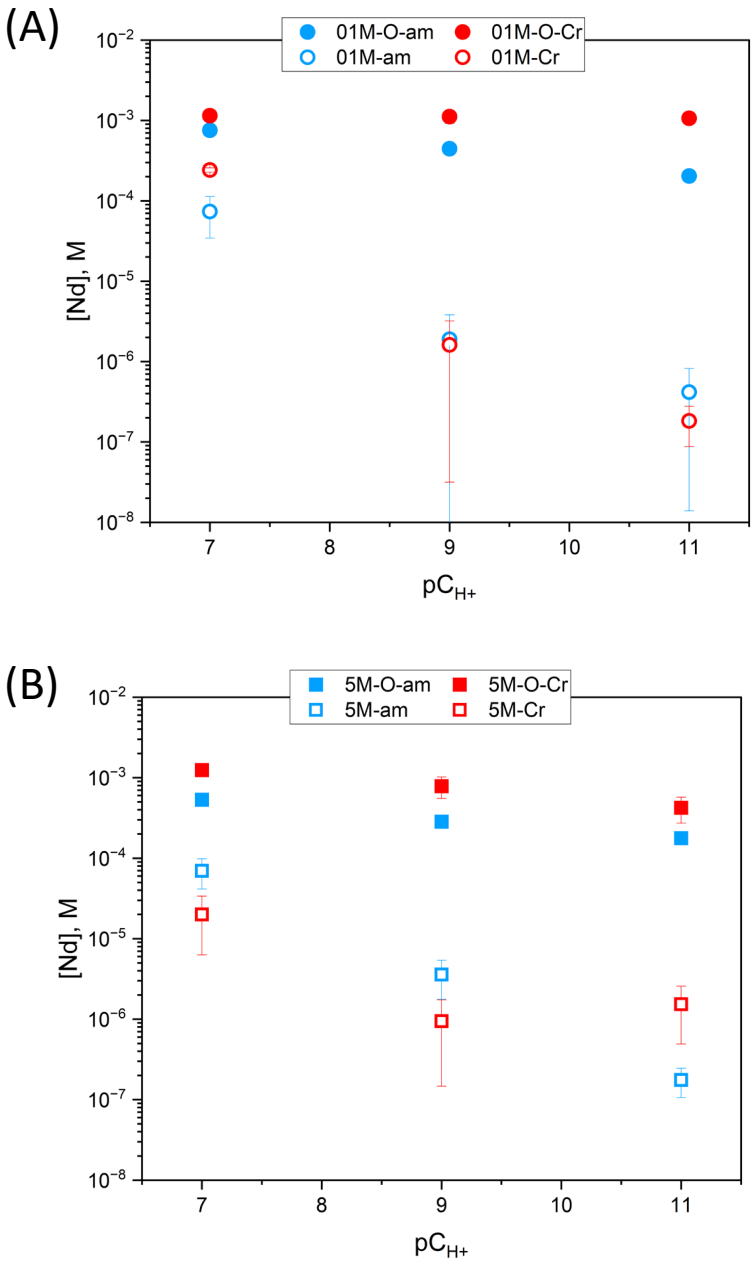


Figure SOTERM-27. [Nd] as a Function of pC_{H+} in 0.1 M NaCl (A) and 5 M NaCl (B). 01M and 5M Denote 0.1 M and 5 M NaCl, O Denotes Organics (EDTA and Citrate), am and Cr Denote Amorphous and Crystalline, Respectively (After ~250 Days of Equilibration) (from Kutahyali Aslani 2022).

The effects of organic ligands on neodymium solubility under repository-relevant conditions are shown in Figure SOTERM-28 as a function of pC_{H+}, both in the presence and absence of organics. As illustrated in Figure SOTERM-28, neodymium solubility is consistently higher across all pC_{H+} values when organic ligands are present.

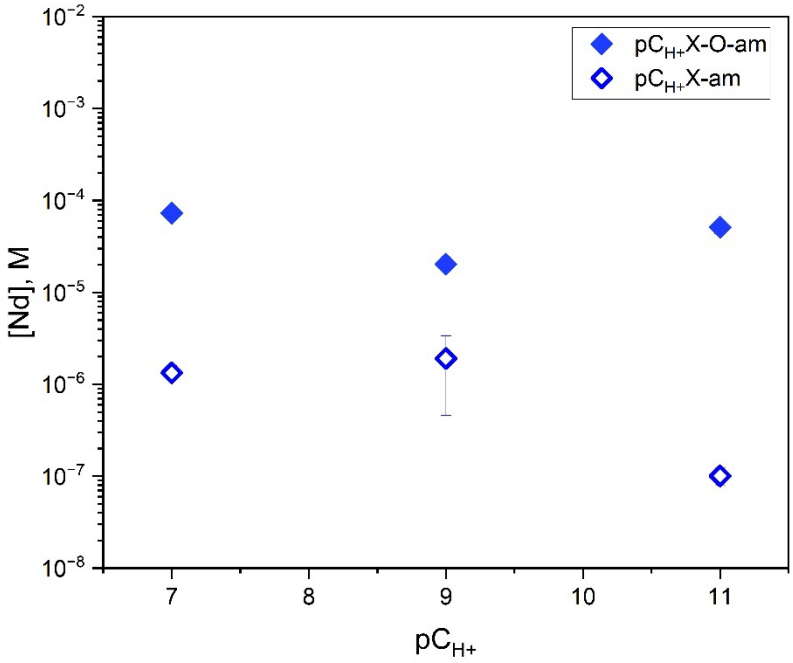


Figure SOTERM-28. [Nd] as a Function of pC_{H+}-specific WIPP Brines. X denotes pC_{H+} 7, 9 and 11, O Denotes Organics (EDTA and Citrate) and am Denotes Amorphous (After ~250 Days of Equilibration) (from Kutahyali Aslani 2022).

Figure SOTERM-29 and Figure SOTERM-30 present Nd(III) concentrations as a function of time in 0.1 M NaCl and 5 M NaCl solutions, with and without organic ligands (citrate and EDTA). In both salt concentrations, the highest solubility was observed at pC_{H+} 7 and 9 in the presence of organics and with the crystalline $Nd(OH)_3$ phase. Over a period of approximately 250 days, neodymium concentrations remained relatively stable in the presence of organics, indicating that steady-state conditions were rapidly achieved in the investigated brines. In contrast, when organics were absent, noticeable changes in Nd solubility occurred over time. A decrease in Nd concentration was observed in the crystalline phase samples at 0.1 M NaCl and pC_{H+} 9.

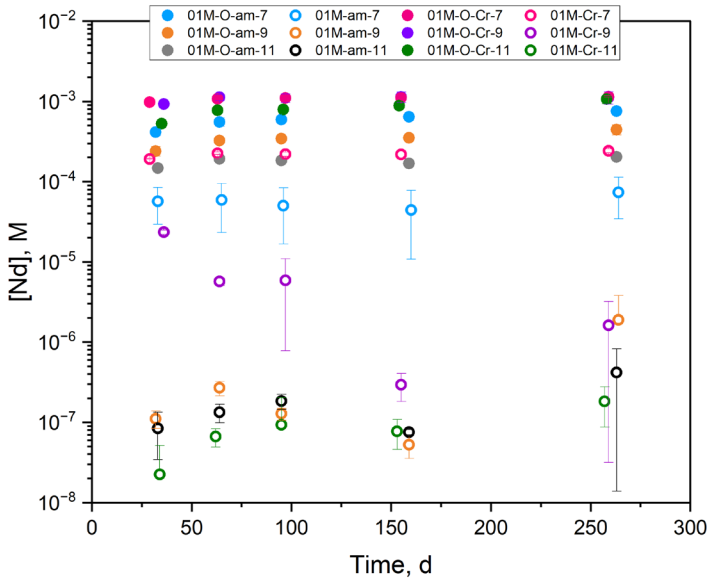


Figure SOTERM-29. [Nd] as a Function of Time in 0.1 M NaCl. 01M Denotes 0.1 M NaCl, O Denotes Organics (EDTA and Citrate), am and Cr Denote Amorphous and Crystalline, Respectively (from Kutahyali Aslani 2022).

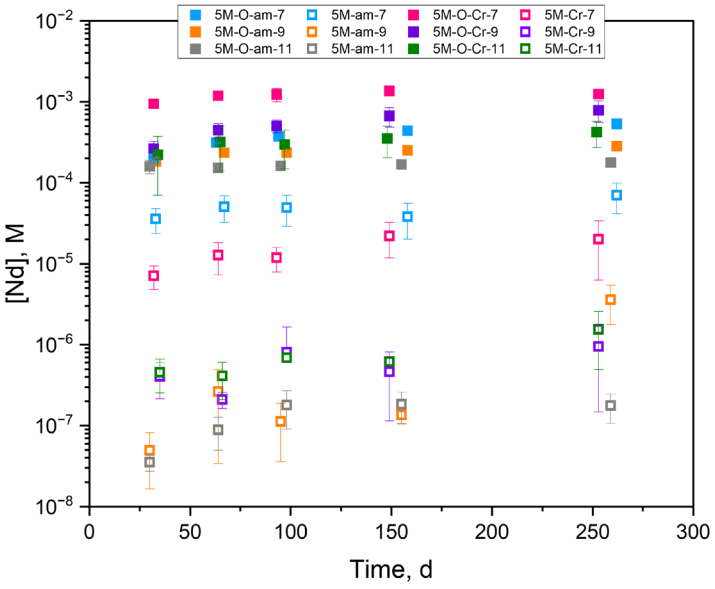


Figure SOTERM-30. [Nd] as a Function of Time in 5 M NaCl. 5M Denotes 5 M NaCl, O Denotes Organics (EDTA and Citrate), am and Cr Denotes Amorphous and Crystalline, Respectively (from Kutahyali Aslani 2022).

Figure SOTERM-31 illustrates the effect of pC_{H+} and organics on the solubility of Nd(III) in the pC_{H+} specific brines. The highest solubility is observed in pC_{H+} 7 brine with organics, while the lowest solubility occurs in the pC_{H+} 11 brine absence of organics.

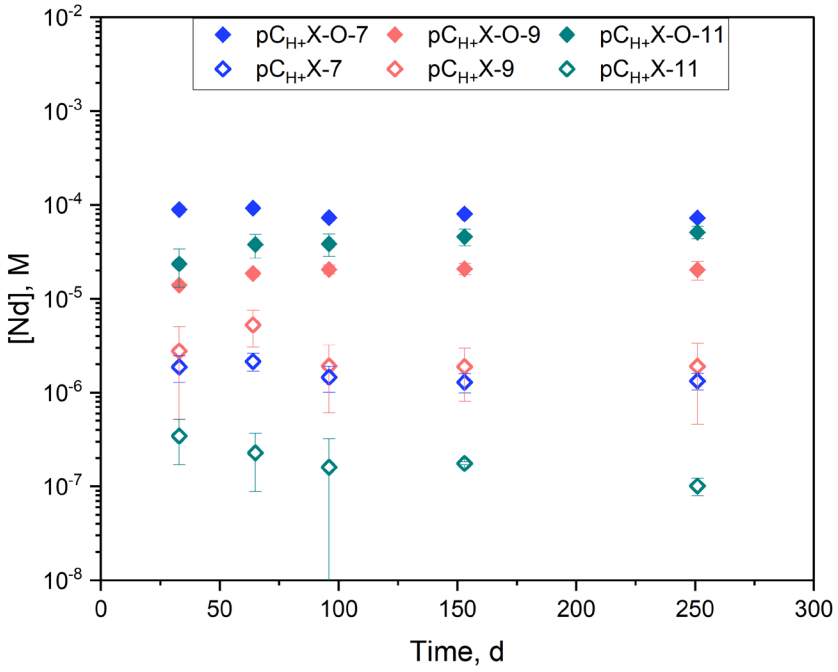


Figure SOTERM-31. [Nd] Concentration as a Function of Time in pC_{H+}-specific Brines. X Denotes 7, 9 and 11, O Denotes Organics (EDTA and Citrate) (from Kutahyali Aslani 2022).

SOTERM-6.0 THE WIPP ACTINIDE SOURCE TERM

The application of the conceptual models to the actinide source term, the assumptions used to simplify the source term model, changes implemented in the CRA-2026 that could affect the source term, and the approach to calculating the actinide source term are given in this section.

SOTERM-6.1 The WIPP Conceptual Models and the Actinide Source Term

There are several assumptions made in the conceptual models that inform actinide source term calculations (U.S. DOE 1996; CCA Appendix-PEER1; McCormick et al. 2024). Some are meant to simplify the modeling approach, while others were made to fill a gap in knowledge.

The chemical conditions model assumes that the repository is homogeneously mixed and at equilibrium. This simplification allows for instantaneous dissolution of actinides to their solubility limits. It also assumes that MgO will control carbon dioxide fugacity and buffer the pH of the repository, and that these alkaline and low carbonate concentrations will limit actinide solubility.

The model specifies a fixed brine composition for solubility calculations, based on the intrusion scenario. Both compositions are used in actinide solubility calculations. The model also specifies that ligand concentrations are fixed. This implies that neither biodegradation nor radiolytic degradation occurs and results in an overprediction of solubilities.

After the early oxic period, anoxic iron corrosion will further promote reducing conditions by producing H_2 and Fe^{2+} species. These will define the redox conditions in the repository, thereby affecting actinide speciation and solubility. E_h values cannot be directly measured or calculated in the repository but are set by H_2 fugacity and Fe^0. Under these conditions, the model assumes that multivalent actinides are in their reduced oxidation state, which can either increase or decrease solubility. Oxidizing processes, such as radiolysis, and oxidizing waste components, such as nitrates, are acknowledged in the conceptual model.

Microbial gas generation will be outweighed by gas generation from iron corrosion. Microbial CO_2 generation is accounted for in the chemical conditions model with the use of MgO. Other gases produced during CPR degradation (i.e., N_2 or H_2S), along with H_2 from iron corrosion, can contribute to pressurization of the repository.

The dissolved actinide source term model assumes different realizations for more or less reduced oxidation states of multi-valent actinides. For redox-invariant actinides, 100% of the realizations are in the one state. The model also assumes that actinides of the same oxidation state behave similarly. This allows for the use of thermodynamic data from analogs, such as Th(IV) or Nd(III), that are easier to work with because of redox-invariance or that behave similarly in complexation experiments. However, the use of Th(IV) as an analog results in overestimated solubilities. A third assumption is that actinides do not adsorb onto fixed substrates. Finally, the model assumes that precipitated solids become crystalline over time but

uses the solubility data for amorphous phases as an upper bound. Both of these assumptions lead to overpredicted solubilities.

The colloidal actinide source term model assumes that all colloids are suspended and mobile and that no competition exists between actinides for humic or microbial colloids. Both assumptions result in an overprediction of colloid enhancement to the source term. Humic and microbial colloid capacities depend upon the dissolved concentration of actinides through the use of the proportionality constant. This ties these colloid contributions to the dissolved actinide source term. In contrast, mineral and intrinsic colloids have fixed values. A final assumption is that microbial and mineral colloid quantities are constant, resulting in a constant amount of available substrate that permits continuous contribution from these colloid types.

SOTERM-6.2 Changes Implemented for the CRA-2026

Several changes were implemented for the CRA-2026 that could affect the actinide source term. These include parameter changes for Pu oxidation state distribution, U(VI) solubility, and various colloids (Kaplan et al. 2025; Appendix GEOCHEM-5.3, Appendix PA-1.1). Changes to brine volume and to reactants used in calculating solubilities are also described.

- The 50:50 distribution for the Pu oxidation state, which was established for the initial CCA, was changed for the CRA-2026 to the following: 75% of the PA vectors model Pu as Pu(IV), and 25% of the PA vectors model Pu as Pu(III) (Kaplan et al. 2025). This change does not alter the method by which mobile Pu concentrations are calculated for each oxidation state, but it does change the distribution of realized oxidation states across PA vectors, resulting in a change in projected releases.
- The minimum volume required for a DBR was changed from 17,400 m^3 (Clayton 2008) to 6,314 m^3 for the interim state repository (Brunell 2025). Docherty (2024) updated the minimum brine volume calculation due to the updated geomechanical model, which Brunell (2025) then recalculated to account for the 12-panel interim state repository configuration. It directly affects the scaling of the reactants used in the solubility model (Domski 2025a). However, almost all actinides are solubility-limited, even with these apparent increases, and there are no changes to the modeling approach. Of the organic ligands, only oxalate is solubility-limited, as in past CRAs.
- During baseline solubility calculations for the actinides, calcite ($CaCO_3$) was suppressed, and aragonite was allowed to precipitate, if it became saturated during the simulations. Furthermore, the magnesium oxy-chloride phase, Phase 5 ($Mg_3Cl(OH)_5{\cdot}4H_2O$), was suppressed (Domski 2025a).
- For the CRA-2026, the lead (II) oxide (PbO) used in the CRA-2019 was replaced with hydrocerussite $2PbCO_3.Pb(OH)_2(s)$. This reactant is included in actinide solubility calculations but does not compete with actinides for ligands, which results in an overprediction of actinide solubilities (Appendix GEOCHEM-3.1.7).

- For the CRA-2026, the iron phase $Fe(OH)_2$ used in CRA-2019 was replaced with hibbingite ($Fe_2Cl(OH)_3$). Iron is included as a reactant in solubility calculations, and speciation affects oxidation state. The calculation does not include competition for complexation with organic ligands other than citrate, which again results in an overprediction of actinide solubilities (Appendix GEOCHEM-3.1.8).
- The plutonium inventory increased significantly due to projected waste stream containing surplus plutonium from the Savannah River Site. This increase, which represents a bounding quantity of surplus plutonium, is reflected in the calculations.
- The solubility of uranium(VI) was reduced from the EPA-mandated 1×10^{-3} M to 3.00×10^{-6} M, based on WIPP-specific experimental data (EPA 2005; Lucchini et al. 2010a, 2010b, 2013a; Kutahyali Aslani 2024; Kaplan et al. 2025). This change has led to a decrease of ~ 3 orders of magnitude in the total mobile U(VI) concentration, as compared to the CRA-2019.
- Microbial colloid enhancement parameters for the actinides were updated, based on new experimental data (Swanson 2024a) and a reanalysis of existing data to address comments received from the EPA (Kaplan et al. 2025; CRA-2026 Appendix GEOCHEM-5). These changes do not have a large impact on the mobile actinide concentrations because of the decrease in uranium solubility, although there are significant increases in the relative contributions of An(III) biocolloids (Appendix SOTERM-6.5).
- The intrinsic colloid enhancement parameters for Th and Am were also updated based on EPA recommendations to use bounding Nd data from Borkowski et al. (2010) and Th data consistent with both Altmaier et al. (2004) and Borkowski et al. (2012) (EPA 2022; Kaplan et al. 2025). These changes do not have a large impact on the release calculations, since neither inventory contributes significantly to releases.

SOTERM-6.3 Oxidation State Distributions

The oxidation states used to model actinide solubility are tabulated in Table SOTERM-10. The multivalent actinides are assumed to exist in one oxidations state, and their distributions are given as a percentage of realizations in which they appear in the specified state. This partitioning addresses the uncertainty in the assumption that actinide redox couples are not in equilibrium.

There is only one change to this distribution, proposed and implemented in the CRA-2026 PA. The oxidation state distribution for Pu was changed from a 50:50 ratio of Pu(III) to Pu(IV) to a 25:75 ratio (Kaplan et al. 2025). Table SOTERM-10 shows the assumed percentage abundance and the speciation data set used in EQ3/6 for each oxidation state. This table is based on the actinide chemistry summarized in Appendix SOTERM-5.0.

Table SOTERM-10. Oxidation State Distribution of the Actinides in the WIPP Used in the CRA-2026 PA.

Actinide Element	Oxidation States, Abundance (%), and Analog Used (If Any)				
	Oxidation State[1]				EQ3/6 Speciation Data Used
	III	IV	V	VI	
Thorium	—	100 %	—	—	Thorium
Uranium	—	50 %	—	50 %	U for VI[2] Th for IV
Neptunium	—	50%	50 %	—	Np for V Th for IV
Plutonium	25 %	75 %	—	—	Am for III Th for IV
Americium	100 %	—	—	—	Americium
Curium	100 %	—	—	—	Americium

[1]Oxidation state distributions (percentage) refer to the percentage of realizations in the specified oxidation state (CRA-2019 Appendix-SOTERM-6.4; Kaplan et al. 2025).
[2]**Note**: there is no EQ3/6 model for U(VI).

SOTERM-6.4 Actinide Speciation Reactions Used in CRA-2026

The version of the database used with the EQ3/6 code for the CRA-2026 PA was DATA0.FM6 (Domski 2023a). The actinide model that is the basis for solubility calculations is summarized in this section.

SOTERM-6.4.1 The Trivalent Actinides: Ac(III), Pu(III), Am(III), Cm(III)

The parameter values currently used for modeling An(III) solubility were originally described in Giambalvo (2002a) and updated by Domski (2023a). EQ3/6 uses the Am(III) data to calculate the solubility for all the III actinides. The formation reactions and associated stability constants for the aqueous and solubility-limiting species representing An(III) are given in Table SOTERM-11 (see also CRA-2026 Appendix GEOCHEM, Table GEOCHEM-18).

Table SOTERM-11. Solubility Constants and Formation Reactions of Am Species in the WIPP Model.

Am(III) Reactions	log K	Equation
Solid Formation Reactions		
$Am^{3+} + 3H_2O \leftrightarrows Am(OH)_3(s) + 3H^+$	-14.9	SOTERM.40
$Am^{3+} + 3H_2O \leftrightarrows Am(OH)_3(am) + 3H^+$	-16.9	SOTERM.41

Am(III) Reactions	log K	Equation
$Am^{3+} + H_2O + HCO_3^- \leftrightarrows AmOHCO_3(c) + 2H^+$	-1.6366	SOTERM.42
$Am^{3+} + Na^+ + 2HCO_3^- + 6H_2O \leftrightarrows NaAm(CO_3)_2 \cdot 6H_2O(cr) + 2H^+$	0.7131	SOTERM.43
$Am^{3+} + HPO_4^{2-} \leftrightarrows AmPO_4(cr) + H^+$	12.4595	SOTERM.44
Inorganic Aqueous Formation Reactions		
$Am^{3+} + HCO_3^- \leftrightarrows AmCO_3^+ + H^+$	-2.2388	SOTERM.45
$Am^{3+} + 2HCO_3^- \leftrightarrows Am(CO_3)_2^- + 2H^+$	-7.6766	SOTERM.46
$Am^{3+} + 3HCO_3^- \leftrightarrows Am(CO_3)_3^{3-} + 3H^+$	-15.8157	SOTERM.47
$Am^{3+} + 4HCO_3^- \leftrightarrows Am(CO_3)_4^{5-} + 4H^+$	-28.3586	SOTERM.48
$Am^{3+} + H_2O \leftrightarrows AmOH^{2+} + H^+$	-7.5556	SOTERM.49
$Am^{3+} + 2H_2O \leftrightarrows Am(OH)_2^+ + 2H^+$	--15.6915	SOTERM.50
$Am^{3+} + 3H_2O \leftrightarrows Am(OH)_3(aq) + 3H^+$	-25.6905	SOTERM.51
$Am^{3+} + Cl^- \leftrightarrows AmCl^{2+}$	0.2393	SOTERM.52
$Am^{3+} + 2Cl^- \leftrightarrows AmCl_2^+$	-0.7400	SOTERM.53
$Am^{3+} + SO_4^{2-} \leftrightarrows Am(SO_4)^+$	3.2485	SOTERM.54
$Am^{3+} + 2SO_4^{2-} \leftrightarrows Am(SO_4)_2^-$	3.7019	SOTERM.55
Organic Aqueous Formation Reactions		
$Am^{3+} + Acetate^- \leftrightarrows AmAcetate^{2+}$	2.7426	SOTERM.56
$Am^{3+} + Citrate^{3-} \leftrightarrows AmCitrate(aq)$	8.7984	SOTERM.57
$Am^{3+} + EDTA^{4-} \leftrightarrows AmEDTA^-$	18.9700	SOTERM.58
$Am^{3+} + Lactate^- \leftrightarrows AmLactate^{2+}$	3.7089	SOTERM.59
$Am^{3+} + Oxalate^{2-} \leftrightarrows AmOxalate^+$	6.1566	SOTERM.60

For CRA-2026, the amorphous phase of americium hydroxide ($Am(OH)_3(am)$) was set as the initial solubility controlling phase (Domski 2023a, 2025a).

The dominant speciation for the An(III) actinides is shown in Table SOTERM-12. The 1:1 organic complex with EDTA accounts for over 98% of the speciation in GWB and ERDA-6. It should be noted that disregarding competition between metals, such as Fe or Pb, for EDTA overestimates the An(III)-EDTA contribution. The 1:2 hydroxide complex ($An(OH)_2^+$) and the 1:1 acetate

complex ($AnAc^{2+}$) are also represented. The contributions of citrate, carbonate, sulfate, borate, and chloride are negligible.

Table SOTERM-12. Predominant Species for the An(III) Actinides (Domski 2025a)

Species	% Contribution in GWB	% Contribution in ERDA-6
$AnEDTA^-$	98.52	98.20
$An(OH)_2^+$	1.16	1.59
$AnAc^{2+}$	0.18	0.08
Total % of Species Present	99.86	99.87

SOTERM-6.4.2 The Tetravalent Actinides: Th(IV), U(IV), Pu(IV), Np(IV)

The IV actinides addressed by the actinide source term conceptual model are Th(IV), U(IV), Pu(IV), and Np(IV). The An(IV) model uses amorphous ThO_2 as the solubility controlling phase. The parameter values currently used for modeling An(IV) solubility were originally described in Giambalvo (2002b) and updated by Domski (2023a). The formation reactions and associated stability constants for the aqueous and solubility-limiting species for Th(IV), representing An(IV), are provided in Table SOTERM-13 (see also CRA-2026 Appendix GEOCHEM, Table GEOCHEM-19).

Table SOTERM-13. Solubility Constants and Formation Reactions of Th Species in the WIPP Model.

Th(IV) Reactions	log K	Equation
Solid Formation Reactions		
$Th^{4+} + 2H_2O \leftrightarrows ThO_2(am) + 4H^+$	-10.4865	SOTERM.61
$Th^{4+} + 2SO_4^{2-} + 9H_2O \leftrightarrows Th(SO_4)_2{\cdot}9H_2O(s)$	12.9982	SOTERM.62
$Th^{4+} + 2SO_4^{2-} + 8H_2O \leftrightarrows Th(SO_4)_2{\cdot}8H_2O(s)$	12.8955	SOTERM.63
$Th^{4+} + 2Na^+ + 3SO_4^{2-} + 6H_2O \leftrightarrows Th(SO_4)_2{\cdot}Na_2SO_4{\cdot}6H_2O(s)$	17.6419	SOTERM.64
$Th^{4+} + 2K^+ + 3SO_4^{2-} + 4H_2O \leftrightarrows Th(SO_4)_2{\cdot}K_2SO_4{\cdot}4H_2O(s)$	18.0740	SOTERM.65
$Th^{4+} + 4K^+ + 4SO_4^{2-} + 2H_2O \leftrightarrows Th(SO_4)_2{\cdot}2K_2SO_4{\cdot}2H_2O$ (s)	21.2301	SOTERM.66
$2Th^{4+} + 14K^+ + 11SO_4^{2-} \leftrightarrows 2[Th(SO_4)_2{\cdot}3.5K_2SO_4(s)]$	49.3193	SOTERM.67

Th(IV) Reactions	log K	Equation
Inorganic Aqueous Formation Reactions		
$Th^{4+} + 4H_2O \leftrightarrows Th(OH)_4(aq) + 4H^+$	-17.5002	SOTERM.68
$Th^{4+} + 3H_2O + HCO_3^- \leftrightarrows Th(OH)_3CO_3^- + 4H^+$	-14.0457	SOTERM.69
$Th^{4+} + 5HCO_3^- \leftrightarrows Th(CO_3)_5^{6-} + 5H^+$	-24.5828	SOTERM.70
$Th^{4+} + 2SO_4^{2-} \leftrightarrows Th(SO_4)_2(aq)$	11.5918	SOTERM.71
$Th^{4+} + 3SO_4^{2-} \leftrightarrows Th(SO_4)_3^{2-}$	12.4273	SOTERM.72
Organic Aqueous Formation Reactions		
$Th^{4+} + Acetate^- \leftrightarrows ThAcetate^{3+}$	7.3617	SOTERM.73
$Th^{4+} + 2Acetate^- \leftrightarrows Th(Acetate)_2^{2+}$	11.2391	SOTERM.74
$Th^{4+} + Citrate^{3-} \leftrightarrows ThCitrate^+$	15.2355	SOTERM.75
$Th^{4+} + EDTA^{4-} \leftrightarrows ThEDTA(aq)$	23.5570	SOTERM.76
$Th^{4+} + Lactate^- \leftrightarrows ThLactate^{3+}$	6.8284	SOTERM.77
$Th^{4+} + 2Lactate^- \leftrightarrows Th(Lactate)_2^{2+}$	11.1913	SOTERM.78
$Th^{4+} + Oxalate^{2-} \leftrightarrows ThOxalate^{2+}$	11.3863	SOTERM.79

The predominant speciation for the An(IV) actinides is given in Table SOTERM-14. This is dominated by two species: the 1:4 neutral hydroxide complex and the 1:3:1 ternary hydroxy-carbonate complex. These two species account for ~ 100% of the speciation calculated based on current modeling assumptions.

Table SOTERM-14. Predominant Species for the An(IV) Actinides (Domski 2025a)

Species	% Contribution in GWB	% Contribution in ERDA-6
$Th(OH)_4$ (aq)	84.26	83.39
$Th(OH)_3CO_3^-$	15.74	16.61
Total % of Species Present	100	100

SOTERM-6.4.3 The Pentavalent Actinides: Np(V)

The only (V) actinide considered in the actinide source term conceptual model is Np(V), which exists as the neptunyl ion, NpO_2^+. The parameter values currently used for modeling An(V) solubility were originally described in Giambalvo (2002c) and updated in Domski (2023a). The formation reactions and associated stability constants for aqueous and solubility-limiting

species for Np(V), representing An(V), are provided in Table SOTERM-15 (see CRA-2026 Appendix GEOCHEM, Table GEOCHEM-20).

Table SOTERM-15. Solubility Constants and Formation Reactions of Np Species in the WIPP Model.

Np(V) Reactions	log K	Equation
Solid formation Reactions		
$NpO_2^+ + H_2O \leftrightarrows NpO_2OH(s, aged) + H^+$	-4.5164	SOTERM.80
$NpO_2^+ + H_2O \leftrightarrows NpO_2OH(s, am) + H^+$	-5.2165	SOTERM.81
$2Na^+ + 2NpO_2^+ + 2HCO_3^- + 7H_2O \leftrightarrows 2[NaNpO_2(CO_3)\cdot 3.5H_2O](s)$	1.5016	SOTERM.82
$3Na^+ + NpO_2^+ + 2HCO_3^- \leftrightarrows Na_3NpO_2(CO_3)_2(s) + 2H^+$	-6.4983	SOTERM.83
$K^+ + NpO_2^+ + HCO_3^{2-} \leftrightarrows KNpO_2(CO_3)(s) + H^+$	3.2646	SOTERM.84
$3K^+ + NpO_2^+ + 2HCO_3^- \leftrightarrows K_3NpO_2(CO_3)_2(s) + 2H^+$	-4.7477	SOTERM.85
Inorganic Aqueous Formation Reactions		
$NpO_2^+ + H_2O \leftrightarrows NpO_2OH(aq) + H^+$	-11.3084	SOTERM.86
$NpO_2^+ + 2H_2O \leftrightarrows NpO_2(OH)_2^- + 2H^+$	-23.5362	SOTERM.87
$NpO_2^+ + HCO_3^- \leftrightarrows NpO_2CO_3^- + H^+$	-5.3223	SOTERM.88
$NpO_2^+ + 2HCO_3^- \leftrightarrows NpO_2(CO_3)_2^{3-} + 2H^+$	6.40	SOTERM.89
$NpO_2^+ + 3HCO_3^- \leftrightarrows NpO_2(CO_3)_3^{5-} + 3H^+$	5.30	SOTERM.90
Organic Aqueous Formation Reactions		
$NpO_2^+ + Acetate^- \leftrightarrows NpO_2Acetate(aq)$	1.3737	SOTERM.91
$NpO_2^+ + Citrate^{3-} \leftrightarrows NpO_2Citrate^{2-}$	3.4969	SOTERM.92
$NpO_2^+ + EDTA^{4-} + 2H^+ \leftrightarrows NpO_2H_2EDTA^-$	20.8648	SOTERM.93
$NpO_2^+ + EDTA^{4-} + H^+ \leftrightarrows NpO_2HEDTA^{2-}$	15.5464	SOTERM.94
$NpO_2^+ + EDTA^{4-} \leftrightarrows NpO_2EDTA^{3-}$	8.5352	SOTERM.95
$NpO_2^+ + Lactate^- \leftrightarrows NpO_2Lactate(aq)$	1.9674	SOTERM.96
$NpO_2^+ + Oxalate^{2-} \leftrightarrows NpO_2Oxalate^-$	4.24	SOTERM.97

The predominant speciation of the An(V) actinides in the WIPP is given in Table SOTERM-16. The dominant species, based on current modeling assumptions, is the acetate complex, followed by the aquo species, the carbonato complex, and the oxalate complex. The EDTA complex is an insignificant contributor.

Table SOTERM-16. Predominant Speciation for the An(V) Actinides in the WIPP (Domski 2025a).

Species	% Contribution in GWB	% Contribution in ERDA-6
$NpO_2(Ac)$ (aq)	63.94	63.07
NpO_2^+ (aq)	20.34	19.24
$NpO_2CO_3^-$	7.48	10.02
NpO_2Ox^-	7.47	6.69
$NpO_2(OH)$ (aq)	0.45	0.55
Total % of Species Present	99.68	99.68

SOTERM-6.4.4 The Hexavalent Actinides: U(VI)

There are no solubilities calculated for U(VI), because a thermodynamic speciation and solubility model has not been implemented in the WIPP database. New data from Kutahyali Aslani (2024) build upon, and are consistent with, previous measurements by Hobart and Moore (1996) and Lucchini et al. (2010a, 2010b, 2013a, 2013b), collectively supporting a more representative value for U(VI) solubility. For the CRA-2026, the previous EPA-prescribed value of 1 mM (U.S. EPA 2006) has been replaced with an experimentally based solubility of 3.00×10^{-6} M (Kaplan et al. 2025; CRA-2026 Appendix SOTERM-3.5, Appendix PA-4.4).

SOTERM-6.5 Calculating the Actinide Source Term

The actinide source term is the sum of the dissolved and colloidal source terms. The dissolved source term requires calculations of actinide solubilities, and the colloidal source term requires the enhancement factors. The following sections outline the approach for calculating both terms. Additional detail can be found in Domski (2025a) and Appendix PA-4.4.

SOTERM-6.5.1 Actinide Solubilities

The oxidation state-specific actinide solubilities calculated for the CRA-2026 are summarized in Table SOTERM-17. The baseline solubility calculations were performed by Domski (2025a, 2025b), using the EQ3/6 Version 8.0a software package (Wolery 2013) and the WIPP thermodynamic database, DATA0.FM6 (Domski 2023a). Activity coefficients needed to calculate the solubilities are derived using the Pitzer model (Appendix GEOCHEM-4.1.2). For these calculations, GWB and ERDA-6 brines are equilibrated with the scaled organic ligand inventory, and actinide concentrations are set in equilibrium with the solubility-controlling phases of the

III, IV, and V actinide oxidation states [$Am(OH)_{3(am)}$ for An(III) in the initial step; $ThO_{2(am)}$ for An(IV); and $KNpO_2CO_3$ for An(V)]. These solutions with dissolved actinides are then reacted with MgO (brucite and hydromagnesite), iron (hibbingite) and lead (hydrocerussite) from waste containers and shielding, and the Salado minerals halite and anhydrite. In this step, calcite, $Am(OH)_{3(s)}$, and $FeEDTA^{2-}$ are suppressed, while iron citrate species are allowed.

For perspective, the calculated solubilities from two prior PA analyses are also tabulated. As shown in Table SOTERM-17, the calculated solubility of the III actinides has increased to ~1.45×10^{-5} M in the CRA-2026 PA. This is due to increases in the concentrations of organic ligands from changes in inventory and decreased brine volume. The expected solubility of the IV actinides ranges between 5.34×10^{-8} M and 5.63×10^{-8} M and is essentially unchanged from the CRA-2019 and independent of brine composition. The solubility of the V actinides has also increased since the CRA-2019, but not significantly. For the CRA-2026, U(VI) solubility is 3×10^{-6} M (Kaplan et al. 2025).

Uncertainty calculations for the An(III) and An(IV) solubility data were performed by Domski (2025b) and are discussed further in the CRA-2026, Appendix PA-4.4 and Appendix GEOCHEM-4.4. Uncertainties are not calculated for An(V) or used in PA, since releases do not affect long-term repository performance (Domski 2025b). An(VI) uncertainties were also not calculated, since there is no current model.

Table SOTERM-17. Actinide Baseline Solubilities Calculated for the CRA-2019 PA (Domski and Sisk-Scott 2019), the RPPCR PA (Domski 2023b), and the CRA-2026 PA (Domski 2025a; King 2025).

Actinide Oxidation State, and Brine	CRA-2019 PA (M)	RPPCR PA (M)	CRA-2026 PA (M)
III, GWB	1.63×10^{-7}	3.40×10^{-6}	1.45×10^{-5}
III, ERDA-6	1.78×10^{-7}	3.51×10^{-6}	1.44×10^{-5}
IV, GWB	5.45×10^{-8}	5.34×10^{-8}	5.34×10^{-8}
IV, ERDA-6	5.44×10^{-8}	5.73×10^{-8}	5.63×10^{-8}
V, GWB	4.02×10^{-7}	4.95×10^{-7}	9.75×10^{-7}
V, ERDA-6	1.20×10^{-6}	1.80×10^{-6}	4.01×10^{-6}

SOTERM-6.5.2 The Dissolved Actinide Source Term

The dissolved actinide source term is constructed from the baseline solubilities for each oxidation state in both brines. The sum of these concentrations is the dissolved actinide source term. In PA calculations, the uncertainty factor is sampled from the distribution specified in Domski (2025b) and applied to the baseline solubility for each oxidation state to derive the dissolved concentration (Appendix PA-4.3.2; King 2025):

$$\text{Dissolved} = \text{Baseline Solubility} \times 10^{\text{Sampled Solubility Uncertainty}}$$

Because there are no uncertainties for An(V) or (VI), the exponent takes on a value of 0.0 in those cases.

SOTERM-6.5.3 The Colloidal Actinide Source Term

The colloidal actinide source term is the sum of humic, microbial, mineral, and intrinsic colloid concentrations. The role of colloids in defining the actinide source term for the WIPP was introduced in Appendix SOTERM-3.5. The method of accounting for the effects of colloids on actinide concentrations, using colloidal enhancement parameters, is the same as that used in previous compliance applications. Parameters used for the CRA-2026 are found in Table SOTERM-4 and discussed in Kaplan et al. (2025) and Mariner (2025).

Mineral and intrinsic colloids are assumed to be present at a fixed concentration equal to their solubility. For mineral colloids, this value has been retained at 2.60×10^{-8} moles of mineral-bound actinide/L of each actinide element. Intrinsic colloid values (moles actinide associated with mobile intrinsic actinide colloids/L) are also fixed, but concentrations differ between elements. Both mineral and intrinsic colloid parameters are implemented in PA on an elemental basis.

Humic and microbial colloid contributions are selected as the minimum of two values: 1) the product of the dissolved concentration and the proportionality constant and 2) the maximum concentration associated with the colloid type. For example,

$$Microbial = \min(Dissolved * PROPMIC, CAPMIC)$$

There are no uncertainties calculated for the colloid enhancement parameters, because all values overestimate colloid contributions. This is due to conservative assumptions and the selection of bounding values (Appendix GEOCHEM-5.4).

SOTERM-6.5.4 The Actinide Source Term

The total mobile concentration of actinides is the sum of dissolved and colloidal contributions:

$$Total\ Mobile = Dissolved + (Humic + Microbial + Mineral + Intrinsic)$$

This source term is calculated for each actinide oxidation state in each brine and is shown in Table SOTERM-18 using the median value of the uncertainty distribution. For historical perspective, these values are presented alongside values from the CRA-2019 in Table SOTERM-19. Overall, An(III) values are higher for all three concentrations relative to the CRA-2019, An(IV) concentrations are generally lower or unchanged, and An(VI) values are lower due to the new SOLMOD6 value.

Table SOTERM-18. Actinide Solubility and Colloidal Contributions for the CRA-2026 (U.S. DOE 2026, Appendix PA-4.4)

An	Brine	Baseline Solubility[1] (mol/L)	Uncertainty Exponent[2] (-)	Dissolved (mol/L)	Mineral (mol/L)	Intrinsic (mol/L)	Humic (mol/L)	Microbial (mol/L)	Sum Colloidal (mol/L)	Total Mobile[3] (mol/L)
Am(III)	Salado (GWB)	1.45E-05	-2.76E-01	7.68E-06	2.60E-08	6.70E-07	2.30E-06	4.97E-07	3.50E-06	1.12E-05
Am(III)	Castile (ERDA-6)	1.44E-05	-2.76E-01	7.63E-06	2.60E-08	6.70E-07	2.29E-06	4.97E-07	3.48E-06	1.11E-05
Np(IV)	Salado (GWB)	5.34E-08	-9.47E-01	6.03E-09	2.60E-08	4.30E-08	1.21E-10	7.24E-08	1.42E-07	1.48E-07
Np(IV)	Castile (ERDA-6)	5.63E-08	-9.47E-01	6.36E-09	2.60E-08	4.30E-08	6.36E-11	7.63E-08	1.45E-07	1.52E-07
Np(V)	Salado (GWB)	9.75E-07	0.00E+00	9.75E-07	2.60E-08	4.30E-08	8.87E-10	1.52E-07	2.22E-07	1.20E-06
Np(V)	Castile (ERDA-6)	4.01E-06	0.00E+00	4.01E-06	2.60E-08	4.30E-08	2.97E-08	1.52E-07	2.51E-07	4.26E-06
Pu(III)	Salado (GWB)	1.45E-05	-2.76E-01	7.68E-06	2.60E-08	4.30E-08	2.30E-06	4.97E-07	2.87E-06	1.06E-05
Pu(III)	Castile (ERDA-6)	1.44E-05	-2.76E-01	7.63E-06	2.60E-08	4.30E-08	2.29E-06	4.97E-07	2.85E-06	1.05E-05
Pu(IV)	Salado (GWB)	5.34E-08	-9.47E-01	6.03E-09	2.60E-08	4.30E-08	1.21E-10	1.81E-09	7.09E-08	7.70E-08

[1] The baseline solubility is calculated using the minimum brine volume.
[2] The median distribution value is used for sampled parameters.
[3] Total Mobile = Dissolved + (Mineral + Intrinsic + Humic + Microbial).

An	Brine	Baseline Solubility[1] (mol/L)	Uncertainty Exponent[2] (-)	Dissolved (mol/L)	Mineral (mol/L)	Intrinsic (mol/L)	Humic (mol/L)	Microbial (mol/L)	Sum Colloidal (mol/L)	Total Mobile[3] (mol/L)
Pu(IV)	Castile (ERDA-6)	5.63E-08	-9.47E-01	6.36E-09	2.60E-08	4.30E-08	6.36E-11	1.91E-09	7.10E-08	7.73E-08
Th(IV)	Salado (GWB)	5.34E-08	-9.47E-01	6.03E-09	2.60E-08	4.80E-07	1.21E-10	1.87E-08	5.25E-07	5.31E-07
Th(IV)	Castile (ERDA-6)	5.63E-08	-9.47E-01	6.36E-09	2.60E-08	4.80E-07	6.36E-11	1.97E-08	5.26E-07	5.32E-07
U(IV)	Salado (GWB)	5.34E-08	-9.47E-01	6.03E-09	2.60E-08	1.40E-06	1.21E-10	1.27E-11	1.43E-06	1.43E-06
U(IV)	Castile (ERDA-6)	5.63E-08	-9.47E-01	6.36E-09	2.60E-08	1.40E-06	6.36E-11	1.34E-11	1.43E-06	1.43E-06
U(VI)	Salado (GWB)	3.00E-06	0.00E+00	3.00E-06	2.60E-08	1.40E-06	3.60E-07	6.30E-09	1.79E-06	4.79E-06
U(VI)	Castile (ERDA-6)	3.00E-06	0.00E+00	3.00E-06	2.60E-08	1.40E-06	1.53E-06	6.30E-09	2.96E-06	5.96E-06

[1]The baseline solubility is calculated using the minimum brine volume.
[2] The median distribution value is used for sampled parameters.
[3]Total Mobile = Dissolved + (Mineral + Intrinsic + Humic + Microbial).

Table SOTERM-19. Concentrations (M) of Dissolved, Colloidal, and Total Mobile Actinides Obtained Using Median Parameter Values for the CRA-2019 PA and CRA-2026 PA (King 2019; 2025).

Actinide Oxidation State and Brine	CRA-2019 PA	CRA-2026 PA
Pu(III), dissolved, Salado brine	3.62×10^{-7}	7.68×10^{-6}
Pu(III), colloidal, Salado brine	1.79×10^{-7}	2.87×10^{-6}
Pu(III), total mobile, Salado brine	5.41×10^{-7}	1.06×10^{-5}
Pu(III), dissolved, Castile brine	3.95×10^{-7}	7.63×10^{-6}
Pu(III), colloidal, Castile brine	1.86×10^{-7}	2.85×10^{-6}
Pu(III), total mobile, Castile brine	5.81×10^{-7}	1.05×10^{-5}
Am(III), dissolved, Salado brine	3.62×10^{-7}	7.68×10^{-6}
Am(III), colloidal, Salado brine	1.10×10^{-7}	3.50×10^{-6}
Am(III), total mobile, Salado brine	4.72×10^{-7}	1.12×10^{-5}
Am(III), dissolved, Castile brine	3.95×10^{-7}	7.63×10^{-6}
Am(III), colloidal, Castile brine	1.17×10^{-7}	3.48×10^{-6}
Am(III), total mobile, Castile brine	5.12×10^{-7}	1.11×10^{-5}
Th(IV), dissolved, Salado brine	4.33×10^{-8}	6.03×10^{-9}
Th(IV), colloidal, Salado brine	7.85×10^{-8}	5.25×10^{-7}
Th(IV), total mobile, Salado brine	1.22×10^{-7}	5.31×10^{-7}
Th(IV), dissolved, Castile brine	4.33×10^{-8}	6.36×10^{-9}
Th(IV), colloidal, Castile brine	7.85×10^{-8}	5.26×10^{-7}
Th(IV), total mobile, Castile brine	1.22×10^{-7}	5.32×10^{-7}
U(IV), dissolved, Salado brine	4.33×10^{-8}	6.03×10^{-9}
U(IV), colloidal, Salado brine	1.44×10^{-6}	1.43×10^{-6}

Actinide Oxidation State and Brine	CRA-2019 PA	CRA-2026 PA
U(IV), total mobile, Salado brine	1.48×10^{-6}	1.43×10^{-6}
U(IV), dissolved, Castile brine	4.33×10^{-8}	6.36×10^{-9}
U(IV), colloidal, Castile brine	1.44×10^{-6}	1.43×10^{-6}

SOTERM-7.0 REFERENCES

(*Indicates a reference that has not been previously submitted.)

Adam, N., K. Hinz, X. Gaona, P.J. Panak, and M. Altmaier. 2021. Impact of Selected Cement Additives and Model Compounds on the Solubility of Nd(III), Th(IV) and U(VI): Screening Experiments in Alkaline NaCl, $MgCl_2$ and $CaCl_2$ Solutions at Elevated Ionic Strength. Radiochim. Acta 109: 431–443. *

Allen, P.G., J.J. Bucher, D.K. Shuh, N.M. Edelstein, and T. Reich. 1997. Investigation of Aquo and Chloro Complexes of UO_2^{2+}, NpO_2^{+}, Np^{4+}, and Pu^{3+} by X-Ray Absorption Fine Structure Spectroscopy. Inorg. Chem. 36: 4676–4683. *

Al Mahamid, I., K.A. Becraft, N.L. Hakem, R.C. Gatti, and H. Nitsche. 1996. Stability of Various Plutonium Valence States in the Presence of NTA and EDTA. Radiochim. Acta 74: 129-134. *

Al Mahamid, I. A., C.F. Novak, K.A Becraft, S.A. Carpenter, and N. Hakem. 1998. Solubility of Np(V) in K-Cl-CO_3 and Na- K-Cl-CO_3 Solutions to High Concentrations: Measurements and Thermodynamic Model Predictions. Radiochim. Acta. 81: 93-101. *

Altmaier, M., V. Neck, and T. Fanghänel. 2004. Solubility and Colloid Formation of Th(IV) in Concentrated NaCl and $MgCl_2$ Solutions. Radiochim. Acta 92: 537–543.

Altmaier, M., V. Neck, R. Müller, and T. Fanghänel. 2005. Solubility of $ThO_2{\cdot}xH_2O$(am) in Carbonate Solution and the Formation of Ternary Th(IV) Hydroxide-Carbonate Complexes. Radiochim. Acta 93: 83-92.

Altmaier, M., V. Neck, and T. Fanghänel. 2008. Solubility of Zr(IV), Th(IV) and Pu(IV) Hydrous Oxides in $CaCl_2$ Solutions and the Formation of Ternary Ca-M(IV)-OH Complexes. Radiochim. Acta 96: 541-550.

Altmaier, M., V. Neck, J. Lützenkirchen, and T. Fanghänel. 2009. Solubility of Plutonium in $MgCl_2$ and $CaCl_2$ Solutions in Contact with Metallic Iron. Radiochim. Acta 97: 187-192.

Altmaier, M., E. Yalçıntaş, X. Gaona, V. Neck, R. Müller, M. Schlieker, and T. Fanghänel. 2017a. Solubility of U(VI) in Chloride Solutions I: the Stable Oxides/Hydroxides in NaCl Systems, Solubility Products, Hydrolysis Constants and SIT Coefficients. J. Chem. Thermodyn. 114: 2-13.

Altmaier, M., D. Fellhauer, X. Gaona, and E. Yalçıntaş . 2017b. Assessment of Np(IV) and U(IV) as Improved Analogs for Pu(IV) in High Ionic-Strength Brine Systems. KIT/INE Report, Karlsruhe, Germany.

Azam, T., I. Ali, X. Chen, and I. Iqbal. 2024. Bacteria were Unable to Tolerate the Radionuclides, while the Halophilic Fungi Tolerated and Efficiently Remediated Them. Int. J. Env. Sci. Tech. 21: 8105-8112. *

Bader, M., A. Rossberg, R. Steudtner, B. Drobot, K. Großmann, M. Schmidt, N. Musat, T. Stumpf, A. Ikeda-Ohno, and A. Cherkouk. 2018. Impact of Haloarchaea on Speciation of Uranium—a Multi-spectroscopic Approach. Environ. Sci. Technol. 52: 12895-12904. *

Balboni, E., K.F. Smith, L.M. Moreau, T.T. Li, M. Maloubier, C.H. Booth, A.B. Kersting, and M. Zavarin. 2020. Transformation of Ferrihydrite to Goethite and the Fate of Plutonium. ACS Earth Space Chem. 4: 1993-2006. *

Barnhart, B.J., E.W. Campbell, E. Martinez, D.E. Caldwell, and R. Hallett. 1980. Potential Microbial Impact on Transuranic Wastes under Conditions Expected in the Waste Isolation Pilot Plant (WIPP). Los Alamos National Laboratory. Los Alamos, NM. LA-8297-PR.

Beam, J. 2022. Actinide(III/IV)-Silica Colloids in the WIPP. Los Alamos National Laboratory. Carlsbad, NM. LCO-ACP-27. *

Beam, J. 2023. Plutonium Oxidation State Distribution under WIPP Relevant Conditions. Los Alamos National Laboratory. Carlsbad NM. Report LCO-ACP-31, Revision 1. *

Belilla, J., D. Moreira, L. Jardillier, G. Reboul, K. Benzerara, J.M. López-Garcia, P. Bertolino, A.I. López-Archilla, and P. López-Garcia. 2019. Hyperdiverse Archaea Near Life Limits at the Polyextreme Geothermal Dallol Area. Nat. Ecol. Evol. 3: 1552-1561. *

Bender, W.M. and U. Becker. 2020. Resolving the Kinetics of Individual Aqueous Reaction Steps of Actinyl (AnO_2^+ and AnO_2^{2+}; An = U, Np, and Pu) Tricarbonate Complexes with Ferrous Iron and Hydrogen Sulfide from First Principles. Radiochim. Acta 108: 165–184. *

Berlemont, R. and A.C. Martiny. 2013. Phylogenetic Distribution of Potential Cellulases in Bacteria. Appl. Environ. Microb. 79: 1545-1554. *

Bonin, L., G. Cote, and P. Moisy. 2008. Speciation of An(IV) (Pu, Np, U and Th) in Citrate Media, Radiochim. Acta 96: 145–152.

Borkowski, M., J.-F. Lucchini, M.K. Richmann, and D.T. Reed. 2009. Actinide (III) Solubility in WIPP Brine: Data Summary and Recommendations. Report LCO-ACP-08. Los Alamos National Laboratory. Carlsbad, NM. Report LCO-ACP-08, Revision 0. LA-UR-10-14360.

Borkowski, M., M.K. Richmann, D.T. Reed, and Y.-L. Xiong. 2010. Complexation of Nd(III) with Tetraborate Ion and its Effect on Actinide(III) Solubility in WIPP Brine. Radiochim. Acta 98: 577–582.

Borkowski, M., M.K. Richmann, and J.-F. Lucchini. 2012. Solubility of An(IV) in WIPP Brine: Thorium Analog Studies in WIPP Simulated Brine. Los Alamos National Laboratory. Carlsbad, NM. LCO-ACP-17. LA-UR-12-24417.

Brandt, K.K., F. Vester, A.N. Jensen, and K. Ingvorsen. 2001. Sulfate Reduction Dynamics and Enumeration of Sulfate-Reducing Bacteria in Hypersaline Sediments of the Great Salt Lake (Utah, USA). Microb. Ecol. 41: 1-11.

Brendebach, B., M. Altmaier, J. Rothe, V. Neck, and M. Denecke. 2007. EXAFS Study of Aqueous Zr(IV) and Th(IV) Complexes in Alkaline $CaCl_2$ Solutions: $Ca_3[Zr(OH)_6]^{4+}$ and $Ca_4[Th(OH)_8]^{4+}$. Inorg. Chem. 46: 6804–6810.

Brunell, S. 2025. Memo to Records Center. Subject: Update to CRA-2026 PA Input Parameters Due to Revised WIPP Repository Dimensions. April 7, 2025. Sandia National Laboratories. Carlsbad, NM. EIMS-0004799007. *

Carré, L., D. Gonzalez, E. Girard, and B. Franzetti. 2023. Effects of Chaotropic Salts on Global Proteome Stability in Halophilic Archaea: Implications for Life Signatures on Mars. Environ. Microbiol. 25: 2216-2230. *

Cevirim-Papaioannou, N., E. Yalçıntaş , X. Gaona, K. Dardenne, M. Altmaier, and M.H. Geckeis. 2018a. Redox Chemistry of Uranium in Reducing, Dilute to Concentrated NaCl Solutions. Appl. Geochem. 98: 286-300.

Cevirim-Papaioannou, N., E. Yalçıntaş, X. Gaona, M. Altmaier, and H. Geckeis. 2018b. Solubility of U(VI) in chloride solutions. II. The stable Oxides/Hydroxides in Alkaline KCl Solutions: Thermodynamic Description and Relevance in Cementitious Systems. Appl. Geochem. 98: 237–246. *

Chapon, V., L. Piette, M.-H. Vesvres, F. Coppin, C. Le Marrec, R. Christen, N. Theodorakopoulos, L. Février, S. Levchuk, A. Martin-Garin, C. Berthomieu, and C. Sergeant. 2012. Microbial Diversity in Contaminated Soils along the T22 Trench of the Chernobyl Experimental Platform. Appl. Geochem. 27: 1375-1383. *

Chen, C., X. Zhang, T. Jiang, M. Li, Y. Peng, and X. Liu. 2021. Removal of Uranium(VI) from Aqueous Solution by $Mg(OH)_2$-Coated Nanoscale Zero-Valent Iron: Reactivity and Mechanism. J. Environ. Chem. Eng. 9: 104706. *

Cho, H.-R., Y.-S. Youn, E.C. Jung, and W. Cha. 2016. Hydrolysis of Trivalent Plutonium and Solubility of $Pu(OH)_3$(am) under Electrolytic Reducing Conditions. Dalton T. 45: 19449-19457.

Cho, S., H.-K. Kim, T-H. Kim, W. Cha, and H.-R. Cho. 2022. Thermodynamic Studies on the Hydrolysis of Trivalent Plutonium and Solubility of $Pu(OH)_3$(am). Inorg. Chem. 61: 12643-12651.*

Choppin, G.R. 1983. Solution Chemistry of the Actinides. Radiochim. Acta 32: 43-53.

Clark, D.L., D.E. Hobart, and M.P. Neu. 1995. Actinide Carbonate Complexes and their Importance in Actinide Environmental Chemistry. Chem. Rev. 95: 25-48.

Clark, D.L. and C.D. Tait. 1996. Monthly reports under Sandia National Laboratories Contract AP2274. Sandia WIPP Central File A: WBS 1.1.10.1.1. WPO 31106.

Clark, D.L., S.S. Hecker, G.D. Jarvinen, and M.P. Neu. 2006. Plutonium. In: The Chemistry of the Actinide and Transactinide Elements, 3rd ed. Morss, L.R., N.M. Edelstein, and J. Fuger, eds. Springer: Dordrecht, Netherlands. pp. 813-1264. *

Clayton, D.J. 2008. Memorandum to Larry Brush. Subject: Update to the Calculation of the Minimum Brine Volume for a Direct Brine Release. April 2, 2008. ERMS 548522. Sandia National Laboratories. Carlsbad, NM.

Cobos, J. E. and E.G. Søgaard. 2022. Chelating Agents for Diluted Geothermal Brine Reinjection. Geotherm. Energy 10: 17. *

Colàs, E., D. García, and L. Duro. 2020. Systematic Calculation of Pu Pourbaix Diagrams: Modelling Support for the LANL ACRSP Team. Amphos21, Barcelona, and Los Alamos National Laboratory. Carlsbad, NM. LA-UR-20-26859. *

Comins, M.B., U. Kaplan, J. Beam, A. Navarrette, and A.E. Hixon. 2024a. Plutonium Speciation and Oxidation State Distributions in the Presence of Citrate. Environ. Sci. Technol. 58: 15766-15778. *

Comins, M.B., C. Shang, R. Polly, A. Skerencak-Frech, M. Altmaier, A.E. Hixon, and X. Gaona. 2024b. Cm(III) Speciation in the Presence of Citrate from Neutral to Hyperalkaline Conditions and the Effect of Calcium. Chemosphere 364: 143233. *

Conradson, S.D., I. Al Mahamid, D.L. Clark, N. Hess, E.A. Hudson, M.P. Neu, P.D. Palmer, W.H. Runde, and C.D. Tait. 1998. Oxidation State Determination of Plutonium Aquo Ions Using X-Ray Absorption Spectroscopy. Polyhedron 17: 599–602.

Cray, J.A., J.T. Russell, D.J. Timson, R.S. Singhal, and J.E. Hallsworth. 2013. A Universal Measure of Chaotropicity and Kosmotropicity. Environ. Microbiol. 15: 287-296. *

Cycil, L.M., S. DasSarma, W. Pecher, R. McDonald, M. Abdulsalam, and F. Hasan. 2020. Metagenomic Insights into the Diversity of Halophilic Microorganisms Indigenous to the Karak Salt Mine, Pakistan. Front. Microbiol. 11: 1567. *

Day, B. 2019. Reassessment of Need and Parameter Justification for Modeling Gas Generation due to Radiolysis of Brine and Cellulose/Plastic/Rubber in WIPP for CRA-2019. Sandia National Laboratories. Carlsbad, NM. ERMS 570873.

Deal, D.E., R.J. Abitz, D.S. Belski, J.B. Case, M.E. Crawley, C.A. Givens, P.P. James Lipponer, D.J. Milligan, J. Myers, D.W. Powers, and M.A. Valdivia. 1995. Brine Sampling and Evaluation Program 1992-1993 Report and Summary of BSEP Data Since 1982. Report DOE-WIPP 94-011. Westinghouse Electric Corporation. Carlsbad, NM. *

Delegard, C.H. and G.S. Barney. 1983. Effects of Hanford High-Level Waste Components on Sorption of Cobalt, Strontium, Neptunium, Plutonium, and Americium on Hanford Sediments. Rockwell Hanford Operations. Richland, Washington. RHO-RE-ST-1 P. *

Deng, T., G. Chi, A.E. Williams-Jones, Z. Li, Y. Wang, D. Xu, and Z. Wang. 2023. Re-evaluation of Equilibrium Relationships Involving U^{6+}/U^{4+} and Fe^{3+}/ Fe^{2+} in Hydrothermal Fluids and Their Implications for U Mineralization. Chem. Geol. 625: 121432. *

Diaz-Arocas, P. and B. Grambow. 1998. Solid-Liquid Phase Equilibria of U(VI) in NaCl Solutions. Geochim. Cosmochim. Ac. 62: 245–263.

DiBlasi, N.A., E. Yalçıntaş, F.E. Stanley, D.T. Reed, and A.E. Hixon. 2021a. Influence of Ethylenediaminetetraacetic Acid on the Long-term Oxidation State Distribution of Plutonium. Chemosphere 274: 129741-129751. *

DiBlasi, N.A., A.G. Tasi, X. Gaona, D. Fellhauer, K. Dardenne, J. Rothe, D.T. Reed, A.E. Hixon, and M. Altmaier. 2021b. Impact of Ca(II) on the Aqueous Speciation, Redox Behavior, and Environmental Mobility of Pu(IV) in the Presence of EDTA. J. Sci. Tot. Environ. 783:146993-147005. *

DiBlasi, N.A., A.G. Tasi, M. Trumm, A. Schnurr, X. Gaona, D. Fellhauer, K. Dardenne, J. Rothe, D.T. Reed, A.E. Hixon, and M. Altmaier. 2022. Pu(III) and Cm(III) in the Presence of EDTA: Aqueous Speciation, Redox Behavior, and the Impact of Ca(II). RSC Adv. 12: 9478-9493. *

Ding, M., J.L. Conca, C. den Auwer, R.I. Gabitov, N.J. Hess, P. Paviet-Hartmann, P.D. Palmer, V. LoPresti, and S.D. Conradson. 2006. Chemical Speciation of Heterogeneously Reduced Pu in Synthetic Brines. Radiochim. Acta 94: 249-259. *

Docherty, P. 2024. Memorandum to WIPP Records Center. Subject: Update to WIPP PA parameter DBRMINBV. Sandia National Laboratories; Carlsbad, NM. ERMS 581499 *

Domski, P.S. and C. Sisk-Scott. 2019. Prediction of Baseline Actinide Solubilities for CRA-2019 with an Updated EQ3/6 Pitzer Thermodynamic Database, DATA0.FM4. Sandia National Laboratories Report. ERMS 571178.

Domski, P.S. 2023a. An Update to the WIPP EQ3/6 Database DATA0.FM1 with the Creation of DATA0.FM6. Sandia National Laboratories. ERMS 579370. *

Domski, P.S. 2023b. Prediction of Baseline Actinide Solubilities for the Replacement Panels Planned Change Request (RPPCR) Performance Assessment. Sandia National Laboratories. Albuquerque, NM. EIMS-57903.*

Domski, P.S. 2025a. Prediction of Baseline Actinide Solubilities for the 2026 WIPP Compliance Recertification Application Performance Assessment Interim-State Analysis (CRA-2026 IS). Sandia National Laboratories. Albuquerque, NM. EIMS-0004838025. *

Domski, P.S. 2025b. Uncertainty Analysis of Actinide Solubilities for the 2026 Compliance Recertification Application (CRA-2026). Sandia National Laboratories. Albuquerque, NM. EIMS-0004446576. *

Dumas, T., D. Fellhauer, D. Schild, X. Gaona, M. Altmaier, and A.C. Scheinost. 2019. Plutonium Retention Mechanisms by Magnetite under Anoxic Conditions: Entrapment versus Sorption. ACS Earth Space Chem. 3: 2197-2206. *

Dumpala, R., M. Sahu, B. Nagar, V. Raut, N. Raje, N. Rawat, J. Subbiah, M. Saxena, and B. Tomar. 2021. Accountancy for Intrinsic Colloids on Thorium Solubility: The Fractionation of Soluble Species and the Characterization of Solubility Limiting Phase. Chemosphere 269: 129327. DOI: org/10.1016/j.chemosphere.2020.129327. *

Elcheninov, A.G., Y.A. Ugolkov, I.M. Elizarov, A.A. Klyukina, I.V. Kublanov, and D.Y. Sorokin. 2023. Cellulose Metabolism in Halo(natrono)archaea: a Comparative Genomics Study. Front. Microbiol. 14: 1112247. *

Emmerich, M., A. Bhansali, T. Losekann-Behrens, C. Schroder, A. Kappler, and S. Behrens. 2012. Abundance, Distribution, and Activity of Fe(II)-Oxidizing and Fe(III)-Reducing Microorganisms in Hypersaline Sediments of Lake Kasin, Southern Russia. Appl. Environ. Microbiol. 78: 4386-4399.

Eriksen, T.E., P. Ndamamba, D. Cui, J. Bruno, M. Caceci, and K. Spahiu. 1993. Stockholm: Svensk Kärnbränsleforsorjning AB. SKB Technical Report 93-18.

Fanghänel, Th., V. Neck, and J.I. Kim. 1995. Thermodynamics of Neptunium(V) in Concentrated Salt Solutions: II. Ion Interaction (Pitzer) Parameters for Np(V) Hydrolysis Species and Carbonate Complexes. Radiochim. Acta, vol. 69: 169–76.

Fanghänel, T. and V. Neck. 2002. Aquatic Chemistry and Solubility Phenomena of Actinide Oxides/hydroxides. Pure Appl. Chem. 74: 1895–1907.

Favela Morales, D. and J.-F. Lucchini. 2024. Radiolytic Degradation of Organics—Progress Report. Los Alamos National Laboratory. Carlsbad, NM. LCO-ACP-39, Revision 0. *

Felipe-Sotelo, M., M. Edgar, T. Beattie, P. Warwick, N.D.M. Evans, and D. Read. 2015. Effect of Anthropogenic Organic Complexants on the Solubility of Ni, Th, U(IV) and U(VI). J. Hazard. Mater. 300: 553–560.

Felipe-Sotelo, M., J. Hinchliff, L.P. Field, A.E. Milodowski, O. Preedy, and D. Read. 2017. Retardation of Uranium and Thorium by a Cementitious Backfill Developed for Radioactive Waste Disposal. Chemosphere 179: 127-138.

Fellhauer, D., J. Rothe, M. Altmaier, V. Neck, J. Runke, T. Wiss, and T. Fanghänel. 2016. Np(V) Solubility, Speciation and Solid Phase Formation in Alkaline $CaCl_2$ Solutions. Part I: Experimental Results. Radiochim. Acta 104: 355-379.

Felmy, A.R., D. Rai, J.A.S. Schramke, and J.L. Ryan. 1989. The Solubility of Plutonium Hydroxide in Dilute Solution and in High-Ionic Strength Chloride Brines. Radiochim. Acta 48: 29–35.

Felmy, A.R., D. Rai, and R.W. Fulton. 1990. The Solubility of $AmOHCO_3$(cr) and the Aqueous Thermodynamics of the System Na^+-Am^{3+}-HCO_3^--CO_3^{2-}-OH^--H_2O. Radiochim. Acta 50: 193–204.

Ferguson, B.O., L.C. Murdoch, M. Trumm, F. Liu, A.M. Rao, and B.A. Powell. 2022. Mechanisms and Kinetics of Citrate-Promoted Dissolution of a Uranyl Phosphate Mineral. Geochim. Cosmochim. Ac. 318: 247–262. *

Fiegel, V., C. Berthon, A. Costagliola, G. Blain, J. Vandenborre, J. Vermeulen, G. Saint-Louis, L. Guerin, T. Sauvage, M. Fattahi-Vanani, L. Venault, and L. Berthon. 2019. Alpha Radiolysis of DOTA Ligand in Aqueous Solutions with Helium Ion Beams. Radiat. Phys. Chem. 165: 108409. *

Francis, A.J. and J.B. Gillow. 1994. Effects of Microbial Processes on Gas Generation under Expected Waste Isolation Pilot Plant Repository Conditions. Sandia National Laboratories. Albuquerque, NM. SAND93-7036.

Francis, A.J., J.B. Gillow, and M.R. Giles. 1997. Microbial Gas Generation under Expected Waste Isolation Pilot Plant Repository Conditions. Sandia National Laboratories. Albuquerque, NM. SAND96-2582.

Francis, A.J., C.J. Dodge, and J.B. Gillow. 2006. Biotransformation of Plutonium Complexed with Citric Acid. Radiochim. Acta 94: 731-737.

Francis, A.J. and C.J. Dodge. 2008. Bioreduction of Uranium (VI) Complexed with Citric Acid by *Clostridia* Affects its Structure and Solubility. Environ. Sci. Technol. 42: 8277–8282.

Fredrickson, J.K., J.K. Zachara, D.L. Balkwill, D. Kennedy, S.W. Li, H.M. Kostandarithes, M.J. Daly, M.F. Romine, and F.J. Brockman. 2004. Geomicrobiology of High-Level Nuclear Waste-Contaminated Vadose Sediments at the Hanford Site, Washington State. Appl. Environ. Microb. 70: 4230-4241.

Fujiwara, K., H. Yamana, T. Fujii, and H. Moriyama. 2002. Solubility Product of Plutonium Hydrous Oxide and its Ionic Strength Dependence. Radiochim. Acta 90: 857-861.

Giambalvo, E.R. 2002a. Memorandum to L.H. Brush. Subject: Recommended Parameter Values for Modeling An(III) Solubility in WIPP Brines. 25 July 2002. Sandia National Laboratories. Carlsbad, NM. ERMS 522982.

Giambalvo, E.R. 2002b. Memorandum to L.H. Brush. Subject: Recommended Parameter Values for Modeling An(IV) Solubility in WIPP Brines. 26 July 2002. Sandia National Laboratories. Carlsbad, NM. ERMS 522986.

Giambalvo, E.R. 2002c. Memorandum to L.H. Brush. Subject: Recommended Parameter Values for Modeling An(V) Solubility in WIPP Brines. 26 July 2002. Sandia National Laboratories. Carlsbad, NM. ERMS 522990.

Gillow, J.B. and A.J. Francis. 2006. Microbial Gas Generation under Expected Waste Isolation Pilot Plant Repository Conditions: Final Report. Sandia National Laboratories. Albuquerque, NM. BNL-96148-2011-IR.

Grabner, M., E. Wächter, K. Nicolussi, M. Bolka, T. Sormaz, P. Steier, E.M. Wild, F.E. Barth, A. Kern, J. Rudorfer, K. Kowarik, T. Stöllner, and H. Reschreiter. 2021. Prehistoric Salt Mining in Hallstatt, Austria. New Chronologies Out of Small Wooden Fragments. Dendrochonologia 66: 125814. *

Grambow, B., R. Müller, D. Schild, and X. Gaona. 2023. Solids, Colloids, and the Hydrolysis of Tetravalent Uranium in Chloride Media. Front. Nucl. Eng. 2:1308064. *

Gregory, S.P., J.R.M. Mackie, and M.J. Barnett. 2024. Radioactive Waste Microbiology: Predicting Microbial Survival and Activity in Changing Extreme Environments. FEMS Microbiol. Rev. 48: fuae001. *

Hallsworth, J.E., M.M. Yakimov, P.N. Golyshin, J.L.M. Gillion, G. D'Auria, F. de Lima Alves, V. La Cono, M. Genovese, B.A. McKew, S.L. Hayes, G. Harris, L. Giuliano, K.N. Timmis, and T.J. McGenity. 2007. Limits of Life in $MgCl_2$-Containing Environments: Chaotropicity Defines the Window. Environ. Microbiol. 9: 801-813.

Haschke, J.M., T.H. Allen, and L.A. Morales. 2000. Reaction of Plutonium Dioxide with Water: Formation and Properties of PuO_{2+x}. Science 287: 285–287.

Hilpmann, S., M. Bader, R. Steudtner, K. Müller, T. Stumpf, and A. Cherkouk. 2022. Microscopi and Spectroscopic Bioassociation Study of Uranium(VI) with an Archaeal *Halobacterium* isolate. PLoS ONE 17: e0262275. *

Hinz, K., M. Altmaier, X. Gaona, T. Rabung, D. Schild, M. Richmann, D. Reed, E. Alekseev, and H. Geckeis. 2015. Interaction of Nd(III) and Cm(III) with Borate in Dilute to Concentrated Alkaline NaCl, $MgCl_2$, and $CaCl_2$ Solutions: Solubility and TRLFS Studies. New J. Chem. 39 (2): 849-859.

Hinz, K., D. Fellhauer, X. Gaona, M. Vespa, K. Dardenne, D. Schild, T. Yokosawa, M.A. Silver, D. T. Reed, T.E. Albrecht-Schmitt, M. Altmaier, and H. Geckeis. 2020. Interaction of Np(V) with Borate in Alkaline, Dilute-to-Concentrated, NaCl and $MgCl_2$ Solutions. Dalton T. 49: 1570-1581.*

Hobart, D.E., K. Samhoun, and J.R. Peterson. 1982. Spectroelectrochemical Studies of the Actinides: Stabilization of Americium (IV) in Aqueous Carbonate Solution. Radiochim. Acta 31: 139–145.

Hobart, D.E. and R.C. Moore. 1996. Analysis of Uranium (VI) Solubility Data for WIPP Performance Assessment. May 28, 1996. Unpublished report. Sandia National Laboratories.

Albuquerque, NM. AP-028.Hoyos-Hernandez, C., C. Courbert, C. Simonucci, S. David, T.M. Vogel, and C. Larose. 2019. Community Structure and Functional Genes in Radionuclide Contaminated Soils in Chernobyl and Fukushima. FEMS Microbiol. Lett. 366: fnz180. *

Hua, Y., W. Wang, N. Hu, T. Gu, L. Ling, and W. Zhang. 2021. Enrichment of Uranium from Wastewater with Nanoscale Zero-Valent Iron (nZVI). Environ. Sci.: Nano, 8, 666–674. *

Icopini, G.A., H. Boukhalfa, and M.P. Neu. 2007. Biological Reduction of Np(V) and Np(V) Citrate by Metal-Reducing Bacteria. Environ. Sci. Technol. 41: 2764–2769.

Ioannis, I., I. Anastopoulos, and I. Pashalidis. 2022. Neptunium Interaction with Microplastics in Aqueous Solutions. J. Mol. Liq. 356: 119056.*Kaplan, U. 2022. Neptunium (V) Solubility in the Presence and Absence of WIPP Relevant Ligands. Los Alamos National Laboratory. Carlsbad, NM. Report LCO-ACP-30, Revision 0. LA-UR-22-33109. *

Kaplan, U., J. Swanson, and C. Kutahyali Aslani. 2025. LANL ACRSP Parameter Recommendations for CRA-2026 Performance Assessment. Los Alamos National Laboratory. Carlsbad, NM. Report LCO-ACP-41, Revision 1. *

Kaplan, U. 2025a. Np(V) Solubility in WIPP Brine: Presence and Absence of WIPP-Relevant Organic and Inorganic Ligands. Los Alamos National Laboratory. Carlsbad, NM. Report LCO-ACP-42, Revision 0. *

Kaplan, U. 2025b. Plutonium Oxidation State Distribution in the Presence of WIPP-Relevant Organics and Iron Corrosion Products. Los Alamos National Laboratory. Carlsbad, NM. Report LCO-ACP-38, Revision 1. *

Karray, F., M. Ben Abdallah, N. Kallel, M. Hamza, M. Fakhfakh, and S. Sayadi. 2018. Extracellular Hydrolytic Enzymes Produced by Halophilic Bacteria and Archaea Isolated from Hypersaline Lake. Mol. Biol. Rep. 45: 1297-1309. *

Kasirajan, L. and J.A. Maupin-Furlow. 2020. Halophilic Archaea and Their Potential to Generate Renewable Fuels and Chemicals. Biotechnol. Bioeng. 118: 1066-1090. *

Kaszuba, J.P. and W.H. Runde. 1999. The Aqueous Geochemistry of neptunium: Dynamic control of soluble concentrations with applications to nuclear waste disposal. Environ. Sci. Technol., 33, 4427. *

Kienzler, B., P. Vejmelka, H.-J. Herbert, H. Meyer, and C. Altenhein-Haese. 2000. Long-Term Leaching Experiments of Full-Scale Cemented Waste Forms: Experiments and Modeling. Nucl. Technol. 129: 101-118. *

Kim, H-K. and H-R. Cho. 2022. Evaluation of Americium Solubility in Synthesized Groundwater: Geochemical Modeling and Experimental Study at Over-Saturation Conditions. J. Nucl. Fuel Cycle Waste Technol. 20: 399-410. https://doi.org/10.7733/jnfcwt.2022.041 *

Kim, H-K., H-R. Cho., and W. Cha. 2024. Solubility of Trivalent Am, Eu, and Sm in the Synthetic KAERI Underground Research Tunnel Groundwater. J. Nucl. Fuel Cycle Waste Technol. 22: 237-249. *

Kim, J.I., M. Bernkopf, C. Lierse, and F. Koppold. 1984. Hydrolysis Reactions of Am(III) and Pu(VI) Ions in Near-Neutral Solutions. In: Geochemical Behavior of Disposed Radioactive Waste (pp. 115–34). G.S. Barney, J.D. Navratill, and W.W. Schultz, eds. Washington, DC: American Chemical Society. ACS Sym. Ser. No. 246.

Kim, J.I., C. Apostolidis, G. Buckau, K. Büppelmann, B. Kanellakopulos, C. Lierse, S. Magirius, R. Stumpe, I. Hedler, C. Rahner, and W. Stoewer. 1985. Chemisches Verhalten von Np, Pu und Am in Verschiedenen Konzentrierten Salzloesunger = Chemical Behaviour of Np, Pu, and Am in Various Brine Solutions. RCM 01085. Munich, Germany: Institut für Radiochemie der Technische Universitaet Muenchen. (Available from National Technical Information Service, 555 Port Royal Road, Springfield, VA 22161, 703/487-4650 as DE857 2334.)

Kim, J.I. 2006. Significance of Actinide Chemistry for the Longterm Safety of Waste Disposal. Nucl. Eng. Technol. 38: 459-482. *

Kim, S.S., M.H. Baik, J.W. Choi, H.S. Shin, and J.I. Yun. 2010. The Dissolution of ThO_2(cr) in Carbonate Solutions and a Granitic Groundwater. J. Radioanal. Nucl. Ch. 286: 91-97.Kim, Y., M.C. Marcano, S. Kim, and U. Becker. 2021. Reduction of Uranyl and Uranyl-Organic Complexes Mediated by Magnetite and Ilmenite: A Combined Electrochemical AFM and DFT Study. Geochim. Cosmochim. Ac. 293: 127–141. *

King, S. 2019. Actinide Solubility and Colloidal Contributions for CRA-2019 for Appendix SOTERM. August 26, 2019. Carlsbad, NM: Sandia National Laboratories. ERMS 571778.

King, S. 2025. Memorandum to WIPP Records Center. Subject: Actinide Solubilities and Colloidal Source Terms in the CRA-2026. July 23, 2025. Sandia National Laboratories. Carlsbad, NM. EIMS-0004842422. *

Kirsch, R., D. Fellhauer, M. Altmaier, V. Neck, A. Rossberg, T. Fanghänel, L. Charlet, and A.C. Scheinost. 2011. Oxidation State and Local Structure of Plutonium Reacted with Magnetite, Mackinawite, and Chukanovite. Environ. Sci. Technol. 45: 7267-7274. *

Kjeldsen, K.U., A. Loy, T.F. Jakobsen, T.R. Thomsen, M. Wagner, and K. Ingvorsen. 2007. Diversity of Sulfate-Reducing Bacteria from an Extreme Hypersaline Sediment, Great Salt Lake (Utah). FEMS Microbiol. Ecol. 60: 287-298.

Kjeldsen, K.U., T.F. Jakobsen, J. Glastrup, and K. Ingvorsen. 2010. *Desulfosalsimonas propionicica gen*. nov., sp. nov., a Halophilic, Sulfate-Reducing Member of the Family *Desulfobacteriaceae* Isolated from a Salt-Lake Sediment. Int. J. Syst. Evol. Micr. 60: 1060-1065.

Klempay, B., N. Arandia-Gorostidi, A.E. Dekas, D.H. Bartlett, C.E. Carr, P.T. Doran, A. Dutta, N. Erazo, L.A. Fisher, J.B. Glass, A. Pontefract, S.M. Som, J.M. Wilson, B.E. Schmidt, and J.S. Bowman. 2021. Microbial Diversity and Activity in Southern California Salterns and Bitterns: Analogues for Remnant Ocean Worlds. Environ. Microbiol. 23: 3825-3839. *

Kobayashi, T., T. Sasaki, and A. Kitamura. 2019. Thermodynamic Interpretation of Uranium(IV/VI) Solubility in the Presence of α-Isosaccharinic Acid. J. Chem. Thermodyn. 138: 151–158. *

Kobayashi, T., D. Fellhauer, and T. Sasaki. 2021. Solubility of PuO_2(am,hyd) and the Formation of Pu(IV) Carbonate Complexes in Carbonate Solutions containing 0.1-5.0 mol.dm^{-3} $NaNO_3$. J. Sol. Chem. 50: 443-457. *

Kulp, T.R., S. Han, C.W. Saltikov, B.D. Lanoil, Z. Zargar, and R.S. Oremland. 2007. Effects of Imposed Salinity Gradients on Dissimilatory Arsenate Reduction, Sulfate Reduction, and Other Microbial Processes in Sediments from Two California Soda Lakes. Appl. Environ. Microb. 73: 5130-5137.

Kutahyali Aslani, C. 2022. Solubility of $An(OH)_{3_am}$ and $An(OH)_{3_cr}$ in the presence of Citrate and EDTA. Los Alamos National Laboratory. Carlsbad, NM. Report LCO-ACP-29, Revision 0. LA-UR-22-32478. *

Kutahyali Aslani, C. 2024. Effects of Borate and Organics on U(VI) Solubility in WIPP Brine. Los Alamos National Laboratory. Carlsbad, NM. Report LCO-ACP-33, Revision 1. *

Kutahyali Aslani, C., U. Kaplan, A. Navarrette, J. Potter, and J. Icenhower. 2024. Uranium (VI) Solubility Behavior in WIPP-Specific Brine and in the Presence of WIPP-Relevant Organics. Presented at Plutonium Futures-The Science Conference. Sept. 8-12, 2024. Charleston, SC. LA-UR-24-29582. *

Kutahyali Aslani, C. 2025. Effect of Citrate on the Solubility of Uranium (VI) in WIPP Brine. Los Alamos National Laboratory. Carlsbad, NM. Report LCO-ACP-43, Revision 0. *

Kuzenkova, A.S., T.V. Plakhova, I.M. Nevolin, E.S. Kulikova, A.L. Trigub, V.O. Yapaskurt, M.D. Shaulskaya, D.M. Tsymbarenko, A.Y. Romanchuk, and S.N. Kalmykov. 2023. Formation of Neptunium(V) Carbonates: Examining the Forceful Influence of Alkali and Alkaline Earth Cations. Inorg. Chem. 62: Article e3c03185. *

Lee, J.-Y., S. Amayri, V. Montoya, D. Fellhauer, X. Gaona, and M. Altmaier. 2019. Solubility and Stability of Liebigite, $Ca_2UO_2(CO_3)_3{\cdot}10H_2O$(cr), in Dilute to Concentrated NaCl and $NaClO_4$ Solutions at T = 22–80 °C. Appl. Geochem. 111: 104374. *

Lemire, R.J., J. Fuger, H. Nitsche, P. Potter, M.H. Rand, J. Rydberg, K. Spahiu, J.C. Sullivan, W.J. Ullman, P. Vitorge, and H. Wanner. 2001. Chemical Thermodynamics of Neptunium and Plutonium. Elsevier. Amsterdam. Chemical Thermodynamics vol. 4. OECD NEA.

Li, D.-D., Z. Zhang, J.-N. Wang, P. Zhang, Y. Liu, and Y-Z. Li. 2023. Estimate of the Degradation Potentials of Cellulose, Xylan, and Chitin Across Global Prokaryotic Communities. Environ. Microbiol. 25: 397-409. *

Lierse, C., W. Treiber, and J.I. Kim. 1985. Hydrolysis Reactions of Neptunium(V). Radiochim. Acta. 38: 27-28. *

Lieser, K.H. and U. Mühlenweg. 1988. Neptunium in the Hydrosphere and in the Geosphere – I. Chemistry of Neptunium in the Hydrosphere and Sorption of Neptunium from Groundwaters on Sediments under Aerobic and Anaerobic Conditions. Radiochim. Acta, 43, 27. *

Lin, M.R., P. Paviet-Hartmann, Y. Xi, and W.H. Runde. 1998. Uranyl Compounds in NaCl Solutions: Structure, Solubility and Thermodynamics. Abstract for the National Meeting of the American Chemical Society, Division of Environmental Chemistry, Boston: 23-27 August. 216th ACS National Meeting: Preprints of Extended Abstracts, vol. 38: 208.

Lloyd, J.R. and L.E. Macaskie. 2002. Biochemical Basis of Microbe-Radionuclide Interactions. In Interactions of Microorganisms with Radionuclides. M.J. Keith-Roach and F.R. Livens, editors. London: Elsevier Science Ltd. pp. 313-342.

Lopez-Fernandez, M., F. Jroundi, M.A. Ruiz-Fresneda, and M.L. Merroun. 2021. Microbial Interaction with and Tolerance of Radionuclides: Underlying Mechanisms and Biotechnological Applications. Microb. Biotechnol. 14: 810-828. *

Lucchini, J.-F., H. Khaing, M. Borkowski, M.K. Richmann, and D.T. Reed. 2010a. Actinide (VI) Solubility in Carbonate-free WIPP Brine: Data Summary and Recommendations. Los Alamos National Laboratory. Carlsbad, NM. Report LCO-ACP-10, Revision 0. LA-UR-10-00497.

Lucchini, J.-F., H. Khaing, and D.T. Reed. 2010b. Uranium (VI) Solubility in Carbonate-Free ERDA-6 Brine. Scientific Basis for Nuclear Waste Management XXXIV, edited by K.L. Smith, S. Kroeker, B. Uberuaga, K.R. Whittle, Mater. Res. Soc. Symp. P. 1265: 21-26.

Lucchini, J.-F., M.K. Richmann, and M. Borkowski. 2013a. Uranium (VI) Solubility in WIPP Brine. Los Alamos National Laboratory. Carlsbad, NM. Report LCO-ACP-14, Revision 0. LA-UR-13-20786.

Lucchini, J.-F., M. Borkowski, M.K. Richmann, and D.T. Reed. 2013b. Uranium (VI) Solubility in Carbonate-Free WIPP Brine. Radiochim. Acta 101: 391-398.

Lucchini, J.-F., M. Borkowski, H. Khaing, M.K. Richmann, J. Swanson, K. Simmons, and D.T. Reed. 2013c. WIPP Actinide-Relevant Brine Chemistry. Los Alamos National Laboratory. Carlsbad, NM. Report LCO-ACP-15, Revision 0. LA-UR-13-20620.

Lumetta, G.J., M.C. Thompson, R.A. Penneman, and P.G. Eller. 2006. Curium. In: The Chemistry of the Actinide and Transactinide Elements, 3rd ed. Morss, L.R., N.M. Edelstein, and J. Fuger, eds. Springer: Dordrecht, Netherlands. pp. 1397-1443. *

Maiwald, M.M., A. Skerencak-Frech, and P.J. Panak. 2018. The Complexation and Thermodynamics of Neptunium(V) with Acetate in Aqueous Solution. New. J. Chem. 42: 7796. *

Maiwald, M.M., M. Trumm, K. Dardenne, J. Rothe, A. Skerencak-Frech, and P.J. Panak. 2020. Speciation, Thermodynamics and Structure of Np(V) Oxalate Complexes in Aqueous Solution. Dalton T. 49: 13359-13371. *

Malmbeck, R. and N.L. Banik. 2020. Radiolytic Behavior of a TODGA Based Solvent under Alpha Irradiation. J. Radioanal. Nucl. Chem. 326: 1609-1615. *

Mariner, P.E. 2025. Memorandum to the WIPP Records Center. Subject: CRA-2026 IS Updates to the WIPP Humic Colloids Models for An(III) and An(IV). July 9, 2025. Sandia National Laboratories. Albuquerque, NM. *

Martin, P., S. Grandjean, C. Valot, G. Carlot, M. Ripert, P. Blanc, and C. Hennig. 2007. XAS Study of (U1-yPuy)O2 Solid Solutions. J. Alloy Compd. 444–445(SPEC. ISS.): 410–414. *

McLean, E., A. Popel, and I. Farnan. 2025. Inhibition of Uranium Dissolution in Mixed Uranium Thorium Dioxide under Geological Disposal Conditions. J. Nucl. Mater.: 605: 155568. *

Megaw, J., S.A. Kelly, T.P. Thompson, T. Skvortsov, and B.F. Gilmore. 2019. Profiling the Microbial Community of a Triassic Halite Deposit in Northern Ireland: an Environment with Significant Potential for Biodiscovery. FEMS Microbiol. Lett. 366: fnz242. *

Micheau, C., M. Virot, S. Dourdain, T. Dumas, D. Menut, P.L. Solari, L. Venault, O. Diat, P. Moisy, and S.I. Nikitenko. 2020. Relevance of Formation Conditions to the Size, Morphology and Local Structure of Intrinsic Plutonium Colloids. Environ. Sci.: Nano, 7, 2252-2266. *

Miralles-Robledillo, J.M., E. Bernabeu, M. Giani, E. Martínez-Serna, R.M. Martínez-Espinoza, and C. Pire. 2021. Distribution of Denitrification among Halarchaea: a Comprehensive Study. Microorganisms 9: 1669. *

Moniruzzaman, M., T. Kobayashi, and T. Sasaki. 2020. Solubility and solid phase of trivalent lanthanide hydroxides and oxides. J. Nucl. Radiochem. Sci. 20: 32-42. *

Moniruzzaman, M., T. Kobayashi, and T. Sasaki. 2021. Solubility of Mixed Lanthanide Hydroxide and Oxide Solid Solutions. J. Nucl. Fuel Cycle Waste Technol. 19: 353-366.Neck, V., W. Runde, and J.I. Kim. 1995. Solid-Liquid Equilibria of Np(V) in Carbonate Solutions at Different Ionic Strengths: II. J. Alloy Compd. 225: 295–302.

Neck, V. and J.I. Kim. 2001. Solubility and Hydrolysis of Tetravalent Actinides. Radiochim. Acta 89: 1–16.

Nemer, M. and J. Stein. 2005. Analysis Package for BRAGFLO: 2004 Compliance Recertification Application Performance Assessment Baseline Calculation. ERMS 540527. Sandia National Laboratories. Albuquerque, NM.

Neretnieks, I. 1982. The Movement of a Redox Front Downstream from a Repository for Nuclear Waste. Stockholm: Svensk Kärnbränsleforsorjning AB. KBS Report TR 82-16.

Nisbet, H., A. Migdisov, A. Williams-Jones, H. Xu, V. van Hinsberg, and R. Roback. 2019. Challenging the Thorium-Immobility Paradigm. Nature Sci. Rep. 9: 17035. *

Nishikawa, S., T. Kobayashi, T. Sasaki, and I. Takagi. 2018. Solubilities and Solubility Products of Thorium Hydroxide under Moderate Temperature Conditions. Radiochim. Acta 106: 655-667. *

Nishinaga T. 2016. Thermodynamics for Understanding Crystal Growth. Prog. Cryst. Growth Ch. 62: 43-57.

Nishizawa, T. 2008. Thermodynamics of Microstructures. pp. 47-53. ASM International: Materials Park, OH. www.asminternational.org.

Nitsche, H., A. Müller, E.M. Standifer, R.S. Deinhammer, K. Becraft, T. Prussin, and R.C. Gatti. 1992. Dependence of Actinide Solubility and Speciation on Carbonate Concentration and Ionic Strength in Groundwater. Radiochim. Acta 58/59: 27-32.

Novak, C.F., H. Nitsche, H.B. Silber, K. Roberts, Ph. C. Torretto, T. Prussin, K. Becraft, S.A. Carpenter, D.E. Hobart, and I. Al Mahamid. 1996. Neptunium(V) and Neptunium(VI) Solubilities in Synthetic Brines of Interest to the Waste Isolation Pilot Plant (WIPP). Radiochim. Acta 74: 31-36. *

Novak, C. F., I. Al Mahamid, and K.A. Becraft. 1997. Measurement and Thermodynamic Modeling of Np(V) Solubility in Aqueous K_2CO_3 Solutions to High Concentrations. J. Solution Chem. 26: 1135–1151.

Nuclear Energy Agency, Thermochemical Database Project (NEA-TDB). 2020. Second Update on the Chemical Thermodynamics of U, Np, Pu, Am, and Tc, Vol 14. Organization for Economic Cooperation and Development (OECD) Publishing; Paris. https://doi.org/10.1787/bf86a907-en *

Oakes, C.S., A.L. Ward, N. Chugunov, and J. Icenhower. 2021. A speciated, conventional Pitzer ion-interaction model for the aqueous Nd^{3+}–H^+–Na^+–K^+–Ca^{2+}–Cl^-–OH^- system at 298 K and 0.1 MPa. Geochim. Cosmochim. Ac. 297: 308–327. *

Okajima, S. and D.T. Reed. 1993. Initial Hydrolysis of Pu(VI). Radiochim. Acta 60: 173–84.

Oren, A. 2011. Thermodynamic Limits to Microbial Life at High Salt Concentrations. Environ. Microbiol. 13: 1908-1923.

Orlandini, J.A., W.R. Penrose, and D.M. Nelson. 1986. Pu(V) as the Stable form of Oxidized Plutonium in Natural Waters. Mar. Chem. 18: 49–57.

Östhols, E., J. Bruno, and I. Grenthe. 1994. On the Influence of Carbonate on Mineral Dissolution: III: The Solubility of Microcrystalline ThO_2 in CO_2-H_2O Media. Geochim. Cosmochim. Ac. 58: 613–623.

Pan, C., Y. Jiao, A.B. Kersting, and M. Zavarin. 2021. Plutonium Redox Transformation in the Presence of Iron, Organic Matter, and Hydroxyl Radicals: Kinetics and Mechanistic Insights. Environ. Sci. Technol. 55: 1800-1810.*

Pan, Z., B. Bártová, T. LaGrange, S.M. Butorin, N.C. Hyatt, M.C. Stennett, K.O. Kvashnina, and R. Bernier-Latmani. 2020. Nanoscale Mechanism of UO_2 Formation through Uranium Reduction by Magnetite. Nat. Commun. 11:4001. *

Paris, E.R., N. Arandia-Gorostidi, B. Klempay, J.S. Bowman, A. Pontefract, C.E. Elbon, J.B. Glass, E.D. Ingall, P.T. Doran, S.M. Som, B.E. Schmidt, and A.E. Dekas. 2023. Single-Cell Analysis in Hypersaline Brines Predicts a Water-Activity Limit of Microbial Anabolic Activity. Sci. Adv. 9: eadj3594. *

Pathak, V.M. and Navneet. 2017. Review on the Current Status of Polymer Degradation: a Microbial Approach. Bioresour. Bioprocess. 4: 15. *

Payler, S.J., J.F. Biddle, B. Sherwood Lollar, M.G. Fox-Powell, T. Edwards, B.T. Ngwenya, S.M. Paling, and C.S. Cockell. 2019. An Ionic Limit to Life in the Deep Subsurface. Front. Microbiol. 10: 426. *

Pedersen, K. 2005. Microorganisms and Their Influence on Radionuclide Migration in Igneous Rock Environments. J. Nucl. Radiochem. Sci. 6: 11-15.

Petrov, V.G., D. Fellhauer, X. Gaona, K. Dardenne, J. Rothe, S.N. Kalmykov, and M. Altmaier. 2017. Solubility and Hydrolysis of Np(V) in Dilute to Concentrated Alkaline NaCl Solutions: Formation of Na-Np(V)-OH Solid Phases at 22 ˚C. Radiochim. Acta 105: 1-20. *

Piñar, G., D. Dalnodar, C. Voitl, H. Reschreiter, and K. Sterflinger. 2016. “Biodeterioration Risk Threatens the 3100 Year Old Staircase of Hallstatt (Austria): Possible Involvement of Halophilic Microorganisms”. PLoS ONE 11: e0148279. *

Pitzer, K.S. 1973. Thermodynamics of Electrolytes. I. Theoretical Basis and General Equations. J. Phys. Chem. 77: 268-277.

Plyasunov, A.V. 2023. The SIT Model Parameters for Interactions of Uranyl Ion with Chloride and Nitrate Ions. J. Solution Chem. 52: 3–18.

Popielak, R.S., R.L. Beauheim, S.R. Black, W.E. Coons, C.T. Ellingson, and R.L. Olsen. 1983. Brine Reservoirs in the Castile Formation, Waste Isolation Pilot Plant (WIPP) Project, Southeastern New Mexico. TME 3153. U.S. Department of Energy. Carlsbad, NM.

Porter, D., A.N. Roychoudhury, and D. Cowan. 2007. Dissimilatory Sulfate Reduction in Hypersaline Coastal Pans: Activity across a Salinity Gradient. Geochim. Cosmochim. Ac. 71: 5102-5116.

Porter, D.A., K.E. Easterling, and M.Y. Sherif. 2009. Phase Transformations in Metals and Alloys. 3rd ed. pp. 1-61. CRC Press: Boca Raton, FL.

Pryke, D.C. and J.H. Rees. 1986. Understanding the Behaviour of the Actinides Under Disposal Conditions: A Comparison between Calculated and Experimental Solubilities. Radiochim. Acta 40: 27–32.

Rai, D., R.G. Strickert, and G.L. McVay. 1982. Neptunium Concentrations in Solutions Contacting Actinide-Doped Glass. Nucl. Technol. 58: 69–76.

Rai, D. and J.L. Ryan. 1985. Neptunium (IV) Hydrous Oxide Solubility under Reducing and Carbonate Conditions. Inorg. Chem. 24: 247–251.

Rai, D., Y. Gorby, J. Fredrickson, D. Moore, and M. Yui. 2002. Reductive Dissolution of PuO_2(am): The Effect of Fe(II) and Hydroquinone. J. Solution Chem. 32: 433-453.

Rai, D., D.A. Moore, K.M. Rosso, A.R. Felmy, and H. Bolton. 2008. Environmental Mobility of Pu(IV) in the Presence of Ethylenediaminetetraacetic Acid: Myth or Reality? J. Solution Chem. 37: 957–986. *

Reed, D.T. and D.R. Wygmans. 1997. Actinide Stability/Solubility in Simulated WIPP Brines (March 21). WPO44625. Actinide Speciation and Chemistry Group, Chemical Technology Group. Argonne National Laboratory. Argonne, IL.

Reed, D.T., S.B. Aase, D. Wygmans, and J.E. Banaszak. 1998. The Reduction of Np(VI) and Pu(VI) by Organic Chelating Agents. Radiochim. Acta 82: 109-114.

Reed, D.T., J.-F. Lucchini, S.B. Aase, and A.J. Kropf. 2006. Reduction of Plutonium (VI) in Brine under Subsurface Conditions. Radiochim. Acta 94: 591–597.

Reed, D.T., S.E. Pepper, M.K. Richmann, G. Smith, R. Deo, and B.E. Rittmann, 2007. Subsurface Bio-Mediated Reduction of Higher-Valent Uranium and Plutonium. J. Alloy. Compd. 444/445: 376–382.

Reed, D.T., J.-F. Lucchini, M. Borkowski, and M.K. Richmann. 2010. Reduction of Higher Valent Plutonium by Iron under Waste Isolation Pilot Plant (WIPP) Relevant Conditions: Data Summary and Recommendations. Los Alamos National Laboratory. Carlsbad, NM. Report. LCO-ACP-09, Revision 0.

Reed, D.T., J.S. Swanson, J.-F. Lucchini, and M.K. Richmann. 2013. Intrinsic, Mineral, and Microbial Colloid Enhancement Parameters for the WIPP Actinide Source Term. Los Alamos National Laboratory. Carlsbad, NM. Report LCO-ACP-18, Revision 0. LA-UR-13-20858.

Reed, D., J. Swanson, and F. Stanley. 2019. LANL/ACRSP Parameter Recommendations for the CRA-2019 Deferred Performance Assessment. Los Alamos National Laboratory. Carlsbad, NM. Report LCO-ACP-24, Revision 1. LA-UR-19-22787.

Reich, T., G. Bernhard, and G. Geipel. 2000. The Rossendorf Beam Line ROBL – A Dedicated Experimental Station for XAFS Measurements of Actinides and Other Radionuclides. Radiochim. Acta, 88: 633–637. *

Reich, T., G. Geipel, H. Funke, C. Hennig, A. Rossberg, and G. Bernhard. 2001. XANES and EXAFS Measurements of Plutonium Hydrates. Biannual Report 1999/2000 Project Group ESRF-Beamline (ROBL-CRG), FZR-322. *

Reiller, P.E. 2024. Predominance of the Alkaline Earth(II) Triscarbonatoactinyl(VI) Complexes in Different Geochemical Contexts: Review of Existing Data and Estimation of Potentially Unidentified Species. Chemosphere. 350: 141049. *

Roedder, E. 1984. The Fluids in Salt. Am. Mineral. 69: 413-439. *

Rogiers, T., J. Claesen, A. van Gompel, N. Vanhoudt, M. Mysara, A. Williamson, N. Leys, R. van Houdt, N. Boon, and K. Mijnendonck. 2021. Soil Microbial Community Structure and Functionality Changes in Response to Long-Term Metal and Radionuclide Pollution. Environ. Microbiol. 23: 1670-1683. *

Rojo, H., X. Gaona, T. Rabung, R. Polly, M. García-Gutierrez, T. Missana, and M. Altmaier. 2021. Complexation of Nd(III)/Cm(III) with Gluconate in Alkaline NaCl and $CaCl_2$ Solutions: Solubility, TRLFS and DFT Studies. Appl. Geochem. 126: 104864. *

Ruiz-Fresneda, M.A., M.F. Martinez-Moreno, C. Povedano-Priego, M. Morales-Hidalgo, F. Jroundi, and M.L. Merroun. 2023. Impact of Microbial Processes on the Safety of Deep Geological Repositories for Radioactive Waste. Front. Microbiol. 14: 1134078. *

Runde, W. 2000. The Chemical Interactions of Actinides in the Environment. Los Alamos Science 26: 330-411.

Runde, W.H. and W.W. Schulz. 2006. Americium. In: The Chemistry of the Actinide and Transactinide Elements, 3rd ed. Morss, L.R., N.M. Edelstein, and J. Fuger, eds. Springer: Dordrecht, Netherlands. pp. 1265-1396. *

Sanchez, A.L., J.W. Murray, and T.H. Sibley. 1985. The Adsorption of Plutonium IV and V on Geothite. Geochim. Cosmochim. Ac. 49: 2297-2307.

Schmeide, K., T. Reich, S. Sachs, and G. Bernhard. 2006. Plutonium(III) Complexation by Humic Substances Studied by X-Ray Absorption Fine Structure Spectroscopy. Inorg. Chim. Acta 359: 237–242. *

Schramke, J.A., E.F.U. Santillan, and R.T. Peake. 2020. Plutonium Oxidation States in the Waste Isolation Pilot Plant Repository. Appl. Geochem. 116: 104561-104576.*

Schwab, L., L. Prinsen, G. Nowack, D. Popp, M. Noll, C. Vogt, and M. Wagner. 2023. Sulfate Reduction and Homoacetogenesis at Various Hypersaline Conditions: Implications for H2 Underground Gas Storage. Front. Energy Res. 11:1125619. *b

Serne, R.J., K.J. Cantrell, C.W. Lindenmeier, A.T. Owen, I.V. Kutnyakov, R.D. Orr, and A.R. Felmy. 2002. Radionuclide-Chelating Agent Complexes in Low-Level Radioactive Decontamination Waste; Stability, Adsorption and Transport Potential. U.S. Nuclear Regulatory Commission NUREG/CR-6758, PNNlL13774. *

Shannon, R.D. 1976. Revised Effective Ionic Radii and Systematic Studies of Interatomic Distances in Halides and Chalcogenides. Acta Crystallogr. A32: 751–67.

Siham, A.-T., J.-T. Souad, K.-G. Salima, L.-I. Nesrine, K.M. Amine, S. Amna, B. Ghania, F. Imen, M. Wafa, and N. Afef. 2020. Diversity of Culturable Halophilic Archaea and Bacteria from Chott Tinsilt and El Malah Salt-Lake in Algeria. Current Res. Bioinform. 8: 46-54. *

Silva, R.J. and H. Nitsche. 1995. Actinide Environmental Chemistry. Radiochim. Acta 70/71: 377-396.

Simonnet, M., N. Barré, R. Drot, C. Le Naour, V. Sladkov, and S. Delpech. 2016. Multiparametric Study of Thorium Oxide Dissolution in Aqueous Media. Radiochim. Acta. 104: 691–700. DOI: org/10.1515/ract-2016-2607.

Smith, K.F., K. Morris, G.T.W. Law, E.H. Winstanley, F.R. Livens, J.S. Weatherill, L.G. Abrahamsen-Mills, N.D. Bryan, J.F.W. Mosselmans, G. Cibin, S. Parry, R. Blackham, K.A. Law, and S. Shaw. 2019. Plutonium(IV) Sorption during Ferrihydrite Nanoparticle Formation. ACS Earth Space Chem. 3: 2437-2442. *

Snider A.C. 2003. Verification of the Definition of Generic Weep Brine and the Development of a Recipe for this Brine. Sandia National Laboratories; Albuquerque, NM. ERMS 527505.

Sorokin, D.Y. and G. Muyzer. 2010. Bacterial Dissimilatory MnO_2 Reduction at Extremely Haloalkaline Conditions. Extremophiles 14: 41-46.

Sorokin, D.Y., S.V. Toshchakov, T.V. Kolganova, and I.V. Kublanov. 2015. Halo(natrono)archaea Isolated from Hypersaline Lakes Utilize Cellulose and Chitin as Growth Substrates. Front. Microbiol. 6: article 942.

Sorokin, D.Y., T.V. Khijniak, N.A. Kostrikina, A.G. Elcheninov, S.V. Toshchakov, N.J. Bale, J.S. Sinninghe Damsté, and I.V. Kublanov. 2018. *Natronobiforma cellulositropha* gen. nov., sp. nov., a Novel Haloalkaliphilic Member of the Family *Natrialbaceae* (Class Halobacteria) from Hypersaline Alkaline Lakes. Syst. Appl. Microbiol. 41: 355-362. *

Sorokin, D.Y., T.V. Khijniak, A.G. Elcheninov, S.V. Toshchakov, N.A. Kostrikina, N.J. Bale, J.S. Sinninghe Damsté, and I.V. Kublanov. 2019. *Halococcoides cellulosivorans* gen. nov., sp. nov., an Extremely Halophilic Cellulose-Utilizing Haloarchaeon from Hypersaline Lakes. Int. J. Syst. Evol. Micro. 69: 1327-1335. *

Swanson, J.S., D.M. Norden, H.M. Khaing, and D.T. Reed. 2013a. Degradation of Organic Complexing Agents by Halophilic Microorganisms in Brines. Geomicrobiol. J. 30: 189-198.

Swanson, J., K. Simmons, D. Norden, and D. Reed. 2013b. Microbial Characterization of Halite and Groundwater Samples from the WIPP. Los Alamos National Laboratory. Carlsbad, NM. Report LA-UR-13-26280. *

Swanson, J., D. Reed, M. Richmann, and D. Cleveland. 2015. Investigation into the Post-Excavation Sources of Methane from INL TRU Waste Drums. Los Alamos National Laboratory. Carlsbad, NM. LA-UR-15-26657.

Swanson, J. 2017. The Projected Impact of Microbial Activity on the Performance of a Salt-Based Nuclear Waste Repository: the Waste Isolation Pilot Plant. Oral presentation ABC-SALT V, Ruidoso, NM (March 2017). LA-UR-17-22431. *

Swanson, J.S. and D.T. Reed. 2018. Update on Microbiology Research for the Waste Isolation Pilot Plant. Los Alamos National Laboratory. Carlsbad, NM. LA-UR-18-31313.

Swanson, J.S., F.E. Stanley, and D.T. Reed. 2019. Review of the Microbial Colloid Contribution to the WIPP Actinide Source Term. Los Alamos National Laboratory. Carlsbad, NM. Report LCO-ACP-23, Revision 0. LA-UR-19-22310.

Swanson, J.S., M. Bader, and A. Cherkouk. 2021a. Potential Microbial Influence on the Performance of Subsurface, Salt-Based Nuclear Waste Repositories. In: The Microbiology of Nuclear Waste Disposal. J.R. Lloyd and A. Cherkouk, editors. Amsterdam: Elsevier Inc. pp. 97-117. *

Swanson, J., A. Navarrette, C. Hazelton, M. Richmann, and F. Stanley. 2021b. Biomass and Salt-Dependent Effects of *Bacillus* Spores on Radionuclide Migration from the Waste Isolation Pilot Plant. Chemosphere 280: 130680. *

Swanson, J. 2022. Effects of Salt Concentration, Ionic Strength, and Water Activity on the Growth of a WIPP Archaeal Isolate, *Halobacterium* sp. Los Alamos National Laboratory. Carlsbad, NM. Report LCO-ACP-28, Revision 0. LA-UR-22-32424. *

Swanson, J., A. Navarrette, J. Knox, H. Kim, and F. Stanley. 2023. Microbial Influence on the Mobility of +3 Actinides from a Salt-Based Nuclear Waste Repository. Microorganisms 11: 1370.*

Swanson, J. 2024a. Biologically Influenced Transport of the +3 Actinide Oxidation State from the WIPP Environment, Using Neodymium as an Analog. Los Alamos National Laboratory. Carlsbad, NM. Report LCO-ACP-32, Revision 1. *

Swanson, J. 2024b. Microbial Influence on Radionuclide Transport Through the Culebra. Los Alamos National Laboratory. Carlsbad, NM. Report LCO-ACP-37, Revision 0. *

Tang, H., W. Cheng, Y. Yi, C. Ding, and X. Nie. 2021. Nano Zero Valent Iron Encapsulated in Graphene Oxide for Reducing Uranium. Chemosphere 278: 130229. *

Tasi, A., X. Gaona, D. Fellhauer, M. Böttle, J. Rothe, K. Dardenne, D. Schild, M. Grivé, E. Colàs, J. Bruno, K. Källström, M. Altmaier, and H. Geckeis. 2018. Redox Behavior and Solubility of Plutonium under Alkaline, Reducing Conditions. Radiochim. Acta 106: 259-279.

Thakur, P., Y. Xiong, and M. Borkowski. 2015. An Improved Thermodynamic Model for the Complexation of Trivalent Actinides and Lanthanide with Oxalic Acid Valid to High Ionic Strength. Chem. Geol. 413: 7-17. *

Theodorakopoulos, N., L. Février, M. Barakat, P. Ortet, R. Christen, L. Piette, S. Levchuk, K. Beaugelin-Seiller, C. Sergeant, C. Berthomieu, and V. Chapon. 2017. Soil Prokaryotic Communities in Chernobyl Waste Disposal Trench T22 are Modulated by Organic Matter and Radionuclide Contamination. FEMS Microbiol. Ecol. 93: fix079. *

Thompson, T.P., S.A. Kelly, T. Skvortsov, G. Plunkett, A. Ruffell, J.E. Hallsworth, J. Hopps, and B.F. Gilmore. 2021. Microbiology of a NaCl Stalactite 'Salticle' in Triassic Halite. Environ. Microbiol. 23: 3881-3895. *

Toste, A.P. 1992. Degradation of Chelating and Complexing Agents in an Irradiated, Simulated Mixed Waste. J. Radioanal. Nucl. Chem. 161: 549-559. *

Toste, A.P. and T.J. Lechner-Fish. 1993. Chemo-Degradation of Chelating and Complexing Agents in a Simulated, Mixed Nuclear Waste. Waste M. 13: 237-244. *

Townsend, L.T., K.F. Smith, E.H. Winstanley, K. Morris, O. Stagg, J.F.W. Mosselmans, F.R. Livens, L. Abrahamsen-Mills, R. Blackham, and S. Shaw. 2022. Neptunium and Uranium Interactions with Environmentally and Industrially Relevant Iron Minerals. Minerals 12: 165. *

Trumm, M., A. Tasi, A. Schnurr, N.A. DiBlasi, and X. Gaona. 2022. Structural Characterisation of Hydrolysed Cm(III)-EDTA Solution Species under Alkaline Conditions: a TRLFS, Vibronic Side-Band and Quantum Chemical Study. Mol. Phys. 120: e2033864. *

Tseng, C.L., C.C. Chan, and P.S. Weng. 1980. Radiolysis of Co(III)-EDTA Solution by Charged Particles through 6Li (n,a) 3H Reaction. Radioisotopes 29: 136-140. *

U.S. Department of Energy (DOE). 1996. Title 40 CFR Part 191 Compliance Certification Application for the Waste Isolation Pilot Plant (October). 21 vols. Carlsbad Field Office. Carlsbad, NM. DOE/CAO-1996-2184.

U.S. DOE. 1996. Title 40 CFR Part 191 Compliance Certification Application for the Waste Isolation Pilot Plant, Appendix SOTERM. Title 40 CFR Part 191, Subparts B and C. Actinide Chemistry Source Term. 1996. United States Department of Energy/Waste Isolation Pilot Plant. Carlsbad Field Office. Carlsbad, NM.

U.S. DOE. 2004. Title 40 CFR Part 191 Compliance Recertification Application for the Waste Isolation Pilot Plant (March). 10 vols. Carlsbad Field Office. Carlsbad, NM. DOE/WIPP 2004-3231.

U.S. DOE. 2019. Title 40 CFR Part 191 Subparts B and C. Compliance Recertification Application for the Waste Isolation Pilot Plant (March 26, 2019 and December 18, 2019). Carlsbad Field Office. Carlsbad, NM. DOE/WIPP 2019-3609.

U.S. Environmental Protection Agency (EPA). 1993. 40 CFR Part 191: Environmental Radiation Protection Standards for the Management and Disposal of Spent Nuclear Fuel, High-Level and Transuranic Radioactive Wastes; Final Rule. Federal Register, vol. 58 (December 20, 1993): 66398–416.

U.S. EPA. 2005. Letter from E. Cotsworth to I. Triay (US DOE-CBFO). Subject: Conducting the Performance Assessment Baseline Change Verification Test. March 2005.

U.S. EPA. 2006. Technical Support Document for Section 194.24: Evaluation of the Compliance Recertification – Actinide Source Term and Culebra Dolomite Distribution Coefficient Values. Washington, DC: Office of Radiation and Indoor Air, Docket A-98-49, Item II-B1-3 (March 2006).

U.S. EPA. 2022. Technical Support Document for Section 194.24: Evaluation of the Compliance Recertification Application (CRA-2019) Actinide Source Term, Gas Generation, Backfill Efficacy, Water Balance, and Culebra Dolomite Distribution Coefficient Values. Washington, DC: Office of Radiation and Indoor Air, EPA-HQ-OAR-2019-0534 (March 2022). *

Vandenborre, J., B. Grambow, and A. Abdelouas. 2010. Discrepancies in Thorium Oxide Solubility Values: Study of Attachment/Detachment Processes at the Solid/Solution Interface. Inorg. Chem. 49: 8736-8748.

Van Soest, G. 2018. Performance Assessment Inventory Report – 2018 (PAIR 2018). Los Alamos National Laboratory. Carlsbad, NM. INV-PA-18. LA-UR-18-31882.

Van Soest, G. 2025. Interim State Performance Assessment Inventory Report – 2024 (IS PAIR 2024). Los Alamos National Laboratory. Carlsbad, NM. INV-PA-24, Revision 0. *

Vitova, T., I. Pidchenko, D. Schild, T. Prüßmann, V. Montoya, D. Fellhauer, X. Gaona, E. Bohnert, J. Rothe, R.J. Baker, and H. Geckeis. 2020. Competitive Reaction of Neptunium(V) and Uranium-

(VI) in Potassium-Sodium Carbonate-Rich Aqueous Media: Speciation Study with a Focus on High-Resolution X-Ray Spectroscopy. Inorg. Chem. 59: 8−22. *

Vreeland, R.H., A.F. Piselli, Jr., S. McDonnough, and S.S. Meyers. 1998. Distribution and Diversity of Halophilic Bacteria in a Subsurface Salt Formation. Extremophiles 2: 321-331.

Wang, Y. and L. Brush. 1996. Memorandum to Martin S. Tierney. Subject: Estimates of Gas Generation Parameters for the Long-Term WIPP Performance Assessment. January 26, 1996. Albuquerque, NM: Sandia National Laboratories. WPO# 35162.

Wang, Y. and A.J. Francis. 2005. Evaluation of Microbial Activity for Long-Term Performance Assessments of Deep Geologic Nuclear Waste Repositories. J. Nucl. Radiochem. Sci. 6: 43-50.

Wang, Y., S. Kim, M.C. Marcano, Y. Cao, and U. Becker. 2022. Effect of EDTA Complexation on the Kinetics and Thermodynamics of Uranium Redox Reactions Catalyzed by Pyrite: A Combined Electrochemical and Quantum-Mechanical Approach. ACS Earth Space Chem. 6, 830−846. *

White, A.F., A. Yee, and S. Flexer. 1985. Surface Oxidation-Reduction Kinetics Associated with Experimental Basalt-Water Reactions at 25˚C. Chem. Geol. 49: 73-86.

Willberger, C., D. Leichtfuß, S. Amayri, and T. Reich. 2019. Determination of the Stability Constants of the Acetate Complexes of the Actinides Am(III), Th(IV), Np(V), and U(VI) Using Capillary Electrophoresis-Inductively Coupled Plasma Mass Spectrometry. Inorg. Chem. 58, 4851−4858. *

Wolery, T.J. 2013. EQ3/6 – Software for Geochemical Modeling, Version 8.0a. LLNL-CODE-2013-683958. Lawrence Livermore National Laboratory. Livermore, CA.

Xiong, Y. and Y. Wang. 2021a. Uranyl Oxalate Species in High Ionic Strength Environments: Stability Constants for Aqueous and Solid Uranyl Oxalate Complexes. Radiochim. Acta 109: 177–185. *

Xiong, Y. and Y. Wang. 2021b. Experimental and Modeling Studies of Pr and Nd Oxalate Solubility to High Ionic Strengths: Insight into Actinide(III) Oxalates. Chem. Geol. 573: 120200. *

Xiong, Y., G. Xu, and Y. Wang. 2023. A Thermodynamic Model for Nd(III)–Sulfate Interaction at High Ionic Strengths and Elevated Temperatures: Applications to Rare Earth Element Extraction. J. Solution Chem. 52: 447–466. *

Yalçıntaş, E., N. Cevirim-Papaioannou, X. Gaona, D. Fellhauer, V. Neck, and M. Altmaier. 2019. Solubility of U(VI) in Chloride Solutions. III. The Stable Oxides/Hydroxides in $MgCl_2$ Systems: Pitzer Activity Model for the System UO_2^{2+}–Na^+–K^+–Mg^{2+}–H^+–OH^-–Cl^-–H_2O(l). J. Chem. Thermodyn. 131: 375–386.

Yamazaki, H., B. Lagerman, V. Symeopoulos, and G.R. Choppin. 1992. Solubility of Uranyl in Brine. Radioact. W. 1992: 1607–1611.

Yan, Y., N. Çevirim-Papaioannou, X. Gaona, D. Fellhauer, and M. Altmaier. 2024. Thermodynamic Description of U(IV) Solubility and Hydrolysis in Chloride Systems: Pitzer Activity Model for the System U^{4+}–Na^{+}–Mg^{2+}–Ca^{2+}–H^{+}–Cl^{-}–OH^{-}–H_2O(l). Appl. Geochem. 171 (2024): 106091. *

Yang, H., D. Cui, D. Grolimund, V.V. Rondinella, R. Brutsch, M. Amme, C. Kutahyali, A.T. Wiss, A. Puranen, and K. Spahiu. 2017. Reductive Precipitation of Neptunium on Iron Surfaces under Anaerobic Conditions. J. Nucl. Mater. 496: 109-116.

Yang, S., Z. Li, and P. Pan. 2023. Americium Solubility and Solubility Limiting Solid Phase (SLSP) Analysis in Groundwater of Beishan, a Proposed Site for the Disposal of High-Level Radioactive Waste in China. Appl. Geochem. 152: 105650. *

Zhang, H., Y. Ruan, A. Liang, K. Shih, Z. Diao, M. Su, L. Hou, D. Chen, H. Lu, and L. Kong. 2019. Carbothermal Reduction for Preparing NZVI/BC to Extract Uranium: Insight into the Iron Species Dependent Uranium Adsorption Behavior. J. Clean. Prod. 239: 117873. *

Zhao, X., W. Liu, Z. Cai, J. Fu, J. Duan, D. Zhao, M. Bozack, and Y. Feng. 2020. Reductive Immobilization of Uranium by Stabilized Zero-Valent Iron Nanoparticles: Effects of Stabilizers, Water Chemistry and Long-Term Stability. Colloid. Surface. A 604: 125315. *

Zhou, Y., Y. Wang, and H. Li. 2019a. Plutonium Speciation in Groundwater: A Comprehensive Study. J. Environ. Radioactiv. 205: 45–54. *

Zhou, X., H. Dang, X. Han, W. Li, Y. Wang, W. Wang, and N. Chai. 2019b. The Speciation, Transformation Kinetics and Fate of Spiked Pu (IV) in Highly Saline Groundwater. J. Contam. Hydrol. 225: 103505-103512. *

Zhou, W., X. Wang, and C. Liu. 2025. Solubility, Speciation and Sorption Calculation of Americium in Far-Field and Near-Field Beishan Groundwaters. J. Radioanal. Nucl. Ch. 334: 863–872. *

Zimmerman, T., M. Zavarin, and B.A. Powell. 2014. Influence of Humic Acid on Plutonium Sorption to Gibbsite: Determination of Pu-Humic Acid Complexation Constants and Ternary Sorption Studies. Radiochim. Acta 102: 629-643. *